Vibration Signal Analysis for Planetary Gearbox Fault Diagnosis

by

Libin Liu

A thesis submitted in partial fulfillment of the requirements for the degree of

Doctor of Philosophy

Department of Mechanical Engineering
University of Alberta

Abstract

Vibration signal analysis has been widely used for planetary gearbox condition monitoring and fault diagnosis. Vibration signals are normally measured by sensors mounted on a planetary gearbox's housing. A vibration signal contains rich information about the health condition of the machinery. However, the vibration characteristics of a planetary gearbox are quite complicated because of the complex structure and kinematics. In a planetary gearbox, multiple sun-planet gear pairs and multiple ring-planet gear pairs are in mesh simultaneously, introducing multiple vibration sources from the sun gear, the ring gear, and the planet gears. In addition, due to carrier rotation, the multiple vibration sources are subject to different transmission path effects. Multiple vibration sources and the different time-varying transmission path effects lead to challenges with understanding vibration characteristics and diagnosing faults in a planetary gearbox by vibration-based methods.

The aim of this thesis study is to develop effective vibration signal analysis methods for planetary gearbox fault diagnosis. Four research topics are addressed. Firstly, a vibration signal model with transmission path effects is developed to characterize the properties of planetary gearbox vibration signals. Using the model, realistic vibration signals are simulated to aid the development of vibration signal analysis methods for planetary gearbox fault diagnosis in the three remaining research topics. As the second research topic, a spectrogram-free copula-based Time-Frequency Distribution (TFD) construction method is developed for energy density representation of a one-dimensional vibration signal with properties of being positive and free from cross-term interference, with correct energy marginals and high time-frequency resolution. It is applied to planetary gearbox fault diag-

nosis in a simulated case study and an experimental case study. The results show that, being free from the Heisenberg uncertainty principle and with high time-frequency resolution, the identification of fault-related frequencies with fine frequency resolution and the location of fault-induced impulses with fine time resolution can be achieved simultaneously. As the third research topic, a method of fault feature extraction via dimension reduction on the time-frequency energy density of a one-dimensional vibration signal is explored and developed by Non-Negative Matrix Factorization (NNMF). The spectrogram-free copula-based TFD constructed in the second research topic serves as the time-frequency energy density. Validation is performed through a simulated case study and an experimental case study. Inspired by the dependence analysis involved in the second research topic and the third research topic, in the fourth research topic, a dependence-based feature vector is developed for planetary gearbox fault classification. The method is tested based on the dependence between the raw one-dimensional vibration signal and its Intrinsic Mode Functions (IMFs). The IMFs are obtained by the Ensemble Empirical Mode Decomposition (EEMD). The dependence is revealed to be an upper tail dependence described by the Gumbel-Hougaard (GH) copula. The proposed dependence-based feature vector is developed through simulated vibration signal analysis and defined as the pair of GH copula coefficients regarding the first two IMFs. Validation is conducted through an experimental case study.

The thesis study would promote the state of the art of research on vibration signal analysis for planetary gearbox fault diagnosis. Knowledge generated from the four research topics will provide practical engineers with powerful tools for diagnosing faults in planetary gearboxes, thus benefiting industrial applications of planetary gearboxes, such as wind turbines and helicopters, with high reliability, safety, and low operation and maintenance cost.

The planetary gearbox of interest in this thesis study is under stationary operation conditions with a single gear tooth fault. Further analysis on cases under non-stationary operation conditions and/or with multiple gear tooth faults will be studied in future work.

Preface

This thesis study is an original research work by Libin Liu. Research topics conducted for this thesis study have been published or submitted for publication. The generated journal papers and conference papers are with Libin Liu as the first author and Dr. Ming J. Zuo as the corresponding author. Dr. Xihui Liang is the co-author for some papers.

Chapter 2 is published with a journal paper and a refereed conference paper. The journal paper is L. Liu, X. Liang, and M. J. Zuo, "Vibration signal modeling for a planetary gear set with transmission path effect analysis," *Measurement*, vol. 85, pp. 20–31, May 2016. The refereed conference paper is L. Liu, X. Liang, and M. J. Zuo, "Vibration signal modeling for a planetary gear set," in *19th World Conference on Non-Destructive Testing*, Munich, Germany, 2016, pp. 1–8. Libin Liu proposed this topic topic and did the primary research work. Reviews and edits on paper manuscripts were provided by Dr. Ming J. Zuo and Dr. Xihui Liang to improve the papers.

Chapter 3 generates a submitted journal paper and a refereed conference paper. The submitted journal paper is L. Liu, X. Liang, and M. J. Zuo, "Energy density construction by spectrogram-free non-parametric copula for planetary gearbox fault diagnosis," *Mechanical Systems and Signal Processing*, revised on May 11, 2018. The refereed conference paper is L. Liu and M. J. Zuo, "Copula-based time-frequency distribution analysis for planetary gearbox fault detection," in *ASME 2017 International Design Engineering Technical Conferences and Computers and Information in Engineering Conference*, Cleveland, Ohio, USA, 2017, pp. 1–8. Libin Liu proposed this research topic and did the primary research work. Reviews and edits on journal paper manuscripts were provided by Dr. Ming J. Zuo

and Dr. Xihui Liang. Dr. Ming J. Zuo gave comments to improve the conference paper.

Chapter 4 produces a submitted journal paper as L. Liu and M. J. Zuo, "Feature extraction by non-negative matrix factorization for planetary gearbox fault diagnosis," *Journal of Sound and Vibration*, submitted on May 09, 2018. Libin Liu proposed this research topic and did the primary research work. Dr. Ming J. Zuo provided reviews and edits to improve the paper.

Chapter 5 brings up a journal paper and a refereed conference paper. The journal paper is L. Liu, X. Liang, and M. J. Zuo, "A dependence-based feature vector and its application on planetary gearbox fault classification," *Journal of Sound and Vibration*, accepted on Jun. 06, 2018. The refereed conference paper is L. Liu, M. J. Zuo, and X. Liang, "Dependence analysis of planetary gearbox vibration marginals," in *2016 Prognostics and System Health Management Conference*, Chengdu, China, 2016, pp. 1–6. Libin Liu proposed this research topic and did the primary research work. Reviews and edits on paper manuscripts were provided by Dr. Ming J. Zuo and Dr. Xihui Liang to improve the papers.

This thesis is dedicated to my family
for their endless love, support, and encouragement

Acknowledgements

I would like to express my grateful gratitude with sincere respect to my supervisor, Dr. Ming J. Zuo, for his guidance, patience, support, and encouragement during my PhD study. Under his guidance, I have gained valuable knowledge with solid logic to deal with academic research work and real world problems. None of my research achievements would be possible without his supervision. I will always treasure the work experience with Dr. Ming J. Zuo throughout my future career.

I sincerely thank my PhD examining committee members, Dr. Zhigang (Will) Tian, Dr. Albert Vette, Dr. Hossein Rouhani, and Dr. Qiao Sun for their valuable comments on my thesis. Thanks to Dr. Tian and Dr. Vette in particular for being my supervisory committee members. Thanks Dr. Qiao Sun for being my external examiner.

I would also like to express my thanks to Dr. Xihui Liang, Dr. Guanghan Bai, Dr. Xiaodong Wang, Dr. Zhipeng Feng, and Dr. Yong Qin for their enlightening suggestions and kind help during my time at the University of Alberta.

My sincere appreciation also goes to all my friends and group members in the Reliability Research Lab for the help, the support, and the happy hours. Being friends and working with them is an exciting and beneficial experience. I wish them all the best and happiness in life.

Finally, my deepest gratitude goes to my parents for their endless love, support and encouragement. They always believe I can do it. Without their believing in me, I cannot finish this journey. Many thanks to my sister for covering my absence at home. I dedicate this thesis to my family.

Contents

List of Figures

List of Tables

List of Acronyms

TI	Torque Increaser
SI	Speed Increaser
AE	Acoustic Emission
AMFM	Amplitude Modulation and Frequency Modulation
TSA	Time Synchronous Averaging
TFD	Time-Frequency Distribution
TFR	Time-Frequency Representation
STFT	Short-Time Fourier Transform
WT	Wavelet Transform
EOM	Equation of Motion
RMS	Root Mean Square
SD	Standard Deviation
DTW	Dynamic Time Warping
CK	Correlated Kurtosis
FRMS	Root Mean Square of Filtered signal
AACO	Accumulative Amplitude of Carrier Orders
ERDS	Energy Ratio based on Difference Spectra
SVD	Singular Value Decomposition

AOK	Adaptive Optimal Kernel
ASR	Adaptive Stochastic Resonance
PCA	Principal Component Analysis
ICA	Independent Component Analysis
EMD	Empirical Mode Decomposition
EEMD	Ensemble Empirical Mode Decomposition
IMF	Intrinsic Mode Function
PMC	Pseudo-Multi-Channel
NNMF	Non-Negative Matrix Factorization
KNN	K-Nearest Neighbor
SVM	Support Vector Machine
NBV	Nearest Boundary Vector
RRL	Reliability Research Lab
TFC	Time-Frequency Copula
GH	Gumbel-Hougaard
FEM	Finite Element Method
QQ	Quantile-Quantile
MISE	Mean Integrated Squared Error
TF	Time-Frequency
AR	Auto-Regressive
MED	Minimum Entropy Deconvolution
CI	Condition Indicator
ANN	Artificial Neural Network

PR	Planet gear tooth crack on Ring gear meshing side
PS	Planet gear tooth crack on Sun gear meshing side
RC	Ring gear tooth Crack
SC	Sun gear tooth Crack
SP	Slight planet gear tooth Pitting
MP	Moderate planet gear tooth Pitting
CP	Critical planet gear tooth Pitting
PB	Planet gear tooth Breakage
RB	Ring gear tooth Breakage
SB	Sun gear tooth Breakage
EBW	Equivalent BandWidth
CDF	Cumulative Distribution Function

List of Symbols

V_p	Planetary gear vibration source
V_s	Sun gear vibration source
V_r	Ring gear vibration source
k_h	Hertzian contact stiffness
k_b	Bending stiffness
k_a	Axial compressive stiffness
k_s	Shear stiffness
k_θ	Total effective gear mesh stiffness
S_p	Transmission path effect inside gearbox for a planet gear
S_r	Transmission path effect inside gearbox for the ring gear
S_s	Transmission path effect inside gearbox for the sun gear
a	Weight of ring-planet meshing induced planet vibration
b	Weight of sun-planet meshing induced planet vibration
w	Transmission path effect along the casing
w_c	Carrier rotation angular frequency
ψ	Initial phase angle of a planet gear
$a(t)$	Resultant vibration signal in acceleration
a_s	Sun gear vibration in acceleration

a_r	Ring gear vibration in acceleration
a_p	Planet gear vibration in acceleration
A	Vibration amplitude
r	Distance to a vibration source
ζ	Radiation damping coefficient for vibration transmission
η	Material damping coefficient for vibration transmission
f_s	Sun gear rotation frequency
f_p	Planet gear rotation frequency
f_c	Carrier rotation frequency
f_{p-p}	Planet gear passing frequency
f_m	Meshing frequency
$\boldsymbol{C}$	Copula cumulative distribution function
C	Copula probability distribution function
u, v	Copula variables
ϕ	Copula generator
θ	Parametric copula parameter
$\boldsymbol{H}(x,y)$	A joint cumulative distribution function
$\boldsymbol{F}(x), \boldsymbol{G}(y)$	Marginal distributions of $\boldsymbol{H}(x,y)$
$\boldsymbol{F}^{-1}(u), \boldsymbol{G}^{-1}(v)$	Pseudo-inverses of $\boldsymbol{F}(x)$ and $\boldsymbol{G}(y)$
R, S	Ranks
O	Pseudo-observation
K	Kernel density
h	Smoothing parameter

B	Beta function
W	Order statistics
$x(t)$	Vibration signal
$X(f)$	Fourier transform of $x(t)$
$T(t), F(f)$	Instantaneous energy and energy spectral density of $x(t)$
$S(t,f)$	Spectrogram of $x(t)$
$p(t,f)$	Time-frequency energy density of $x(t)$
c_i	The ith IMF of $x(t)$
r_n	Residue of $x(t)$ after n IMFs are extracted
t_c	Time center of an oscillating impulse
ξ	Damping ratio of an oscillating impulse
N_p	Teeth number of a planet gear
N_s	Teeth number of the sun gear
N_r	Teeth number of the ring gear
M_p	Number of planet gears
$\boldsymbol{w}$	SVM weight vector
L	SVM penalty parameter
χ	SVM slack variable
Φ	SVM mapping function

Chapter 1

Introduction

This chapter consists of four sections. The background is introduced in Section 1.1. A review of the literature on vibration signal modeling and vibration signal analysis for planetary gearbox fault diagnosis is presented in Section 1.2. Then, the research scope and thesis structure are described in Section 1.3 and Section 1.4, respectively.

1.1 Background

Planetary gearboxes are commonly used as compact alternatives to fixed-shaft gearboxes in industrial applications when space, torque versus weight, and multiple transmission mechanisms are principal concerns. Such industrial applications, as shown in Fig. 1.1, include wind turbines, construction machinery, vehicle automatic transmissions, and helicopters. The primary transmission structure of a planetary gearbox is the planetary gear set. A planetary gear set has three sets of gears with distinct degrees of freedom, including a centrally rotating sun gear, a ring gear, and multiple planet gears which are held by a carrier and mesh with the sun gear and the ring gear simultaneously [1]. Fig. 1.2 shows the structure of a planetary gear set with 4 planets.

As shown in Fig. 1.2, a planetary gear set has inherent in-line shafting from the power input end to the power output end as the carrier is concentric with the sun gear and the ring gear. This design eliminates the offset between different gear pairs in a fixed shaft gear set, as shown in Fig. 1.3. In this way, the compact structure of a planetary gear set is

Fig. 1.1: Planetary gearbox industrial applications

realized. With different power input and power output configurations, the planetary gear set can function as either a Torque Increaser (TI) or a Speed Increaser (SI) [1]. Table 1.1 lists different kinematics a planetary gear set can achieve with different configurations. TI-1 has a larger torque-increasing capacity than TI-2 because it has a smaller driving gear, the sun gear, than the TI-2 whose driving gear is the ring gear; SI-1 has a larger speed-increasing capacity than SI-2 because SI-1 has a smaller driven gear, the sun gear, than the SI-2 whose driven gear is the ring gear. In this thesis, the investigated planetary gear set has the sun gear and the carrier as the power input and the power output, respectively, and the ring gear fixed, i.e., the TI-1 configuration. With this configuration of a small gear (the sun gear) driving a large "gear" (the carrier), it delivers low-speed and high-torque output.

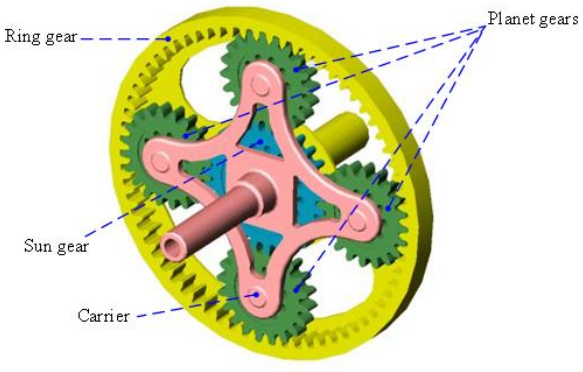

Fig. 1.2: Structure of a planetary gear set

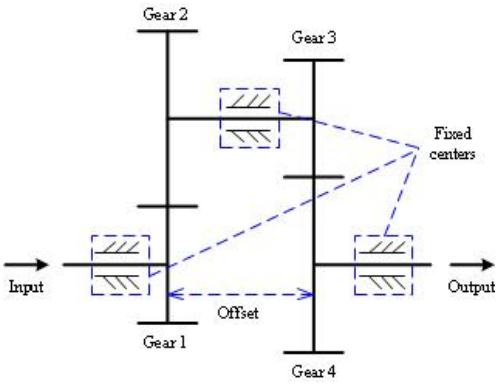

Fig. 1.3: Diagram of a fixed shaft gear set

Table 1.1: Configurations for differnet kinematics of a planetary gear set

Configuration	Planetary components			
Driving input	Sun gear	Ring gear	Carrier	Carrier
Driven output	Carrier	Carrier	Sun gear	Ring gear
Fixed component	Ring gear	Sun gear	Ring gear	Sun gear
Achieved kinematics	TI-1	TI-2	SI-1	SI-2

Despite the advantages of a planetary gear set, a planetary gearbox may suffer gear faults due to tough working environment and heavy load [2]. A gear fault is any phenomenon that causes the gear to be unable to conduct the job for which it was designed satisfactorily. As reported in [3], 19.1% of the fault modes in a helicopter transmission system involve gear faults. In another report [4], among transmission system faults in wind turbines that were recorded in a database, approximately 59.4% included gear faults.

If a gear fault occurs but cannot be detected and diagnosed properly, the transmission system will continuously deteriorate, which may result in the shutdown of the whole system, leading to major economic losses and even human casualties. For instance, on February 22, 2008, a Vestas (Nordtank) 600 KW wind turbine at Halling in Hornslet (Denmark) collapsed catastrophically during a storm. The turbine was wrecked, and large pieces of blades landed 200-300 meters away. Luckily, no one was hurt. In the final report on the turbine failure investigation [5], it was pointed out that "the likely chain of events is that the gear fails and causes a short, abrupt stop so the engaged airbrakes are broken loose and then thrown off". Meanwhile, with the strong wind, "it was no longer practically possible to stop the turbine and a wreck is inevitable." On April 29, 2016, a Eurocopter EC225 Super Puma helicopter that was carrying 11 passengers and 2 crew members crashed near Turoy. The main rotor head detached from the body of the helicopter, and all 13 persons on board were killed. The investigation showed that the accident was a result of a fatigue fracture in one of the eight second-stage planet gears in the epicyclic module of the main rotor gearbox [6].

Generally, gear fault modes are classified into two basic categories: lubrication-related mode and strength-related mode [7]. The American Gear Manufacturers Association [8], which is accredited by the American National Standards Institute to write U.S. standards on gearing, has divided the common gear failures into four broad categories: wear, surface fatigue, plastic flow, and breakage [9]. Wear and surface fatigue are lubrication-related fault modes, and plastic flow and breakage are strength-related fault modes [9].

Condition monitoring and fault diagnosis for gearboxes have been attracting considerably increasing attention as a significant research area [10–12]. Condition monitoring and fault diagnosis are realized by the health information extracted from the acquired condition monitoring data [13], which may include vibration signals, Acoustic Emission (AE) signals, strain data, and oil debris data. A vibration signal contains rich information about the machinery health condition, as different faults in the system introduce different changes in the measured vibration signal [14]. An AE signal is defined as a transient elastic wave generated by the rapid release of energy within a material [15] that provides symptoms of a fault in a device. For example, an application of AE signals to detect the spur gear pitting in a gearbox is reported in [16]. Condition monitoring based on strain analysis is achieved by the stress and/or strain analysis subject to the load. Examples of such strain analysis methods include the method using a single piezoelectric strain sensor for planetary gearbox fault diagnosis as reported in [17] and the backface strain-monitoring technique based on the elastic fracture scaling law and the classical linear elastic fracture mechanic theory as reported in [18]. Oil debris monitoring is used to identify conditions related to abnormal wear through the monitoring of particle counts, size, and accumulated mass [19]. Vibration signals, acoustic emission signals, and strain signals are measured by a vibration transducer, an acoustic transducer, and a piezoelectric strain sensor, respectively, mounted normally on the housing of a gearbox [14, 15, 17, 18]. Oil debris monitoring mainly contains off-line oil analysis and plug-type chip detectors. For off-line oil analysis, oil samples are collected, sent to a lab, and analyzed while a plug-type chip detector captures debris us-

ing a magnet, leading to a change in the indicator state when the debris forms an electrical bridge between the contacts [19]. Specifically, the focus of this thesis study is the use of the vibration signal analysis for planetary gearbox fault diagnosis, as vibration signals are easily measured and contain rich information about the health condition of a gearbox [14].

Compared with fixed-shaft gearboxes, planetary gearboxes have much more complicated vibration characteristics because of their complex structures and kinematics [20–22]. As shown in Fig. 1.2, there are multiple gear pairs in mesh simultaneously in a planetary gear set, including the sun-planet gear pairs and the ring-planet gear pairs. The multiple sun-planet meshes and ring-planet meshes generate multiple vibration sources from the sun gear, the ring gear, and the planet gears, as shown in Fig. 1.4, with similar forms but different phases [23]. It is assumed that each vibration source starts from the center of each gear component. In Fig. 1.4, V_{pi}, V_s, and V_r denote the ith planet gear vibration source, the sun gear vibration source, and the ring gear vibration source, respectively. The resultant vibration signal measured by the transducer mounted on the gearbox housing is the weighted summation of the individual vibration sources. Because of the phase differences, some of the components are reinforced while some others are neutralized [24]. Moreover, vibration sources are subject to the time-varying transmission path effect due to carrier rotation, introducing Amplitude Modulation (AM) in the measured resultant vibration signal [24]. Multiple vibration sources and the time-varying transmission path effect cause challenges to the understanding of vibration characteristics and fault diagnosis for planetary gearboxes.

Vibration models are commonly employed to understand the vibration characteristics of planetary gearboxes, as they are helpful revealing the mechanism generating the vibration signals. Both mathematical models [22, 25] and dynamic models [26, 27] have been established by researchers. Mathematical models refer to those following general mathematical forms that are subject to theoretical principles but not necessarily in terms of detailed physical quantities, such as sinusoidal waves to represent the vibration of rotating machinery

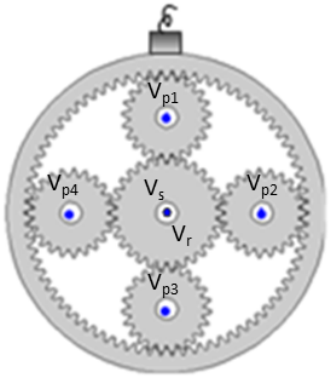

Fig. 1.4: Vibration sources from different gears

with perfect gears, as in [22, 25]. Dynamic models refer to those that utilize physical laws, such as conservation of energy and Newton's laws of motion, to simulate dynamic response with detailed physical quantities, as in [26, 27]. Through such models, the connection of the vibration signal with the system structure and the operation condition as well as the gear damage can be established, which aids in the development of effective methods of vibration signal analysis for planetary gearbox fault diagnosis. Mathematical models are useful for understanding the spectrum structure of a planetary gearbox vibration, yet they lack a connection with physical parameters, such as the meshing stiffness and the fault magnitude. A dynamic model is more familiarly related to those physical parameters by relating the changes in the resultant vibration to the faults of different types and/or different levels [27]. As multiple vibration sources are synthesized at the transducer position through different transmission paths, both multiple vibration sources and transmission path effects need to be considered for a comprehensive vibration signal model. However, in the reported work, the resultant vibration was only partially modeled, either vibration sources were partially covered or part of the whole transmission path was considered [25, 27].

In addition to possible changes in the operation condition and the presence of noise, changes in the health condition of a gear system can also lead to changes in the vibration generated by a machine [28]. For machinery condition monitoring and fault diagnosis, an important task is to extract fault-related changes from the transducer-acquired vibra-

tion signal. Fault-related changes are defined as fault features. Various signal processing methods to extract fault features have been reported, including the ones applied in the time domain, the frequency domain, and the time-frequency domain. Fig. 1.5 shows a flowchart for machinery condition monitoring and fault diagnosis by vibration signal analysis.

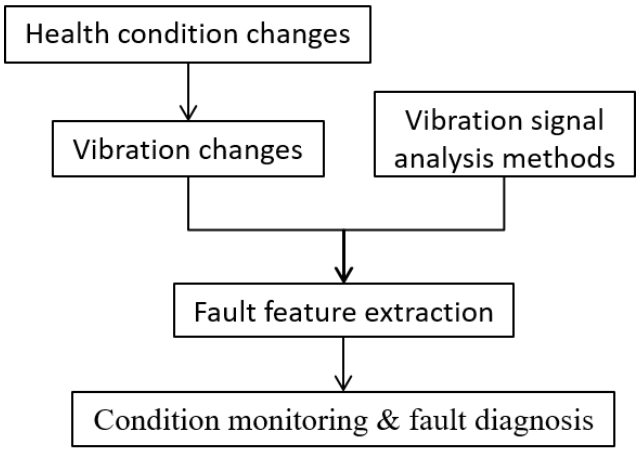

Fig. 1.5: Scheme of fault diagnosis by vibration signal analysis

The time domain representation shows the waveform of the vibration signal. Characteristics such as peaks, shapes, and randomness of the vibration signal are commonly used as time domain features to characterize the vibration signal for condition monitoring and fault diagnosis. Generally, the extracted features are statistical parameters, including standard deviation, skewness, kurtosis, impulse factor, energy ratio, and crest factor [29]. The extracted features simplify the diagnostic tasks greatly by reducing the complex vibration signals to a handful of parameters characterizing the signal. However, such statistical parameters cannot distinguish the vibration changes caused by a gear fault, changing operation condition, or noise. In order to remove redundant information and noise from the raw vibration signal for better fault feature extraction, a preprocessing procedure is normally conducted before feature extraction to enhance the fault-related information in the vibration signal. Typical preprocessing methods include filter-based methods (e.g., adaptive noise cancellation [30] and demodulation techniques [31, 32]) and Time Synchronous Averaging (TSA) methods [24, 33].

The frequency domain representation demonstrates the spectrum of the signal. Frequency domain methods are based on Fourier transform and allow the decomposition of a vibration signal into individual frequency components with relative intensities. For fixed-shaft gearboxes in normal operation with healthy gears, vibration components with sizable amplitudes occur at the tooth meshing frequency and its harmonics. When a gear fault occurs, symmetric sidebands around the meshing frequency and its harmonics arise as a result of fault-related modulating rotational motion [34]. By analyzing the number and amplitude of sidebands, the health condition of a fixed-shaft gearbox can be identified [35]. However, for a planetary gearbox, even with healthy gears, sizable vibration energy may arise at various sidebands of the gear meshing frequency and its harmonics [24]. This phenomenon is due to the modulation of amplitude with carrier rotation [22]. Moreover, the phase differences among multiple planet gears will cause interference in the symmetric sidebands produced by each individual planet gear [36], leading to asymmetric sidebands in the spectrum. When a gear fault occurs in a planetary gearbox, fault-induced amplitude modulation and fault-related frequency modulation will be introduced, exciting distinct spectral features and interfering with normal ones [25]. For diagnosis of planetary gearbox fault by frequency domain methods, in addition to the specialized skills required for spectral analysis, the complex structure of the planetary gearbox vibration spectrum generates more challenges and difficulties [1].

The time-frequency domain representation captures the density/intensity of the signal in time and frequency simultaneously. Joint time-frequency analysis techniques were originally developed in the field of quantum mechanics in the 1930s [37, 38]. Starting with the classical works of Gabor [39], Ville [40], and Page [41], time-frequency analysis techniques were introduced to the field of signal processing. The practical motivation for time-frequency analysis is that the classical Fourier analysis assumes that the signal is infinite or periodic in time, whereas many signals in real life are of short duration and change substantially over the duration [42]. For such signals, a TFD is effective in revealing the con-

stituent time-varying frequency components and transient events, including fault-related features such as fault characteristic frequencies and fault-induced impulses. Such fault-related features are the main judgments for machinery condition monitoring and fault diagnosis [43]. Various time-frequency analysis techniques have been reported, as reviewed in [42] and [43], with the aim of improving the existing signal feature extraction methods and exploring new ones in the joint time-frequency domain. Typically, time-frequency analysis methods can be categorized into linear TFDs such as Short-Time Fourier Transform (STFT) [44] and Wavelet Transform (WT) [45], bilinear TFDs like Wigner-Ville distribution [46] and Cohen's class distribution [42], and positive TFDs as reported in [47] and [48].

1.2 Literature review

This section contains a review of the literature on vibration signal modeling for planetary gear sets and vibration signal analysis methods for planetary gearbox fault diagnosis. A literature review on intelligent diagnosis methods is also presented, as they are involved in Chapter 5. Specifically, this section is organized as follows: Subsection 1.2.1 presents a review of the research on vibration signal modeling for planetary gear sets, including the phase difference among multiple vibration sources, the time-varying transmission path effect, mathematical vibration signal modeling, and dynamic vibration signal modeling; Subsection 1.2.2 presents the literature review regarding vibration signal analysis methods in the time domain, frequency domain, and joint time-frequency domain, and the other vibration signal analysis methods. Finally, the review on intelligent diagnosis methods for planetary gearbox fault diagnosis is provided in Subsection 1.2.3.

1.2.1 Vibration signal modeling

Vibration signal modeling is helpful for researchers and engineers to understand the generation mechanism of the dynamic response and the vibration characteristics of a planetary

gearbox [25]. Taking advantages of the vibration signal modeling, effective vibration signal analysis methods can be explored and developed for planetary gearbox fault diagnosis [1]. In this subsection, the literature reviews on the unique behaviors of a planetary gear set, i.e., the phase difference among multiple planet meshes and the time-varying transmission path effect due to the carrier rotation, are presented. Subsequently, the vibration signal modeling methods including the mathematical ones and the dynamic ones are reviewed.

1.2.1.1 Phase differences among multiple vibration sources

For a planetary gearbox vibration signal, the spectrum is typically asymmetric [27]. McFadden and Smith [20] firstly recognized this phenomenon as a result of the phase differences among the multiple vibration sources. With different relative phases, some components in the spectrum are reinforced while others are neutralized or cancelled after the summation of all the individual vibration sources [20, 24].

To reveal the meshing phase relationship, researchers have conducted various investigations. Focusing on planetary gearboxes with equally spaced planets, Kahraman [49] derived three possible phasing conditions, namely in-phase, sequentially phased, and counter phased. Parker and Lin [50] investigated the meshing phase relationship in planet gears, considering three quantities: phase differences among the sun-planet meshes, phase differences among the ring-planet meshes, and phase difference between the ring-planet mesh and sun-planet mesh for a given planet gear. More generally, taking the number of planets, the numbers of teeth of the gears, and the planet position angles into consideration, Inalpolat and Kahraman [22] gave general formulations to categorize planet phasing relationship into three categories: in-phase, sequentially phased, and arbitrarily phased, with equally spaced planets or unequally spaced planets. In-phase planet meshing phase condition is defined as the condition that each planet meshing phase angle is an integer multiple of 2π [22]. The sequential planet meshing phase condition is defined as the condition that the sum of planet meshing phase angles is an integer multiple of π [22]. Arbitrarily phased condition

is the condition of neither in-phase condition nor sequentiall phased condition [22], which means the counter phased condition in [49] is one case of the arbitrarily phased condition in [22].

The work in [22, 49, 50] provides necessary insight into planet phasing relationship. It is beneficial for the proper incorporation of the meshing phases in the gear mesh stiffness evaluation [23] and the vibration signal modeling for a planetary gear set [25, 27, 51, 52].

1.2.1.2 Time-varying transmission path effect

The time-varying transmission path effect is introduced by the carrier rotation while the transducer is fixed on the gearbox housing, leading to the AM effect on the transducer-perceived vibration signal [22]. This inherent AM effect would lead to sizable spectral amplitudes arising at modulation sidebands of the carrier rotation frequency around the tooth meshing frequency and its harmonics [22, 24].

Focusing on the vibration source at a sun-planet meshing point, Fig. 1.6 illustrates the three possible transmission paths in a planetary gearbox [25]. As discussed in [25], vibration signals transmitted through path 2 and path 3 are negligible due to the long transmission lengths and the great bearing damping. Through path 1, increasing vibration information is captured as the planet gear approaches the transducer, reaching the maximum when the planet gear is closest to the transducer, then decreasing vibration information is perceived with the planet gear moving away from the transducer. This phenomenon is the defined AM effect introduced by the time-varying transmission path. To model the AM effect, some researchers employed a Hanning function [22, 25, 26], assuming no vibration is captured when the planet gear reaches the farthest position to the transducer. For the cases that some vibration from the farthest position is captured, Liang et al. [27] introduced a modified Hamming function. However, the modified Hamming function in [27] has a shortcoming that the vibration from the farthest position may be amplified with improper parameter selection. This vibration amplification is unrealistic as the vibration from

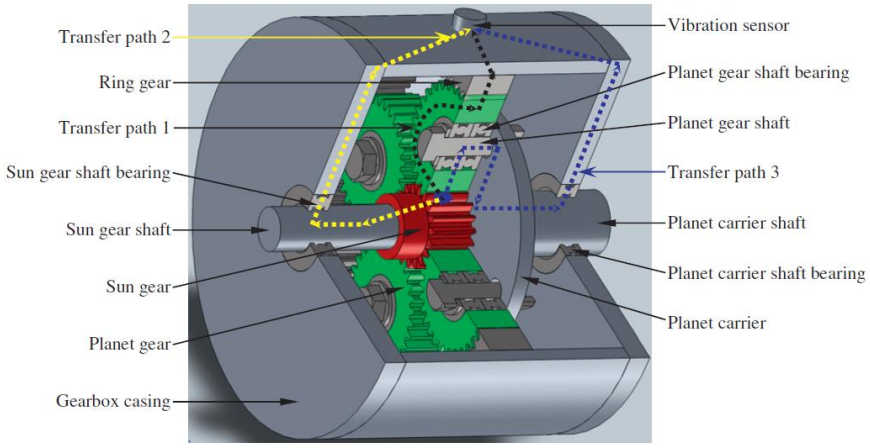

Fig. 1.6: Possible vibration transmission paths [25]

the farthest position should have the biggest attenuation. The shortcomings of the reported time-varying transmission path effect models will be addressed in the first topic as defined in Section 1.3.

The AM effect, together with the phase differences, could further attenuate the fault-related symptoms in the transducer-perceived vibration signal [27]. The fault signature would be masked and submerged by other vibration components and the noise [24], increasing the complexity of a planetary gearbox vibration signal and leading to more challenges to planetary gearbox fault diagnosis by the vibration signal analysis [1].

1.2.1.3 Mathematical vibration signal modeling

Following the general theoretical principles but not necessarily in terms of the detailed physical quantities, a mathematical model can indicate the complex vibration characteristics for a planetary gearbox by an abstract model [22, 25].

Mathematical modeling contributes to the understanding on the vibration spectral sidebands of a normal planetary gearbox. McFadden and Smith [20], using a mathematical model, predicted the vibration signal of a planetary gear set to be captured by a fixed transducer on the ring gear. Their model was able to reveal the frequency components with dominant vibration peaks for the exampled planetary gear set. Based on the mathematical model in [20], McNames [53] explored the relative amplitudes of the dominant peaks that

possibly show up in the spectrum by employing the continuous-time Fourier series. McNames [53] showed that the spectrum of the total vibration (i.e., the sum of the vibrations from each individual planet gear perceived by a fixed transducer) has sizable amplitudes at frequencies that are integer multiples of the number of planets in the gear system. However, this conclusion was only presented for a class of planetary gear sets with equally spaced planets and sequential planet meshing phase condition while its validity was not tested for other types of planetary gear sets with unequally spaced planets and in-phase/arbitrarily phased planet meshing phase condition. A variety of other works [36, 54–57] have been conducted by researchers to deal with sidebands in a wider context of planetary gear vibration signals. More comprehensively, Inalpolat and Kahraman [22] proposed a systematic mathematical model to investigate the mechanisms of sideband harmonics in the spectrum, showing that there are various classes of planetary gear sets with distinct sideband behaviors. They classified the sideband behaviors into 5 categories in terms of frequencies and amplitudes subject to the gear parameters (i.e., the number of planets and the number of gear teeth), the configuration of the planet spacing condition (equally or uneqully spaced) and the planet meshing phase condition (in-phase, sequentially phased, or arbitrarily phased).

Besides the vibration signal modeling for a healthy planetary gearbox, a mathematical vibration signal model can also incorporate the Amplitude Modulation and Frequency Modulation (AMFM) effect caused by gear tooth damages and periodic changes in working conditions. Feng and Zuo [25], considering the AMFM effect due to gear tooth damages and periodically time-varying running speed and load, presented a mathematical vibration signal model for planetary gearbox fault diagnosis and summarized the spectral characteristics in closed form. Theoretical derivations conducted on a mathematical vibration signal model as in [25] provide theoretical guides for detecting and locating gear tooth faults of a planetary gearbox by spectral analysis.

1.2.1.4 Dynamic vibration signal modeling

A dynamic model utilizes physical laws, such as equilibrium, conservation of energy, and Newton's laws of motion, to simulate the gear system response [51]. Thus, it is directly related to the physical quantities and can reflect the distinct vibration behaviors with different gear tooth damages [58].

Lin and Parker [59] demonstrated that mesh stiffness variation is one of the major internal excitation sources to gear vibration. To evaluate the gear system response by a dynamic model, gear mesh stiffness has to be evaluated explicitly [51]. Therefore, in the following contents, the study on the gear mesh stiffness evaluation are reviewed first, then the review on the gear dynamic models follows.

Gear mesh stiffness

Fig. 1.7 illustrates the meshing behavior of a spur gear pair with a transmission ratio between 1 and 2 [58]. The meshing zone along the meshing line N_pN_g is bounded by point A and point E. Point A and point E are the intersection points of the gear adendum circle and the pinion addendum circle with the meshing line, respectively. Yu [58] divided the meshing zone AE into three phases: AB, BD, and DE where point B and point D indicate the starting point and the ending point of the single meshing tooth pair area, respectively. There are two tooth pairs in mesh within the meshing phases AB and DE whereas there is one tooth pair in mesh with the meshing phase BD. The changes in the meshing tooth pair number and the contact position lead to the time variant of gear mesh stiffness [23].

To approximate gear mesh stiffness for a healthy gear pair with constant running speed, some researchers [2, 60] employed a square waveform as shown in Fig. 1.8. The square waveform can reflect the change in the meshing tooth pair number and easy to use. However, the square waveform ignores the tooth contact position change [61]. Additionally, the flatness of the stiffness curve could lead to unwanted frequency components in the gear train dynamic response [61]. Besides, the determination of the mesh stiffness amplitude

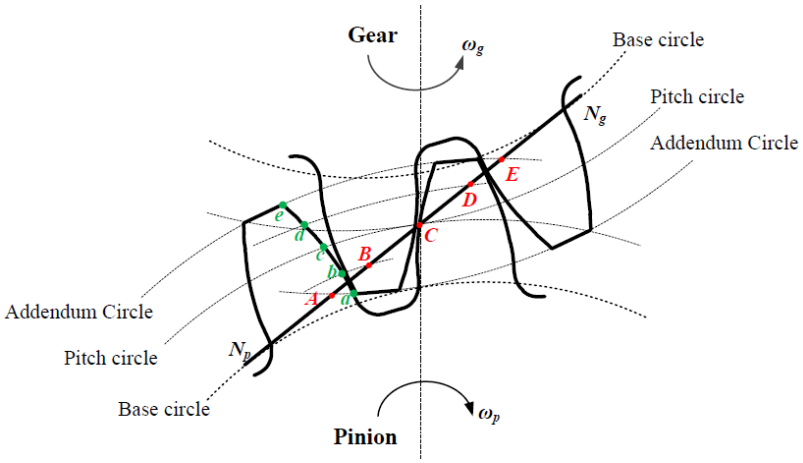

Fig. 1.7: Gear meshing process [58]

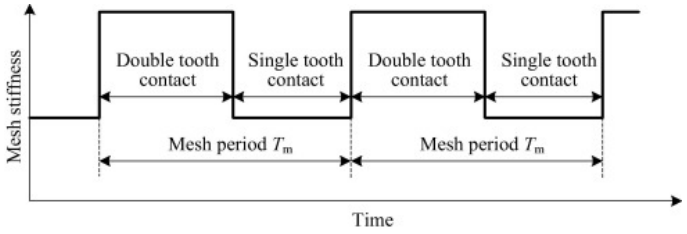

Fig. 1.8: Gear mesh stiffness with square waveform [51]

and the mesh stiffness reduction caused by a gear tooth fault are without the confirmation of gear physical parameters [51].

To provide a more accurate estimation to gear mesh stiffness, Yang and Lin [62] proposed the potential energy method, treating the gear tooth as a non-uniform cantilever beam and applying the beam theory to evaluate the gear mesh stiffness. The total energy in a gear pair considered in [62] was the summation of Hertzian contact energy, bending energy, and axial compressive energy which corresponds to Hertzian contact stiffness k_h, bending stiffness k_b and axial compressive stiffness k_a, respectively. Later, Tian, Zuo and Fyfe [63] took the shear energy into consideration for the shear stiffness k_s estimation. To reflect the gear mesh stiffness variation with the tooth contact position, the stiffness terms subject to different energies are functions of the gear rotation angle [23, 64, 65]. Eventually, the total

effective gear mesh stiffness $k(\theta)$ of a gear pair is calculated by [63]

$$k(\theta) = \sum_{i=1}^{m} \frac{1}{\frac{1}{k_{h,i}} + \frac{1}{k_{b1,i}} + \frac{1}{k_{s1,i}} + \frac{1}{k_{a1,i}} + \frac{1}{k_{b2,i}} + \frac{1}{k_{s2,i}} + \frac{1}{k_{a2,i}}} \tag{1.1}$$

where m is the number of tooth pairs in mesh; the subscripts 1 and 2 denote the pinion and the gear, respectively; and θ represents the gear rotation angle.

For a planetary gear set with multiple gear mesh pairs, the gear mesh stiffness of the whole gear system is synchronized by the mesh stiffness of each gear pair, incorporating the meshing phase relationship [61]. Fig. 1.9 demonstrates the procedures of the mesh stiffness evaluation for a planetary gear set [66]. The mesh stiffness of a sun-planet gear pair and that of a ring-planet gear pair are evaluated individually by the methods developed for external-external gear pairs and external-internal gear pairs, respectively [61]. Then, incorporating the meshing phase relationships, the mesh stiffness of the whole planetary gear set can be calculated [61].

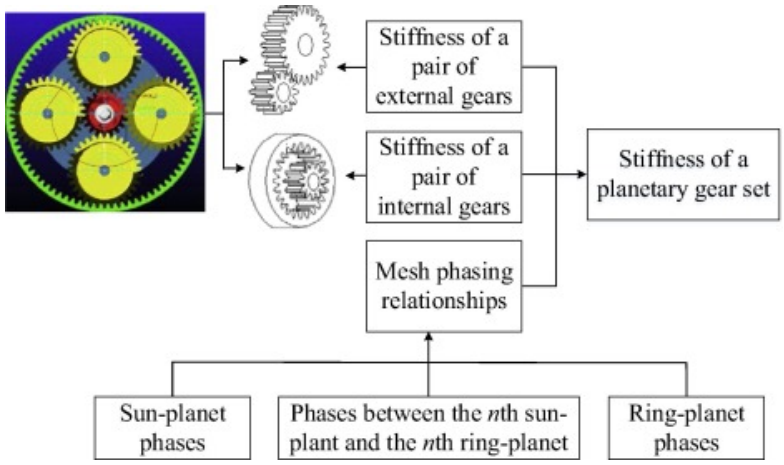

Fig. 1.9: Mesh stiffness evaluation for a planetary gear set [66]

When a damage occurs on a gear tooth, the effective tooth thickness and/or gear tooth contact length and/or effective tooth length are changed [51]. By potential energy methods, the gear mesh stiffness reduction induced by the gear tooth damage can be captured [23, 67, 68]. In [23], a gear tooth crack propagation model was developed and the mesh stiffness reductions were quantified. For illustration purposes, Fig. 1.10 is used to show the gear

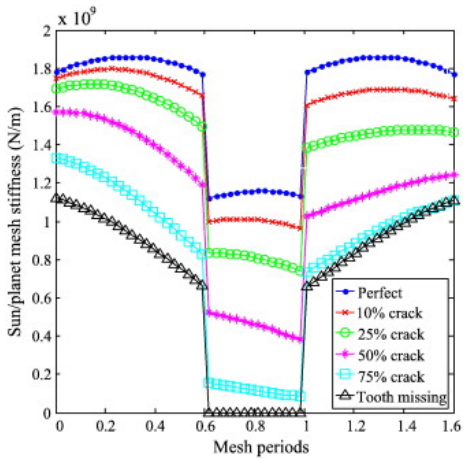

Fig. 1.10: Gear mesh stiffness with different gear tooth cracks [23]

mesh stiffness reduction of the sun-planet gear pair with different sun gear tooth crack levels. In this thesis study, the time-varying gear mesh stiffness obtained by the method in [23] is incorporated directly to generate the vibration sources from each gear.

Gear dynamic models

Lumped-parameter models have been commonly used for gear dynamic modeling as reviewed by Cooley and Parker [69]. A lumped-parameter model is the one where the components are considered to be solid with the masses concentrated at a set of points [70].

Various lumped-parameter dynamic models have been developed for dynamic behavior analysis of a planetary gear set. Kahraman [71] presented a nonlinear dynamic model to investigate the load sharing characteristics of a planetary gear set. Lin and Parker [72] modified the dynamic model in [71] to investigate the free vibration properties of a planetary gear set. Inalpolat and Kahraman [26] applied the dynamic model in [71] to predict the modulation sidebands of a planetary gear set with manufacturing errors. Chaari et al. [73] employed a similar dynamic model as reported in [72] to investigate the effect of manufacturing errors on the dynamic behavior of planetary gears. Cheng et al. [74] developed a pure torsional dyanmic model to investigate the properties of a planetary gear set with a single pit on a sun gear tooth. Chaari et al. [2] employed the dynamic model developed

in [73] to investigate the vibration properties of a planetary gear set with tooth cracking and tooth pitting on the sun gear. Chen and Shao studied the dynamic features of a planetary gear set when a sun/planet gear tooth crack was under different sizes and inclination angles [68] and investigated the vibration properties of a planetary gear set with the ring gear tooth crack [75]. Liang, Zuo, and Hoseini [27] developed a dynamic model based on the one proposed in [72] by taking the gyroscopic force and the centrifugal force into consideration. With the developed dynamic model, they investigated the vibration properties in the healthy condition and in the cracked tooth condition for the purpose of tooth crack detection [27] where the resultant vibration signal was modeled as the weighted summation of the vibration sources from the multiple planet gears. The rationality in [27] to only include the planet gear vibration sources in the modeled resultant vibration signal is that the sun gear vibration characteristics and the ring gear vibration characteristics can be reflected by the planet gear vibrations as they are excitations to the planet gear vibrations [27]. However, the sun gear vibration and the ring gear vibration actually have two roles for the resultant vibration: excitations to planet gear vibrations and individual vibration sources in the measured vibration [25, 28]. In the sense of individual vibration sources, it is not reasonable to ignore the sun gear vibration and the ring gear vibration in the resultant vibration. Consequently, to generate more realistic resultant vibration signal, vibration sources from the sun gear, the ring gear, and planet gears as shown in Fig. 1.4 should be included. This issue will be addressed in the first research topic as defined in Section 1.3 considering the transmission path effect.

The gear dynamic model developed in [27] is employed directly to generate the individual vibration sources from the sun gear, the ring gear, and planet gears. Fig. 1.11 illustrates the two-dimensional lumped-parameter model of a planetary gear set used in [27]. The planetary gear set consists of a sun gear (s), a ring gear (r), a carrier (c), and multiple planet gears (p), each of which has three degrees of freedom: transverse motions in the x- and y-directions, and the angular rotation. In the model, gear mesh interfaces are modeled as

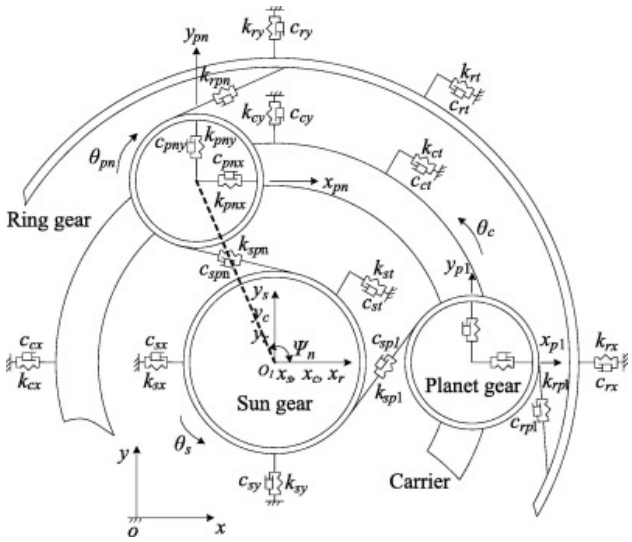

Fig. 1.11: Dynamic model of a planetary gear set [27]

spring-damper systems. The time-varying gear mesh stiffness is evaluated by the potential energy method in [23]. The damping is assumed to be proportional to the gear mesh stiffness [76]. The transmission errors in the gears, the frictions between the gear teeth, and other practical phenomena such as backlash are ignored. A rotating frame of reference fixed on the carrier is used to evaluate the gear motions. The final gear motions are described in the horizontal and vertical coordinates. Detailed Equations Of Motion (EOMs) subject to the dynamic model in Fig. 1.11 for each gear component, i.e., the sun gear, the ring gear, the planet gears, and the carrier, can be found in [27]. By the EOMs, the vibration sources from individual gear components can be calculated.

1.2.2 Vibration signal analysis methods

The main task of the vibration-based machinery condition monitoring and fault diagnosis is to extract the fault-related information from the vibration signal. For this purpose, large amounts of intensive and fruitful work have been conducted aiming to develop effective vibration signal analysis methods. In this subsection, the vibration signal analysis methods as defined in the time domain, in the frequency domain, and in the joint time-frequency domain as well as other vibration signal analysis methods are reviewed.

1.2.2.1 Time domain vibration signal analysis methods

Time domain vibration signal analysis methods extract fault features from the waveform of the vibration signal. Compared with frequency domain methods and time-frequency domain methods, time domain methods are relatively easy and direct. Through fault feature extraction with sufficient health status information, time domain methods have been widely applied in the condition monitoring and fault diagnosis for a planetary gearbox.

Conventional time domain methods include the statistical indicators and the TSA methods [1]. Statistical indicators require the operation condition of speed and load to keep the same to reduce the influence of those operation condition rather than the machinery health condition. Keller and Grabill [77] modified the traditional condition indicators such as kurtosis, FM0, energy ratio, and FM4 for the detection of a crack in the carrier of a UH-60A Blackhawk main transmission. Wu et al. [78] used statistical Root Mean Square (RMS) and Standard Deviation (SD) to distinguish the cracked planetary carrier and a healthy one for a UH-60 Blackhawk main transmission. To make possible of early fault detection for a planetary gearbox, McFadden [24] developed a TSA technique for calculating the time domain averages of the tooth meshing vibration of individual planet gears and of the sun gear. The signal average enhancement technique in the individual gear level was demonstrated by the vibration data of a planetary gearbox with seeded faults in [79] where the vibration data were collected by a single transducer. McFadden [80] revised the TSA technique reported in [79] to permit the use of other window functions rather than the rectangular window function used in [79]. The results in [80] showed that the tapered windows such as triangular and Hanning windows lead to lower noise levels in the resultant averaged signal. The TSA methods in [24, 79, 80] require a speed signal to transform the vibration signal to the angular domain from the time domain. To apply TSA method on a vibration signal for the cases without speed sensor, Combet and Gelman [81] investigated an automated methodology to find the best locations of the window functions. Sparis and Vachtsevanos [82] differentiated the faulty carrier plate from the healthy one for a U.S. Army helicopter based

on the vibration signal energy. They used experimental data from ground and aircraft tests and applied TSA as the pre-processing before the feature extraction [82].

In recent years, researchers investigated new time domain methods for the planetary gearbox fault diagnosis. Hong and Dhupia [83] developed a time domain diagnostic algorithm combining the fast Dynamic Time Warping (DTW) and the Correlated Kurtosis (CK). Fast DTW was used to extract the periodic fault-induced impulses and CK was employed to identify the position of the local gear fault in the gearbox [83]. Liang et al. [66], inspired by the TSA methods, developed a windowing and mapping strategy in the time domain to interpret the vibration signal of a planetary gearbox at the tooth level. They showed that the fault symptoms generated by a gear tooth fault can be detected and extracted effectively [66].

Despite the various time domain methods applied in the planetary gearbox fault diagnosis, a time domain method may suffer the shortcoming of weak robustness to noise. The reason is that the fault-related peaks and the noise-related peaks in the waveform can not be distinguished explicitly. Even with the pre-processing by TSA to denoise the raw vibration signal, the discontinuities at window boundaries would introduce new noise in the averaged signal [24]. Thus, novel time domain methods to extract fault features with great robustness to the noise should be explored and developed. This issue will be addressed in the fourth research topic as defined in Section 1.3.

1.2.2.2 Frequency domain vibration signal analysis methods

Compared with the time domain vibration signal analysis methods, the power of the frequency domain vibration signal analysis methods is to allow the decomposition of a signal into individual frequency components and establishes the relative intensity of each component [42]. The fundamental of frequency domain vibration signal analysis is the Fourier transform with equal sampling intervals either in the time domain or in the angular domain. If the running speed is varying, meaning that the time sampling intervals are changing,

the vibration signal needs to be tranformed to the angular domain with equal angular sampling intervals [84]. Various frequency domain methods have been reported for condition monitoring and fault diagnosis of a planetary gearbox.

Hines et al. [85] developed a frequency domain feature for the diagnosis of a UH-60A planetary carrier crack, showing that higher harmonic regions provide a more sensitive feature response for an early detection horizon. Sparis and Vachtsevanos [86] designed index vectors containing the frequency information in a digital form to distinguish the spectrum of the faulty from the spectrum of a healthy helicopter planetary gearbox. Mark and Hines [87] derived the effect of the non-uniform load carried by the multiple planets on the frequency spectrum. As an extension of the analysis in [87], Mark [88] predicted the additional sidebands in the frequency spectrum produced by planet-carrier torque modulations, which might potentially mask the sidebands induced by gear damages in a planetary gearbox. With the spectral understanding gained by [87] and [88], Mark et al. [89] further developed a simple frequency domain damage detection algorithm for early fault detection by minimizing the time varying transmission path effect and the attenuating effect of multiple tooth contact.

Besides the above-mentioned fault feature extraction techniques based on the raw spectrum, fault feature enhancement techniques by frequency filtering and spectral difference were also investigated by researchers. Lei et al. [90] developed two diagnostic parameters based on the vibration characteristics of a planetary gearbox, i.e., the Root Mean Square of the Filtered signal (FRMS) and the normalized summation of positive amplitudes of the difference spectrum between the unknown signal and the healthy signal. The filtered signal for FRMS was obtained by filtering out the shaft frequency and its five-order harmonics, the gear meshing frequency and its three-order harmonics, and the modulation sidebands with its harmonics in the frequency spectrum [90]. Later, Lei et al. [91] presented two other features for condition monitoring and fault diagnosis of planetary gearboxes, i.e., the Accumulative Amplitudes of Carrier Orders (AACO) and Energy Ratio based on Difference

Spectra (ERDS). The AACO is developed based on the order spectrum which is obtained through normalizing the frequency spectrum by the rotating frequency of the carrier; the ERDS is introduced based on the difference spectrum between the signal measured on a planetary gearbox with unknown healthy condition and the signal of a healthy planetary gearbox [91].

Although frequency domain methods have been widely studied and applied in the fault diagnosis for a planetary gearbox, the modulated sidebands induced by the gear fault are often difficult to extract accurately from a practical spectrum. One reason is the complexity of the spectral structure due to the AM effect with carrier rotation and the AMFM effect with a gear tooth fault [25]; the other reason is the ambiguity of the vibration spectrum due to the limited frequency resolution and small fluctuations in the operating speed [83].

1.2.2.3 Time-frequency domain vibration signal analysis methods

Compared with the time domain analysis and the frequency domain analysis, the time-frequency analysis studies a vibration signal in the joint time-frequency domain. By time-frequency analysis, the constituent frequency components of the vibration signal and the transient time events in the signal such as fault characteristic frequency and fault-induced impulses can be revealed effectively [43]. Thus, time-frequency analysis is more useful for the non-stationary vibration signals with time-varying running speed and/or time-varying load. Various time-frequency analysis methods have been developed for planetary gearbox fault diagnosis.

Samuel and Pines [92] performed a harmonic wavelet transform algorithm to characterize the vibration signature of a planetary gearbox and computed the mean square wavelet map to classify the gear faults. They also analyzed the TSA-separated vibration signals by the continuous wavelet transform for detection of planet gear faults incorporating the use of multiple sensors [93]. Meltzer and Ivanov [94, 95] conducted the planetary gearbox fault diagnosis for a passenger car by a time-frequency analysis method during the non-

stationary start-up and run-down of the gear drive. Saxena et al. [96] suggested a wavelet domain methodology with complex Morlet wavelets to extract features from the vibration data of a helicopter planetary gear system to distinguish the faulted carrier and the healthy carrier. Chaari et al. [2] simulated two fault modes in a planetary gearbox, i.e., tooth pitting and tooth crack, and compared the dynamic responses with and without the gear tooth faults by the Wigner-Ville distribution. Samuel and Pines [97] presented a methodology based on the constrained adaptive lifting algorithm to detect and to diagnose gear faults in the planetary stage of a helicopter transmission. Zimroz et al. [98, 99] identified the load variations and instantaneous shaft speed based on the extracted information from the vibration signal via time-frequency spectrogram analysis, aiming at the influence investigation of the non-stationary operations on the used diagnostic features. Jiang et al. [100] introduced a denoising method based on adaptive Morlet wavelet and then applied Singular Value Decomposition (SVD) to detect the impulsive feature components in a wind turbine planetary gearbox vibration signal. Feng and Liang [101] presented a time-frequency analysis method based on the Adaptive Optimal Kernel (AOK) to reveal the constituent frequency components of non-stationary signals and their time-varying features for wind turbine planetary gearbox fault diagnosis.

Traditional time-frequency analysis methods can be categorized as linear Time-Frequency Representations (TFRs), e.g. STFT and WT [45, 102, 103], and bilinear Time-Frequency Distributions (TFDs), such as Wigner-Ville distribution and Cohen's class TFD [42, 104]. For linear TFRs, there is a trade-off between the time localization and the frequency resolution subject to the Heisenberg uncertainty principle [42]. Wigner-Ville distribution is free from the Heisenberg uncertainty but it suffers from the intrinsic cross-term interference for a multi-component vibration signal [42]. By carefully choosing kernel functions as low-pass filters in the joint time-frequency domain, Cohen's class bilinear TFDs can mitigate the cross-term interference but with the compromise of time-frequency resolution [42]. For the fine time-frequency resolution and the cross-term free nature simultaneously, one can

employ the AOK introduced in [101] which modifies the kernel adaptively. Besides, the energy reassignment method is another alternative which has been reported to suppress the cross-terms and to improve the time-frequency resolution of a time-frequency representation [105, 106]. More detailed literature review on linear and bilinear time-frequency analysis methods with application examples can be found in review articles by Feng et al. [43] and Yan et al. [107].

As pointed out in [42], neither linear TFR nor bilinear TFD possess correct energy marginals and are positive simultaneously which are the basic requirements for an energy density representation [108]. Cohen and Posch [47] demonstrated the existence of positive TFDs with correct marginals for arbitrary signals and proposed a method to construct positive TFDs. Later, Fonollosa [109], Groutage [110], Emresoy et al. [111] and Yoshida et al. [112] proposed recursive algorithms as optimization problems to minimize the cross entropy [109, 110] or the least square error [111, 112] with a template as Wigner-Ville distribution. Positive TFDs have been employed in a variety of applications with multicomponent signals [113] and speech processing [114]. However, the above-mentioned positive TFDs lose some correlation information in the signal [112].

Sklar's theorem [115] indicates that a TFD admits a copula that contains all the correlation information about the signal. Davy and Doucet [48] established the connection between the positive TFD construction method in [47] and the copula theory. A copula-based positive TFD construction method was presented sequentially in [48]. As demonstrated in [48], a copula-based TFD has desirable properties of being positive, free from cross-term interference and having high time-frequency resolution and correct marginals to serve well for an energy density representation, showing great potential for the planetary gearbox fault diagnosis. For the copula-based TFD construction method reported in [48], a template, i.e., the spectrogram by STFT, is needed. However, the spectrogram would introduce the influence of the window length on the constructed copula-based TFD, which is still an open question [48]. To eliminate the spectrogram influence, a spectrogram-free

copula-based TFD construction method will be developed as being addressed in the second research topic as defined in Section 1.3.

1.2.2.4 Other vibration signal analysis methods

In the literature, there are other vibration signal analysis methods for condition monitoring and fault diagnosis of a planetary gearbox such as techniques with deconvolution, spectral kurtosis, cyclo-stationary analysis, dimension reduction, stochastic resonance, etc., while they do not belong to the time domain, the frequency domain, or the joint time-frequency domain methods as reviewed above. Literature review on these techniques is given here.

Zhang et al. [116–118] developed a de-noising scheme based on the blind deconvolution and applied the scheme to vibration signals collected from a helicopter planetary gearbox with seeded carrier crack to validate the gear fault diagnosis performance. Barszcz and Randall [119] applied the spectral kurtosis technique for tooth crack detection in a wind turbine planetary gearbox, showing that the proposed spectral kurtosis based method is able to detect the existence of the tooth crack several weeks before the gear failure. Bartelmus [120] summarized the research work of his group on vibration analysis for planetary gearbox condition monitoring and stressed the application of cyclo-stationary analysis on fault signature extraction for planetary gearboxes. Zimroz and Bartelmus [121] showed possibilities of using cyclo-stationarity for a gearbox condition evaluation and developed a spectral coherence map based diagnostic measure to evaluate the condition of a planetary gearbox used in the mining industry. The results in [121] suggested the advantages of such an approach with signal cyclo-stationarity properties on the multi-fault problem. Zimroz and Bartkowiak [122] employed two multivariate methods, namely principal component analysis and canonical discriminant analysis, to reduce the dimensionality of the multidimensional diagnostic data into lower dimensional space for data behavior understanding and better discriminant function generation for fault classification. Lei et al. [123] proposed an Adaptive Stochastic Resonance (ASR) method to discover the weak fault char-

acteristics from a noisy planetary gearbox vibration signal for diagnosing the sun gear faults of a chipped tooth and a missing tooth. Zuo et al. [124] proposed a fault feature separation method by Principal Component Analysis (PCA) and Independent Component Analysis (ICA) for an one-dimensional time series. They used WT to pre-process the one-dimensional vibration data and then used the coefficients of the wavelet transform at different scales as the input to PCA and ICA to meet the requirement of multiple data series. The results in [124] showed that the method of combining WT and ICA works better than the method of combining WT and PCA for impulse detection. Later, Wang et al. [125] presented a fault component separation method integrating the Ensemble Empirical Model Decomposition (EEMD) with ICA for wind turbine planetary gearbox fault diagnosis. They used EEMD to decompose an one-dimensional vibration signal into a series of Intrinsic Mode Functions (IMFs) as Pseudo-Multi-Channel (PMC) signals, then ICA was performed on PMC signals to reduce the dimensionality for fault feature extraction [125].

Aforementioned summary gives a brief description regarding the so-called other signal processing techniques. These advanced signal processing techniques may inspire new ideas for better performance on the planetary gearbox fault diagnosis, such as the dimension reduction method for fault feature discrimination and extraction. Zuo et al. [124] and Wang et al. [125] used PCA and ICA to extract fault features from the decomposed multiple data series. However, as argued by Sotiras et al. [126], PCA and ICA result in the decomposition with high overlap that lack specificity because PCA and ICA model the data through complex mutual cancellation between components of opposite signs by taking both negative and positive values. On the other hand, Non-Negative Matrix Factorization (NNMF) is an alternative for dimension reduction decomposition and enjoys more increased interpretability and specificity than PCA and ICA with the non-negative constraint on the decomposition [126]. Inspired by this theoretical idea, fault feature extraction by dimension reduction can also be achieved by the NNMF applied on the copula-based TFD thanks to

the positive property of the copula-based TFD and should have better performance than the decomposition by PCA and ICA. This hypothesis with the application on planetary gearbox fault diagnosis will be addressed in the third research topic as defined in Section 1.3.

1.2.3 Intelligent diagnosis methods

Despite the achieved success in planetary gearbox fault diagnosis by signal processing methods, the diagnosis decision largely relies on a high degree of expertise of the analyst to reveal the revelation of a fault in the vibration signal. On the other hand, intelligent fault diagnosis methods overcome this shortcoming. With the aid of artificial intelligence techniques, intelligent fault diagnosis methods can "learn" and "remember" the underlying knowledge regarding a gear fault of a planetary gearbox so as to identify the fault intelligently when a similar fault occurs afterwards [127]. Some of the reported intelligent diagnosis methods are reviewed in the following.

Chin et al. [128] investigated fault detection for a helicopter planetary gearbox as a pattern classification problem by combining a quantization matrix, flagging the measurements, and a multi-valued influence matrix. Implementation results on a helicopter planetary gearbox at healthy and at faulty instances indicated that the presented method can provide accurate detection [128]. Samuel and Pines [129] presented a fault classification scheme using a Kohonen self-organizing neural network and a back-propagation neural network to classify seeded faults of the sun gear spalling and the spiral bevel gear scoring in an OH-58A helicopter planetary gear transmission. They adopted the normalized energy metric accounting for the energy redistribution at the sidebands of the dominant meshing frequency and its harmonics as the feature vector to serve as the input to the classification scheme [129]. Dong et al. [130] investigated the hidden semi-Markov models to detect a crack in the planetary carrier used in the UH-60A Blackhawk main transmission. Li et al. [131] applied k-nearest neighbor algorithm for fault detection of a planetary gearbox. Liu et al. [132] proposed a method based on linear discriminant analysis and the Support Vector Machine

(SVM) to identify planet tooth pitting fault with different levels, namely, baseline, slight, moderate, and severe as defined in [132], in an experimental planetary gearbox. To improve classification and to speed up computation, Qu et al. [133] reported an SVM-based feature selection method to address the fault classification problem with reduced feature dimension for the same experimental planetary gearbox in [132]. The method in [133] used the norm of the weighted vector of SVM as the measure to evaluate the importance of a particular feature to the fault classification problem. Liu et al. [134] investigated a feature ranking criterion for multi-class SVM classification. In their work, the feature effectiveness was estimated for each individual feature by its contribution to class separability, measured by cosine similarity, in the kernel space [134]. Khazaee et al. [135] presented a least-square SVM based approach for planetary gearbox fault classification with extracted features from the vibration frequency spectrum, considering three health conditions, namely healthy gears, ring gear with worn tooth face, and planet gear with worn tooth face. To take advantage of the complementary information from multiple sensors mounted on different locations, Lei et al. [136] introduced a planetary gearbox fault detection method with multi-sensor data fusion by adaptive neuro-fuzzy inference systems. The effectiveness of the method was demonstrated by experimental data with sun gear tooth crack, sun gear tooth pitting, sun gear tooth chipping, and sun gear tooth missing [136]. Dybała [137] presented a classifier based on Nearest Boundary Vector (NBV) for the fault recognition of planetary gearboxes used in bucket wheel excavators. The NBV-based classifier employed diagnostic parameters extracted by the noise-assisted feature subset evaluation method and enabled the semi-soft classification to evaluate the classification certainty [137].

With the above literature review, it can be seen that intelligent diagnosis methods are essentially the classifiers to solve the fault diagnosis problem as a pattern classification problem. Given a specific classifier, its classification accuracy is determined by the input: more health information contained in the input, higher classification accuracy can be obtained by the classifier. For the cases of planetary gearbox fault diagnosis, the inputs are the

employed fault features. Consequently, to measure the health status information contained in the fault feature developed in the fourth research topic as defined in Section 1.3, one intelligent diagnosis method available in the literature is used.

1.3 Research scope

The objective of this thesis study is to develop effective methods of vibration signal analysis for planetary gearbox fault diagnosis aided by vibration signal modeling. First of all, as reviewed in Subsection 1.2.1, the planetary gear set vibration signal modeling method reported in [27] needs to be improved to include all vibration sources from the sun gear, the ring gear, and planet gears with the incorporation of the transmission path effect for each individual vibration source. In this way, more realistic resultant vibration signals can be generated for a planetary gear set. The resultant vibration signal can then be analyzed as an aid to develop novel vibration signal analysis methods to address the shortcomings of the reported work as reviewed in Subsection 1.2.2, including the spectrogram-free copula-based TFD construction for representation of the energy density in the time-frequency domain, the extraction of fault features through dimension reduction of the copula-based TFD by NNMF, and the development of fault features in the time domain with great robustness to noise interference. Overall, through this thesis research, it is expected that industrial engineers can benefit from having more powerful tools for planetary gearbox fault diagnosis, thus improving the reliability and safety of industrial power transmission systems with planetary gearboxes.

Specifically, four research topics are proposed as shown in Fig. 1.12. The planetary gearbox of interest has a single gear tooth fault. The vibration signal model and vibration signal analysis methods are developed in condition of stationary operation with constant load and constant speed. Lab experimental planetary gearbox vibration signals from the Reliability Research Lab at the University of Alberta, acquired by former group members in the year of 2011, are employed to validate the proposed resultant vibration signal model and

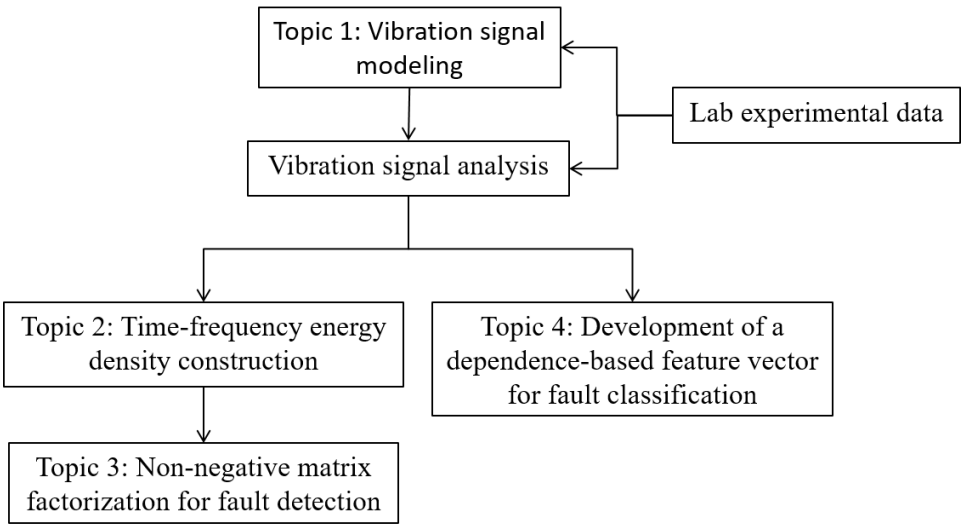

Fig. 1.12: Outline of research topics

the novel methods of vibration signal analysis. Further studies of non-stationary operation and/or multiple gear tooth faults could be carried out in the future.

In the first research topic, a comprehensive vibration signal model is proposed for a planetary gear set. As shown in Fig. 1.4, vibration sources come from the sun gear, the ring gear, and the planet gears; as shown in Fig. 1.6, the transmission path consists of two parts: the part inside the gearbox to the casing and the part along the casing to the transducer position. In reported works, the resultant vibration is partially modeled, either because the sources of vibration are partially covered (i.e., only planet gear vibration sources are covered) or only part of the transmission path is considered (i.e., only the part along the casing is considered) [27]. To comprehensively reflect and understand the vibration characteristics of a planetary gear set, the proposed resultant vibration signal model considers vibration sources from the sun gear, the ring gear, and the planet gears, and the transmission path effects both inside the gearbox and along the casing. The proposed resultant vibration signal model generates more realistic simulated vibration signals for the development of the vibration signal analysis methods proposed in the following research topics. The vibration sources are generated by the two-dimensional lumped-parameter dynamic model shown as in Fig. 1.11 and reported in [27]; the time-varying mesh stiffness is calculated with the

potential energy methods reported in [23]. This topic is covered in Chapter 2.

In the second research topic, for the energy density representation of a vibration signal in the time-frequency domain, an energy density construction method is proposed based on a spectrogram-free non-parametric copula. As reviewed in Subsection 1.2.2, compared with linear TFRs and bilinear TFDs, copula-based TFDs serve better for energy density representation with the four desirable properties [48]. The core idea in copula-based TFD is the Time-Frequency Copula (TFC) estimation, which is used to represent the energy marginal dependence [48]. In the reported copula-based TFD construction methods [48], TFC estimation relies on spectrogram-based marginals. However, due to the overlap of adjacent windowed segments in STFT,spectrogram-based marginals are with great redundancy for energy marginal representation. Besides, the spectrogram would introduce the influence of the window length on the constructed copula-based TFD, i.e., different windowing lengths and overlapping length lead to different copula-based TFDs with different estimated TFCs [48]. To address the above shortcomings of the reported spectrogram-based TFC estimation in [48], a spectrogram-free TFC estimation method is proposed that starts with the instantaneous energy and the energy spectral density instead of the spectrogram-based marginals. Technically, TFC estimation is conducted by a non-parametric copula. Compared with a parametric copula [138], a non-parametric copula is free from the assumption that the data belong to a particular distribution or the model structure is fixed [139]. After construction of the copula-based TFD with spectrogram-free TFC estimation, its performance on planetary gearbox fault diagnosis in identifying fault-related frequencies and locating fault-induced impulses will be investigated through a simulated case study and an experimental case study. This topic is covered in Chapter 3.

The focus of the third research topic is the fault feature extraction for detection of planetary gearbox faults by dimension reduction of the developed copula-based TFD in Topic 2. As reviewed in Subsection 1.2.2, PCA and ICA have been reported as dimension-reduction methods for diagnosing planetary gearbox faults by discriminating the fault information in

a lower-dimensional space. However, PCA and ICA estimate the decomposition by taking both negative and positive values, thus modeling the original data through complex mutual cancellation between components of opposite signs. The mutual cancellation leads to high overlap among decomposed components, which leads the results of PCA and ICA to lack interpretability and specificity [126]. On the other hand, NNMF enjoys increased interpretability and specificity by estimating decomposition with pure non-negative values. This non-negative constraint is the core difference between NNMF and PCA/ICA. It is feasible to apply NNMF to the constructed copula-based TFD in Topic 2 thanks to the property of being positive. Eventually, the performances on planetary gearbox fault diagnosis by fault feature extraction in lower-dimensional spaces decomposed by NNMF and PCA/ICA are analyzed and compared. Through the comparison, the application and effectiveness of NNMF-based decomposition on positive TFD are rationalized for planetary gearbox fault diagnosis. This topic is covered in Chapter 4.

In the fourth research topic, a dependence-based feature vector for planetary gearbox fault classification is developed. As reviewed in Subsection 1.2.3, intelligent diagnosis methods solve the fault diagnosis problem as a pattern classification problem, for which it is critical to extract fault features with adequate health status information as the input to a classifier. For planetary gearbox fault classification, Lei et al. [91] reported a fault feature called AACO that was designed especially for planetary gearbox fault diagnosis. AACO is based on the mechanism that the gear characteristic frequencies of a planetary gearbox are integer multiples of the carrier rotating frequency [91]. However, this mechanism is not always true, as demonstrated in detail in Chapter 5. Consequently, it is desirable to develop new fault features with better extraction of the health status information from a vibration signal. Accordingly, in this research topic, a novel feature vector is explored and developed based on the dependence between the raw vibration signal and its IMFs. The IMFs are obtained by EEMD. The gist of this topic is that with different faults, different transient fault-induced impulses will be excited and distributed differently in the EEMD-

decomposed IMFs, resulting in different dependence between the raw vibration signal and the IMFs. Parametric copulas are used to capture this dependence. In a parametric copula, the copula parameter works as the coefficient to describe the dependence [138]. As different faults may correspond to different dependence, copula parameters should be different accordingly. Following this logic and hypothesis, the novel feature vector is developed with the parameter of a parametric copula. The robustness of the developed feature vector to noise is checked. The performance of the developed feature vector in terms of the fault classification accuracy is compared with that of the reported AACO in [91]. This topic is covered in detail in Chapter 5.

With the knowledge and results generated in this thesis, this PhD research project will advance the state of the art of the research on vibration signal analysis for planetary gearbox fault diagnosis. The proposed comprehensive vibration signal model can provide more realistic resultant vibration signals to generate more useful fault features for planetary gearbox fault diagnosis. The aim of the developed vibration signal analysis methods is to make contributions to industrial power transmission systems with planetary gearboxes by providing more effective fault diagnosis tools to prevent unexpected failures, thus reducing the operation and maintenance costs.

1.4 Thesis organization

The guidelines from the Faculty of Graduate Studies and Research at the University of Alberta are followed to prepare this paper-based thesis. This thesis is composed of 6 chapters. The list of chapters and the main theme of each chapter are presented as follows:

- Chapter 1 gives the introduction to the thesis study, including the background and the literature review on planetary gear set vibration signal modeling and vibration signal analysis methods for planetary gearbox fault diagnosis. The research scope and the thesis structure are also described in Chapter 1.

- Chapter 2 reports a comprehensive vibration signal modeling method for a planetary gear set. The vibration sources from the sun gear, the ring gear, and the planet gears are included in the resultant vibration signal subject to the transmission path effects. The transmission path effects are modeled as two parts: the part inside the gearbox to the casing and the part along the casing to the transducer position. Given gear sizes, the transmission path effect modeling parameters are estimated. The influences of different transmission paths on the resultant vibration signals are analyzed. The major contribution of this chapter is documented in a published journal paper [140] and a refereed conference paper [141].
- Chapter 3 proposes a time-frequency energy density construction method based on a non-parametric copula. The non-parametric copula density, i.e., the TFC, is estimated by the instantaneous energy and the energy spectral density to be free from the spectrogram-based marginals. A beta kernel estimator is employed to construct the density of the non-parametric copula. To find the optimal smoothing parameter for the Beta kernel, a method integrating the spectrogram as the approximate energy distribution and the mean integrated squared error is proposed and validated. The copula-based TFD is then constructed to represent the energy density in the time-frequency domain. Its performance on planetary gearbox fault diagnosis is achieved by identifying fault-related frequencies in its frequency energy marginal and locating fault-induced impulses in the time-frequency domain, which is free from the Heisenberg uncertainty principle. The results of this chapter are published in a refereed conference paper [142] and documented in [143] which is submitted to *Mechanical Systems and Signal Processing* for possible publication.
- Chapter 4 discusses the method of fault feature extraction by NNMF for planetary gearbox fault detection. NNMF is applied to the copula-based positive TFD constructed in Chapter 3 for dimension reduction with matrix factorization. Then the decomposed components are analyzed to extract the fault feature, i.e., the identifi-

cation of the gear tooth fault characteristic frequency. To demonstrate the advantage of the developed NNMF-based method, a reported method based on ICA is applied as well. They are compared in terms of the accuracy at identifying the gear tooth fault characteristic frequency. The major work and contribution of this chapter are documented in [144] and submitted to *Journal of Sound and Vibration* for possible publication.

- Chapter 5 demonstrates the development of a dependence-based feature vector for planetary gearbox fault classification. The feature vector is based on the tail dependence between the raw vibration signal and its EEMD-decomposed IMFs. The tail dependence is revealed to be an upper tail dependence and is described by the Gumbel-Hougaard (GH) copula, a parametric Archimedean copula with upper tail dependence structure. The parameter of the GH copula is used to develop the dependence-based feature vector through a simulated vibration signal analysis. With the developed feature vector as input, different gear tooth faults in an experimental planetary gearbox are classified by SVM for planetary gearbox fault classification. To demonstrate the advantage of the developed feature vector, the classification accuracy associated with the developed feature vector is compared with the classification accuracy associated with the reported AACO by Lei et al. [91]. The major work and contribution of this chapter is published in a refereed conference paper [145] and documented in an accepted journal paper [146] submitted to *Journal of Sound and Vibration* for publication.
- Chapter 6 summarizes this thesis study with conclusions and discussions. Some possible directions for moving forward in future work are also discussed based on the outcomes of the thesis research.

Chapter 2

Vibration signal modeling of a planetary gear set with transmission path effect

As indicated in Fig. 1.12, the focus of this chapter is on the first research topic, planetary gear set vibration signal modeling, which generates a resultant vibration signal for a planetary gear set. The generated vibration signal provides aid in the development of vibration signal analysis methods, as discussed in Chapter 3, Chapter 4, and Chapter 5, for planetary gearbox fault diagnosis. The organisation of this chapter is as follows. In Section 2.1, an introduction to planetary gear set vibration signal modeling is provided with a literature review. Section 2.2 presents the proposed planetary gear set vibration signal model considering multiple vibration sources and transmission path effects. In Section 2.3, an analysis of the modeled resultant vibration signal is conducted, including influence analysis of the transmission path effect inside the gearbox, influence analysis of the overall transmission path effect, and properties of the modeled resultant vibration signal. Experimental validation for the proposed vibration signal model is performed in Section 2.4. Section 2.5 concludes the study. The results of this chapter have been published in a journal paper [140] and a refereed conference paper [141].

2.1 Introduction

Planetary gear sets are widely used in heavy industry applications such as wind turbines and helicopters as a planetary gear set can provide a high transmission ratio and a high

power density within a compact structure. A planetary gear set, normally, consists of a centrally rotating sun gear, a ring gear, several planet gears that mesh with the sun gear and the ring gear simultaneously, and a carrier that holds the planets. Fig. 2.1 shows a planetary gear set with four planet gears [1]. With different power input and power output configurations, a planetary gear set can achieve different kinematic combinations. In this study, the investigated planetary gear set has the ring gear fixed, the sun gear as the power input and the carrier as the output.

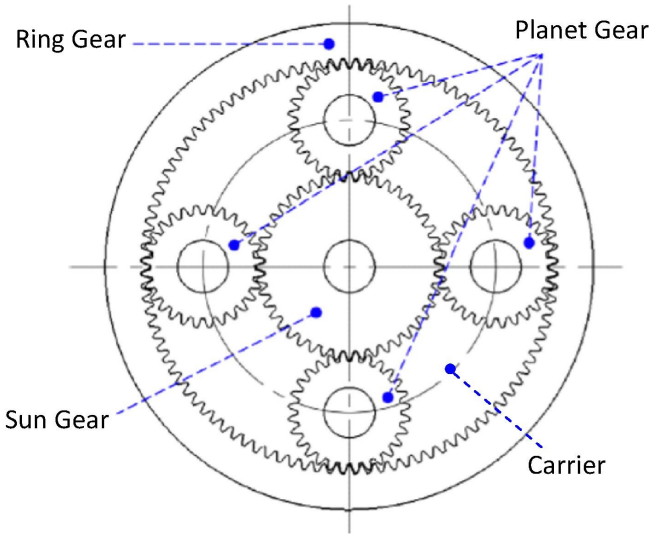

Fig. 2.1: Schematic of a planetary gear set with four planet gears [1]

With the complex kinematics, vibration signals of planetary gear sets are more complicated than those of fixed shaft gear sets. In a planetary gear set, multiple sun-planet gear pairs are in mesh simultaneously with similar vibration forms but different phases [23]. So are the multiple ring-planet meshes. Moreover, the transmission path effect is time varying with the carrier rotation [20]. Multiple vibration sources and time-varying transmission path effects lead to the complexity of the vibration signal for a planetary gear set [20–22].

As investigated by Lin and Parker [59], mesh stiffness variation is one of the major sources of gear vibration. To evaluate gear pair mesh stiffness, numerical Finite Element Methods (FEMs) and analytical methods have been employed by researchers. Meagher et al. [147] built a gearbox dynamic model by FEM to predict the mesh stiffness and in-

vestigated the gear mesh stiffness effect on the dynamic response. Jia and Howard [148] developed a three-dimensional finite element model to evaluate the mesh stiffness of gears with spalling and crack damage. FEM modeling has the advantages of being flexible for any type of gear profile and gear fault while it has the disadvantages of being time-consuming and with discretization errors [147]. On the other hand, with analytical equations, analytical methods have advantages of being simple and effective in evaluating gear mesh stiffness [23]. Chaari et al. [149] proposed an analytical model to quantify the gear mesh stiffness reduction due to spalling and breakage. Chaari et al. [150] derived an analytical formulation of the time varying gear mesh stiffness and quantified the gear mesh stiffness reduction for gears with a cracked tooth. The object in [149, 150] was mainly focused on external-external gear pairs. As demonstrated in Fig. 2.1, besides the sun-planet gear meshes as external-external gears, a planetary gear set has ring-planet gear meshes as external-internal gears. Thus, the study on the mesh stiffness of a pair of external-internal gears is necessary for dynamic analysis of a planetary gear set. Pintz et al. [151] evaluated the mesh stiffness of a pair of external-internal gears analytically by digitizing the tooth profile into a large scale of discrete points.

Despite the advantages, a challenge on analytical methods is to express analytical equations with various tooth profile and various gear faults [23]. Among the reported works, there are two approaches, one of which assumes a function form and the other of which uses the potential energy concept. Al-shyyab and Kahraman [152] and Kim et al. [60] approximated the time-varying mesh stiffness of a planetary gear set by a square waveform. However, they did not specify on how to get the magnitudes of the time-varying stiffness. Besides, the square waveform only reflects the mesh change of tooth contact number but ignores the mesh stiffness variation caused by the change of tooth contact position. Moreover, the flatness of the stiffness curve could lead to unwanted frequency components in the dynamic response [61]. To overcome shortcomings mentioned above, Liang et al. [61] applied potential energy method to evaluate the time-varying mesh stiffness of a planetary

gear set. The obtained time-varying mesh stiffness can reflect not only the stiffness variation caused by the change in the number of contact tooth pairs but also the variation caused by the change in the contact position of a gear pair. However, the gear tooth was assumed starting from the gear base circle in [61]. Later, Liang et al. [23] refined the modeling of the gear tooth of an external gear rigorously by considering the gear tooth starting from the gear root circle. The method reported in [23] will be applied directly in this study to evaluate the mesh stiffness of a planetary gear set. Fig. 2.2 shows the ring-planet mesh stiffness and the sun-planet mesh stiffness for a healthy planetary gear set [23]. The physical parameters are shown in Table 2.1 [27].

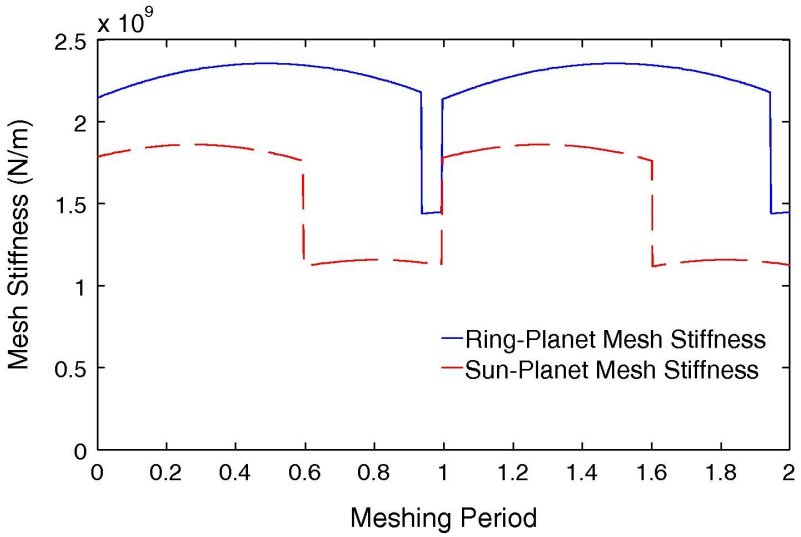

Fig. 2.2: Time-varying gear mesh stiffness of a healthy planetary gear set [23]

Various dynamic models of a planetary gear set have been established and studied by researchers. McFadden and Smith [20], McNames [53], and Mosher [153] investigated the vibration spectral structure of a healthy planetary gear set, and demonstrated the asymmetry of modulation sidebands and the suppression of the meshing frequency in the vibration spectrum for a healthy planetary gear set. Inalpolat and Kahraman [22] proposed a mathematical model to describe the mechanisms leading to modulation sidebands of planetary gear sets, taking the configuration parameters such as the number of planets, planet position angles, and the number of gear teeth into consideration. The planetary gearboxes were

Table 2.1: Physical parameters of planetary gear set [27]

Parameters	Sun gear	Planet gear	Ring gear
Number of teeth	19	31	81
Module (mm)	3.2	3.2	3.2
Pressure angle	20°	20°	20°
Mass (kg)	0.7	1.822	5.982
Young's modulus (Pa)	2.068×10^{11}	2.068×10^{11}	2.068×10^{11}
Poisson's ratio	0.3	0.3	0.3
Base circle radius (mm)	28.3	46.2	120.8
Reference circle radius (mm)	30.4	49.6	129.6
Bearing stiffness	$k_{sx} = k_{sy} = k_{rx} = k_{ry} = k_{cx} = k_{cy} = k_{pnx} = k_{pny}$ $= 1.0 \times 10^8$N/m		
Bearing damping	$c_{sx} = c_{sy} = c_{rx} = c_{ry} = c_{cx} = c_{cy} = c_{pnx} = c_{pny}$ $= 1.5 \times 10^3$Ns/m		

classified into five distinct categories according to the modulation sideband orders and relative amplitude distribution in the vicinity of the mesh frequency harmonic orders, namely equally spaced planets and in-phase gear meshes, equally spaced planets and sequentially phased gear meshes, unequally spaced planets and in-phase gear meshes, unequally spaced planets and sequentially phased gear meshes, and unequally spaced planets and arbitrarily phased gear meshes as defined in [22]. Later, Inalpolat and Kahraman [26] proposed a nonlinear dynamic model to predict the modulation sidebands of planetary gear sets with gear manufacturing errors. Feng and Zuo [25] proposed mathematical models to investigate the vibration spectral characteristics of planetary gear sets for fault diagnosis. In their model they considered the amplitude modulation and the frequency modulation induced by different gear damages and periodically time-varying working condition, as well as the vibration transmission path effect. Cheng et al. [74] built a pure torsional dynamic model to investigate the properties of a planetary gear set with a pit on a tooth of the sun gear. Liang et al. [27] developed a dynamic model with 3 degrees of freedom for each component in a planetary gear set to obtain vibration sources and then estimated the resultant vibration signal of a planetary gear set at the sensor location. The resultant vibration signal

was modeled as the weighted summation of the vibrations of the planet gears. However, the resultant signal modeling method reported in [27] has two shortcomings. Firstly, they ignored the vibration components generated by the sun gear and the ring gear. In practical applications, sensors are commonly mounted on the housing of the gearbox to acquire the vibration from the whole gearbox. As illustrated by Feng and Zuo [25] and Forrester [28], the overall resultant vibration of a planetary gear set should consist of ring gear vibration, sun gear vibration and each planet gear vibration. Secondly, the transmission path was partially modeled. The transmission path regarding each gear comprises two parts: the transmission path from the vibration source to the casing and the transmission path along the casing to the transducer [25]. In [27], they only modeled the transmission path along the casing to the transducer, but ignored the transmission path from the vibration source to the casing inside the gearbox. These two shortcomings are addressed in this study. Accordingly, a more comprehensive signal model for a planetary gear set is proposed. In the proposed model, sun gear vibration, ring gear vibration and each planet gear vibration are all included. Moreover, the transition path effect to be modeled will cover not only the part along the casing to the transducer position but also the part from the vibration source to the casing for each gear.

In Section 2.2, we firstly refer to the dynamic model of a planetary gear set proposed in [27]. With this model, vibration sources from gear components, i.e., the sun gear, the ring gear, and the multiple planet gears, are obtained. Then the transmission path effects are modeled, including the part inside the planetary gearbox, the part along the casing, and the overall transmission path effect combining the two parts. Finally, with vibration sources and the overall transmission path effect ready, the resultant vibration signal for a planetary gear set is constructed. In Section 2.3, the analysis on the resultant vibration signal is performed. The influence of different transmission paths and the properties of the resultant vibration signal are investigated. In Section 2.4, the proposed vibration signal model is validated with experimental data. Finally, conclusions are drawn in Section 2.5.

2.2 Modeling of vibration signals

In Subection 2.2.1, a lumped-parameter dynamic model developed in [27] is adopted to generate vibration sources in a planetary gear set from the sun gear, the ring gear, and the multiple planet gears. A dynamic model has close connection with physical parameters of a gearbox, like the gear mesh stiffness and the damping. Compared with the dynamic models developed in [26, 74], the adopted one has the following advantages [27]: (1) the gear vibration is described in the horizontal and vertical directions so that it is more convenient to compare with the experimental vibration in a certain direction; (2) both the gyroscopic force and the centrifugal force are considered in the equations of motion as the inertial forces; and (3) more accurate physical parameters are adopted including the time-varying mesh stiffness and the physical damping. In Subsection 2.2.2, the transmission path effect modeling is studied. In [27], only the transmission path effect along the casing is modeled while the transmission path effect inside the gearbox is ignored. In addition, in order to model the transmission path effect so that the vibration from the farthest position can be captured, the parameter in their model which controls the window bandwidth needs to be positive. However, the positive parameter value amplifies the vibration from the farthest position, which is not proper for transmission path effect representation. To overcome the above shortcomings, in this study, the value of the parameter used in [27] is constrained so that there is no amplification for the vibration from the farthest position. With this added constraint, the model in [27] can be used only when the vibration from the farthest position has zero effect on the resultant signal perceived by the sensor. For the scenario wherein the vibration from the farthest position has a positive impact on the sensor-perceived signal, the transmission path effect model reported in [154] is referred to and modified with an added constraint on the parameter. In addition to modifying models in [27, 154] for the modeling of the transmission path effect along the casing, the modeling of the transmission path effect inside the gearbox is proposed as well. Then the overall transmission path effect is modeled by combining the part inside the gearbox and the part along the casing. Subsequently,

in Subsection 2.2.3, the resultant vibration signal model is proposed by considering the multiple vibration sources and the overall tranmssion path effect.

2.2.1 Dynamic modeling of a planetary gear set

Fig. 1.11 shows the dynamic model of a planetary gear set reported in [27]. It is a two-dimensional lumped-parameter dynamic model. The local coordinate systems are fixed on the carrier. The global coordinate system is fixed on the ground. Fig. 1.11 shows original positions of all coordinate systems at the initial time. The gear mesh interface is modeled as a spring-damper system. The effects of transmission errors, frictions between gear teeth, and other practical phenomenon such as backlash are ignored [27]. Differential equations which can be found in [27] are used to represent the equations of motion for the dynamic model.

The time-varying mesh stiffness involved in this dynamic model is evaluated using the potential energy method as reported in [23]. Fig. 2.2 illustrated the mesh stiffness of a pair of ring-planet gears and a pair of sun-planet gears for a perfect planetary gear set with physical parameters listed in Table 2.1. The damping in this dynamic model is assumed to be proportional to the gear mesh stiffness as reported in [76].

For the planetary gear set to be investigated in this study, the sun gear and the carrier are the power input and the power output, respectively. The ring gear is fixed and the four planet gears are spaced equally. In this study, the sun gear rotational speed is constant at 46.667r/min and the torque load applied on the carrier shaft is 2367Nm. All gears are in healthy condition. By solving equations of motion numerically, vibration sources from the sun gear, the ring gear, and multiple planet gears can be obtained in both the horizontal direction (x direction) and the vertical direction (y direction) [27]. In this study, only the vertical components of the vibration sources are focused. The vibration sources go through different transmission paths and are acquired by the transducer eventually.

2.2.2 Modeling of transmission path effect

In practical applications, transducers are commonly mounted on the housing of a gearbox to acquire the vibration of the whole gearbox. Fig. 1.6 illustrates the possible transmission paths for the vibration from a sun-planet meshing point [25]. As discussed in [25], vibration transmitting along paths 2 and 3 is negligible because of the long transmission lengths and the great bearing damping. On the other hand, the vibration transmitting through path 1 are dominant in the transducer-perceived vibration. The rationale is that the path 1 is shorter and without bearings involved, leading to less attenuation [25]. Consequently, for the transmission path effect analysis in this study, only transfer path 1 is considered and modeled.

As shown in Fig. 1.6, transfer path 1 can be divided into two parts: transmission path inside the gearbox from the vibration source to the casing and transmission path along the casing to the sensor position. The transmission path inside the gearbox has a constant length while the transmission path along the casing has a time-varying length with the rotation of the carrier. Vibrations lose energy during the propagation in the structure, resulting in the amplitude attenuation. If the length of transmission path is constant, the attenuation is constant; if the transmission path has a time-varying length, the attenuation can be modeled as a time-varying amplitude modulation [22]. Correspondingly, in this study, the transmission path effect inside the gearbox is represented by a constant smaller than 1 and the transmission path effect along the casing is represented by functions modified based on Hamming function [27, 154]. It should be noted that the phase differences induced by different lengths of transmission paths are not considered because of the short length differences among transmission paths and the high transmission velocity of vibration signals.

2.2.2.1 Modeling of the transmission path effect inside a planetary gearbox

As discussed previously, the transmission path length inside a gearbox (from the vibration source to the casing) is constant for a gear, which introduces constant vibration attenuation in terms of the vibration amplitude. In this part, the transmission path effects inside

a planetary gearbox for planet gears, the ring gear, and the sun gear are modeled by constants S_p, S_r, and S_s, respectively. For the values of S_p, S_r, and S_s, we have the following considerations and assumptions:

- In practical applications, sensors are mounted on the housing which is connected or fixed to the ring gear directly. Thus, it is reasonable to assume that there is no attenuation for the ring gear vibration transmitting to the casing. Thus, we assume that S_r=1.
- As the sun gear vibration transmits to the casing through planet gears, the sun gear vibration would have been attenuated when reaching the casing somehow. For the value of S_s, one value smaller than 1 should be chosen. The value varies with different levels of attenuation caused by different transmission paths.
- As modeled by the equations of motion in the dynamic model [27] for planet gears, the planet gear vibrations have two excitation sources: dynamic force of sun-planet gear meshing and dynamic force of ring-planet gear meshing. Accordingly, the overall planet gear vibration can be considered as the summation of two separated parts: planet vibration induced by ring-planet meshing and planet vibration induced by sun-planet meshing. Considering the lengths of transmission paths from the two excitation sources to the casing, the transmission path effect inside the gearbox for planet gear vibrations can be expressed as

$$S_p = aS_r + bS_s \tag{2.1}$$

  where a and b are constants to represent the weights of ring-planet meshing induced planet vibration and sun-planet meshing induced planet vibration in the overall planet vibration with $0 < a < 1, 0 < b < 1$.

2.2.2.2 Modeling of the transmission path effect along the casing

The vibration signal transmitting along the casing is under the amplitude modulation due to the time-varying transmission path induced by the carrier rotation [154]. As a planet gear

approaches the transducer, its influence increases, reaching the maximum when the planet gear arrives in the closest position to the transducer, then the influence decreases as the planet gear moves away from the transducer. Some researchers modeled the transmission path effect by a Hanning function [22], assuming the influence would be zero when the planet gear is at the farthest position to the transducer. However, it should be noted that even if the planet gear is at the farthest position, the transducer can obtain some of the vibration in some cases. Accordingly, Liang et al. [27] proposed a modified Hamming function to suit such scenarios. However, their model has a shortcoming that when a planet gear is at the farthest position to the transducer, the vibration from this planet gear may be amplified with improper parameter values. The vibration amplification is not reasonable as the largest attenuation should always be achieved when a planet gear is at the farthest position to the transducer. In this study, a comprehensive modeling method for the transmission path effect is proposed to overcome the shortcomings of previous models.

With different properties of a planetary gearbox, like its size and the ring gear flexibility, the vibration transmitting along the casing has two different situations based on how much vibration from the farthest position can be captured by the transducer: (1) the vibration is perceived by the transducer with attenuation and (2) no vibration is perceived by the transducer. Accordingly, two different window functions are adopted to model the transmission path effects for these two different situations in this study. The window functions are generated based on the Hamming function. Specifically, Eq. (2.2) [154] and Eq. (2.3) [27] with certain constraints on parameters are employed for situation 1 and situation 2, respectively. The constraints are applied to ensure $0 \leqslant w_i(t) \leqslant 1$, and the farther the planet gear are to the transducer, the more attenuation the vibration has.

$$w_i(t) = \alpha - (1-\alpha)\cos(w_c t + \psi_n) \tag{2.2}$$

where α controls the minimal value and the bandwidth of the window function with $0.5 \leqslant \alpha < 1$. If $\alpha \geqslant 1$, $w_i(t)$ would have values greater than 1; if $\alpha < 0.5$, $w_i(t)$ would be smaller

than 0. These situations are not acceptable for the transmission path effect representation.

$$w_i(t) = e^{\beta(\mathrm{mod}(w_c t+\psi_n,2\pi)-\pi)^2}(0.54-0.46\cos(w_c t+\psi_n)) \tag{2.3}$$

where β controls the bandwidth of the Hamming function with $\beta < 0$. If $\beta = 0$, Eq. (2.3) converts to one specific case expressed by Eq. (2.2). If $\beta > 0$, the effect corresponding to the vibration at the farthest position would be amplified, even overweight 1, which is not appropriate for the representation of the transmission path effect.

In Eqs. (2.2) and (2.3), w_c is the carrier angular frequency and ψ_n is the initial phase angle for nth planet gear. Fig. 2.3 demonstrates the window shapes defined by Eqs. (2.2) and (2.3) with different values of α and β.

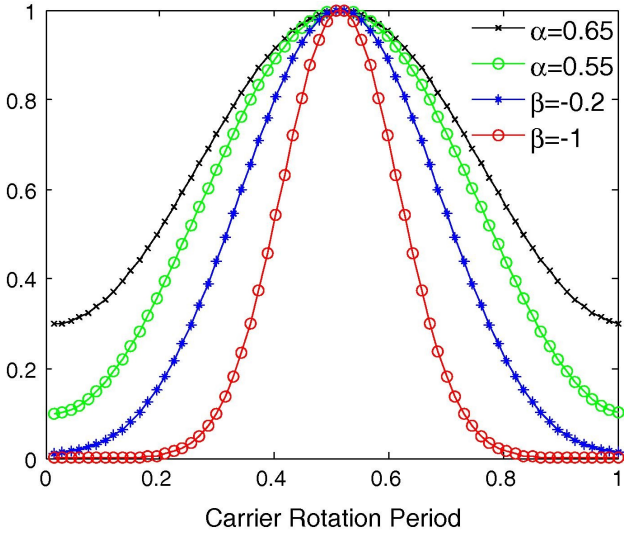

Fig. 2.3: Transmission path effects

As demonstrated in Fig. 2.3, Eq. (2.2) can be used to represent the transmission path effect in the situation that the transducer can perceive the vibration signal with attenuation even when the vibration is at the farthest position. With the increase of α, more vibration can be captured as the window function has a greater minimal value and a broader bandwidth. Eq. (2.3) can be used to represent the transmission path effect for the cases that the transducer cannot acquire any vibration from the farthest position. With the decrease of β, the bandwidth of the window function decreases, meaning that less portion of the vibration transmitting along the casing would be measured.

2.2.2.3 Modeling of the overall transmission path effect

As discussed previously, the overall transmission path considered in this study (i.e., transfer path 1 in Fig. 1.6) has two parts: transmission path inside the gearbox from the vibration source to the casing and the transmission path along the casing to the transducer position. The transmission path effect modeling for each part has been discussed in Subsubsections 2.2.2.1 and 2.2.2.2. In this part, the overall transmission path effect is modeled, which is proposed as the product of the transmission path effect inside the gearbox (constant) and the transmission path effect along the casing (time-varying). It indicates the cumulative attenuation induced by the overall transmission path.

In the following contents, an example is used to illustrate the modeling of the overall transmission path effect. In this example, the physical parameters of the planetary gear set in Table 2.1 are used. Accordingly, certain values are assigned to the parameters involved for the transmission path effect modeling.

For the values of a and b in Eq. (2.1), it is assumed that $a = b = 0.5$, meaning that the planet gear vibration induced by the ring-planet meshing and the planet gear vibration induced by the sun-planet meshing have the same weight in the overall planet gear vibration.

The value of S_s indicates the attenuation of the sun gear vibration to the casing inside the gearbox. It should be determined by the properties of the planetary gear set related to the attenuation such as gear sizes and gear flexibilities. Here, considering the physical parameters of the planetary gear set in Table 2.1 and for simplicity, the value of S_s is assumed to be 0.8. The value of S_r is chosen to be 1, as discussed in Subsubsection 2.2.2.1. With $a = b = 0.5$, $S_s = 0.8$, and $S_r = 1$, it would be given that $S_p = 0.5 \times 1 + 0.5 \times 0.8 = 0.9$ according to Eq. (2.1).

As for the modeling of the transmission path effect along the casing to the transducer position, considering the physical parameters in Table 2.1 and the waveform shape of the experimental vibration as shown lately in Fig. 2.12, Eq. (2.2) is employed with $\alpha = 0.6$. With $\alpha = 0.6$, the transducer can still perceive some of the vibration even when the planet

gear is at the farthest position to the transducer.

Consequently, given $S_s = 0.8$, $S_p = 0.9$, $S_r = 1$, and $\alpha = 0.6$, the overall transmission path effects for the sun gear vibration, planet gear vibrations, and the ring gear vibration can be expressed by Eq. (2.4), Eq. (2.5), and Eq. (2.6), respectively.

$$S_s w_i(t) = 0.8 \times [0.6 - 0.4\cos(w_c t + \psi_n)] \tag{2.4}$$

$$S_p w_i(t) = 0.9 \times [0.6 - 0.4\cos(w_c t + \psi_n)] \tag{2.5}$$

$$S_r w_i(t) = 1 \times [0.6 - 0.4\cos(w_c t + \psi_n)] \tag{2.6}$$

2.2.3 Modeling of resultant vibration

In previous studies like in [26, 27], the resultant vibration is modeled as the weighted summation of planet gear vibrations. The rationale is that the planet gear vibration can reflect the properties of sun gear vibration and ring gear vibration as they are parts of the excitations to the planet gear vibration [27]. However, sun gear vibration and ring gear vibration also act as the individual components to the overall resultant vibration subject to certain transmission path effects [25]. Thus, in this study, the overall resultant vibration for a planetary gear set is modeled in a more comprehensive way that the resultant vibration equals to the weighted summation of the sun gear vibration, the ring gear vibration and planet gear vibrations, expressed by Eq. (2.7). The weights reflect the overall transmission path effects for individual gear vibrations.

$$a(t) = \sum_{i=1}^{N} S_s w_i(t) \frac{1}{N} a_s + \sum_{i=1}^{N} S_r w_i(t) \frac{1}{N} a_r + \sum_{i=1}^{N} S_p w_i(t) a_{pi} \tag{2.7}$$

where $a(t)$ is the resultant vibration signal; N is the number of planet gears; a_s, a_r, and a_{pi} are sun gear vibration, ring gear vibration, and the ith planet gear vibration, respectively.

In this proposed model, the sun gear vibration is assumed to transfer through the N planet gears to the casing equally, meaning that $1/N$ of sun gear vibration will go through each planet gear to the casing, as expressed by the first term. Similarly, the ring gear vibration is assumed to transfer from the N different planet-ring meshing points to the

transducer position equally so that it has the second term in Eq. (2.7). The third term in Eq. (2.7) is the weighted summation of planet gear vibrations.

One of the advantages of this proposed modeling method for the resultant vibration is that the sun gear vibration and the ring gear vibration are modeled directly in the resultant vibration instead of being reflected by the planet gear vibrations. Moreover, the modeling of the transmission path effect not only can reflect the time-varying attenuation induced by the transmission path along the casing but also can reflect the attenuation caused by the transmission path inside the gearbox.

2.3 Resultant vibration analysis

2.3.1 Influence analysis of transmission path inside a gearbox

The overall transmission path effect is modeled as the product of the transmission path effect along the casing and the transmission path effect inside the gearbox as discussed in Subsubsection 2.2.2.3. The transmission path effect along the casing has been reported in [22, 25–27, 154]. The transducer-perceived signal is under amplitude modulation effect due to the time-varying transmission path along the casing. In this study, the models reported in [27, 154] are employed to model the transmission path effect along the casing by adding constraints on their parameters as discussed in Subsubsection 2.2.2.2 to make sure that there is no amplification for the vibration at the farthest position and the values of the transmission path effect is between 0 and 1. With the transmission path effect along the casing, before the overall transmission path effect analysis, the influence of transmission path effect inside the gearbox is focused and analyzed in this subsection. To do this, the transmission path effect along the casing is fixed and modeled by Eq. (2.2) with $\alpha = 0.6$ as discussed in Subsubsection 2.2.2.3. Fig. 2.4 illustrates the vibration components with the transmission path effect along the casing but without the attenuation caused by the transmission path inside the gearbox. The resultant vibration is the weighted summation of those vibration components in Fig. 2.4. The weights reflect the attenuations induced by the

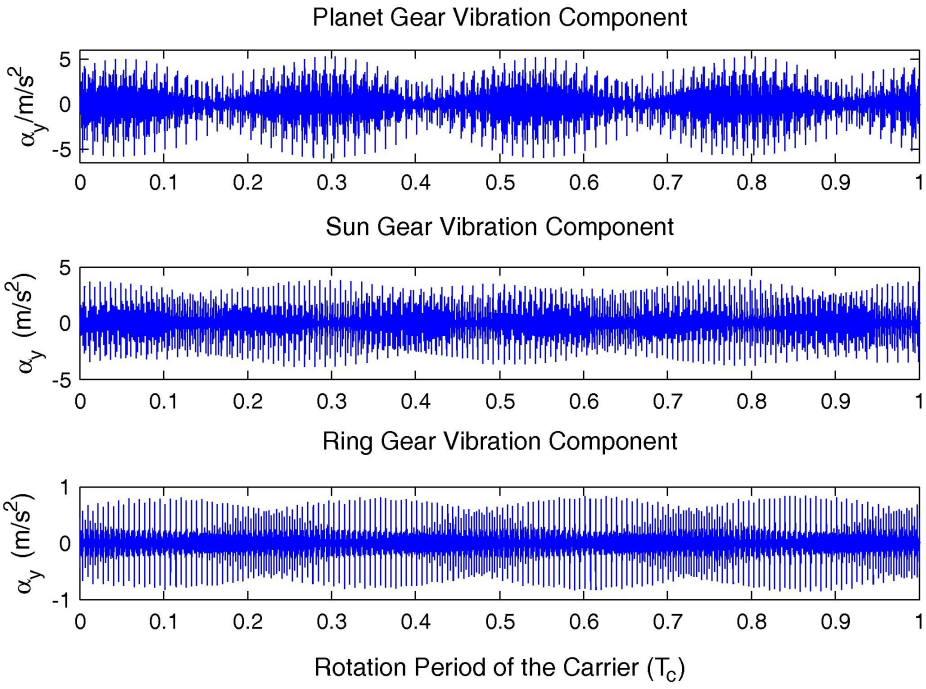

Fig. 2.4: Vibration components induced by planet gears, sun gear and ring gear

transmission paths inside the gearbox.

The vibration components demonstrated in Fig. 2.4 are the vertical acceleration signals from different gears within one period of the carrier rotation for a healthy planetary gear set. It can be noticed that the planet gear vibration component is subject to the amplitude modulation without overlap; while the sun gear vibration component and the ring gear vibration component are subject to the amplitude modulation as well but with a certain overlap. This overlap can affect the waveform shape of the resultant vibration as discussed later. The amplitude modulation for each vibration component fluctuates four times within one revolution of the carrier, corresponding to the number of planet gears.

To illustrate the influence of the transmission path effect inside the gearbox, two extreme conditions are considered: no sun gear vibration is captured and all the sun gear vibration is captured by the transducer, i.e., $S_s = 0$ and $S_s = 1$, respectively. In addition, a moderate condition is considered with $S_s = 0.5$ to illustrate a general case. As $S_r = 1$ has the value of 1 as discussed in Subsubsection 2.2.2.1, the value for S_p is calculated through Eq. (2.1) to be 0.5, 0.75, and 1 for $S_s = 0$, $S_s = 0.5$, and $S_s = 1$, respectively.

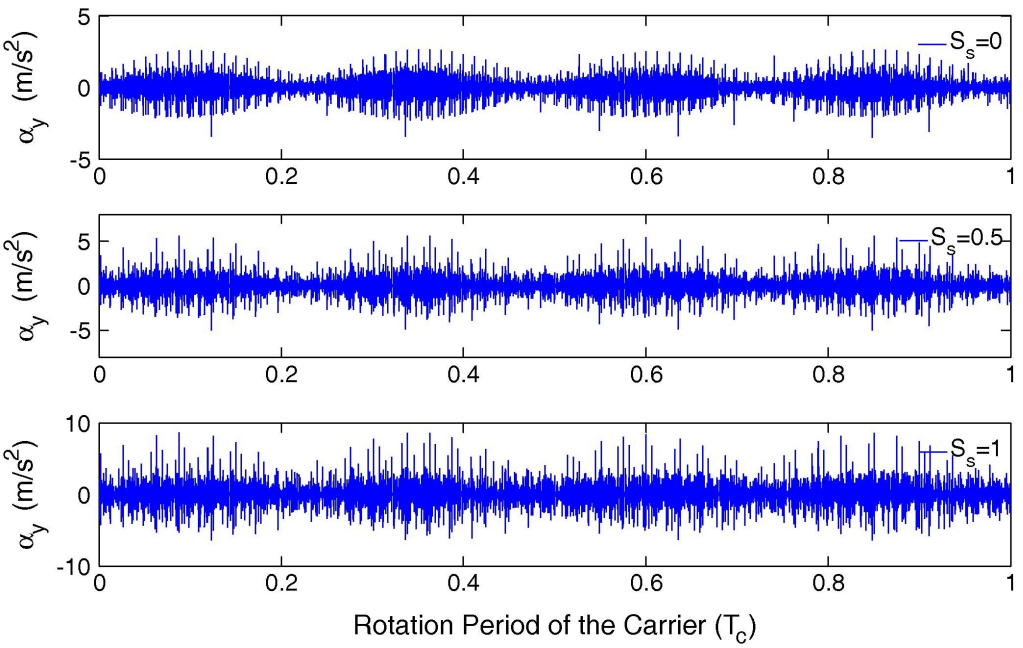

Fig. 2.5: Resultant vibration with different transmission path effects inside gearbox

Fig. 2.5 shows the resultant vibrations of a healthy gearbox with different transmission path effects inside the gearbox. For the case with $S_s = 0$, the resultant vibration is the weighted summation of planet gear vibrations and the ring gear vibration. The resultant vibration proposed in [27] is only the weighted summation of planet gear vibrations and it has the waveform shape as shown in the first plot in Fig. 2.4. It is noticed that the resultant vibration with $S_s = 0$ proposed in this study get some spikes and, additionally, it indicates that the resultant vibration is not necessary to be symmetric about the horizontal axis while the model in [27] indicates so. The rationale is that different vibration sources have different phases. Thus with more vibration sources involved, some of the vibration would be strengthened while some of others would be attenuated, resulting in the spikes and the asymmetry.

For the other two cases in Fig. 2.5, the sun gear vibration is contained in the resultant vibration besides the planet gear vibrations and the ring gear vibration. With the increase of S_s value, i.e., the decrease of the attenuation caused by the transmission path inside the gearbox on the sun gear vibration and planet gear vibrations, more spikes are presented

with greater amplitude and the resultant vibration remains asymmetric about the horizontal axis, showing similar properties as discussed in the case with $S_s = 0$. Besides, for each case in Fig. 2.5, the envelope of the resultant vibration fluctuates four times within one period of the carrier rotation, corresponding to the number of planet gears. It is noticeable that with the decrease of the attenuation inside the gearbox, joints between two envelopes get larger amplitudes. This is one result of the involvement of more vibration portions from different gears. In addition, the overlaps from the sun gear vibration and the ring gear vibration illustrated in Fig. 2.4 also make contribute to the larger amplitudes at the joint positions.

2.3.2 Influence analysis of different overall transmission path effects

In Subsection 2.3.1, the influence of the transmission path effect inside the gearbox is analyzed, given the effect of the transmission path along the casing fixed. However, in practical applications, the effect of the transmission path along the casing and the effect of the transmission path inside the gearbox are normally related to each other with positive correlation. In this subsection, these two transmission path effects are modeled in a way that if one increases/decreases, the other one would increase/decrease correspondingly. This setup is compatible well with the practical situation that with the increase/decrease of gear sizes inside a planetary gearbox, the size of the ring gear, i.e., the casing, increases/decreases as well. In the following contents, the transmission path effects are firstly estimated for four different gearboxes with different gear sizes, taking both the radiation damping and the material damping into consideration [155]; the influences of different overall transmission path effects on the resultant vibration are then analyzed.

To illustrate the influence of different overall transmission path effects on the resultant vibration, four cases are considered. Gear reference circle radiuses of the four planetary gear sets are listed in Table 2.2. The sizes of the four planetary gear sets increase gradually from case 1 to case 4. As discussed in Subsubection 2.2.2.3, case 1 has the following parameters for transmission path effect modeling: $S_s = 0.8$, $S_p = 0.9$, $S_r = 1$, $\alpha = 0.6$.

Table 2.2: Reference circle radius for each gear in planetary gear sets

Case #	Case 1	Case 2	Case 3	Case 4
Ring gear (mm)	129.6	170.2	304.2	506.9
Planet gear (mm)	49.6	53.05	55.2	57.9
Sun gear (mm)	30.4	64.1	193.8	391.1

The vibration amplitude decay subject to the transmitting distance is expressed by Eq. (2.8) [155]

$$A_2 = A_1(\frac{r_1}{r_2})^{\zeta} e^{-\eta(r_2-r_1)} \tag{2.8}$$

where A_1 and A_2 are vibration amplitudes at distances r_1 and r_2 from the vibration source; ζ is the radiation damping coefficient; η is the material damping coefficient.

The radiation damping is related to the type and the location of a vibration source and the material damping depends on material properties [155]. According to the study in [156], metals within the elastic range and metal structure with joints have the material damping smaller than 0.01 and between 0.03 and 0.07, respectively. Based on the analysis on radiation damping [157], for a planetary gearbox with gear masses equal to or greater than the ones in Table 2.1, the radiation damping coefficient should be bigger than 0.181. Correspondingly, in this study, it is assumed that the transmission path along the casing for the four cases has the material damping and the radiation damping as 0.005 and 0.2, respectively, while the transmission path inside the gearbox for the four cases has the material damping and the radiation damping as 0.04 and 0.2, respectively. Given case 1 has the transmission path effect modeling parameters as $S_s = 0.8$, $S_p = 0.9$, $S_r = 1$, $\alpha = 0.6$, the transmission path effect modeling parameters for case 2, case 3, and case 4 can be calculated by Eq. (2.8) based on gear sizes. The results are calculated being: $S_s = 0.6$, $S_p = 0.8$, $S_r = 1$, $\alpha = 0.55$ for case 2; $S_s = 0.5$, $S_p = 0.75$, $S_r = 1$, $\beta = -0.2$ for case 3; $S_s = 0.4$, $S_p = 0.7$, $S_r = 1$, $\beta = -1$ for case 4.

With the transmission path effects, resultant vibrations for the four cases are constructed by Eq. (2.7) and are illustrated in Fig. 2.6, Fig. 2.7, Fig. 2.8, and Fig. 2.9, respectively.

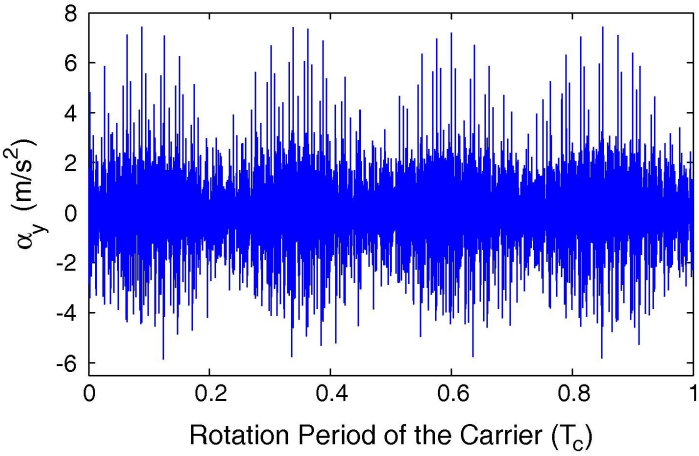

Fig. 2.6: Resultant vibration with $S_s = 0.8$, $S_p = 0.9$, $S_r = 1$, $\alpha = 0.6$

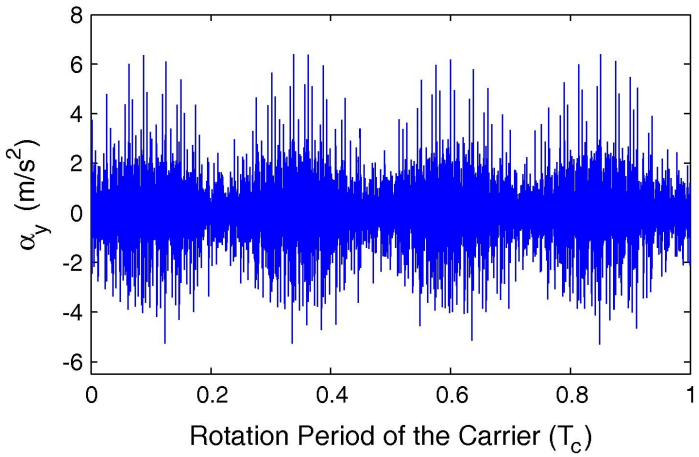

Fig. 2.7: Resultant vibration with $S_s = 0.6$, $S_p = 0.8$, $S_r = 1$, $\alpha = 0.55$

As shown in these four figures, with the increase of the attenuation, the amplitude of the resultant vibration decreases while the degree of amplitude modulation increases. Similar with the discussion in Subsection 2.3.1, all these four cases are with spikes induced by the phase differences and none of these four cases is symmetric about the horizontal axis.

2.3.3 Properties of resultant vibration signal

In this subsection, the properties of the vibration signals for the above four cases are discussed in the frequency domain. Fig. 2.10 illustrates the frequency spectra of the resultant vibration signals. With the physical parameters in Table 2.1 and the input rotational speed as 46.667r/min, the characteristic frequencies of the planetary gear set are calculated using

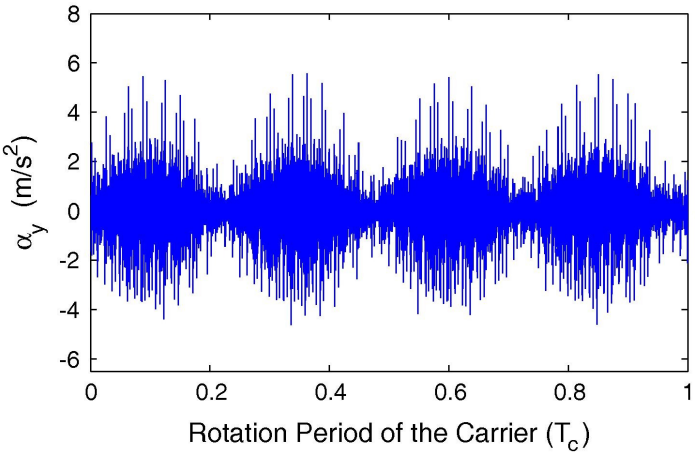

Fig. 2.8: Resultant vibration with $S_s = 0.5$, $S_p = 0.75$, $S_r = 1$, $\beta = -0.2$

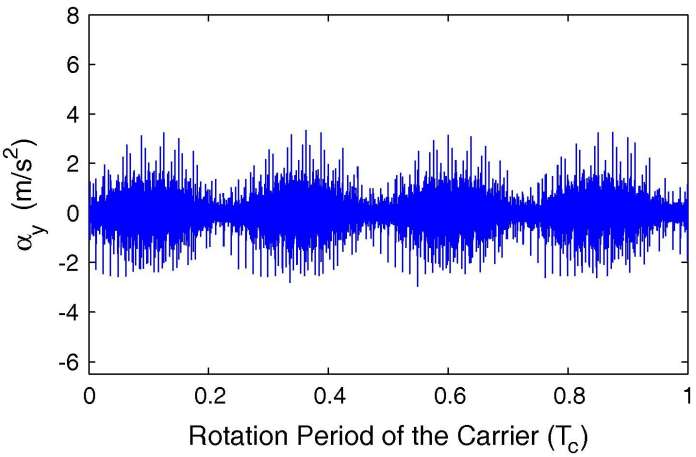

Fig. 2.9: Resultant vibration with $S_s = 0.4$, $S_p = 0.7$, $S_r = 1$, $\beta = -1$

Eqs. (9)-(12) in [1]. The results are obtained as follows: $f_s = 0.7778$Hz (sun gear rotation frequency), $f_p = 0.23836$Hz (planet gear rotation frequency), $f_c = 0.1478$Hz (carrier rotation frequency), $f_{p-p} = 0.5913$Hz (planet gear passing frequency), $f_m = 11.97$Hz (meshing frequency). As the characteristic frequencies are very low, the low frequency bands of the frequency spectra are focused. In Fig. 2.10, the frequency spectra are plotted from 0Hz to 90Hz, up to the 7th order of the meshing frequency.

According to the physical parameters in Table 2.1, the planetary gear set is with equally spaced planets and sequentially phased gear meshes as defined in [22]. As demonstrated in Fig. 2.10, the amplitudes are almost zero at the meshing frequency and its harmon-

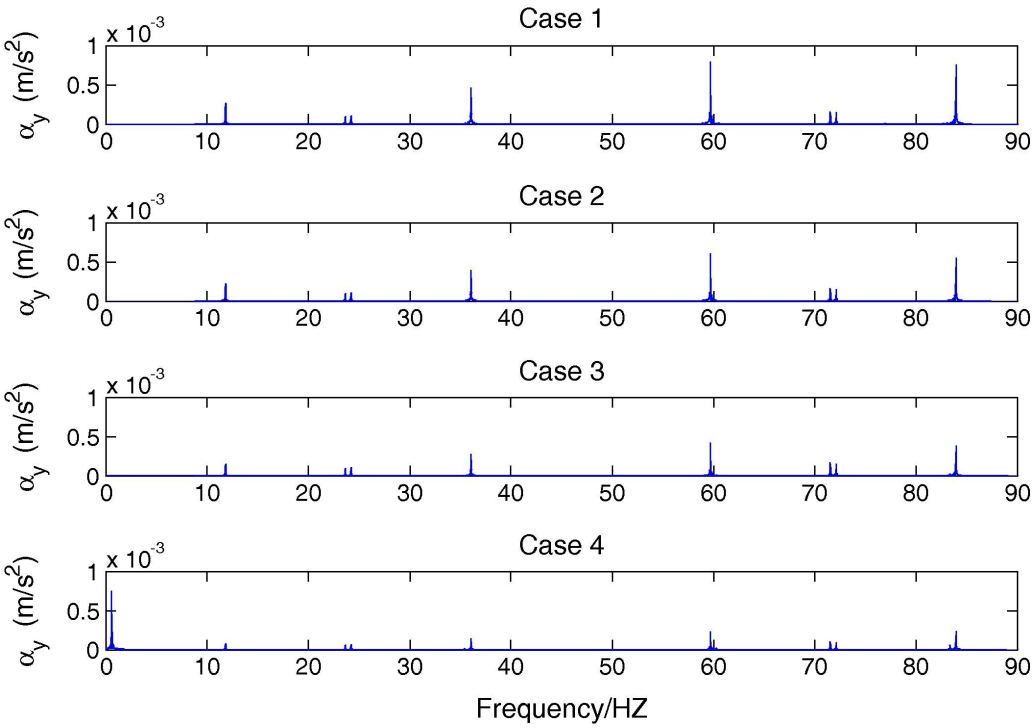

Fig. 2.10: Frequency spectra of resultant vibration signals

Table 2.3: Frequency components and corresponding amplitudes. Unit: m/s^2

Frequency \Hz	0.5913	11.83	23.65	24.24	36.05	59.7	71.53	72.12	83.94
Case 1 ($\times 10^{-4}$)	0	26	9.3	10	46	79	16	15	75
Case 2 ($\times 10^{-4}$)	0	22	9.3	10	39	61	16	15	55
Case 3 ($\times 10^{-4}$)	1	15	9.5	10	27	42	16	15	38
Case 4 ($\times 10^{-4}$)	76	7.8	5.9	7	14	23	11	9	24

ics, compatible well with the conclusion in [22]. The frequency components with sizable amplitudes from 0Hz to 90Hz are listed in Table 2.3. Sizable amplitudes are located at: $nf_m \pm f_c$ (11.83Hz, 36.05Hz, 59.7Hz, 83.94Hz) if n is an odd integer ($n = 1,3,5,7$), and $nf_m \pm 2f_c$ (23.65Hz, 24.24Hz, 71.53Hz, 72.12Hz) if n is an even integer but not 4 ($n = 2,6$) for each case. This characteristic agres well with the results in [27].

With the increasing of the attenuation from case 1 to case 4, the amplitudes at $f = nf_m \pm f_c$ where n is an odd integer decrease while the amplitudes at $f = nf_m \pm 2f_c$ almost keep constant for the cases 1 to 3. In addition, for cases 1 to 3, there is no sizable amplitude at the planet gear passing frequency. If the attenuation induced by the transmission

path is such great like the condition in case 4, the amplitudes of all the frequency components have smaller values when compared with those in cases 1 to 3 except the planet gear passing frequency. The amplitude is non-zero at the planet gear passing frequency for case 4. The sizable amplitude at the planet gear passing frequency indicates the larger degree of the amplitude modulation. This phenomenon agrees well with the observation in the time domain as discussed previously in Subsection 2.3.2 that greater attenuation by the transmission path introduces greater degree of amplitude modulation.

2.4 Experimental validation

In this section, the modeling method for the resultant vibration signal proposed in this study is validated by the experimental vibration signal. The experimental vibration signal was acquired from the planetary gearbox test rig in the Reliability Research Lab at the University of Alberta in the year of 2011 by former group members. Fig. 2.11 shows the configuration of the planetary gearbox test rig. Table 2.4 lists the number of teeth for each gear. All the gears are standard spur gears without tooth profile modification and each gear is healthy without gear faults. An acceleration sensor was installed in the vertical direction of the casing of the second stage planetary gearbox. The sampling frequency was 5000Hz. The second stage planetary gear set has the same configuration and gear parameters with the simulated planetary gear set. During the experiments, the driving motor speed was 1200r/min. Thus the rotational speed of the sun gear in the second planetary gear set was 46.667r/min with a meshing frequency of 11.97Hz. The load applied on the carrier shaft of the second stage planetary gearbox was 2367Nm which is the same as the applied load on the simulated planetary gear set in Subsection 2.2.1. The experimental planetary gear set had the same characteristic frequencies as the simulated planetary gear set. Repeatability tests were conducted with detailed description in [158], showing that the frequency components of two identical runs were similar to each other.

Fig. 2.12 shows the experimental vibration signal of the second stage planetary gear-

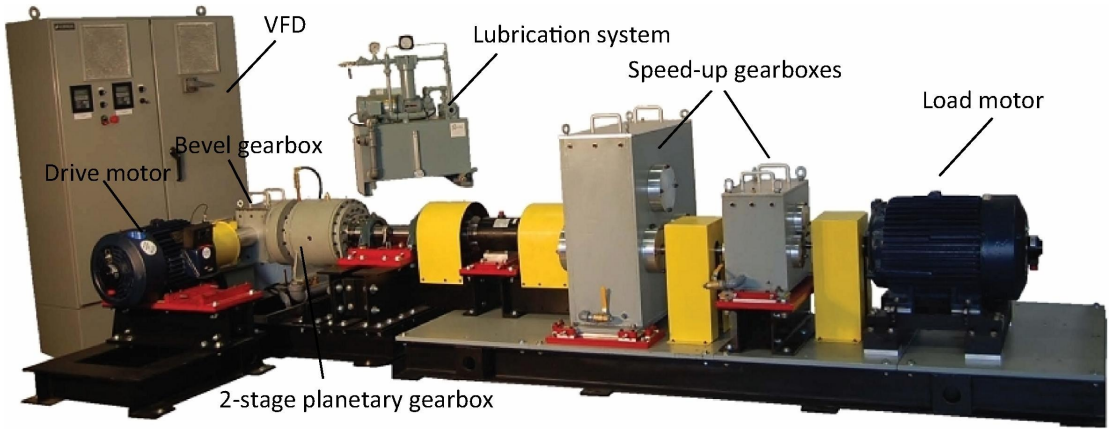

Fig. 2.11: Planetary gearbox test rig

Table 2.4: Parameters of experimental planetary test rig

Gearbox gear	Bevel stage		1st planetary stage			2nd planetary stage		
	Input	Output	Sun	Planet	Ring	Sun	Planet	Ring
No. of teeth	18	72	28	62(4)	152	19	31(4)	81

box in the vertical direction under healthy condition. The amplitude modulation presents in the experimental vibration signal and signal envelope fluctuates four times within one revolution of the carrier. Moreover, as shown in Fig. 2.12, the experimental vibration signal is not symmetric about the horizontal axis. As the modeled resultant vibration signal presents these two properties as discussed in Section 2.3, the proposed model for the resultant vibration signal is validated by the experimental vibration signal in the time domain to some extent. When comparing the experimental vibration with the modeled vibrations of the four cases presented in Subsection 2.3.2, it is noticed that the case 1 matches best with the experimental signal in the time domain. Consequently, in the following content, the frequency spectrum of the experimental vibration will be compared with the frequency spectrum of the case 1.

Fig. 2.13 illustrates the frequency spectrum of the experimental vibration signal. The spectrum was plotted from 0Hz to 90Hz. Compared with the frequency spectrum of the simulated case 1, it is obvious that the experimental vibration frequency spectrum is much more complex with more frequency components and sidebands. This makes sense because

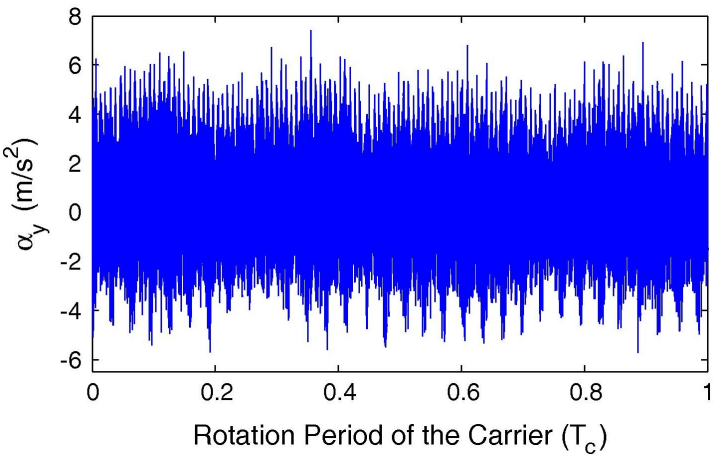

Fig. 2.12: Experimental resultant vibration signals in healthy condition

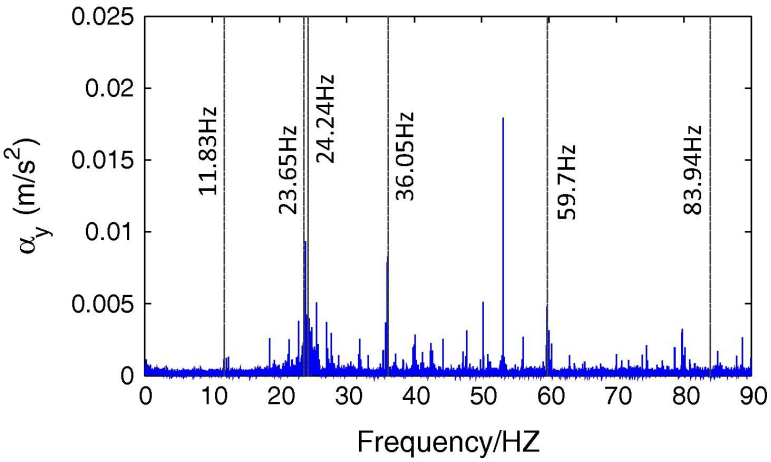

Fig. 2.13: Frequency spectrum of experimental vibration signal

of the complexity of the practical planetary gearbox test rig and the fact that the transducer mounted on the second stage planetary gearbox can acquire the vibration from other components of the test rig. On the other hand, when looking into details in Fig. 2.13, there are sizable amplitudes at following positions: 11.83Hz, 23.65Hz, 24.24Hz, 36.05Hz, 59.7Hz, and 83.94Hz. All these frequency components are with sizable amplitudes in the spectrum of the simulated case 1 as well. Moreover, the experimental vibration has amplitude of nearly zero at the planet gear passing frequency, 0.5913Hz. This characteristic agrees well with the vibration characteristic of the simulated case 1. Thus, the experimental data validates the modeled resultant vibration in the frequency domain to some extent.

Basically, according to the discussion above, although the experimental vibration signal in Fig 2.12 has more high frequency background noise and more vibrations from other components of the test rig than the simulated case 1 in Fig. 2.6, the resultant vibration signal simulated using the proposed modeling method matches the experimental vibration signal well in both the time domain in terms of the waveform appearance and the frequency domain in the low frequency range, which indicates the usefulness of the proposed modeling method for the resultant vibration signal of a planetary gear set. Further validation can be conducted by considering vibrations from the carrier and the bearings in the simulated vibration signal and/or reducing the vibrations of the other test rig components and the background noise in the experimental vibration signal.

2.5 Conclusions

In this chapter, a comprehensive resultant vibration signal modeling method for a planetary gear set is proposed. A lumped-parameter dynamic model is employed to generate the vibration sources from the sun gear, the ring gear, and planet gears. The transmission path comprises two parts: the part inside the gearbox from the vibration source to the casing and the part along the casing to the transducer position. The effect of each transmission path part is modeled. The overall transmission path effect is then modeled by synthesizing the effects of the two transmission path parts. The proposed transmission path model can better reflect the vibration attenuation than the existing models in the literature. Moreover, given the gear sizes in a planetary gear set, the attenuation coefficients are estimated with the radiation damping and the material damping. Incorporating multiple vibration sources and corresponding transmission path effects, the resultant vibration signal at the transducer position is obtained for a healthy planetary gear set. In the time domain, the resultant vibration signals are subject to amplitude modulation caused by the rotation of the carrier. The level of amplitude modulation increases with the growth of the attenuation. Moreover, the resultant vibration signal is not necessarily symmetric with respect to the horizontal

axis in the time domain because of the phase differences among the multiple vibration sources. For the spectrum structure in the frequency domain, frequency components with sizable amplitudes are located and the location of these frequency components agrees well with the reports of previous studies. Finally, the proposed planetary gear set vibration signal modeling method is validated with experimental data in both the time domain and the frequency domain.

The vibration signal modeling method reported in this chapter will be used to generate simulated planetary gearbox vibration signals for the development of vibration signal analysis methods for planetary gearbox fault diagnosis as in Chapter 3, Chapter 4, and Chapter 5.

Chapter 3

Energy density construction in time-frequency domain by spectrogram-free non-parametric copula for planetary gearbox fault diagnosis

As indicated in Fig. 1.12, the focus of this chapter is on the second research topic, the construction of time-frequency energy density for planetary gearbox fault diagnosis. To represent the time-frequency energy density of a transient vibration signal, besides linear time-frequency representations and bilinear Time-Frequency Distributions (TFDs), copula-based TFDs are also reported in the literature with properties of being positive, free from cross-term interference, having correct marginals, and with high time-frequency resolution. The core in the copula-based TFD is the Time-Frequency Copula (TFC) estimation to represent the energy marginal dependence. In the reported copula-based TFD construction methods, the TFC estimation relies on spectrogram-based marginals. However, spectrogram-based marginals would introduce the influence of window length used for the spectrogram on the estimated TFC shape. To eliminate the influence of the spectrogram, a spectrogram-free TFC estimation method is proposed in this chapter. Then the time-frequency energy density is constructed with the proposed spectrogram-free TFC. Performance of the constructed spectrogram-free copula-based TFD on planetary gearbox fault diagnosis is demonstrated. The constructed time-frequency energy density in this chapter

will be used in Chapter 4 to develop a fault feature extraction method for planetary gearbox fault detection.

The organization of this chapter is as follows. In Section 3.1, an introduction to time-frequency energy density is provided with the literature review. Section 3.2 presents theoretical fundamentals of copula theory, non-parametric copula, and copula-based TFD construction with TFC. In Section 3.3, detailed procedures are developed for constructing copula-based TFD with spectrogram-free TFC. In Section 3.4, case studies with simulated and experimental planetary gearbox vibration signals are conducted to demonstrate the advantages of the developed spectrogram-free TFD over the reported spectrogram-based TFD as time-frequency energy density representation in terms of marginal accuracy. The simulated signals are generated with the vibration signal modeling method proposed in Chapter 2. In Section 3.5, the performance of the constructed spectrogram-free copula-based TFD on planetary gearbox fault diagnosis is demonstrated and compared with the performance of the spectrogram. The study is concluded in Section 3.6. The results of this chapter are documented in a journal paper [143] and submitted to *Mechanical Systems and Signal Processing* for possible publication.

3.1 Introduction

Due to highly volatile working environment and heavy load, a planetary gearbox is prone to gear tooth faults such as tooth crack, tooth pitting, and tooth breakage [25]. Such gear tooth malfunctions would lead to the entire system failure and result in considerable economic losses and even human casualties. Consequently, it is of critical importance to detect gear tooth faults in a planetary gearbox early, aiming at improving the reliability of the system to reduce chances of catastrophic failures, and enabling cost-effective operation and maintenance practices [159].

For vibration signal analysis, various signal processing methods have been developed and applied for gear fault detection and diagnosis, including time domain methods, fre-

quency domain methods, and time-frequency domain methods. In both time domain methods and frequency domain methods, the time variable t and the frequency variable f are treated as independent. To obtain a representation in terms of one variable, the other one is integrated out, which leads to non-localization with respect to the excluded variable. In other words, the waveform in the time domain is averaged over all frequencies, and the spectrum in the frequency domain is averaged over all time points [160]. On the contrary, these limitations can be overcome by a Time-Frequency Distribution (TFD) by which the signal is represented as the energy density in the joint time-frequency domain [42]. A TFD can effectively reveal the constituent frequency components and the transient time events such as fault-induced impulses [43].

In the literature, different TFD analysis methods have been reported, including linear TFDs, bilinear TFDs, and positive TFDs. Linear TFDs, such as Short-Time Fourier Transform (STFT) [44] and Wavelet Transform (WT) [45], are essentially a process to decompose a signal into a weighted summation of variants of a basis function in the joint time-frequency domain. They are subject to Heisenberg uncertainty principle, i.e., there is a trade-off between the time localization and the frequency resolution for a linear TFD [42]. On the other hand, bilinear TFDs, like Wigner-Ville distribution [46] and Cohen's class distributions [42], are free from Heisenberg uncertainty principle by representing the energy distribution with the Fourier transform of local autocorrelation function [42]. Wigner-Ville distribution has the best time-frequency resolution among bilinear TFDs but it suffers from the intrinsic cross-term interference for a multi-component vibration signal [101]. Without pre-knowledge about a vibration signal, cross terms would result in the misunderstanding on the time-frequency structure. By a carefully chosen kernel function, acting as a low-pass filter in the time-frequency domain, a Cohen's class bilinear TFD can mitigate the cross-term interference, but with the compromise of time-frequency resolution [42]. Besides, a bilinear TFD cannot be interpreted as energy density because of the existence of possible negative values even though they are designed for energy densities [42]. For a better energy

density representation, Cohen and Posch [47] demonstrated the existence of positive TFDs for arbitrary signals. Davy and Doucet [48] presented a copula-based positive TFD construction method by Sklar's theorem. Sklar's theorem [115] indicates that a joint TFD can be constructed by the time marginal, the frequency marginal and a Time-Frequency Copula (TFC) which captures the dependence between the two individual marginals. As demonstrated in [48], for a transient signal, a copula-based TFD has desirable properties of being positive, free from cross-term interference, and having high time-frequency resolution and correct marginals to serve well for an energy density representation. Note that for a transient signal with finite energy, the correct energy marginals are defined as the instantaneous energy of the signal, i.e., amplitude squared of the time waveform, and the energy spectral density, i.e., amplitude squared of the Fourier transform, to represent the way the energy is distributed in the time domain and in the frequency domain, respectively [42, 47, 48].

The core of the copula-based TFD construction is the TFC estimation [48]. In [48], the TFC is estimated by the spectrogram-based marginals where the spectrogram is computed by STFT with a windowing function. However, due to the overlap of adjacent windowed segments in STFT, spectrogram-based marginals are with great redundancy for energy marginal representation. Besides, as stated in [48], the spectrogram would introduce the influence of window length used for STFT on the constructed copula-based TFD. Different choices of window length and overlap length for STFT lead to different shapes of copula-based TFDs, which is still an open question [48].

To address the above concerns regarding the spectrogram-based TFC estimation in [48], an alternative approach is proposed in this study for the TFC estimation. Ref. [48] uses the spectrogram-based marginals for TFC estimation. We propose to use the instantaneous energy and the energy spectral density of a truncated vibration signal to achieve the spectrogram-free TFC estimation. We truncate the original vibration signal using a rectangular window in order to get a transient signal with finite energy. Rationales to use rectangular window are given in Section 3.3. A low-pass filter is implemented to limit the

frequency range of the truncated vibration signal. In digital signal processing, a vibration signal is represented by a sequence of amplitudes in the time domain with equal sampling interval subject to Nyquist theorem. Its frequency spectrum is a sequence of absolute values of the Fast Fourier Transform (FFT) coefficients, representing amplitudes at discrete frequencies in the frequency domain. Note that a FFT coefficient is a complex number whose real part and imaginary part correspond to Fourier series with cosine and sine, respectively. The instantaneous energy and the energy spectral density are defined by the amplitude squared in the time domain and the amplitude squared in the frequency domain to represent the energy distribution in the time domain and the energy distribution in the frequency domain, respectively. Then the dependence is modeled by a non-parametric copula as the non-parametric copula is free from the assumption that the data belong to a particular distribution with a fixed model structure [139], compared with a parametric copula [138]. A fitness measure, the distance to the reference diagonal line in the Quantile-Quantile plot (QQ plot), is used for comparison of the proposed spectrogram-free TFC with the reported spectrogram-based TFC.

In Section 3.2, fundamentals of copula theory, non-parametric copula estimation and copula-based TFD construction are reviewed. In Section 3.3, the use of rectangular window to truncate vibration signal is rationalized, subsequently followed by the proposed construction method of copula-based TFD with spectrogram-free non-parametric TFC estimation. In Section 3.4, simulated and experimental planetary gearbox vibration signals with sun gear tooth crack are employed to conduct the TFC estimation by both the proposed spectrogram-free method and the reported spectrogram-based method. Their fitness to the marginal dependence, i.e., the dependence between the instantaneous energy and the energy spectral density of the truncated vibration signal, is compared. In Subsection 3.4.2, copula-based TFDs are constructed with the proposed spectrogram-free TFCs and the reported spectrogram-based TFCs. Their marginal deviations from the instantaneous energy and the energy spectral density of the truncated vibration signal are compared to demonstrate the

benefit gained in the TFD with a better marginal dependence fitness. In Section 3.5, performance of the constructed spectrogram-free copula-based TFD on planetary gearbox fault diagnosis is demonstrated. At last, conclusions are drawn in Section 3.6.

3.2 Fundamentals of time-frequency copula and time-frequency distribution

In this section, fundamentals of Time-Frequency Copula (TFC) estimation and the generation of copula-based Time Frequency Distribution (TFD) are provided as they are needed in Section 3.3 for development of the proposed method. The bold characters in the following contents represent Cumulative Distribution Functions (CDF) and the non-bold characters denote probability distribution functions.

3.2.1 Copulas

Copula, proposed by Sklar [115], is a mathematical theory to describe the dependence between random variables [161]. A copula $\boldsymbol{C}$ is a function from $[0,1]^2$ to $[0,1]$ with following properties [112]:

1) $\boldsymbol{C}(u,0)=\boldsymbol{C}(0,v)=0$ for all $(u,v)\in[0,1]^2$;
2) $\boldsymbol{C}(u,1)=u$ and $\boldsymbol{C}(1,v)=v$ for all $(u,v)\in[0,1]^2$;
3) For all $(u_1,u_2,v_1,v_2)\in[0,1]^4$ where $u_1\leqslant u_2$ and $v_1\leqslant v_2$
   $\boldsymbol{C}(u_2,v_2)$-$\boldsymbol{C}(u_1,v_2)$-$\boldsymbol{C}(u_2,v_1)$+$\boldsymbol{C}(u_1,v_1)\geqslant 0$;
4) For all $(u,v)\in[0,1]^2$
   $\max(u+v-1,0)\leqslant\boldsymbol{C}(u,v)\leqslant\min(u,v)$

A core idea in copula theory is Sklar's Theorem. Sklar's theorem states that a joint CDF $\boldsymbol{H}(x,y)$=P($X\leqslant x$,$Y\leqslant y$) of random variables (X,Y) can be expressed by [115]

$$\boldsymbol{H}(x,y)=\boldsymbol{C}(\boldsymbol{F}(x),\boldsymbol{G}(y)) \tag{3.1}$$

where $\boldsymbol{F}(x)$ and $\boldsymbol{G}(y)$ are the marginal distributions of $\boldsymbol{H}(x,y)$. According to Eq. (3.1), copulas are essentially a way to transform variables from X and Y to their cumulative distributions $\boldsymbol{F}(x)$ and $\boldsymbol{G}(y)$. Furthermore, derived from Eq. (3.1), a copula $\boldsymbol{C}$ can be constructed by [162]

$$\boldsymbol{C}(u,v) = \boldsymbol{H}(\boldsymbol{F}^{-1}(u), \boldsymbol{G}^{-1}(v)) \tag{3.2}$$

where $\boldsymbol{F}^{-1}(u)$ and $\boldsymbol{G}^{-1}(v)$ denote the pseudo-inverses of $\boldsymbol{F}(x)$ and $\boldsymbol{G}(y)$ given by $\boldsymbol{F}^{-1}(u)$= $\inf\{x|\boldsymbol{F}(x) \geqslant u\}$ and $\boldsymbol{G}^{-1}(v)$=$\inf\{y|\boldsymbol{G}(y) \geqslant v\}$, respectively, where $\inf\{S\}$ is the infimum of the data set S, defined as its greatest lower bound that is less than or equal to all elements in the data set. Eq. (3.2) suggests that, given two marginals $\boldsymbol{F}(x)$ and $\boldsymbol{G}(y)$, one can construct a joint distribution $\boldsymbol{H}(x,y)$ whose marginals are $\boldsymbol{F}(x)$ and $\boldsymbol{G}(y)$ by a copula $\boldsymbol{C}$ [48].

3.2.2 Non-parametric copula density estimation

For copula model estimation, both parametric models [138] and non-parametric models [163] are reported in the literature. Compared with a parametric copula, a non-parametric copula can provide a greater generality for the estimation of the underlying dependence between the data with less model error as it is unconstrained by a fixed structure of how the variables interact [164]. Non-parametric copulas will be used in this study.

3.2.2.1 Pseudo-observation generation

According to Sklar's theorem, a copula is invariant with the monotone transformation of marginals [165]. Thus, it is intuitively expected that, for consistent copula model estimation, the described dependence associated with variables should be invariant with the monotone transformation of marginals [165]. However, the dependence between marginal value pairs cannot remain invariant with the monotone transformation of marginals as they not only incorporate information about the dependence between variables but also have information about marginal behaviors [145]. Consequently, proper pseudo-observations that are free from marginal behaviors have to be sought for the copula analysis.

Statistically, ranking refers to the data transformation by which data values are replaced by their ranks when the data values are sorted [145]. The ranks are invariant with monotone transformation of data values [145]. Genest and Favre [165] reported an equation to generate rank-based pseudo-observations for a vector Q as given by Eq. (3.3)

$$O_i(q) = \frac{R_i(q)}{(n+1)} \tag{3.3}$$

where q is the variable of vector Q; $R_i(q)$ is the ith rank associated with vector Q in ascending order; $O_i(q)$ is the pseudo-observation associated with $R_i(q)$ which is between 0 and 1; and n is the number of data samples in Q. Charpentier, Fermanian, and Scaillet [166] showed that this rank-based method can produce $O_i(q)$ that leads to an empirical copula estimation with lower variance. With these properties, Eq. (3.3) is used in this study to generate pseudo-observations for the copula analysis.

3.2.2.2 Beta kernel estimator

On strength of rank-based pseudo-observations, an approach for copula density estimation is the Beta kernel method [166]. The Beta kernel estimator at point (u,v) for copula density estimation is obtained by the product of Beta kernels as given by Eq. (3.4) [166].

$$C(u,v) = \frac{1}{n}\sum_{i=1}^{n} K(O_i(T), \frac{u}{h}+1, \frac{1-u}{h}+1)K(O_i(F), \frac{v}{h}+1, \frac{1-v}{h}+1) \tag{3.4}$$

where $K(x,\alpha,\beta)$ denotes the Beta distribution density for $0 \leqslant x \leqslant 1$ with parameters α and β; $O_i(T)$ and $O_i(F)$ denote rank-based pseudo-observations for vector T and vector F, respectively; h is the smoothing parameter for Beta kernel density estimation. The Beta distribution density $K(x,\alpha,\beta)$ is formulated by

$$K(x,\alpha,\beta) = \frac{x^{\alpha}(1-x)^{\beta}}{B(\alpha,\beta)} \tag{3.5}$$

where $B(\alpha,\beta)$ is the Beta function as defined by

$$B(\alpha,\beta) = \int_0^1 t^{\alpha-1}(1-t)^{\beta-1}dt \tag{3.6}$$

The Beta kernel estimator has following advantages [166]: it can match the compact support on the interval of $[0,1]$ for the copula to be estimated, which eliminates boundary bias; it is an adaptive kernel density estimation approach as the Beta kernel changes its shape naturally in a smooth way as the variable t in Eq. (3.6) moving from boundaries. With the above advantages, Beta kernel estimators are free from boundary bias and produce smooth estimates with small variance [166]. The kernel smoothing parameter h influences the quality of the estimation [167]. Consequently, before the copula density estimation by Eq. (3.4), the optimal value of h needs to be determined first.

3.2.2.3 Smoothing parameter determination

To find the optimal value of smoothing parameter h for Beta kernel estimator, Chen [168] reported the Mean Integrated Squared Error (MISE) method. The MISE is given by

$$\mathrm{MISE}(h) = \frac{1}{n}\sum_{n}\int (\widetilde{f}_h(\bar{x}) - f(\bar{x}))^2 d\bar{x} \tag{3.7}$$

where $\bar{x}$ is the variable vector; n is the number of generated $\widetilde{f}_h(\bar{x})$ with the smoothing parameter h; and $f(\bar{x})$ is the true distribution. The h with the smallest MISE is selected as the optimal smoothing bandwidth [168]. However, for a vibration signal, the true energy distribution $f(\bar{x})$ is unknown. Thus, one cannot apply Eq. (3.7) directly to find the optimal smoothing parameter h for a vibration signal. An approximate energy distribution is needed. Accordingly, a MISE method with spectrogram as the approximate energy distribution is presented and rationalized in this study as covered in Section 3.3. Spectrograms are obtained by the Matlab command "spectrogram" with default Hamming window function.

3.2.2.4 Goodness-of-fit test

In statistics, the goodness-of-fit describes how well a model fits a set of given data. QQ plot, short for quantile-quantile plot, is a well-known method for goodness-of-fit test [165]. By plotting quantiles against each other, QQ plot is a graphical technique for comparing

two probability distributions [138]. In this study, the QQ plot is made by plotting pairs $\{W_{EC(i)}, W_{(i)}\}$ with $i \in \{1,2,...,n\}$ where $W_{(1)} \leqslant W_{(2)} \leqslant \cdots \leqslant W_{(n)}$ are the order statistics associated with $W_i = \frac{1}{n}\#\{j : T(j) \leqslant T(i), F(j) \leqslant F(i)\}$ [165] where (T,F) are data pairs with the instantaneous energy and the energy spectral density of the truncated vibration signal, and $W_{EC(1)} \leqslant W_{EC(2)} \leqslant \cdots \leqslant W_{EC(n)}$ are the order statistics associated with $W_{ECi} = \frac{1}{n}\#\{j : X(j) \leqslant X(i), Y(j) \leqslant Y(i)\}$ where (X,Y) are the generated samples from the estimated copula density. In statistics, the *i*th order statistic is equal to the *i*th-smallest value in the sample [145]. In QQ plot, a reference diagonal line $(W_{EC(i)} = W_{(i)})$ is plotted to indicate the perfect fit. The distance away from the reference line reflects the fitness of the estimated copula model to the dependence between the instantaneous energy and the energy spectral density. The distance is calculated as the average of the absolute differences of the point coordinates. The shorter the distance is, the greater the evidence that the model provides a better fit to the underlying dependence.

Specifically, the QQ plot is used in this study for the goodness-of-fit test of different TFC estimations to address the rational and advantage of the proposed spectrogram-free TFC estimation method.

3.2.3 Time-frequency distribution construction with time-frequency copula

After the TFC is estimated, it comes to the construction of the copula-based TFD for energy density representation in the joint time-frequency domain. According to Sklar's theorem, the copula-based TFD can be constructed by Eq. (3.8) [48].

$$p(t,f) = C(U(t),V(f)) * T(t) * F(f) \tag{3.8}$$

where $p(t,f)$ is the estimated copula-based TFD; C represents the estimated copula density; $T(t)$ and $F(f)$ are the instantaneous energy and the energy spectral density with rank-based pseudo-observations $U(t)$ and $V(f)$, respectively. Copula density function C retains the marginal dependence between $T(t)$ and $F(f)$ [145].

Properties of a copula-based TFD to be positive and free from cross-term interference have been demonstrated in [142]. Besides, a copula-based TFD should have correct energy marginals for a transient vibration signal [42]. As rationalized in Section 3.3, the truncated vibration signal by a rectangular window function can approximate the correct energy marginals of the vibration signal within the frequency range as filtered by a low-pass filter. Consequently, in this study, the deviation of the constructed copula-based TFD's marginals from the instantaneous energy and the energy spectral density are selected as the criterion to reflect the benefit gained by the proposed spectrogram-free TFC in terms of the marginal correctness as demonstrated in Section 3.4.

3.3 A construction method for time-frequency distribution with spectrogram-free time-frequency copula

In this study, we use a rectangular window to get a transient vibration signal with finite energy. The rationales to use rectangular window are given in the following two paragraphs.

Different from Hanning window, Hamming window, and triangle window with decaying amplitude, rectangular window has uniform amplitude [169]. The truncated vibration signal by a rectangular window remains the same amplitude as the original while the truncated vibration signals by other window functions have decayed amplitudes with the multiplication of coefficients smaller than 1. As the correct time energy marginal is defined by the instantaneous energy, i.e., the magnitude squared in the time domain, the truncated vibration signal by a rectangular window retains the correct time energy marginal while the truncated vibration signals by other window functions distort the time energy marginal with attenuation.

In the frequency domain, the frequency spectrum of a window function is characterized by a main lobe and several side lobes. The main lobe is centered at each frequency component of a vibration signal with certain bandwidth indicating the frequency resolution; the side lobes reflect the spectral leakage around the main lobe [169]. Recall the

trade-off between frequency resolution and spectral leakage of a window function [169], the suitability of a window function should be estimated for a specific application. For the studied planetary gearbox with low speed as specified in Section 3.4, to identify the low fault characteristic frequency as specified in Section 3.5, the frequency resolution should be addressed. On the other hand, as the energy density is on the amplitude squared scale, the side lobes could be negligible with further reduced by squaring. Thus we emphasize the frequency resolution for fault-related frequency identification rather than the spectral leakage with side lobes. Compared with Hanning window, Hamming window, and triangle window, rectangular window has the highest frequency resolution [169].

Consequently, we use the rectangular window to truncate the vibration signal to obtain transient vibration signal with finite energy. As a transient vibration signal is infinite in the frequency domain, we apply a low-pass filter to limit the frequency range. Then the instantaneous energy and the energy spectral density of the truncated vibration signal are used as the energy marginals in the analysis of the spectrogram-free copula-based TFD.

After the energy marginals are determined, for copula-based TFD construction by Eq. (3.8), the core is the TFC estimation. Two challenges are addressed in this study for the TFC estimation. The first challenge is how to deal with the disadvantages of the reported spectrogram-based TFC estimation method in [48]. The second challenge is how to determine the optimal smoothing parameter for the Beta kernel estimator by MISE method while one does not know the true time-frequency energy distribution of a vibration signal. To address the first challenge, we propose a spectrogram-free TFC estimation method starting with the instantaneous energy and the energy spectral density. To address the second challenge, we propose to use the spectrogram as the approximate energy distribution and subsequently prove the validity of this approximation in terms of accuracy and efficiency. In the following, we illustrate the details on how we address these two challenges.

Fig. 3.1 shows the flowchart of the proposed spectrogram-free TFC estimation method. Given a vibration signal truncated by a rectangular window function, the first step is to

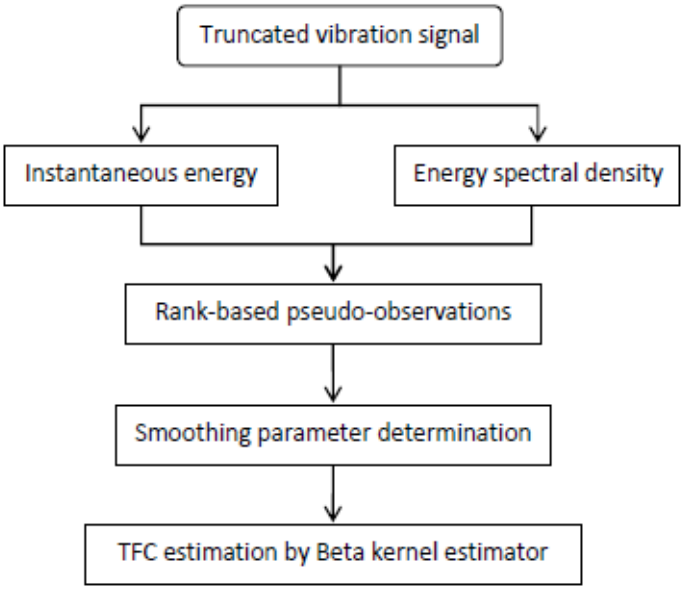

Fig. 3.1: Proposed TFC estimation procedure

calculate its instantaneous energy and its energy spectral density, followed by the optimal smoothing parameter determination. At last, the TFC estimation is conducted with Beta kernel estimator.

As described in the above procedures, the pseudo-observations for the proposed TFC estimation are generated by the instantaneous energy and the energy spectral density rather than the spectrogram-based marginals. For this reason, the proposed method is named as spectrogram-free TFC estimation method. The advantage of the proposed spectrogram-free TFC estimation over the reported spectrogram-based TFC estimation is demonstrated by the case study in Section 3.4. Note that the term of spectrogram-free only means the TFC estimation relies on the instantaneous energy and the energy spectral density rather than spectrogram-based marginals while the smoothing parameter determination still involves spectrogram as in the following contents. The involvement of spectrogram in the smoothing parameter determination does not influence the accuracy of the obtained optimal smoothing parameter as analyzed in following three paragraphs.

For the optimal smoothing parameter determination, we propose to use the spectrogram as the approximate energy distribution for the MISE method. The initially inspiring reason

is the spectrogram is believed to represent the time-frequency contents correctly as it is positive and free from cross-term interference [48]. However, at this point, we are not sure whether the smoothing parameter with the smallest MISE regarding the spectrogram can provide the best fit to the dependence between the instantaneous energy and the energy spectral density or not. To be sound by answering this concern, the goodness-of-fit test by QQ plot is conducted with different h values. The QQ plot is obtained by the construction method as stated in Subsubsection 3.2.2.4. The smoothing parameter value h with the shortest distance to the reference diagonal line in the QQ plot is the optimal smoothing parameter as it provides the best fit.

To rationalize the setup of choosing spectrogram as the approximate energy distribution for the MISE method, we present Fig. 3.2. Fig. 3.2(a) demonstrates the MISE plot by Eq. (3.7) against the smoothing parameter h for a simulated planetary gear set vibration signal with 10% sun gear tooth crack while taking spectrogram as the approximate energy distribution. Note that we denote 10% sun gear tooth crack as Crack10 in Fig. 3.2. More details on the simulated planetary gear set vibration signal are given in Subsubsection 3.4.1.1. The smoothing bandwidth h with the smallest MISE in Fig. 3.2(a) is 0.1885, meaning the Beta-kernel estimator with smoothing parameter h as 0.1885 provides the best fit to the spectrogram. Fig. 3.2(b) shows QQ plots with h being 0.05, 0.1684, 0.1885, 0.2086, and 0.4. The values of 0.1684 and 0.2086 are adjacent to 0.1885 and values of 0.05 and 0.4 are two random values farther away from 0.1885. The averaged distances of the curves with h being 0.05, 0.1684, 0.1885, 0.2086, and 0.4 to the reference diagonal line in Fig. 3.2(b) are calculated being 0.0039, 0.0032, 0.0030, 0.0038, and 0.0042, respectively, as intuitively presented by the bar chart in Fig. 3.2(c). The shortest distance is 0.0030 happening when h is 0.1885. The value of h with shortest distance in Fig. 3.2(b) is the same as the value of h with smallest MISE in Fig. 3.2(a). Thus, it is confirmed and validated that the smoothing parameter with the smallest MISE regarding the spectrogram can provide the best fit to the dependence between the instantaneous energy and the energy spectral density.

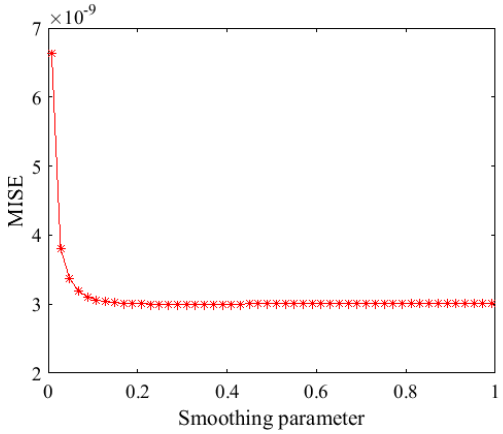

(a) MISE plot with respect to the spectrogram

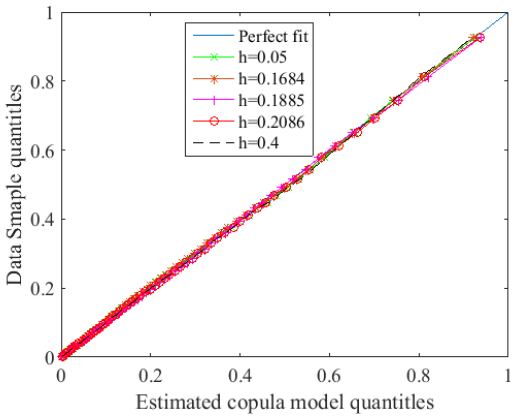

(b) QQ plot for goodness-of-fit test

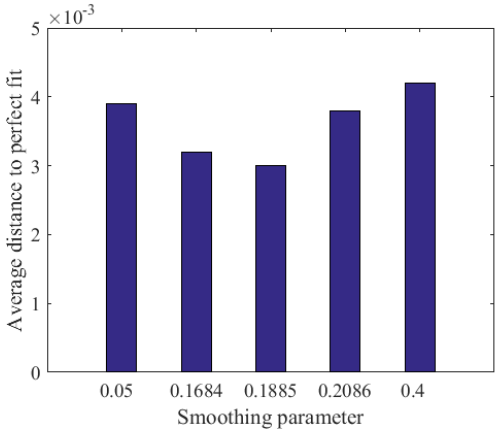

(c) Average distance to the reference diagonal line

Fig. 3.2: Smoothing parameter determination for simulated Crack10 case

Moreover, the MISE method taking spectrogram as the approximate energy distribution requires less computational cost. With an i7 computer machine, the computational time to generate Fig. 3.2(a) is about 5.41 hours with 50 candidate values of h equally spaced between 0 and 1 while the computational time to generate Fig. 3.2(b) is much more up to around 113.2 hours with only 5 candidates, indicating that the MISE method with spectrogram has much cheaper computational cost. One reason is the significant reduction of the data size from 7518×1, the size of the instantaneous energy and the energy spectral density, to 129×1, the size of spectrogram-based marginals. Thus, thanks to the higher efficiency while keeping accurate, we use the MISE method with spectrogram as the approximate energy distribution to determine the optimal smoothing parameter h for the Beta

kernel estimator.

With the above two challenges being addressed, the detailed procedures to constructe the copula-based TFD for a vibration signal $x(t)$ with the proposed spectrogram-free TFC are as follows:

1) To calculate the instantaneous energy and the energy spectral density

$$T(t) = |x(t)|^2 \tag{3.9}$$

$$F(f) = |X(f)|^2 \tag{3.10}$$

where $x(t)$ is the truncated vibration signal by a rectangular window function subject to a low-pass filter, $X(f)$ is the fast Fourier transform of $x(t)$;

2) To generate the rank-based pseudo-observations for $T(t)$ and $F(f)$ by Eq. (3.3);
3) To find the optimal smoothing parameter h for the Beta kernel estimator:
   (a) To generate the spectrogram $S(t,f)$ of the vibration signal $x(t)$;
   (b) To calculate the time marginal $\widetilde{T}(t)$ and the frequency marginal $\widetilde{F}(f)$ of the spectrogram $S(t,f)$ by the summation over the columns and the rows, respectively;
   (c) To generate the rank-based pseudo-observations of $\widetilde{T}(t)$ and $\widetilde{F}(f)$ by Eq. (3.3);
   (d) To estimate the non-parametric copula density $\widetilde{C}_h$ by Eq. (3.4) with different smoothing parameters h;
   (e) To construct the TFD with $\widetilde{C}_h$, $\widetilde{T}(t)$, and $\widetilde{F}(f)$ by Eq. (3.8) as the estimated spectrogram;
   (f) To calculate the MISE between the estimated spectrograms and the original one by Eq. (3.7);
   (g) To select the h value with the smallest MISE regarding the spectrogram as the optimal smoothing parameter for the spectrogram-free non-parametric copula estimation;

4) To estimate the non-parametric copula density C_h as the spectrogram-free TFC by Eq. (3.4) with pseudo-observations generated in Step 2) and the optimal smoothing parameter h determined in Step 3);

5) To construct the copula-based TFD by Eq. (3.8) with $T(t)$, $F(f)$ in Step 1) and the estimated C_h in Step 4).

3.4 Case study of spectrogram-free copula-based TFD construction

To demonstrate the advantage of the proposed spectrogram-free TFC over the reported spectrogram-based TFC, simulated and experimental case studies are conducted. Simulated and experimental vibration signals are truncated by rectangular window. The fitness to the marginal dependence between the instantaneous energy and the energy spectral density of the truncated vibration signal is compared by QQ plot. To indicate the benefit gained with a better marginal dependence fitness as an energy density representation, copula-based TFDs with the proposed spectrogram-free TFC and the reported spectrogram-based TFC are constructed and compared in terms of their marginal deviations from the instantaneous energy and the energy spectral density. Vibration sources of the simulated vibration signals are generated by the dynamic model in [27] and the simulated vibration signals are constructed by the modeling method in the [140]. The experimental vibration signal is acquired from the planetary gearbox test rig in the Reliability Research Lab at the University of Alberta [140].

3.4.1 Energy marginal dependence estimation by spectrogram-free time-frequency copula

3.4.1.1 Simulated planetary gear set vibration signal analysis

The simulated planetary gear set has the sun gear and the carrier as the power input and the power output, respectively, while the ring gear is fixed [27]. The physical parameters of the planetary gear set are listed in Table 3.1. The input rotational speed is constant at

Table 3.1: Physical parameter of simulated planetary gear set [140]

Parameters	Sun gear	Planet gear	Ring gear
Number of teeth	19	31	81
Module (mm)	3.2	3.2	3.2
Pressure angle	20°	20°	20°
Mass (kg)	0.7	1.822	5.982
Base circle radius (mm)	28.3	46.2	120.8
Reference circle radius (mm)	30.4	49.6	129.6

46.667r/min and the torque applied on the carrier shaft is 2367Nm [27].

Three simulated planetary gear set vibration signals are analyzed with different sun gear tooth crack levels. The crack starts from the gear root circle with a 45° crack angle along the whole tooth width. When the crack line reaches the tooth central line, we call it 50% crack as demonstrated in Fig. 3.3. Three sun gear tooth crack levels are considered, namely 10% crack, 30% crack and 50% crack with crack lengths of 0.78mm, 2.34mm, and 3.90mm, respectively [23]. To mimic the background noise, white Gaussian noise is added to the simulated signal with a 25dB signal-to-noise ratio. The noisy simulated signals are processed by a Chebyshev low-pass filter with a cutoff frequency of 800Hz for the following analysis. The cutoff frequency of 800Hz covers the low characteristic frequencies and the frequencies with energy concentration around 500Hz and 700Hz as shown in Fig. 3.4.

The instantaneous energy and the energy spectral density of each simulated vibration signal are shown in Fig. 3.4 which are used as $T(t)$ and $F(f)$ as in Eq. (3.8). Their spectrograms and the spectrogram-based marginals are illustrated in Fig. 3.5 where the spectrogram matrices are square. The time marginal and the frequency marginal are calculated by the summation of the spectrogram over the whole frequency range at each time instant and the summation of the spectrogram over the whole time range at each specific frequency, respectively [145]. The energy marginals in Fig. 3.4 and Fig. 3.5 are normalized by their maximum values.

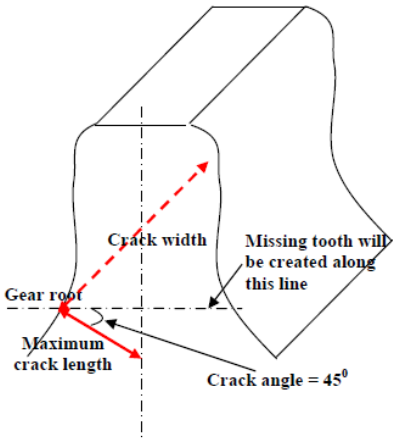

Fig. 3.3: Tooth crack model [23]

After spectrogram-based marginals are ready, rank-based pseudo-observations are generated by Eq. (3.3). Scatter plots of the pseudo-observations are shown in Fig. 3.6. To find the optimal smoothing parameter for the Beta kernel estimator, 50 smoothing parameters equally spaced between 0 and 1 are tried and for each smoothing parameter 100 estimated TFCs are generated, which is followed by the spectrogram estimation with the estimated TFCs. Then the MISE between the estimated spectrograms and the original spectrogram is calculated for each smoothing parameter by Eq. (3.7). The MISE plots against smoothing parameter are plotted as shown in Fig. 3.2(a), Fig. 3.7(a), and Fig. 3.7(b) for 10% sun gear tooth crack case, 30% sun gear tooth crack case, and 50% sun gear tooth crack case, respectively.

As shown in Fig. 3.2(a) and Fig. 3.7, the optimal smoothing parameters with smallest MISEs are 0.1885, 0.1684, and 0.1484 for 10% sun gear tooth crack case, 30% sun gear tooth crack case, and 50% sun gear tooth crack case, respectively, which are used in the following spectrogram-free TFC estimation. For the purpose of comparison, the spectrogram-based copula reported in [48] is estimated with the same smoothing parameters for each simulated vibration signal.

Fig. 3.8 shows the densities of the spectrogram-free TFC and the spectrogram-based TFC for each vibration signal. It can be noticed that even with the same smoothing param-

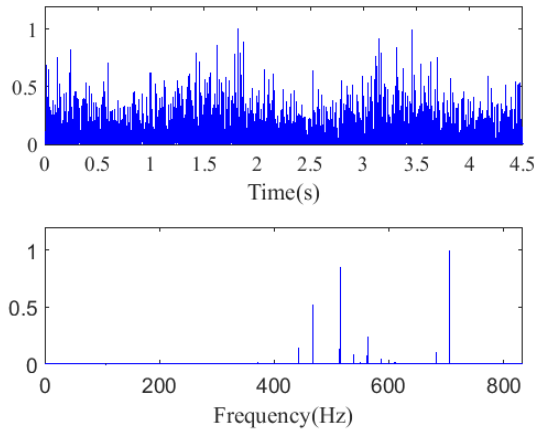

(a) 10% sun gear tooth crack case

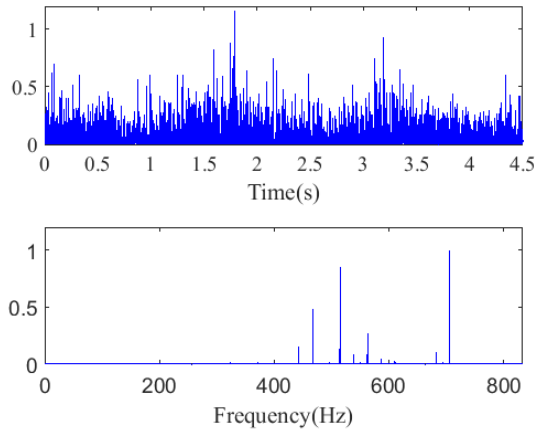

(b) 30% sun gear tooth crack case

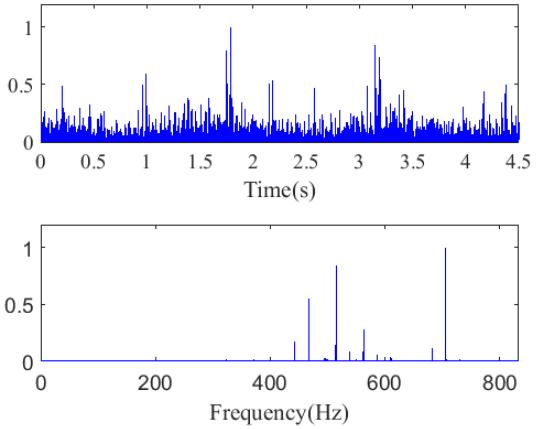

(c) 50% sun gear tooth crack case

Fig. 3.4: Instantaneous energy and energy spectral density of simulated signals

eter, the spectrogram-free TFCs and the spectrogram-based TFCs have different shapes. To compare their fitness to the marginal dependence, i.e., the dependence between the instantaneous energy and the energy spectral density, QQ plots are plotted in Fig. 3.9 where the data samples for the estimated copula model quantiles are generated by the copula densities in Fig. 3.8.

The average distance to the reference diagonal line in the QQ plot is calculated to suggest the fitness to marginal dependence. Table 3.2 lists the average distance values and the improvement in percentage of the proposed spectrogram-free TFC over the reported spectrogram-based TFC for studied cases. From Table 3.2, it can be seen that the proposed

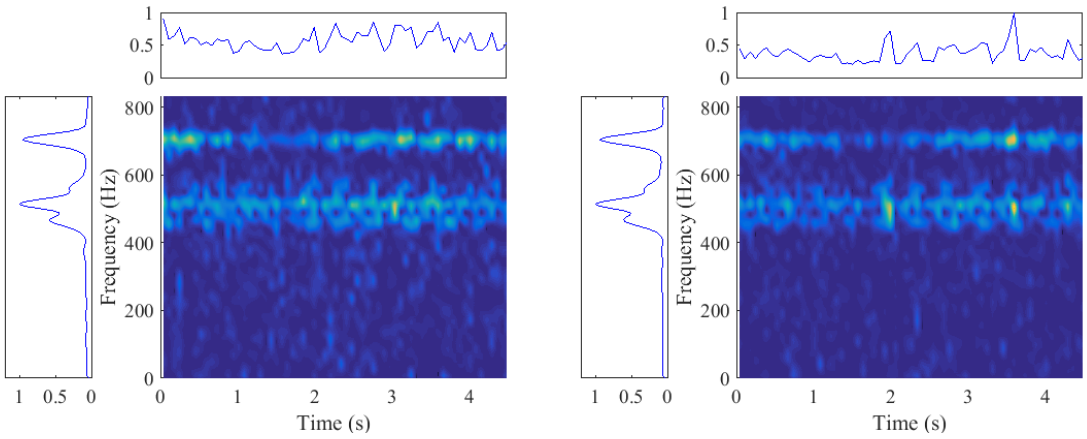

(a) 10% sun gear tooth crack case

(b) 30% sun gear tooth crack case

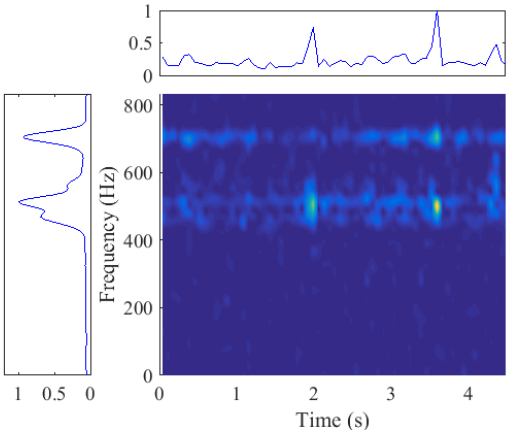

(c) 50% sun gear tooth crack case

Fig. 3.5: Spectrogram and Spectrogram-based marginals of simulated signals

spectrogram-free TFC have smaller average distances to the reference diagonal line than the reported spectrogram-based TFC with improvements in percentage of 88.89%, 70.8%, and 71.9% for 10% crack case, 30% crack case, and 50% crack case, respectively. Thus, it can be concluded that the proposed spectrogram-free TFC provides a better fit than the reported spectrogram-based TFC in [48] for simulated planetary gear set vibration signals.

Table 3.2: Average distance to reference diagonal line

Estimation model	Average distance to reference diagonal line		
	10% crack case	30% crack case	50% crack case
Spectrogram-free copula	0.0022	0.0047	0.0025
Spectrogram-based copula	0.0198	0.0161	0.0089
Improvement in percentage	88.89%	70.8%	71.9%

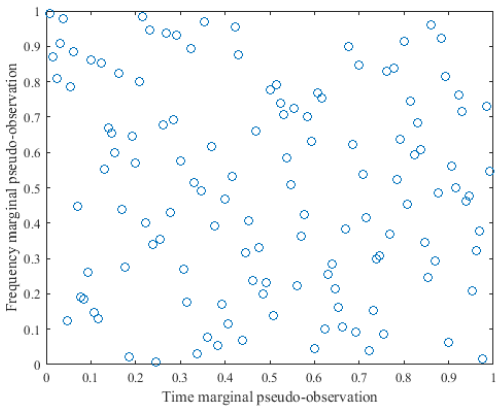

(a) 10% sun gear tooth crack case

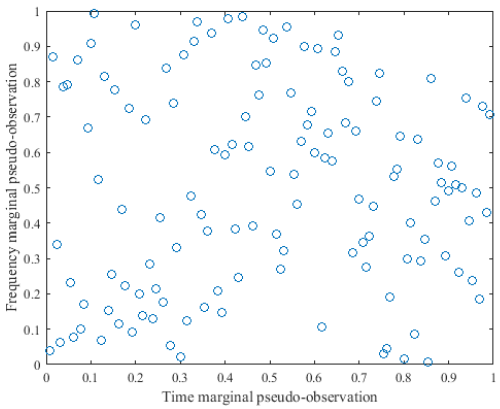

(b) 30% sun gear tooth crack case

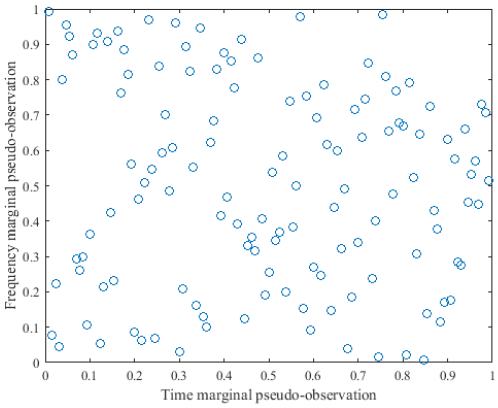

(c) 50% sun gear tooth crack case

Fig. 3.6: Scatter plot of pseudo-observations for simulated signals

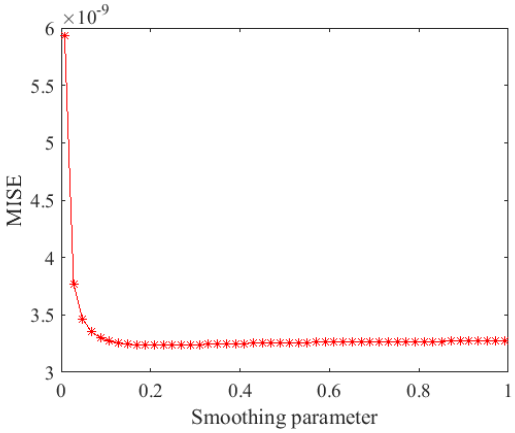

(a) 30% sun gear tooth crack case

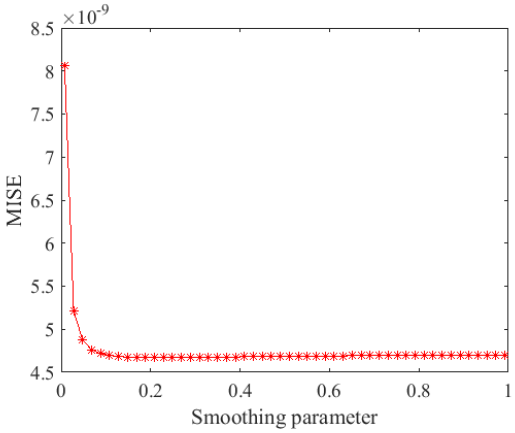

(b) 50% sun gear tooth crack case

Fig. 3.7: MISE plot against smoothing parameter for simulated signals

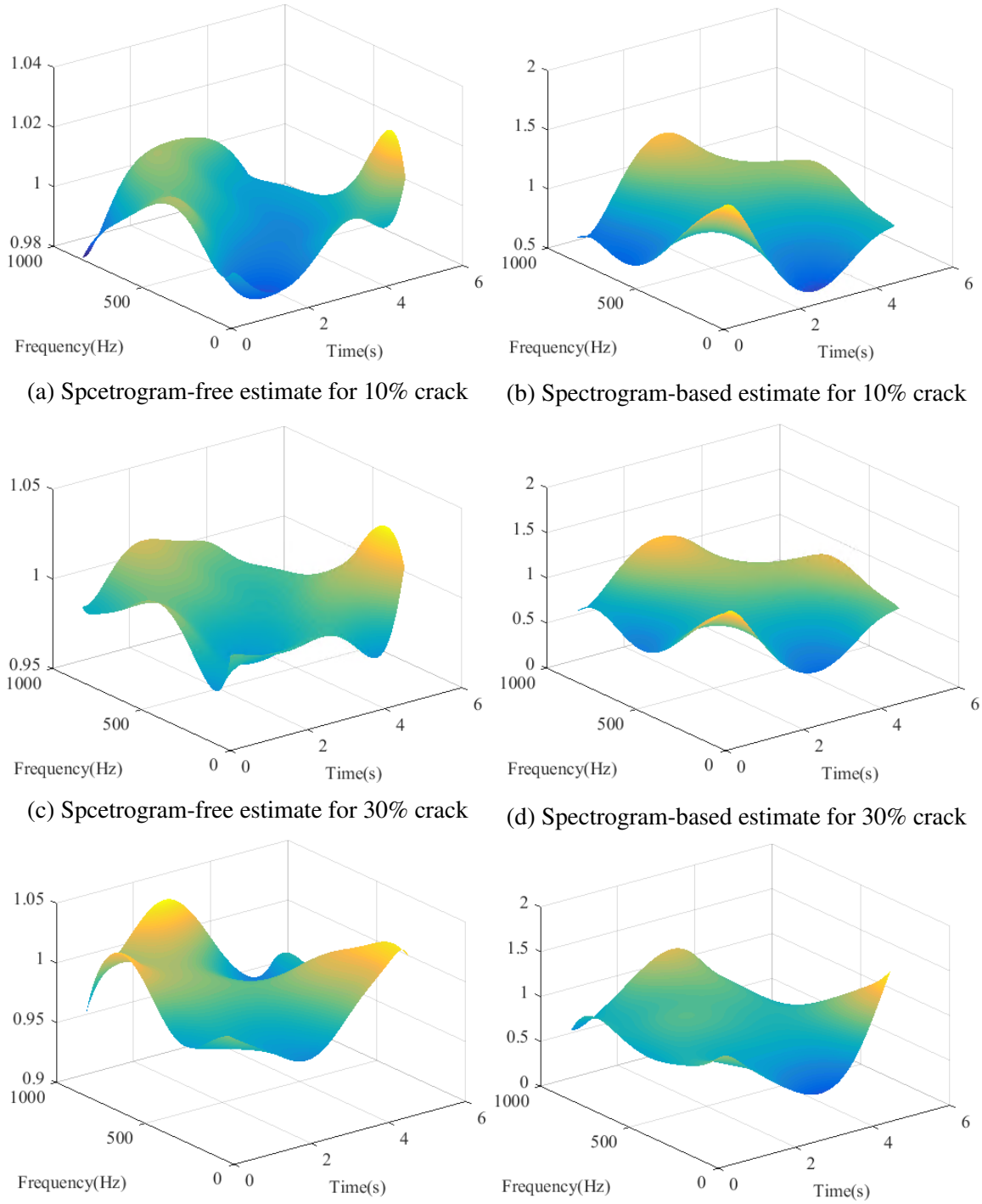

(a) Spcetrogram-free estimate for 10% crack

(b) Spectrogram-based estimate for 10% crack

(c) Spcetrogram-free estimate for 30% crack

(d) Spectrogram-based estimate for 30% crack

(e) Spcetrogram-free estimate for 50% crack

(f) Spectrogram-based estimate for 50% crack

Fig. 3.8: Estimated copula densities with different estimation methods for simulated signals

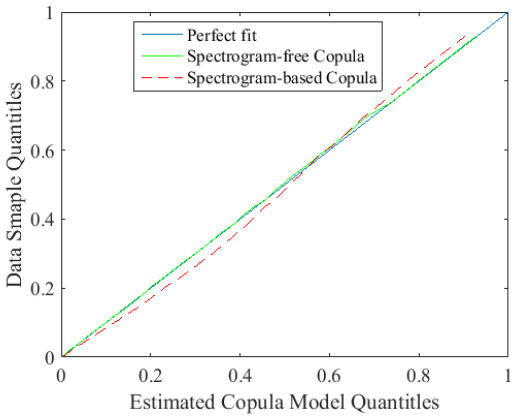

(a) 10% sun gear tooth crack simulated case

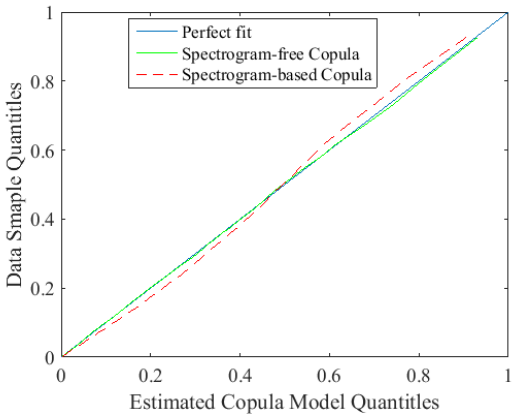

(b) 30% sun gear tooth crack simulated case

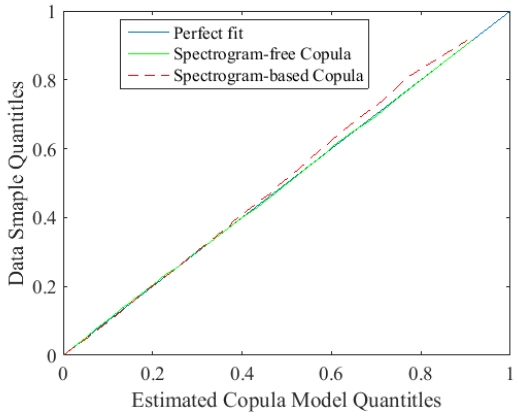

(c) 50% sun gear tooth crack simulated case

Fig. 3.9: QQ plot for copula models with different estimation methods for simulated signals

3.4.1.2 Experimental planetary gearbox vibration signal analysis

The planetary gearbox test rig in the Reliability Research Lab at the University of Alberta has a configuration as shown in Fig. 2.11. The number of teeth for each gear in the test rig is as presented in Table 2.4 where the number 4 in the parenthesis is the number of the planet gears. All gears are standard spur gears without tooth profile modification. An accelerometer was installed in the vertical direction of the casing of the second stage planetary gearbox. The second stage planetary gearbox has gear parameters as shown in Table 3.1 and is with the same configuration as the simulated planetary gear set. During the experiment, the sun gear rotational speed of the second stage planetary gearbox was 46.667r/min with the driving motor speed being 1200r/min; the load applied on the carrier

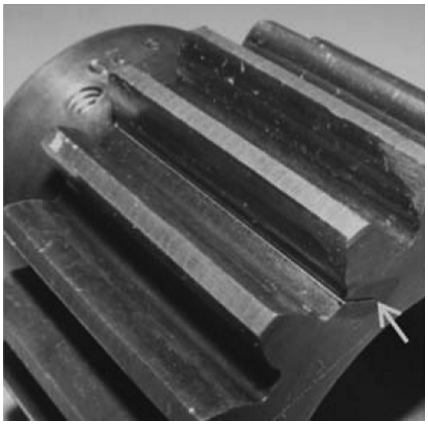

Fig. 3.10: Sun gear tooth crack

shaft of the 2nd stage planetary gearbox was 2367Nm [140].

The experimental vibration signal was subject to a 50% sun gear tooth crack level with a crack length of 3.9mm, acquired in the year of 2011 by former group members [170]. The sampling frequency was 5000Hz. The crack is developed as described in Fig. 3.3 and shown physically in Fig. 3.10. Other gears are without gear tooth faults. The experimental vibration signal was processed by a Chebyshev low-pass filter with a cutoff frequency of 800Hz, covering the low characteristic frequencies and the frequencies with energy concentration around 350Hz and 700Hz as shown in Fig. 3.11.

Fig. 3.11 shows the instantaneous energy and the energy spectral density of the experimental vibration signal. Fig. 3.12 demonstrates the spectrogram and the spectrogram-based marginals. The energy marginals in Fig. 3.11 and Fig. 3.12 are normalized by their maximum values. Fig. 3.13 illustrates the scatter plot of rank-based pseudo-observations of the spectrogram-based marginals in Fig. 3.12 which are obtained by Eq. (3.3) as needed for optimal smoothing parameter determination. The MISE plot regarding the spectrogram with 50 smoothing parameter candidates equally spaced between 0 and 1 is plotted in Fig. 3.14 to find the optimal smoothing parameter for the non-parametric copula estimation by Beta kernel estimator. With the optimal smoothing parameter being 0.1885 as found in Fig. 3.14 with the smallest MISE, both the spectrogram-free TFC and the spectrogram-based TFC are estimated by Eq. (3.4) as given in Fig. 3.15. To compare their fitness to the marginal de-

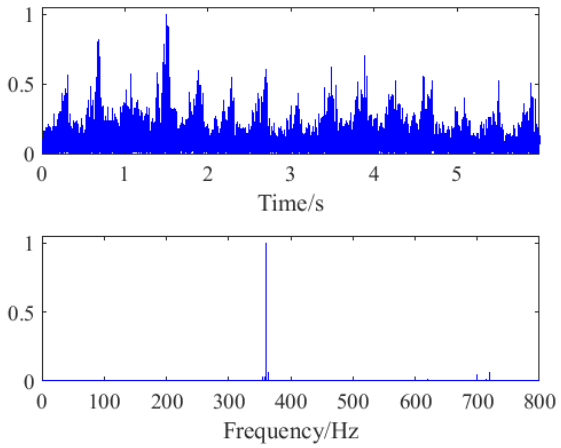

Fig. 3.11: Marginals of experimental signal

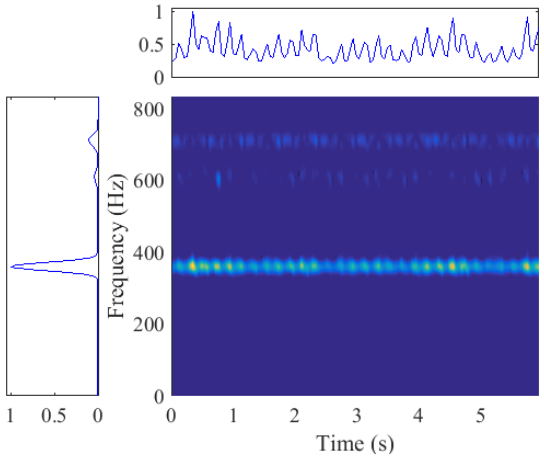

Fig. 3.12: Spectrogram-based marginals of experimental signal

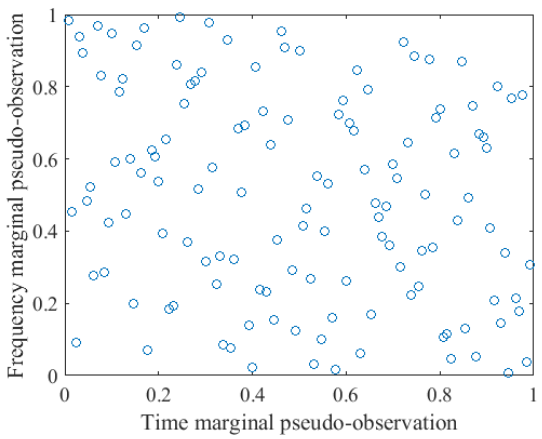

Fig. 3.13: Scatter plot of pseudo-observations for experimental signal

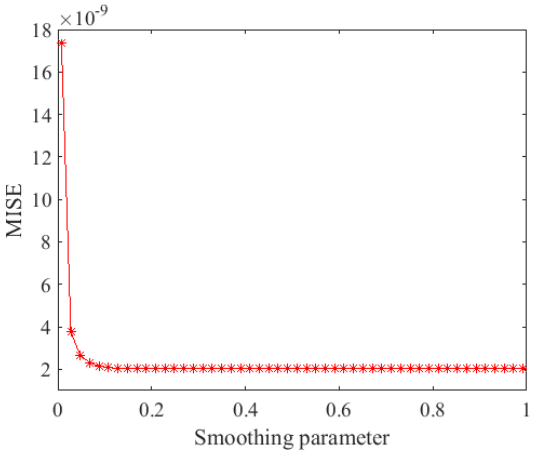

Fig. 3.14: MISE plot with smoothing parameter for experimental signal

pendence, QQ plot is plotted in Fig. 3.16 where data samples for quantiles of the estimated copula are generated with the TFC densities in Fig. 3.15.

Average distances of the curves in Fig. 3.16 to the reference diagonal line are calculated to indicate the fitness of the estimated copulas to the marginal dependence. The average distance of the spectrogram-free TFC is 0.0024 with an improvement in percentage of 63.08% relative to that of the spectrogram-based TFC which is 0.0065. Thus, it is concluded that the proposed spectrogram-free TFC provides a better fit to the marginal dependence than the reported spectrogram-based TFC for the experimental planetary gearbox vibration signal.

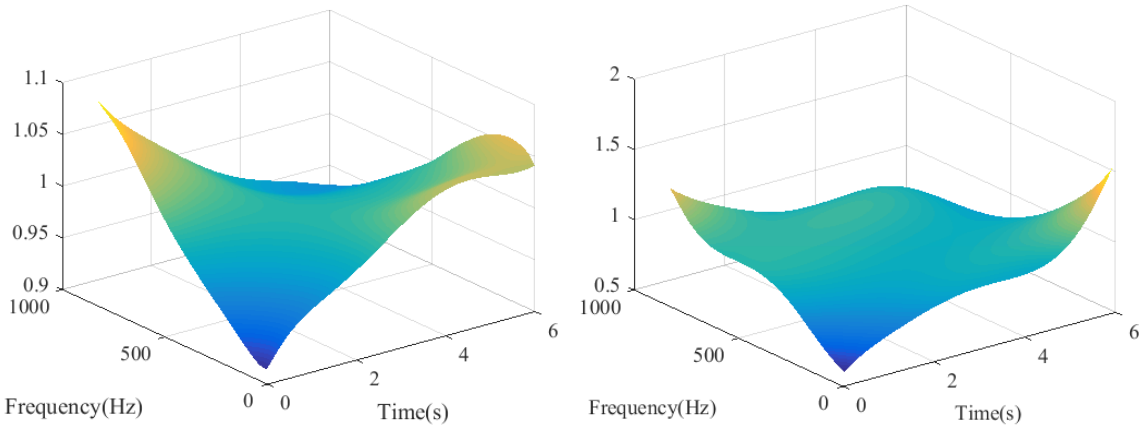

(a) Spectrogram-free estimation (b) Spectrogram-based estimation

Fig. 3.15: Estimated copula densities for experimental signal

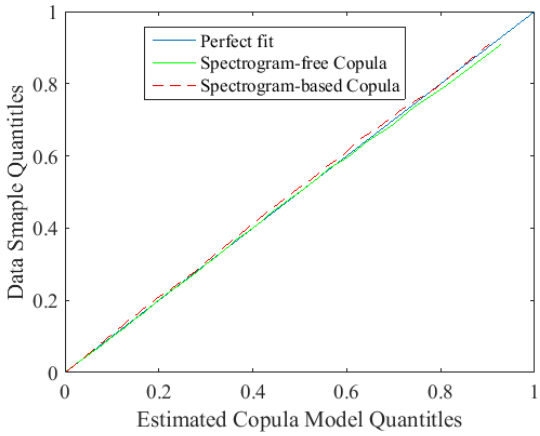

Fig. 3.16: QQ plot for estimated copula models of experimental signal

3.4.2 Energy density representation by estimated spectrogram-free time-frequency copula

By the analysis in Subsection 3.4.1, the proposed spectrogram-free TFC provides a better fit to the marginal dependence than the reported spectrogram-based TFC for both simulated and experimental planetary gearbox vibration signals. In this section, the copula-based TFDs with the spectrogram-free TFCs and the spectrogram-based TFCs are constructed and compared to reflect the benefit gained by the better fit to the marginal dependence.

Fig. 3.17 and Fig. 3.18 show the contour plots and marginals of the spectrogram-free and spectrogram-based copula-based TFDs for the simulated vibration signal and the ex-

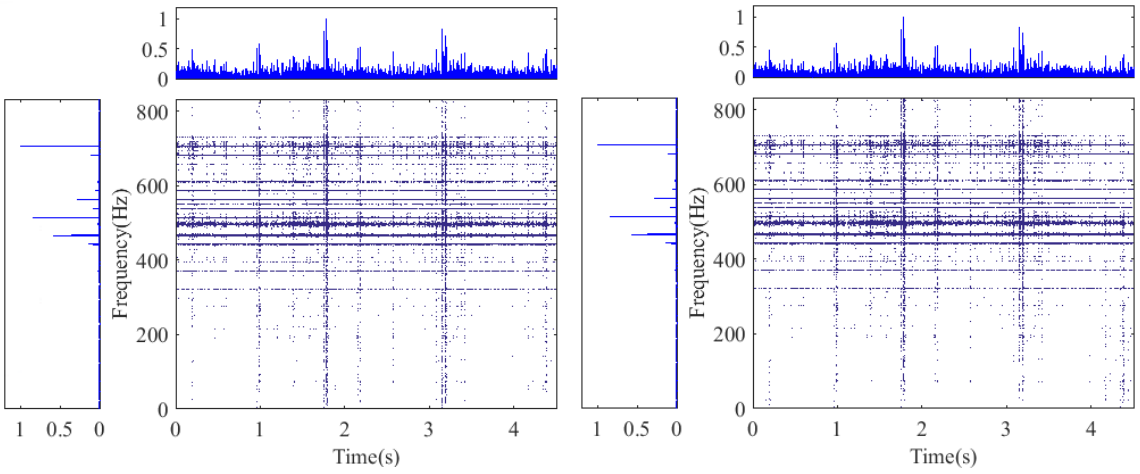

(a) Spectrogram-free copula-based TFD (b) Spectrogram-based copula-based TFD

Fig. 3.17: Copula-based TFD of simulated signal

perimental vibration signal, respectively. The simulated and experimental vibration signals are subject to the 50% sun gear tooth crack. The energy marginals are normalized by their maximum values. The contour plots are plotted in the whole frequency range with energy density values higher than 2e-7 and 0.3e-7 for the simulated vibration signal and the experimental vibration signal, respectively.

From Fig. 3.17 and Fig. 3.18, one can notice that the fault-induced impulses in the waveform are represented by the vertical lines in the time-frequency domain. The theory behind this observation is that a fault induced impulse has a broad frequency range which is represented by the primary impulse in the joint time-frequency domain [101].

However, one cannot visually see the improvement of the spectrogram-free copula-based TFD over the spectrogram-based copula-based TFD through Fig 3.17 and Fig 3.18. To illustrate the improvement, summations of the absolute difference between the marginals of the constructed TFDs and the instantaneous energy and the energy spectral density of the truncated vibration signal are calculated. For the simulated vibration signal, the summations of the absolute difference between marginals of the spectrogram-free copula-based TFD in Fig. 3.17(a) and the ones in Fig. 3.4(c) are 2.1960 and 0.0164 for the time marginal and the frequency marginal, respectively, while those values are 12.8459 and 0.1599 for

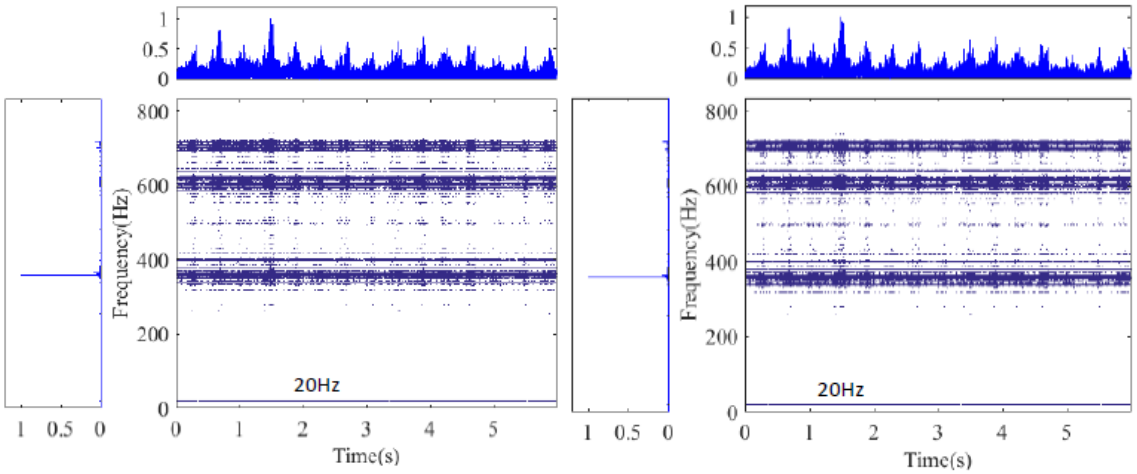

(a) Spectrogram-free copula-based TFD (b) Spectrogram-based copula-based TFD

Fig. 3.18: Copula-based TFD of experimental signal

the spectrogram-based copula-based TFD in Fig. 3.17(b). For the experimental vibration signal, the summations of the absolute difference between marginals in Fig. 3.18(a) and the ones in Fig. 3.11 are 2.6664 and 5.12e-4 for the time marginal and the frequency marginal, respectively, while those values are 29.46 and 0.0124 for the spectrogram-based copula-based TFD in Fig. 3.18(b). The results show that the marginal deviations of the spectrogram-free copula-based TFD are smaller than those values of the spectrogram-based copula-based TFD in the whole range.

More intuitively to show the local marginal deviation, marginals in Fig. 3.17 and Fig. 3.18 and the ones in Fig. 3.4(c) and Fig. 3.11 are divided into 10 segments. The summations of the absolute differences are compared as illustrated by the bar charts in Fig. 3.19 and Fig. 3.20 for each segment. The x-axes in Fig. 3.19 and Fig. 3.20 show the values of the central time instants and the central frequencies, respectively, of the segments. Specifically, Fig. 3.19 shows marginal difference of the spectrogram-free copula-based TFD and the spectrogram-based copula-based TFD for the simulated vibration signal. Fig. 3.20 shows marginal difference of the spectrogram-free copula-based TFD and the spectrogram-based copula-based TFD for the experimental vibration signal.

As visually observed from Fig. 3.19 and Fig. 3.20, it is obvious that the spectrogram-

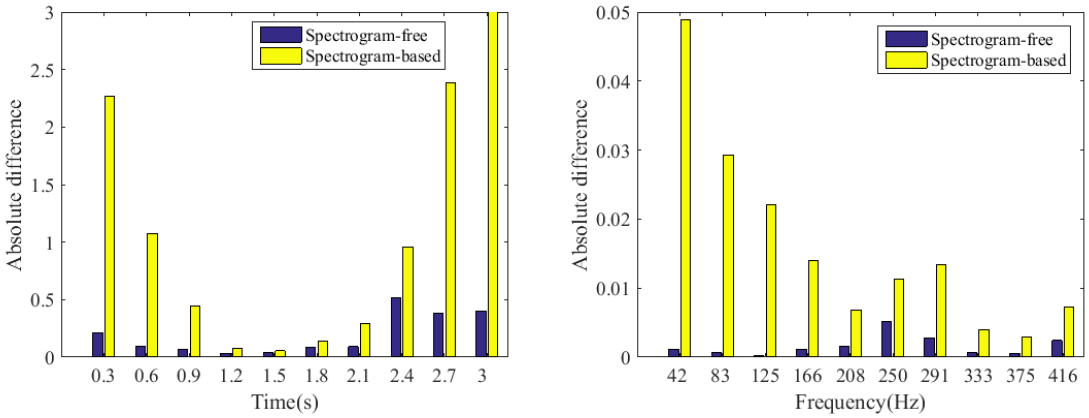

(a) Time marginal difference (b) Frequency marginal difference

Fig. 3.19: marginal difference of simulated signal

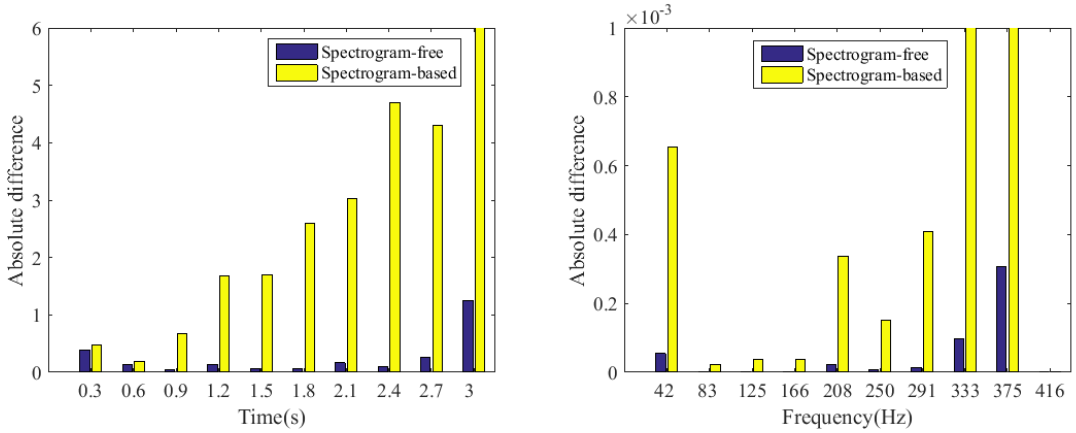

(a) Time marginal difference (b) Frequency marginal difference

Fig. 3.20: marginal difference of experimental signal

free copula-based TFD provides smaller marginal difference than the spectrogram-based copula-based TFD for each segment in the time marginal and the frequency marginal for both the simulated vibration signal and the experimental vibration signal. Note that for the bar charts centered at 416Hz in Fig. 3.20(b), the spectrogram-free bar chart has a smaller value of 1.61e-7 than the spectrogram-based bar chart whose value is 1.26e-6.

Consequently, by the analysis on Fig. 3.17, Fig. 3.18, Fig. 3.19, and Fig. 3.20, the conclusion is drawn that the spectrogram-free copula-based TFD has smaller marginal deviations from the instantaneous energy and the energy spectral density of the truncated vibration signal in both the global sense and the local sense than the spectrogram-based

copula-based TFD, thus serving better for energy density representation. This benefit is gained by the better fit to marginal dependence by the proposed spectrogram-free TFC estimation.

3.5 Performance of spectrogram-free copula-based TFD on planetary gearbox fault diagnosis

In this section, to demonstrate the advantages of the constructed spectrogram-free copula-based TFD on planetary gearbox fault diagnosis, its performances on identifying fault-related frequencies in the frequency energy marginal and locating fault-induced impulses in the time-frequency domain are examined and compared with the performances of the spectrogram. For a planetary gearbox with sun gear tooth crack, according to [25], a fault-related frequency f is associated with meshing frequency f_m, sun gear tooth crack characteristic frequency f_{sc}, and carrier rotational frequency f_c in the form of $f = a_1 f_m + a_2 f_{sc} + a_3 f_c$ with a_1, a_2, and a_3 are integers as harmonic orders. With the input as the sun gear and rotational speed being 46.667Hz, f_m, f_c, and f_{sc} were calculated in [140] and [142] to be 11.97Hz, 0.1478Hz, and 2.52Hz, respectively, which are low frequencies. Thus we focused on low frequency band analysis for fault-related frequency identification in following. Specifically, the frequency range is between 0Hz to 25Hz to cover the 2nd harmonic of f_m and its sidebands of f_{sc}.

Fig. 3.21 shows time-frequency energy densities and its energy marginals within the frequency range of 0Hz to 25Hz for the simulated vibration signal with 50% sun gear tooth crack. Fig. 3.21(a) and Fig. 3.21(b), i.e., the spectrogram-free copula-based TFD and the spectrogram, are obtained by zooming Fig. 3.17(a) and Fig. 3.5(c) into frequency range of 0Hz to 25Hz, respectively. Contour plots are plotted with energy density values higher than 1.2e-7 and 6e-5 for Fig. 3.21(a) and Fig. 3.21(b), respectively.

Frequency components with sizable amplitudes in the frequency marginal of the constructed spectrogram-free copula-based TFD are marked in Fig. 3.21(a). Table 3.3 lists the

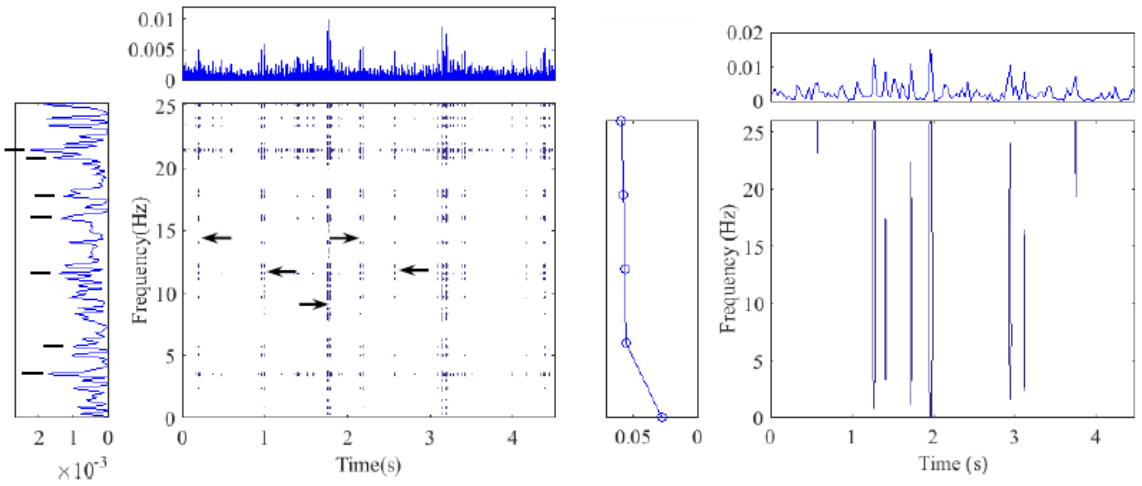

(a) Spectrogram-free copula-based TFD

(b) Spectrogram

Fig. 3.21: Time-frequency energy distributions for simulated vibration signal

Table 3.3: Decomposition of frequency components in energy marginal of constructed copula-based TFD for simulated Crack50 case

Frequency component/Hz	f_m order a_1	f_{sc} order a_2	f_c order a_3
3.548	0	1	7
5.765	0	2	5
11.53	1	0	-3
15.96	1	2	-7
17.74	1	2	5
20.84	2	-1	-4
21.51	2	-1	0

harmonic orders of f_m, f_{sc}, and f_c to decompose the marked frequency components into summations of f_m, f_{sc}, and f_c. From Table 3.3, it can be seen that the marked frequency components in Fig. 3.21(a) meet the relationship of $f = a_1 f_m + a_2 f_{sc} + a_3 f_c$ as defined in [25]. Consequently, they are frequencies relating to the sun gear tooth crack, indicating that the constructed spectrogram-free copula-based TFD can identify the fault-related frequencies by its frequency marginal with high frequency resolution.

Meanwhile, with fine time localization, vertical lines in the time-frequency domain representing fault-induced impulses are located at 0.19s, 0.98s, 1.78s, 2.17s, and 2.58s

as marked in Fig. 3.21(a). With the sun gear tooth crack characteristic frequency being 2.52Hz, fault-induced impulses occur with a nominal time interval of 0.397s. As marked in Fig. 3.21(a), the time intervals between two adjacent vertical lines are 0.79s, 0.8s, 0.39s, and 0.39s, either around two times of 0.397s, i.e., 0.794s, or around 0.397s. So we deduce that the marked vertical lines in Fig. 3.21(a) represent the fault-induced impulses even though not all fault-induced impulses are located.

On the other hand, when we look at the performance of the spectrogram on identifying fault-related frequencies in its frequency energy marginal and locating fault-induced impulse in the time-frequency domain as shown in Fig. 3.21(b) for the simulated vibration signal, because of the poor frequency resolution, there is only 5 points in its frequency marginal without showing any information on fault-related frequencies. Additionally, the vertical lines in the time-frequency domain are located at 0.576s, 1.272s, 1.411s, 1.724s, 1.968s, 2.942s, 3.116s, and 3.743s with time intervals of 0.696s, 0.139s, 0.313s, 0.244s, 0.974s, 0.174s, and 0.627s, from which no pattern on the time intervals can be deduced for planetary gearbox fault diagnosis.

For the experimental vibration signal with 50% sun gear tooth crack, as shown in Fig. 3.18, there is a 20Hz frequency component with sizable amplitude which corresponds to the driving motor speed 1200r/min. It should be noted that due to the energy leakage with rectangular window, there would exist disturbing frequencies around 20Hz without discernible relationship with the 2nd stage sun gear tooth crack. To eliminate the influence of the driving motor rotational frequency and its energy leakage on the identification of fault-related frequencies, we set energy density values being zero with a frequency range from 19Hz to 21Hz for the constructed spectrogram-free copula-based TFD. Then Fig. 3.22(a) is obtained by zooming Fig. 3.18(a) with zero values from 19Hz to 21Hz into frequency range of 0Hz to 25Hz. On the other hand, from Fig. 3.12, we cannot notice any disturbing frequencies around 20Hz. So we keep all the values and zoom Fig. 3.12 into frequency range of 0Hz to 25Hz to get Fig. 3.22(b). The contour plots are plotted with energy density

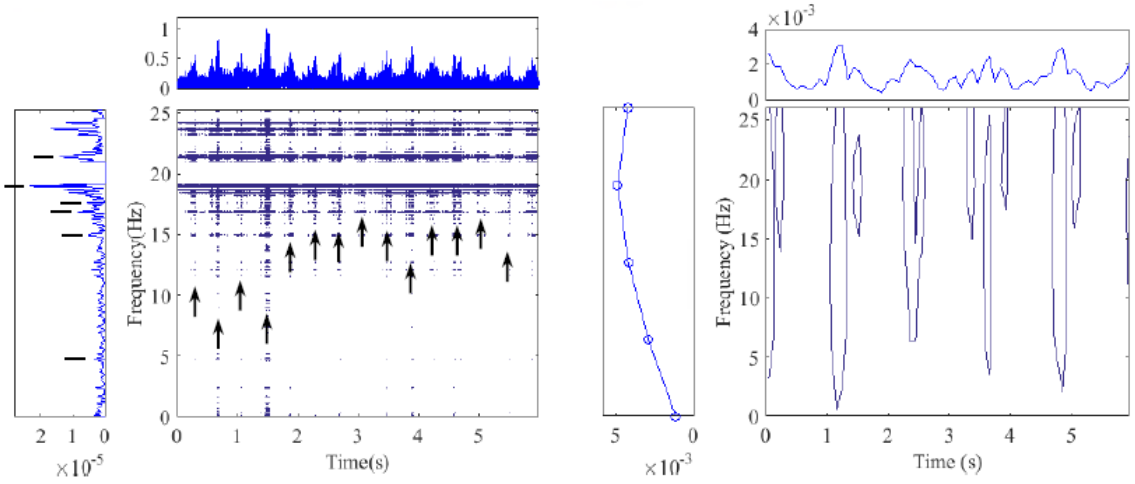

(a) Spectrogram-free copula-based TFD (b) Spectrogram

Fig. 3.22: Time-frequency energy distributions for experimental vibration signal

values higher than 4.5e-10 and 1.7e-5 for Fig. 3.22(a) and Fig. 3.22(b), respectively.

Frequency components with sizable amplitudes are marked in the frequency marginal of the spectrogram-free copula-based TFD in Fig. 3.22(a) to identify fault-related frequencies for the experimental vibration signal. Harmonic orders of f_m, f_{sc}, and f_c are listed in Table 3.4 for decomposition of frequency components marked in Fig. 3.22(a) into summations of f_m, f_{sc}, and f_c. As shown in Table 3.4, the marked frequency components in Fig. 3.22(a) meet the relationship of $f = a_1 f_m + a_2 f_{sc} + a_3 f_c$ as defined in [25]. Therefore, they are frequencies relating to the sun gear tooth crack. Thus, the spectrogram-free copula-based TFD can identify fault-related frequencies by its frequency marginal with high frequency resolution.

Meanwhile, with fine time localization, vertical lines in the time-frequency domain representing fault-induced impulses are located at 0.2948s, 0.6692s, 1.06s, 1.489s, 1.881s, 2.292s, 2.684s, 3.093s, 3.486s, 3.878s, 4.218s, 4.663s, 5.091s, and 5.484s as marked in Fig. 3.22(a). The average time interval between two adjacent vertical lines is 0.3992s with an occurring frequency of 2.505Hz, approximately equal to the sun gear tooth crack characteristic frequency 2.52Hz with a deviation of 0.6%. So it can be deduced that the marked vertical lines in Fig. 3.22(a) indicate locations of fault-induced impulses.

Table 3.4: Decomposition of frequency components in energy marginal of constructed copula-based TFD for experimental Crack50 case

Frequency component/Hz	f_m order a_1	f_{sc} order a_2	f_c order a_3
4.757	0	2	-2
14.94	1	1	3
16.86	1	2	-1
17.61	1	2	4
18.95	1	3	-4
21.37	2	-1	0

On the other hand, when we look at the performance of the spectrogram on identifying fault-related frequencies in its frequency energy marginal and locating fault-induced impulse in the time-frequency domain for the experimental vibration signal as shown in Fig. 3.22(b), same as the simulated case, because of the poor frequency resolution, there is only 5 points in its frequency marginal without showing any information on fault-related frequencies. Additionally, the vertical lines in the time-frequency domain are located at 0.1434s, 1.16s, 2.453s, 3.655s, and 4.856s. The average time interval of located vertical lines in Fig. 3.22(b) is 1.178s with an occurring frequency of 0.8488Hz which cannot be used for diagnosing the sun gear tooth crack without the supplementary information from the frequency energy marginal.

To summarize, through the above analysis, by the spectrogram-free copula-based TFD, fault-related frequencies can be identified in the frequency energy marginal with fine frequency resolution and vertical lines representing fault-induced impulses can be located in the time-frequency domain with fine time localization. Fault-related frequency identification and fault-induced impulse localization support each other mutually for planetary gearbox fault diagnosis without trade-off, i.e., they are free from the Heisenberg uncertainty principle. Consequently, the constructed spectrogram-free copula-based TFD serves better than the spectrogram for planetary gearbox fault diagnosis. Future experiments under various levels of load, speed, and gear tooth fault can be conducted to check the performance

of the constructed spectrogram-free copula-based TFD on fault diagnosis for cases with different operation conditions and/or fault levels.

3.6 Conclusions

In this chapter, a method to construct spectrogram-free copula-based TFD with non-parametric TFC is proposed to represent the time-frequency energy density of a vibration signal for planetary gearbox fault diagnosis. The analyzed vibration signals are truncated by rectangular window and filtered by a low-pass filter to be finite in both time and frequency. The proposed method starts with determining the instantaneous energy and the energy spectral density of the truncated vibration signal. Non-parametric TFC estimation procedures include rank-based pseudo-observation generation, kernel smoothing parameter determination, and the TFC estimation by Beta kernel estimator. Rank-based pseudo-observations are generated with the instantaneous energy and the energy spectral density instead of the spectrogram-based marginals to eliminate the spectrogram influence on the TFC estimation and, eventually, the constructed copula-based TFD. For the determination of smoothing parameter, a criterion based on MISE regarding spectrogram is proposed and validated. With the proposed spectrogram-free copula estimation method, the non-parametric copula is estimated for simulated and experimental planetary gearbox vibration signals. The goodness-of-fit of the proposed spectrogram-free copula to marginal dependence is compared with that of the reported spectrogram-based copula using QQ plot. The result shows that the spectrogram-free copula model can provide a better marginal dependence fitness.

Subsequently, based on the strength of the estimated spectrogram-free TFC, a copula-based time-frequency distribution (TFD) is constructed for energy density representation by which fault-induced impulses in time waveform are represented as the vertical lines in the time-frequency domain. Moreover, the spectrogram-free copula-based TFD has energy marginals with smaller deviations from the instantaneous energy and the energy spectral density of the truncated vibration signal than the spectrogram-based copula-based TFD,

which is a result of a better marginal dependence fitness.

Finally, performance of the spectrogram-free copula-based TFD on planetary gearbox fault diagnosis is demonstrated and compared with the performance of spectrogram. The results show that, with high time-frequency resolution, the spectrogram-free copula-based TFD can identify fault-related frequencies with fine frequency resolution and simultaneously locate fault-induced impulses with fine time localization, i.e., free from the Heisenberg uncertainty principle, thus serving better for planetary gearbox fault diagnosis.

The spectrogram-free copula-based TFD as constructed in this chapter will be employed in Chapter 4 to develop a fault feature extraction method by non-negative matrix factorization for planetary gearbox fault detection.

Chapter 4

Feature extraction by non-negative matrix factorization for planetary gearbox fault detection

As indicated in Fig. 1.12, the focus of this chapter is on the third research topic, fault feature extraction by Non-Negative Matrix Factorization (NNMF) from a one-dimensional vibration signal for planetary gearbox fault detection. To make a one-dimensional vibration signal available for NNMF, the one-dimensional vibration signal is preprocessed to generate its copula-based Time-Frequency Distribution (TFD) based on the spectrogram-free non-parametric copula as documented in Chapter 3. Unlike Independent Component Analysis (ICA), NNMF is a multivariate data analysis method with the non-negativity constraint. As constrained by non-negativity, NNMF decomposition intrinsically leads to a part-based representation with pure additions. Part-based decomposition would alleviate the shortcomings of ICA as a global-support decomposition in revealing useful information in the original data. We treat time waveforms at different frequency positions in the copula-based positive TFD as the input to NNMF. In this way, the requirements of multi-dimensional data series and non-negativity for NNMF are met. Fault-induced impulses can be extracted through dimension reduction of the copula-based TFD by NNMF decomposition, which is suggested by the identification of the fault characteristic frequency, thus serving for planetary gearbox fault detection.

The organization of this chapter is as follows. Section 4.1 presents an introduction to

fault feature extraction by methods of multivariate data analysis from a one-dimensional signal. Section 4.2 gives theoretical principles on copula-based TFD and NNMF decomposition. In Section 4.3, the proposed NNMF-based fault feature extraction method is developed. In Section 4.4, applications on simulated and experimental planetary gearbox vibration signals are studied to demonstrate the advantage of the developed NNMF-based method over the reported ICA-based method in terms of the accuracy of identifying the fault characteristic frequency. The simulated signals are generated with the vibration signal modeling method described in Chapter 2. Discussions of sparsity are given in Section 4.5 to reveal the driving force behind the better performance. The study is concluded in Section 4.6. The results of this chapter are documented in [144] and submitted to *Journal of Sound and Vibration* for possible publication.

4.1 Introduction

With a gear tooth fault, corresponding fault-induced impulses would be excited in the measured vibration signal [51]. However, in real working environment, a vibration signal measured from a practical planetary gearbox usually carries heavy environmental background noise, which would bury the fault-induced impulses [171]. Besides, vibrations from meshing gear pairs are often stronger than the transient fault-induced impulses and dominate in the spectrum of the measured vibration signal. The background noise and the dominated gear meshing vibrations render the measured vibration signal with a low Signal-to-Noise Ratio (SNR) for fault-induced impulses, posing difficulties and challenges on fault feature extraction for fault detection [172].

To achieve fault feature extraction from a measured vibration signal, researchers have made numerous efforts with plentiful reported work. Lee and Nandi [173] applied two blind deconvolution algorithms, i.e., the objective function method and the eigenvector algorithm, to estimate an optimal inverse filter for impulsive impacting signal extraction. Yang and Peter [174] developed a method to identify the fault information from a noise-

contaminated signal with the aid of singular entropy based on Singular Value Decomposition (SVD). Antoni and Randall [175] presented a review on self-adaptive noise cancellation from the standpoint of prediction theory and gave guidelines for setting algorithm parameters of time delay and filter length. To alleviate the requirement of tuning parameters, they then reported a direct estimation method for noise cancellation frequency gain in the frequency domain, leading to an algorithm based on fast Fourier transform with computational advantages [176]. Jiang et al. [100] applied a de-noising method based on adaptive Morlet wavelet and SVD to wind turbine vibration signals for fault feature extraction. Skrimpas et al. [177] calculated statistical features measuring the signal energy and the Gaussianity from residual signals of a multi-stage wind turbine gearbox for planetary stage fault detection. The residual signal was obtained by filtering frequency components not related to the planetary stage [177].

While the above methods are applied in either the time domain or the frequency domain, feature extraction methods from the joint Time-Frequency (TF) domain were also explored. The TF feature extraction can be achieved through energy concentration analysis of a TF energy density representation [101, 106, 178]. Sejdić et al. [179] presented an overview on the TF feature extraction based on energy concentration as being performed by visual inspection and classification schemes. However, the approach of visual inspection is not an automated decision process as it relies on human expertise and requires initial training for difference recognition among patterns [179]. On the other hand, even though the approach of feature classification is an automated process, its accuracy is affected by the TF energy density representation [179]. Besides, the development of a unifying classification framework is limited as various practical problems require different classification approaches [179]. Alternatively, dimension reduction by multivariate data analysis is a promising approach to extract fault features from the TF density representation. Zuo et al. [124] investigated the application of Principal Component Analysis (PCA) and Independent Component Analysis (ICA) on the extraction of fault-induced impulses from a

one-dimensional vibration signal. PCA and ICA are multivariate data analysis techniques to transform multiple data series into uncorrelated data series and independent data series, respectively [124]. To make PCA and ICA available for the cases with a one-dimensional vibration signal, they used Wavelet Transform (WT) to pre-process the one-dimensional vibration signal and then employed coefficients of WT at different scales as the Pseudo-Multi-Dimensional (PMD) input to PCA and ICA. The results in [124] demonstrate the effectiveness of the multivariate data analysis on the PMD signals for fault-induced impulse extraction and show that the WT-ICA method works better than the WT-PCA method for fault-induced impulse extraction from a one-dimensional vibration signal. As noted in [124], the idea of generating PMD signals as input to ICA has real applications where the number of sensors is less than the number of signal sources for fault-induced impulse extraction through multivariate data analysis. Later, based on WT-ICA method, Shao et al. [180] reported a separation strategy for sources related to a milling cutter and spindle from a one-dimensional power signal in milling process. Yang et al. [181] reported a damage identification method from a one-dimensional structural vibration signal for structural damage monitoring. However, the performance of WT-ICA method relies on proper wavelet basis selection [125]. To address this limitation, Wang et al. [125] presented an integrative method of Ensemble Empirical Mode Decomposition (EEMD) and ICA to extract fault-induced impulses from a one-dimensional vibration signal. The PMD signals in [125] are Intrinsic Mode Functions (IMFs) by EEMD rather than the WT coefficients. In this way, as EEMD is an adaptive data-driven signal decomposition method without requiring bases [182], the integrative EEMD-ICA method is not affected by base selection as WT-ICA method is [125].

Essentially, ICA is a global-support multivariate analysis method by matrix factorization [126]. However, the global-support characteristic realizes ICA decomposition by taking both negative and positive values, and models the data through complex mutual cancelation of components with opposite signs [126]. Thus, components decomposed by ICA

tend to highly overlap with each other [126]. Besides the information in the original signal, there is also information in ICA-decomposed components which does not exist in the original signal. As argued by Sotiras et al. [126], this phenomenon would lead to ICA-decomposed components lacking specificity and intuitive meaning.

To demonstrate the lack of specificity and intuitive meaning of ICA-decomposed components in fault-induced impulse extraction, analysis on a noisy synthetic signal with a 5dB SNR is presented. The synthetic signal has three constant frequency components, 15Hz, 22Hz, and 289Hz, with amplitude of one unit and ten transient oscillating impulses with amplitude of one unit. The function to generate transient oscillating impulses is given in Section 4.3 as Eq. (4.18). Oscillating impulses are added at 0.4s, 1s, 1.6s, 2.2s, 2.8s, 3.4s, 4s, 4.6s, 5.2s, and 5.8s with occurring frequency of 1.67Hz. Fig. 4.1 shows waveforms and spectra of the first four decomposed components by EEMD-ICA method reported in [125] where the components are ordered with decreasing waveform kurtosis. Through Fig. 4.1(b), it can be observed that besides the characteristic frequencies of 15Hz, 22Hz, and 289Hz, EEMD-ICA decomposed components have rich frequencies between 0Hz and 200Hz with sizable amplitudes. As suggested in [125], for the EEMD-ICA method, the decomposed component with maximum waveform kurtosis is adopted to identify the occurring frequency of transient impulses through its envelope spectrum. Fig. 4.2 illustrates the envelope waveform and the envelope spectrum of the C1 waveform shown in Fig. 4.1. The outstanding frequencies with sizable amplitudes in Fig. 4.2 are 1.33Hz, 3.83Hz, 5.5Hz, 7.17Hz, 8.5Hz, 10.66Hz, 12.16Hz, 14.16Hz, etc. which are neither the occurring frequency of transient oscillating impulses (1.67Hz) nor its harmonics (3.34Hz, 5.01Hz, 6.68Hz, 8.35Hz, 10.02Hz, 11.69Hz, 13.36Hz, etc.), indicating the reported EEMD-ICA method in [125] cannot identify the occurring frequency of transient impulses properly for the noisy synthetic signal.

According to [126], the reason to the appearance of the information in the EEMD-ICA decomposed components that does not exist in the original signal is the global-support

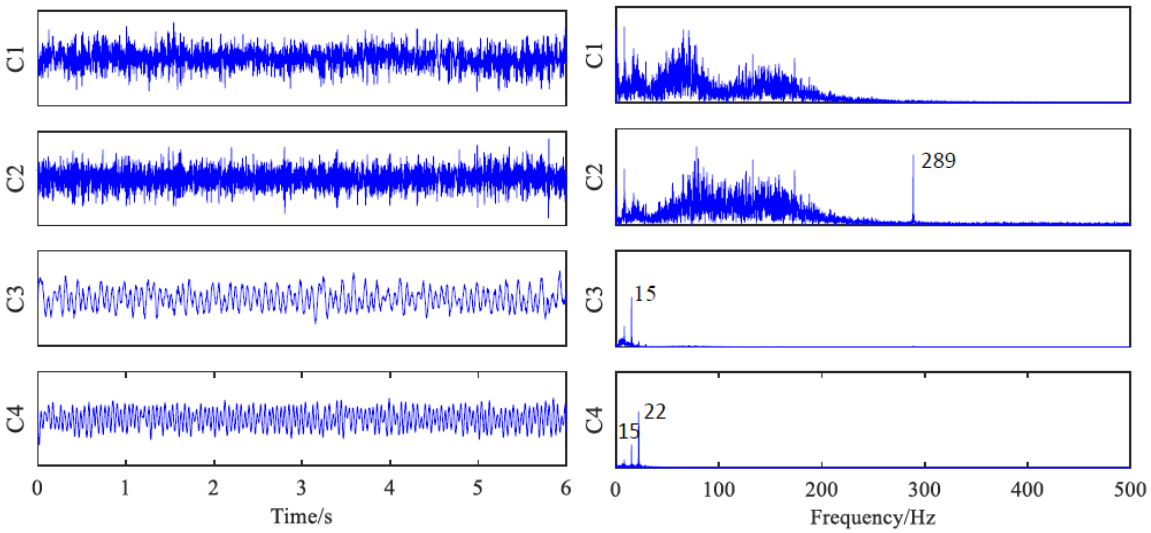

(a) Component waveforms

(b) Component spectra

Fig. 4.1: Decomposed components by EEMD-ICA method for synthetic signal

characteristic of ICA. To transcend the shortcoming induced by the global-support characteristic of ICA, a multivariate data analysis method without holistic nature is investigated for fault-induced impulse extraction in this study. Specifically, a part-based decomposition method by Non-Negative Matrix Factorization (NNMF) [126] is explored, developed and analyzed. Different from ICA, NNMF is a multivariate data analysis method that finds the non-negative factorization of a non-negative matrix [126]. The core difference between NNMF and ICA is the non-negativity constraint [126]. The non-negativity constraint makes the NNMF-decomposed components purely additive while allowing no subtractions, thus leading to a part-based representation [183]. Besides, studies show that NNMF emerges as a promising clustering method [184, 185]. Furthermore, Ding et al. [186] generalized the NNMF decomposition to bipartite graph clustering. Gao et al. [187] utilized the NNMF clustering property to enhance fault feature extraction and recognition of a bearing fault.

As constrained by NNMF, PMD signals need to be non-negative. In this study, the copula-based Time-Frequency energy Distribution (TFD) reported in Chapter 3 is employed as the PMD signals to NNMF for its characteristics of being positive and having high time-frequency resolution. Note that the PMD signals used in [124, 125, 180, 181]

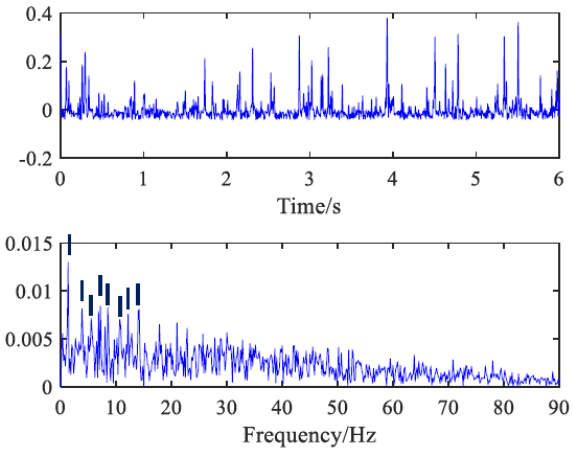

Fig. 4.2: Envelope waveform and spectrum of EEMD-ICA decomposed C1 for synthetic signal

as WT coefficients and IMFs have both positive and negative values, so they cannot be used for the NNMF decomposition. Besides, the bilinear TFD (e.g. Wigner-Ville distribution and Cohen's class distribution) and short-time Fourier transform are not employed to provide PMD signals in this study due to the negative values and the poor time-frequency resolution, respectively [143].

Consequently, the proposed method is on the strength of the copula-based positive TFD [143] and the non-negative NNMF decomposition [126]. As the occurring frequency suggests the proper extraction of transient fault-induced impulses [125], to address the performance of the proposed method on fault-induced impulse extraction, the performance measure employed in this study is the accuracy of the identification for the gear tooth fault characteristic frequency.

In Section 4.2, theoretical principles on copula-based TFD and NNMF decomposition are presented. The development of the proposed positive TFD-NNMF method for fault-induced impulse extraction from a one-dimensional vibration signal is given in Section 4.3. In Section 4.4, applications of the developed positive TFD-NNMF method on faulty simulated and experimental planetary gearbox vibration signals are studied to demonstrate its performance on the fault feature extraction. The performance of the EEMD-ICA method reported in [125] is presented as well for comparison purpose. In Section 4.5, discussions

on the sparsity representation is given to reveal the driving force leading to the advantage of the developed positive TFD-NNMF method over the reported EEMD-ICA method. At last, conclusions are given in Section 4.6.

4.2 Theoretical principles

In this section, we provide theoretical principles of copula-based TFD and NNMF decomposition as they are needed to develop the positive TFD-NNMF method for fault-induced impulse extraction from a one-dimensional vibration signal in Section 4.3. The copula-based TFD is to provide non-negative PMD signals and the NNMF decomposition serves for fault feature extraction through dimension reduction of the non-negative PMD signals.

4.2.1 Copula-based time-frequency distribution

Compared with linear TFDs and bilinear TFDs, copula-based TFDs have desirable properties of being positive, free from cross-term interference, having high time-frequency resolution and correct energy marginals [48]. The property of being positive meets the requirement of non-negativity for NNMF decomposition.

A copula-based TFD is constructed based on Sklar's theorem [115] which admits a joint TFD can be constructed by the time marginal, the frequency marginal, and a Time-Frequency Copula (TFC) [48]. The core for copula-based TFD construction is the TFC estimation. In [48], the TFC estimation is based on the marginals of the spectrogram of short-time Fourier transform. However, the spectrogram introduces the window influence on the constructed copula-based TFD, i.e., different windows produce different copula-based TFDs [48]. To alleviate the influence of the spectrogram on the copula-based TFD construction, as documented in Chapter 3, a TFC estimation based on the instantaneous energy and the energy spectral density rather than the spectrogram-based marginals is proposed. The copula model used in Chapter 3 is a non-parametric copula which is free from the assumption that the model structure is fixed with a particular distribution. In this

way, compared with a parametric copula [138], a non-parametric copula model provides a greater generality for the model estimation with less model error [143].

Procedures to construct a copula-based TFD for a vibration signal $x(t)$ are as follows as documented in Chapter 3:

1) To calculate the instantaneous energy $T(t)$ and the energy spectral density $F(f)$

$$T(t) = |x(t)|^2 \tag{4.1}$$

$$F(f) = |X(f)|^2 \tag{4.2}$$

where $X(f)$ is the Fourier transform of $x(t)$;

2) To generate rank-based pseudo-observations $O_i(T)$ and $O_i(F)$ for $T(t)$ and $F(f)$, respectively, by

$$O_i(T) = R_i(T(t))/(n+1) \tag{4.3}$$

$$O_i(F) = R_i(F(f))/(n+1) \tag{4.4}$$

where $R_i(T(t))$ and $R_i(F(f))$ are the ranks [145] associated with $T(t)$ and $F(f)$, respectively, in ascending order;

3) To find the optimal smoothing parameter h for the estimation of non-parametric copula density C_h [143];

4) To estimate the non-parametric copula density C_h by Eq. (4.5) with the rank-based pseudo-observations $O_i(T)$ and $O_i(F)$ and the optimal smoothing parameter h

$$C(u,v) = \frac{1}{n}\sum_{i=1}^{n} K(O_i(T), \frac{u}{h}+1, \frac{1-u}{h}+1)K(O_i(F), \frac{v}{h}+1, \frac{1-v}{h}+1) \tag{4.5}$$

where $K(x,\alpha,\beta) = x^{\alpha}(1-x)^{\beta}/B(\alpha,\beta)$ and $B(\alpha,\beta) = \int_0^1 t^{\alpha-1}(1-t)^{\beta-1}dt$;

5) To construct the copula-based TFD $p(t,f)$ with $T(t)$, $F(f)$ and C_h by Eq. (4.6).

$$p(t,f) = C_h(u,v) * T(t) * F(f) \tag{4.6}$$

After the copula-based TFD construction, NNMF can then be employed for fault feature extraction through dimension reduction of the copula-based TFD. Following contents give theoretical principles about NNMF.

4.2.2 Non-negative matrix factorization

Non-Negative Matrix Factorization (NNMF) is a multivariate analysis method by matrix factorization [126]. Matrix factorization decomposes a matrix $\boldsymbol{V} \in \mathbb{R}^{M \times N}$ into two matrices $\boldsymbol{W} \in \mathbb{R}^{M \times K}$ and $\boldsymbol{H} \in \mathbb{R}^{K \times N}$ as

$$\boldsymbol{V} \approx \boldsymbol{W}\boldsymbol{H} \tag{4.7}$$

Matrix multiplication as in Eq. (4.7) can be implemented by computing column vectors of $\boldsymbol{V}$ as linear combination of column vectors of $\boldsymbol{W}$ using coefficients in columns of $\boldsymbol{H}$, i.e., each column of $\boldsymbol{V}$ can be computed as

$$\boldsymbol{v}_j = \boldsymbol{W}\boldsymbol{h}_j \tag{4.8}$$

where $\boldsymbol{v}_j$ and $\boldsymbol{h}_j$ are the jth column of $\boldsymbol{V}$ and the jth column of $\boldsymbol{H}$, respectively. Following this idea, with the decomposition by Eq. (4.7), the interpretations to $\boldsymbol{W}$ and $\boldsymbol{H}$ are the decomposed component matrix and the expansion coefficient matrix, respectively. Columns of $\boldsymbol{V}$ and columns of $\boldsymbol{W}$ are the original components and the decomposed components, respectively.

NNMF estimates the component matrix and the expansion coefficient matrix by constraining the elements to be non-negative [183]. NNMF decomposition for a non-negative matrix $\boldsymbol{V}$ is achieved by solving the following minimization problem [126]:

$$\min_{\boldsymbol{W},\boldsymbol{H}} \quad \|\boldsymbol{V}-\boldsymbol{W}\boldsymbol{H}\|_F^2 \tag{4.9}$$

$$\text{subject to} \quad \boldsymbol{W} \geq 0, \boldsymbol{H} \geq 0 \tag{4.10}$$

where $\|\cdot\|_F^2$ is the squared Frobenius norm, i.e., $\|\boldsymbol{X}\|_F^2 = \text{trace}(\boldsymbol{X}^T\boldsymbol{X})$, $\boldsymbol{W} \in \mathbb{R}^{M \times K}$ and $\boldsymbol{H} \in \mathbb{R}^{K \times N}$ with $(M+N)K \ll MN$ for dimension reduction.

The non-negative constraint is what differentiates NNMF with the other matrix factorization methods such as PCA and ICA. Theoretical principles about PCA and ICA can be found in [126] with more details. The non-negative constraint leads to NNMF-decomposed

components with unique properties. Firstly, the non-negative constraint realizes the component estimation through pure additions, leading the NNMF decomposition to be part-based [183]. One benefit of part-based decomposition is the suppression on the information as in ICA-decomposed components which is introduced by the global-support characteristic but does not exist in the source of origin. Secondly, as a part-based decomposition, NNMF naturally produces sparse components [126], meaning that the decomposed components as columns in $\boldsymbol{W}$ are with few non-zero values. Thirdly, as suggested by Turkmen in [188], the interpretability of the NNMF-decomposed sparse components has a direct link to the NNMF clustering characteristic. As studied by Yoo and Choi [185], the non-zero values in columns of $\boldsymbol{W}$ can be interpreted as cluster centers as explained in the following with the probabilistic interpretation of $\boldsymbol{W}$.

To understand the clustering characteristic of NNMF, probabilistic interpretation of NNMF was given and elaborated by Gaussier and Goutte [189] and Ding et al. [190] with the equivalence between NNMF and probabilistic latent semantic indexing. Here a brief overview of this probabilistic interpretation of NNMF is given for a joint TFD.

Assuming t_i and f_j are conditionally independent given c_k [190], a joint TFD $p(t,f)$ can be factorized by [185]

$$p(t_i,f_j)=\sum_k p(t_i,f_j|c_k)p(c_k)=\sum_k p(t_i|c_k)p(f_j|c_k)p(c_k) \tag{4.11}$$

where $p(c_k)$ is the prior probability for clustering c_k. Relating Eq. (4.7) and Eq. (4.11), it can be noted that the probabilistic interpretation of elements v_{ij} in matrix $\boldsymbol{V}$ corresponds to $p(t_i,f_j)$; the probabilistic interpretation of element w_{ik} in matrix $\boldsymbol{W}$ corresponds to $p(t_i|c_k)$ representing the significance of t_i in clustering c_k and serving for basis vectors associated with cluster centers [185].

To reveal the probabilistic interpretation of element h_{kj} in matrix $\boldsymbol{H}$, Yoo and Choi [185] have the following derivation:

1) Applying sum-to-one normalization to each column of $\boldsymbol{W}$, i.e., $\boldsymbol{W}\boldsymbol{D}_{\boldsymbol{W}}^{-1}$ where $\boldsymbol{D}_{\boldsymbol{W}}=$

$\text{diag}(\mathbf{1}^T \boldsymbol{W})$ with $\mathbf{1} = [1, 1, \ldots, 1]^T$, an exact relation as Eq. (4.12) can be had

$$[\boldsymbol{W}\boldsymbol{D}_{\boldsymbol{W}}^{-1}]_{ik} = p(t_i|c_k) \tag{4.12}$$

2) Defining a scaling matrix $\boldsymbol{D}_{\boldsymbol{H}} = \text{diag}(\mathbf{1}^T \boldsymbol{H}^T)$ for sum-to-one normalization to each row of $\boldsymbol{H}$, i.e., $\boldsymbol{D}_{\boldsymbol{H}}^{-1}\boldsymbol{H}$, the factorization of Eq. (4.7) can be rewritten as

$$\boldsymbol{V} = (\boldsymbol{W}\boldsymbol{D}_{\boldsymbol{W}}^{-1})(\boldsymbol{D}_{\boldsymbol{W}}\boldsymbol{D}_{\boldsymbol{H}})(\boldsymbol{D}_{\boldsymbol{H}}^{-1}\boldsymbol{H}) \tag{4.13}$$

3) Relating Eq. (4.13) with Eq. (4.11), following relations can be marked

$$[\boldsymbol{D}_{\boldsymbol{W}}\boldsymbol{D}_{\boldsymbol{H}}]_{kk} = p(c_k) \tag{4.14}$$

$$[\boldsymbol{D}_{\boldsymbol{H}}^{-1}\boldsymbol{H}]_{kj} = p(f_j|c_k) \tag{4.15}$$

4) Applying Bayes' theorem, the following relation can be derived for the posterior probability of cluster $p(c_k|f_j)$

$$p(c_k|f_j) \propto p(f_j|c_k)p(c_k) = [\boldsymbol{D}_{\boldsymbol{W}}\boldsymbol{D}_{\boldsymbol{H}}]_{kk}[\boldsymbol{D}_{\boldsymbol{H}}^{-1}\boldsymbol{H}]_{kj} = [\boldsymbol{D}_{\boldsymbol{W}}\boldsymbol{H}]_{kj} \tag{4.16}$$

By Eq. (4.16), the probabilistic interpretation of element h_{kj} in matrix $\boldsymbol{H}$ corresponds to $p(c_k|f_j)$, the posterior probability of cluster, with the multiplication by the diagonal matrix $\boldsymbol{D}_{\boldsymbol{W}}$. The frequency marginal f_j is assigned to cluster k^* if [185]

$$k^* = arg\max_k [\boldsymbol{H}^T \boldsymbol{D}_{\boldsymbol{W}}]_{jk} \tag{4.17}$$

In this way, the dimension reduction of a joint TFD is achieved by the clustering of frequency marginal in matrix $\boldsymbol{H}$ while retaining the prototype components of time marginal with the cluster centers in matrix $\boldsymbol{W}$. Those cluster centers in $\boldsymbol{W}$ have the potential to highlight the localized features of interest, i.e., the fault-induced impulses, in the vibration signal analysis.

4.3 Development of proposed method with non-negative matrix factorization

In this section, the noisy synthetic signal generating Fig. 4.1 and Fig. 4.2 is employed to develop the positive TFD-NNMF method for fault feature extraction from a one-dimensional

vibration signal. As locations and the occurring frequency of transient oscillating impulses are known in the synthetic signal, it can serve well to exam the performance of the proposed positive TFD-NNMF method on the targeted transient impulse extraction by comparing positions of extracted impulses and the original positions of the added transient oscillating impulses.

Complementing the description of the noisy synthetic signal in Section 4.1, the function to generate oscillating impulses is given by Eq. (4.18) [142].

$$y = A\exp(-\xi f_r(t-t_c))\cos(2\pi f_r(t-t_c)) \tag{4.18}$$

where A denotes the maximum amplitude of the oscillating impulse; ξ is the damping ratio; f_r is the oscillating frequency; t_c is the time center of the oscillating impulse; and t starts from t_c. Eq. (4.18) generates the right half of the oscillating impulse starting from time instant t_c. To obtain the left half of the impulse, one needs to mirror the right half against the vertical line through t_c. Eq. (4.18) is a mathematical impulse signal model where the damping ratio ξ controls the lasting time of the impulse. Intuitively, with a local fault such as gear tooth crack, the impulse has a short lasting time, meaning that the damping ratio ξ has a big value; on the other hand, with a distributed fault like gear tooth pitting, the impulse has a longer lasting time, meaning that the damping ratio ξ has a smaller value.

Given values of A, ξ, and f_r are 1, 0.99, and 80, respectively, the waveform of a generated oscillating impulse is shown in Fig. 4.3 as centered at 0.4s. Fig. 4.4 shows the waveform of the noisy synthetic signal as described in Section 4.1 with impulses generated by Eq. (4.18).

It has been proved that signal pre-whitening by removing the predictable part of the signal can enhance the detection of fault-induced impulses from a vibration signal [172]. With this idea, we come to the NNMF decomposition for the copula-based TFD of the pre-whitened vibration signal rather than the original vibration signal. The technique used in this study to pre-whiten the vibration signal is the AR-MED method reported in [191]. AR and MED are short for Auto-Regressive and Minimum Entropy Deconvolution, respec-

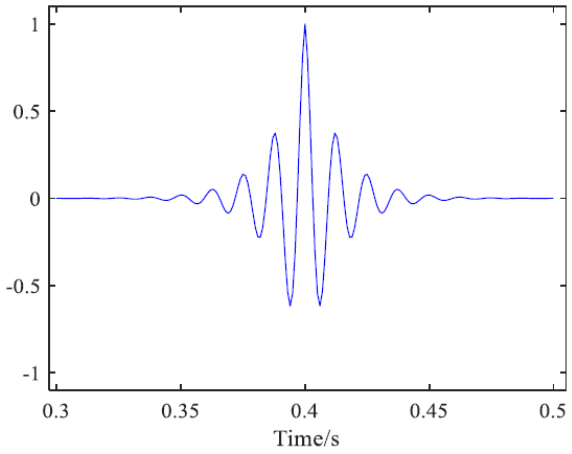

Fig. 4.3: Transient oscillating impulse

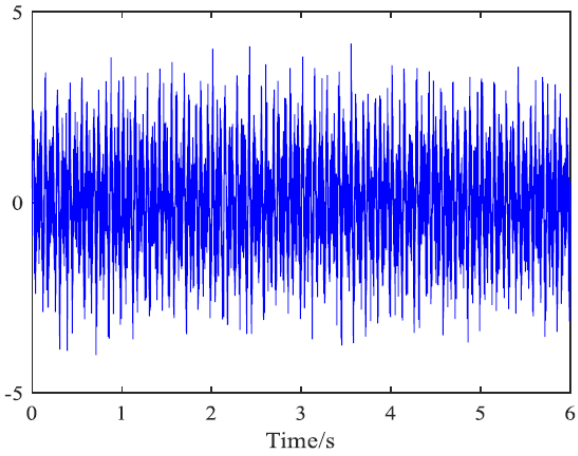

Fig. 4.4: Synthetic signal with 5dB SNR

tively [191].

For a TFD, its rows and columns represent the time waveforms at different frequency locations and the frequency spectra at different time instants, respectively [143]. As discussed in Subsection 4.2.2, a time-frequency matrix to be decomposed by NNMF should have time waveforms and frequency spectra as columns and rows, respectively. Consequently, the copula-based TFD is transposed for the decomposition by NNMF.

Fig. 4.5 shows waveforms of the decomposed components by NNMF decomposition for the transposed copula-based TFD of the pre-whitened noisy synthetic signal. Note that in this chapter the presentation of the copula-based TFD is omitted as it is generated by the standard construction procedure as presented in Subsection 4.2.1 [143]. The components in Fig. 4.5 are ordered with increasing sparsity. More details about sparsity are given in Section 4.5. To intuitively demonstrate its performance on transient oscillating impulse extraction, locations of the extracted transient impulses are marked in Fig. 4.5. From Fig. 4.5, following observations are had:

1) The number of decomposed components is 12, which is significantly reduced from 6001, the number of time waveforms in the original copula-based TFD. This is the result of the clustering in frequency marginal by NNMF decomposition as presented in Subsection 4.2.2;

2) With the cluster centers stored in $\boldsymbol{W}$ as explained in Subsection 4.2.2, the NNMF-decomposed components can highlight the transient impulses while suppressing the other vibrations;
3) The extracted transient impulses are located at 0.41s, 1.02s, 1.61s, 2.21s, 2.83s, 3.41s, 4.01s, 4.61s, 5.21s, and 5.81s as marked in Fig. 4.5. Comparing with the seeded positions as given in Section 4.1, the positions of extracted transient impulses are compatible well with the original seeded positions within the error of 0.01s to 0.03s;
4) With the part-based representation of NNMF decomposition, no individual NNMF-decomposed component can detect all the transient impulses. For example, C11 in Fig. 4.5 only contains the extracted impulses at 1.02s, 1.61s, and 5.21s;
5) On the other hand, with the part-based representation of NNMF decomposition, a transient impulse at a specific time instant would distribute in different NNMF-decomposed components. For example, extracted impulses at 1.61s are found in C2, C5, C6, C7, C9, C10, and C11 as shown in Fig. 4.5.

Consequently, multiple NNMF-decomposed components are needed to mutually support each other to extract all transient oscillating impulses. In this study, following the sum-to-one normalization as in the probabilistic interpretation of NNMF decomposition in Subsection 4.2.2, the sum-to-one normalization for each decomposed component is conducted and then all the normalized components are combined to generate an integrated signal for occurring frequency identification of transient oscillating impulses.

To identify the occurring frequency of transient oscillating impulses, the envelope analysis of the integrated signal is employed [125]. The envelope waveform and the envelope spectrum of the integrated signal are shown in Fig. 4.6. From Fig. 4.6, the sizable amplitudes in the envelope spectrum can be found at 1.687Hz, 3.375Hz, 5Hz, 6.625Hz, 8.312Hz, 10Hz, 11.62Hz, 13.37Hz, and 15Hz which agrees well with the occurring frequency of the seeded oscillating impulses (1.67Hz) and its harmonics (3.34Hz, 5.01Hz, 6.68Hz, 8.35Hz,

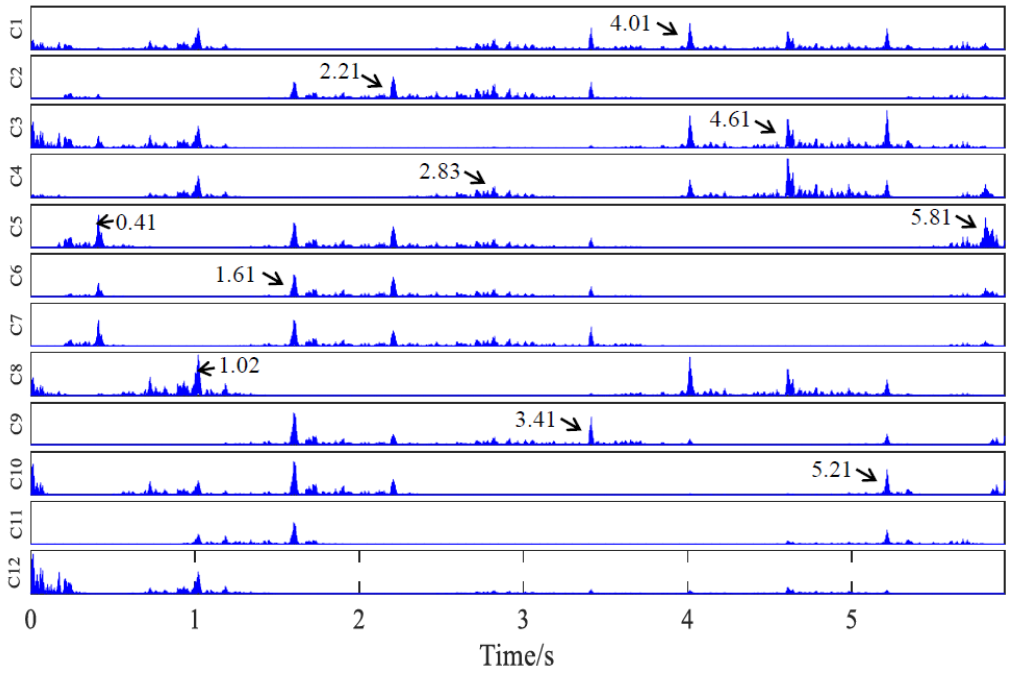

Fig. 4.5: Decomposed components by TFD-NNMF method for synthetic signal

10.02Hz, 11.69Hz, 13.36Hz, 15.03Hz) within the error of 0.075% to 1.05%.

Comparing the locations of sizable amplitudes in envelope spectra in Fig. 4.2 and Fig. 4.6, it can be concluded that the proposed positive TFD-NNMF method can better identify the occurring frequency of the transient oscillating impulses than the reported EEMD-ICA method in [125].

To summarize, the proposed positive TFD-NNMF method is with following procedures:

1) Pre-whiten the original vibration signal by the AR-MED method reported in [191];
2) Construct the copula-based TFD by the method documented in Chapter 3 for the pre-whitened vibration signal;
3) Transpose the copula-based TFD to have the columns of the matrix being time waveforms;
4) Apply the NNMF decomposition to the transposed TFD for fault-induced impulse extraction by the means of dimension reduction;

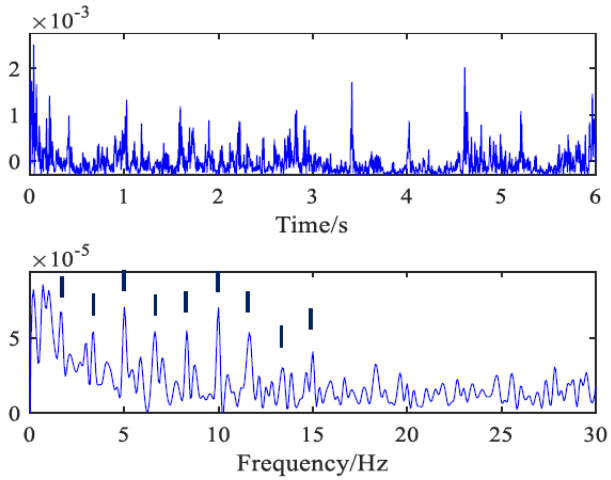

Fig. 4.6: Envelope waveform and spectrum obtained by TFD-NNMF for synthetic signal

5) Conduct the post-processing on the NNMF-decomposed components for fault feature extraction:

   (a) Conduct the sum-to-one normalization for each NNMF-decomposed component by the summation of elements in that component;

   (b) Add all sum-to-one normalized components to generate an integrated signal containing all extracted fault-induced impulses;

   (c) Analyze the envelop spectrum of the integrated signal for fault characteristic frequency identification, eventually leading to fault detection.

4.4 Applications to simulated and experimental planetary gearbox vibration signals

In this section, the proposed positive TFD-NNMF method as developed in Section 4.3 is applied to simulated planetary gear set vibration signals with different sun gear tooth crack levels and an experimental vibration signal with sun gear tooth crack. The simulated and the experimental vibration signals are filtered by a Chebyshev low-pass filter with cutoff frequency of 800Hz as in Chapter 3 to cover the low characteristic frequencies and the frequencies containing fault information with energy concentration. The simulated case

study and the experimental case study are used to demonstrate the performance of the proposed method on fault-induced impulse extraction for cases with different gear tooth fault levels and a real case, respectively, as measured by the accuracy in the fault characteristic frequency identification. The EEMD-ICA method reported in [125] is applied to the same vibration signals for comparison purpose. Note that as the vibration signal is pre-whitened in the proposed positive TFD-NNMF method, to be consistent in the data pre-processing, the same pre-whitened vibration signal is sued for the application of the reported EEMD-ICA method, i.e., the PMD signals of the pre-whitened vibration signal rather than the original vibration signal are generated by EEMD.

4.4.1 Simulated planetary gear set vibration signal analysis

4.4.1.1 Simulated vibration signal setup

The simulated planetary gear set has a power configuration with the sun gear and the carrier as the power input and the power output, respectively, and the ring gear fixed [27]. The physical parameters are shown in Table 3.1 where the number 4 in the parentheses is the number of planet gears. The input sun gear rotating speed and the torque applied on the carrier are 46.667r/min and 2367Nm, respectively [27]. The sun gear tooth crack starts from the gear root circle throughout the whole tooth width with a crack angle of 45° [27]. We call the crack level 50% crack when the crack line reaches the tooth central line as illustrated in Fig. 3.3. Two different sun gear tooth crack levels are considered in the simulated case study, namely 30% crack and 50% crack with crack length of 2.34mm and 3.90mm, respectively [143]. We denote 30% crack level case and 50% crack level case by Crack30 and Crack50, respectively, in the following contents. The simulated gear vibration sources are generated by the dynamic model in [27] and the resultant vibration signal is constructed by the modeling method as in Chapter 2. To mimic background noise, white Gaussian noise is added to simulated signals to have SNR being 25dB.

Fig. 4.7 shows waveforms and spectra of the original vibration signal and the pre-

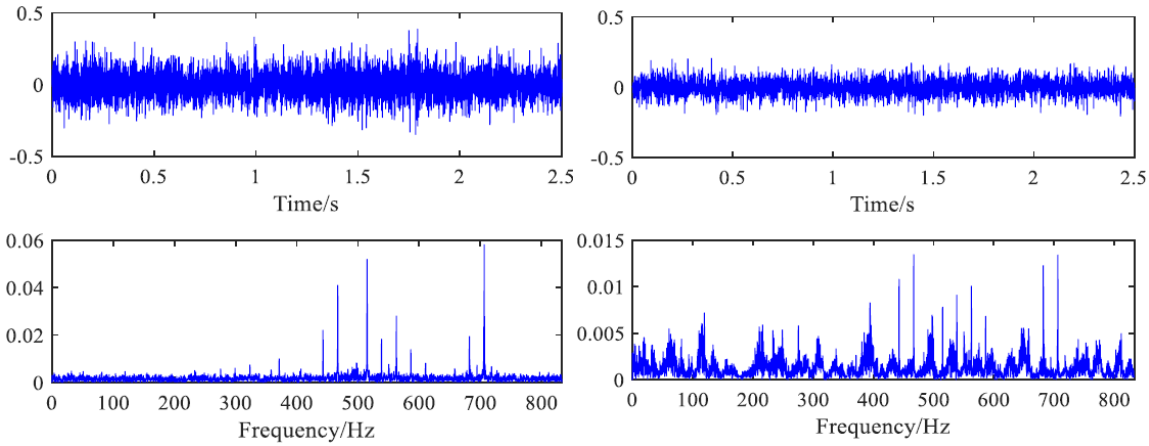

(a) The original (b) The pre-whitened

Fig. 4.7: Waveforms and spectra for simulated Crack30 case

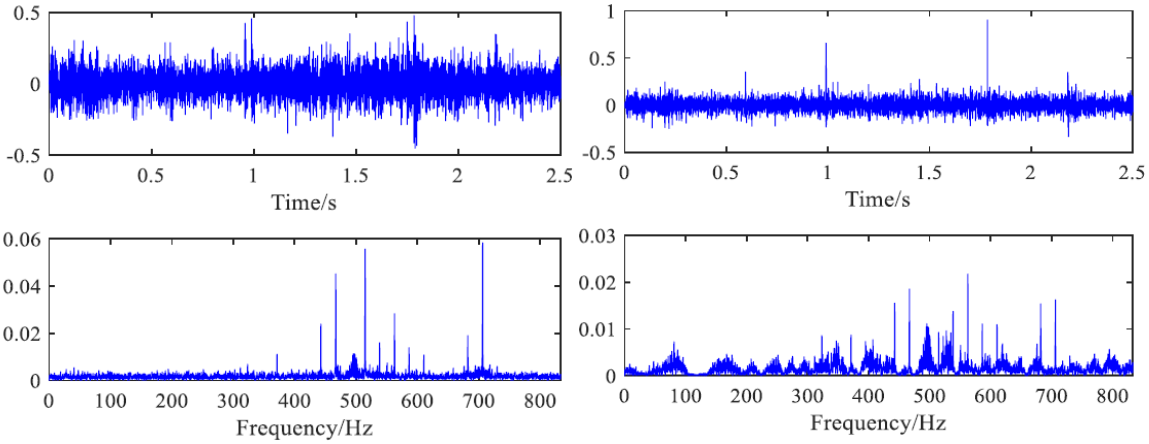

(a) The original (b) The pre-whitened

Fig. 4.8: Waveforms and spectra for simulated Crack50 case

whitened vibration signal for the simulated Crack30 case with Fig. 4.7(a) and Fig. 4.7(b), respectively. For the simulated Crack50 case, the waveforms and the spectra of the original vibration signal and the pre-whitened vibration signal are shown in Fig. 4.8(a) and Fig. 4.8(b), respectively. With the pre-whitened vibration signals ready for the simulated Crack30 case and the simulated Crack50 case, the proposed positive TFD-NNMF method is then applied for fault feature extraction. Meanwhile, for comparison purpose, the reported EEMD-ICA method in [125] is applied to the pre-whitened vibration signals as well. Then their performances on the fault feature extraction are compared in terms of the accuracy of

identifying the sun gear tooth crack characteristic frequency and its harmonics. Note that the sun gear tooth crack characteristic frequency is 2.52Hz as calculated in [142].

4.4.1.2 Results and performance comparison

Fig. 4.9 and Fig. 4.10 show waveforms of decomposed components for simulated Crack50 case by the developed positive TFD-NNMF method and the reported EEMD-ICA method, respectively. The components in Fig. 4.9 are ordered with increasing sparsity. The components in Fig. 4.10 are ordered with decreasing kurtosis. To identify the fault characteristic frequency by the proposed positive TFD-NNMF method, components in Fig. 4.9 are normalized and combined to generate the integrated signal as defined in Section 4.3; then the envelope analysis is conducted on the integrated signal. The envelope waveform and the envelope spectrum of the integrated signal with components in Fig. 4.9 are shown in Fig. 4.11(a). To identify the fault characteristic frequency by the reported EEMD-ICA method, as reported in [125], the envelope analysis is conducted on the decomposed component with the highest kurtosis value, i.e., the C1 in Fig. 4.10. The envelope waveform and the envelope spectrum of the C1 in Fig. 4.10 are shown in Fig. 4.11(b).

As shown in Fig. 4.11(a), the envelope spectrum obtained by the proposed positive TFD-NNMF method has sizable amplitudes at 2.50Hz, 5.11Hz, 7.61Hz, 10Hz, 12.71Hz, etc. for the simulated Crack50 case. As shown in Fig. 4.11(b), the envelope spectrum obtained by the reported EEMD-ICA method has sizable amplitudes at 2.40Hz, 5.21Hz, 7.61Hz, 10Hz, 12.4Hz, etc. for the simulated Crack50 case. Table 4.1 shows the comparison and errors of the frequency components with sizable amplitudes in Fig. 4.11 to the fault characteristic frequency (2.52Hz) and its harmonics up to the fifth order. The FC in Table 4.1 is short for Frequency Component. The numbers in the parentheses in Table 4.1 are the harmonic orders. As shown in Table 4.1, both the proposed positive TFD-NNMF method and the reported EEMD-ICA method can indicate the existence of the fault characteristic frequency and its harmonics with certain errors while the proposed positive TFD-

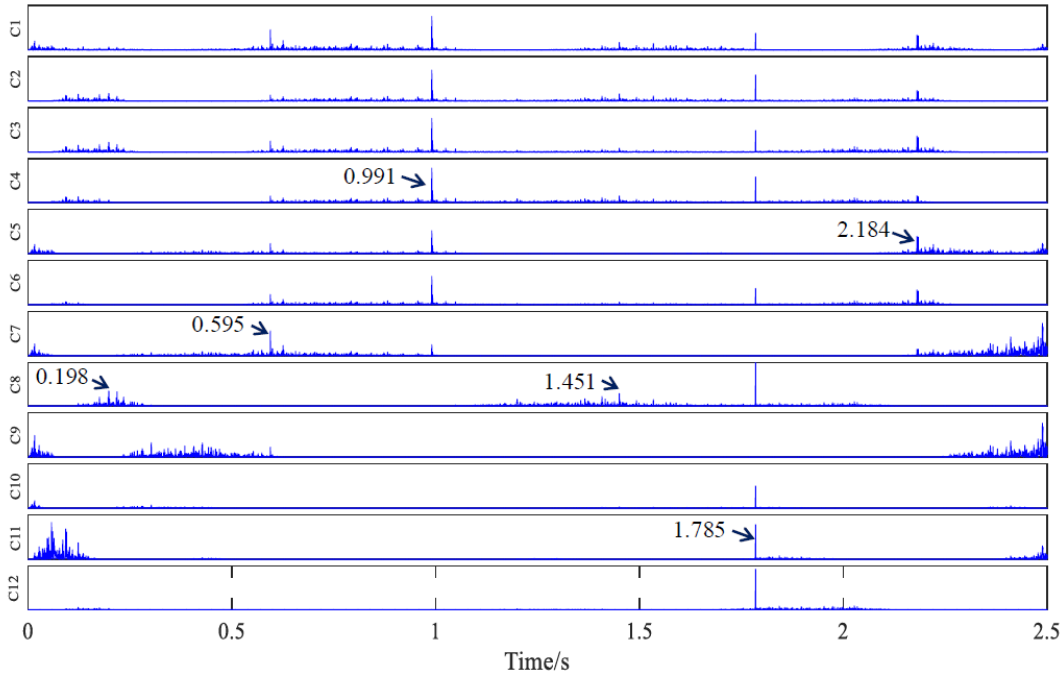

Fig. 4.9: Decomposed components by TFD-NNMF method for simulated Crack50 case

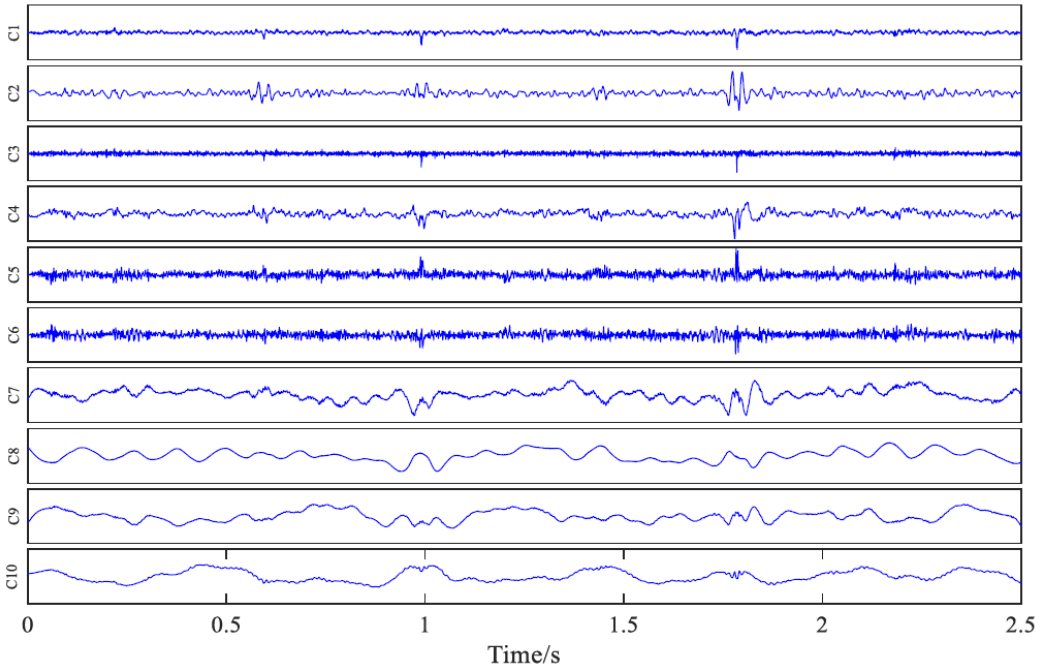

Fig. 4.10: Decomposed components by EEMD-ICA method for simulated Crack50 case

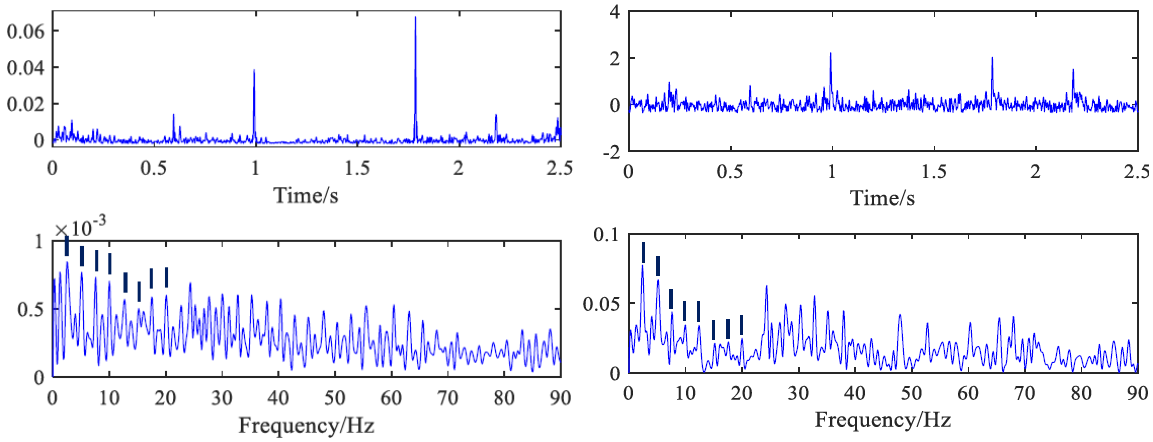

(a) By TFD-NNMF method

(b) By EEMD-ICA method

Fig. 4.11: Envelope waveforms and spectra for simulated Crack50 case

Table 4.1: Frequency components with sizable amplitudes for simulated Crack50 case

	Fault Characteristic Frequency and Harmonics				
FC/Hz	2.52(1)	5.04(2)	7.56(3)	10.08(4)	12.6(5)
	Proposed TFD-NNMF method				
FC/Hz	2.50	5.11	7.61	10	12.71
Error	0.79%	1.39%	0.66%	0.79%	0.87%
	Reported EEMD-ICA method				
FC/Hz	2.40	5.21	7.61	10	12.4
Error	4.76%	3.37%	0.66%	0.79%	1.59%

NNMF method has errors no greater than the reported EEMD-ICA method. Consequently, for the simulated Crack50 case, although both the proposed positive TFD-NNMF method and the reported EEMD-ICA method can identify the sun gear tooth crack fault characteristic frequency and its harmonics, the proposed positive TFD-NNMF method provides less error.

To demonstrate the performance of the proposed method for a case with smaller gear tooth fault, the simulated Crack30 case is analyzed. Fig. 4.12 and Fig. 4.13 show waveforms of decomposed components for simulated Crack30 case by the developed positive TFD-NNMF method and the reported EEMD-ICA method, respectively. Following the same procedure as in the simulated Crack50 case analysis, the envelope waveforms and the

envelope spectra obtained by the proposed positive TFD-NNMF method and the reported EEMD-ICA method are presented in Fig. 4.14(a) and Fig. 4.14(b), respectively.

Table 4.2 shows the comparison and errors of the frequency components with sizable amplitudes in Fig. 4.14 to the fault characteristic frequency (2.52Hz) and its harmonics up to fifth order. As shown in Table 4.2, the proposed positive TFD-NNMF method can properly identify the sun gear tooth crack characteristic frequency with an error of 0.79% while the reported EEMD-ICA method cannot identify the characteristic frequency with a great error of 42.82%. Moreover, for the identification of the first five harmonics, the proposed positive TFD-NNMF method has the mean error as 2.65% while the reported EEMD-ICA method has a larger mean error as 12.35%. Consequently, for the simulated Crack30 case, the reported EEMD-ICA method cannot detect the fault of sun gear tooth crack by identifying the fault characteristic frequency and its harmonics. On the other hand, the proposed positive TFD-NNMF method can detect the sun gear tooth crack by identifying the fault characteristic frequency and its harmonics with smaller errors, compared with the reported EEMD-ICA method.

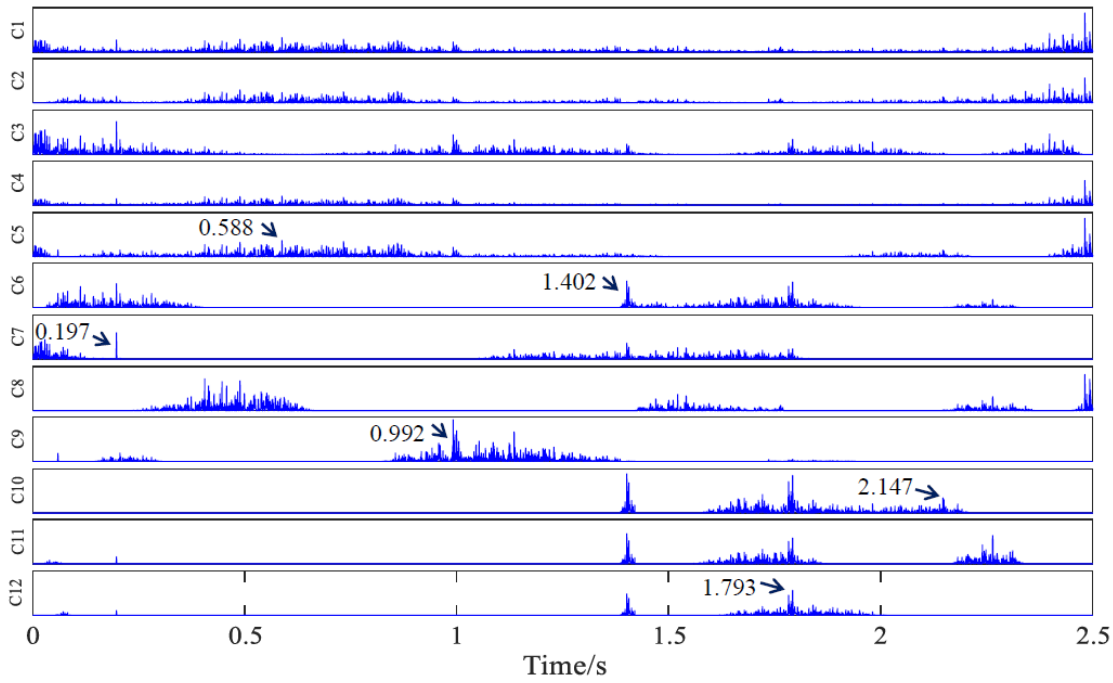

Fig. 4.12: Decomposed components by TFD-NNMF method for simulated Crack30 case

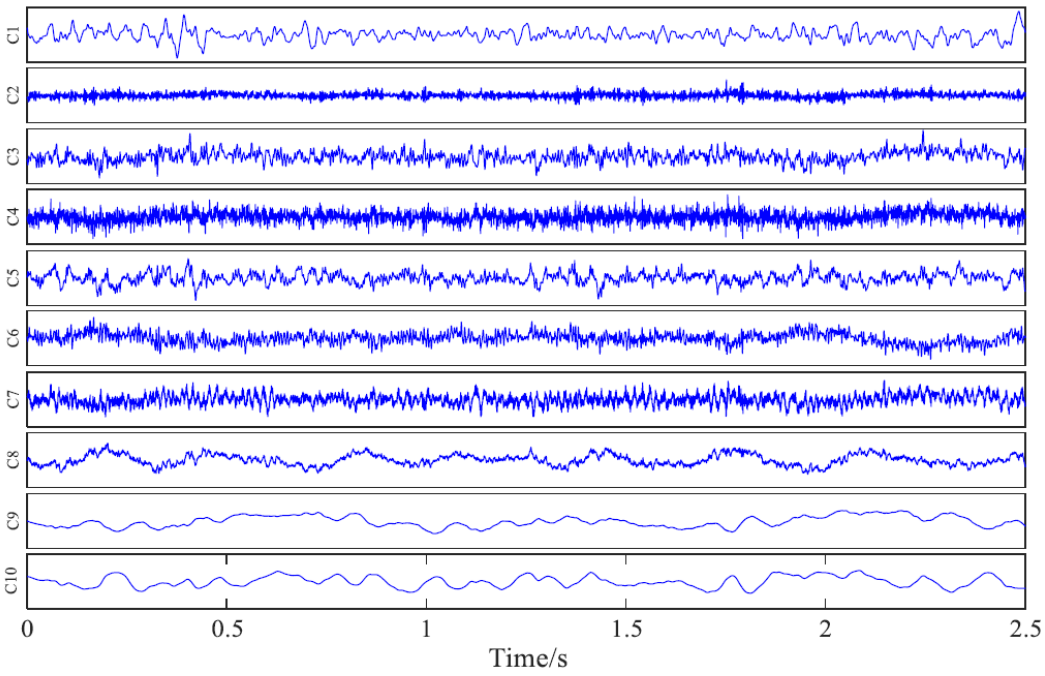

Fig. 4.13: Decomposed components by EEMD-ICA method for simulated Crack30 case

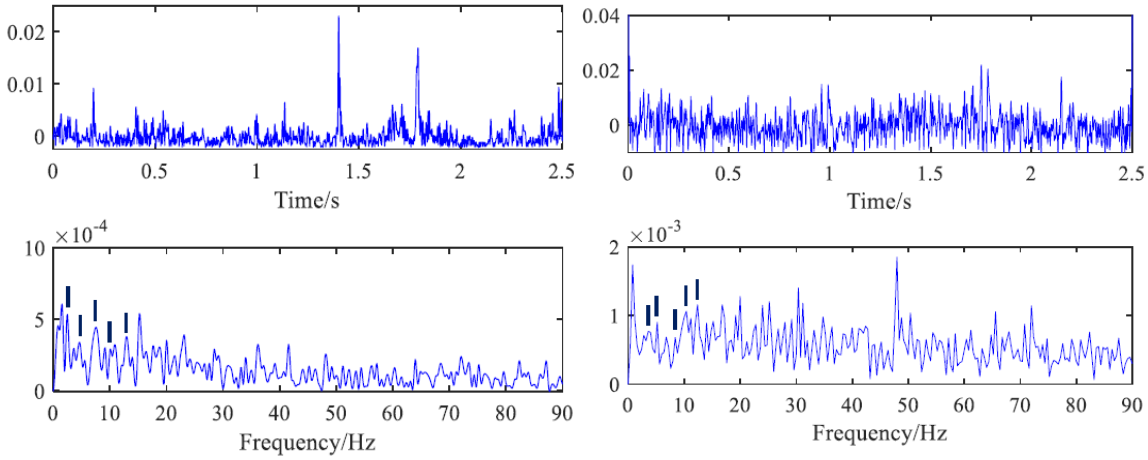

(a) By TFD-NNMF method

(b) By EEMD-ICA method

Fig. 4.14: Envelope waveforms and spectra for simulated Crack30 case

Table 4.2: Frequency components with sizable amplitudes for simulated Crack30 case

	Fault Characteristic Frequency and Harmonics				
FC/Hz	2.52(1)	5.04(2)	7.56(3)	10.08(4)	12.6(5)
	Proposed TFD-NNMF method				
FC/Hz	2.50	4.584	7.605	10.11	12.92
Error	0.79%	9.05%	0.60%	0.30%	2.54%
	Reported EEMD-ICA method				
FC/Hz	3.599	5.198	8.397	10.4	12.4
Error	42.82%	3.13%	11.07%	3.17%	1.59%

To summarize, through the analysis on the simulated signals with different sun gear tooth crack levels, i.e., the simulated Crack30 case and the simulated Crack50 case, results show that for the cases with a severe fault as in the simulated Crack50 case, the proposed positive TFD-NNMF method can identify the fault characteristic frequency and its harmonics with less errors than the reported EEMD-ICA method; for the cases with an early fault as in the simulated Crack30 case, the proposed positive TFD-NNMF method can achieve the fault detection by identifying the fault characteristic frequency and its harmonics while the reported EEMD-ICA method cannot do so.

4.4.2 Experimental planetary gearbox vibration signal analysis

4.4.2.1 Experimental test rig setup

The planetary gearbox test rig in the Reliability Research Lab at the University of Alberta has a layout as shown in Fig. 2.11. The planetary gearbox test rig has main components of a 20HP drive motor, a one-stage bevel gearbox, a two-stage planetary gearbox, two speed-up gearboxes, and a 40HP load motor. To isolate the planetary gearbox from the vibration interference from other components, there are three foundations for different test rig components: the drive motor is on the first foundation; the bevel gearbox and the planetary gearbox are on the second foundation; the two speed-up gearboxes and the load motor are on the third foundation.

For the two-stage planetary gearbox, all gears are spur gears without tooth profile mod-

ification. The second stage planetary gearbox has the same structure configuration and the same gear parameters with the simulated planetary gear set as given in Subsubection 4.4.1.1. The input rotational speed of the second stage planetary gearbox and the torque on the carrier are the same with those values in the simulated cases, i.e., 46.667r/min and 2367Nm, respectively [140]. An accelerometer was installed vertically on the casing of the second stage planetary gearbox for vibration signal acquisition. The acquired experimental vibration signal is subject to 50% sun gear tooth crack in the second stage planetary gearbox with a crack length of 3.9mm, acquired in the year of 2011 by former group members [170]. The sampling frequency was 5000Hz. The sun gear tooth crack is developed as modeled in Fig. 3.3 and physically shown in Fig. 3.10. Other gears are without gear tooth faults.

Fig. 4.15 shows the waveforms and the spectra of the acquired experimental vibration signal and the pre-whitened experimental vibration signal with Fig. 4.15(a) and Fig. 4.15(b), respectively. With the pre-whitened experimental vibration signal ready, the proposed positive TFD-NNMF method is applied for fault feature extraction. Meanwhile, for the purpose of comparison, the EEMD-ICA method reported in [125] is applied to the pre-whitened experimental vibration signal as well. The accuracies of identifying the sun gear tooth crack characteristic frequency by the proposed positive TFD-NNMF method and the reported EEMD-ICA method are then compared.

4.4.2.2 Results and performance comparison

The decomposed components of the pre-whitened experimental vibration signal by the developed positive TFD-NNMF method and the reported EEMD-ICA method are shown in Fig. 4.16 and Fig. 4.17, respectively. Following the same procedure as in the simulated case study, the envelope waveforms and the envelope spectra obtained by the positive TFD-NNMF method and the EEMD-ICA method are illustrated in Fig. 4.18(a) and Fig. 4.18(b), respectively.

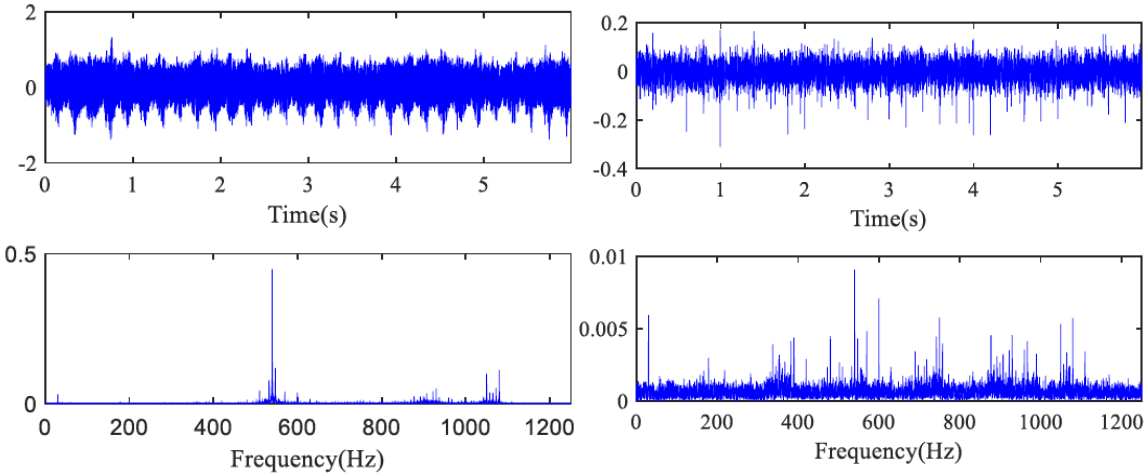

(a) The original (b) The pre-whitened

Fig. 4.15: Waveforms and spectra for experimental signal

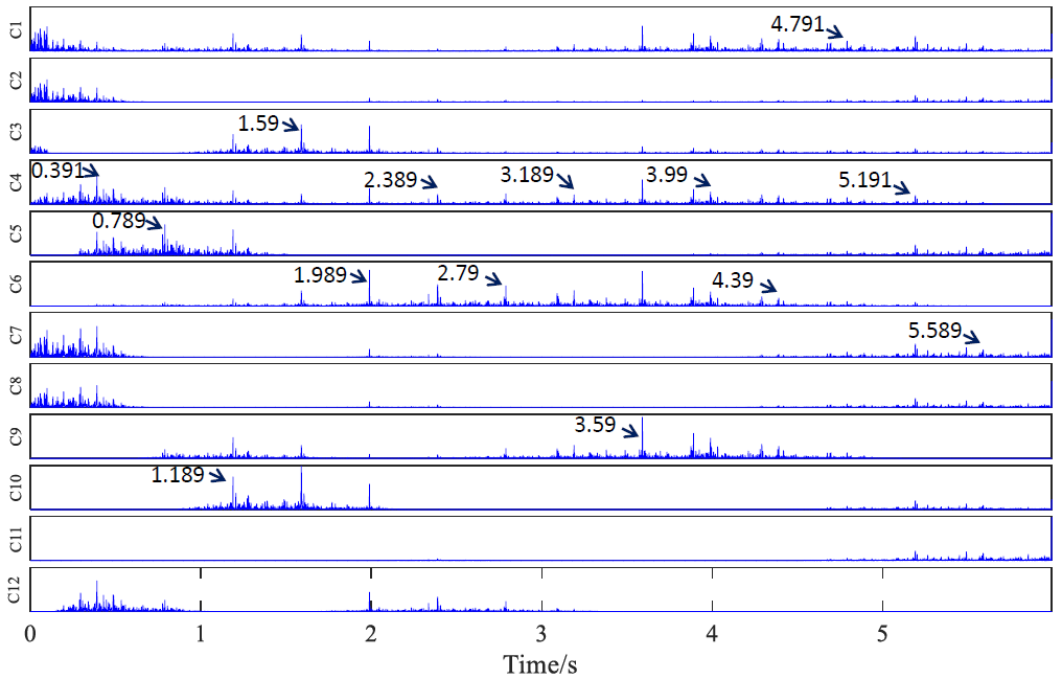

Fig. 4.16: Decomposed components by TFD-NNMF method for experimental signal

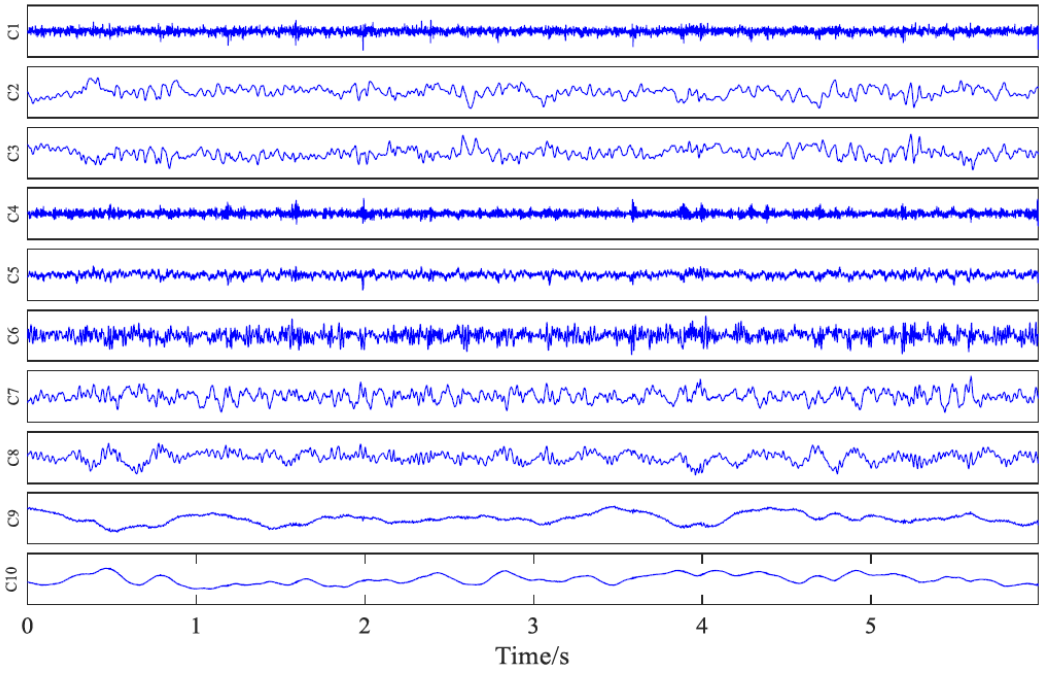

Fig. 4.17: Decomposed components by EEMD-ICA method for experimental signal

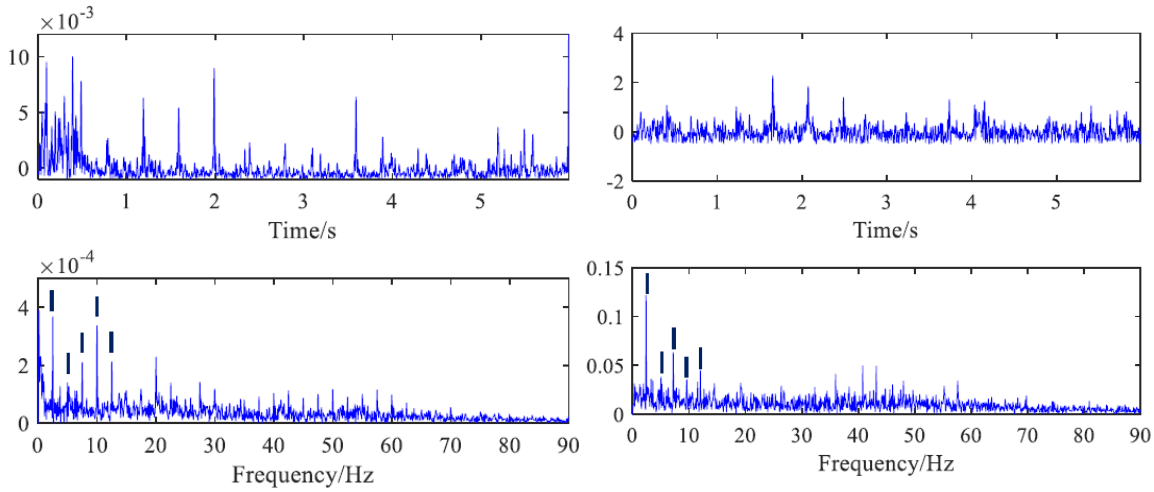

(a) By TFD-NNMF method

(b) By EEMD-ICA method

Fig. 4.18: Envelope waveforms and spectra for experimental signal

Table 4.3: Frequency components with sizable amplitudes for experimental case

	Fault Characteristic Frequency and Harmonics				
FC/Hz	2.52(1)	5.04(2)	7.56(3)	10.08(4)	12.6(5)
	Proposed TFD-NNMF method				
FC/Hz	2.50	5	7.5	10	12.5
Error	0.79%	0.79%	0.79%	0.79%	0.79%
	Reported EEMD-ICA method				
FC/Hz	2.40	5.1	7.2	9.6	12
Error	4.76%	1.19%	4.76%	4.76%	4.76%

Table 4.3 shows the comparison and errors of the frequency components with sizable amplitudes in Fig. 4.18 to the fault characteristic frequency (2.52Hz) and its harmonics to the fifth order. As shown in Table 4.3, both the proposed positive TFD-NNMF method and the reported EEMD-ICA method can identify the fault characteristic frequency and its harmonics with certain errors while the proposed TFD-NNMF method has smaller errors than the reported EEMD-ICA method. Consequently, for the experimental case with 50% sun gear tooth crack, it can be concluded that although both the proposed positive TFD-NNMF method and the reported EEMD-ICA method can identify the sun gear tooth crack characteristic frequency and its harmonics, the proposed positive TFD-NNMF method has less errors than the reported EEMD-ICA method. Future experiments under various levels of load, speed, and gear tooth fault can be conducted to check the performance of the developed positive TFD-NNMF method on fault detection for cases with different operation conditions and/or fault levels.

4.5 Discussion

To reveal the driving force of the proposed positive TFD-NNMF method to a better performance on fault feature extraction, a discussion on the sparsity of the decomposed components by the positive TFD-NNMF method and the EEMD-ICA method is presented in this section for simulated vibration signals. As introduced in Subsection 4.2.2, NNMF naturally

produce sparse components with part-based representation and the clustering property. A sparse representation encodes much of the data using few non-zero values [192]. To evaluate the sparsity of a decomposed component, Eq. (4.19) from [192] is employed

$$\text{sparsity}(\boldsymbol{x}) = \frac{\sqrt{n} - (\sum |x_i|)/\sqrt{\sum x_i^2}}{\sqrt{n} - 1} \tag{4.19}$$

where n is the length of vector $\boldsymbol{x}$ and x_i is the ith element of vector $\boldsymbol{x}$. Eq. (4.19) evaluates to unity if and only if $\boldsymbol{x}$ contains only a single non-zero component, and takes a value of zero if and only if all components are with same absolute value [192].

In this section, besides simulated Crack30 case and simulated Crack50 case as involved in Subsection 4.4.1, simulated Crack00 case, i.e., the simulated perfect case without sun gear tooth crack, is analyzed as well. With the three simulated cases, the sparsity changes with different gear tooth health conditions from the perfect condition to different gear tooth fault levels can be revealed. Specifically, sparsity values of decomposed components by the reported EEMD-ICA method and the proposed positive TFD-NNMF method for the three simulated cases are shown in Table 4.4. Note that the numbers of decomposed components are not necessarily to be the same for different cases. In this analysis, the numbers of decomposed components by the EEMD-ICA method for Crack00, Crack30, and Crack50 are 6, 10, and 10, respectively, while the numbers of decomposed components by the positive TFD-NNMF method for the three cases are all 12. Thus, in Table 4.4, we have N/As for C7-C12 of Crack00 in the third column and N/As for C11-C12 of Crack30 and Crack50 in the fourth column and the fifth column, respectively.

As NNMF decomposition naturally leads to a sparse representation with part-based representation and clustering property while ICA does not [126], from Table 4.4, it can be noticed that decomposed components by positive TFD-NNMF method have greater sparsity than decomposed components by EEMD-ICA method for each crack level case.

For decomposed components by the positive TFD-NNMF method for different crack level cases, as shown in Table 4.4, it can be noted that an individual NNMF-decomposed

Table 4.4: Sparsity of decomposition components for simulated signals

Components	Method	Crack00	Crack30	Crack50	Method	Crack00	Crack30	Crack50
C1	EEMD-ICA	0.234	0.245	0.281	TFD-NNMF	0.547	0.54	0.662
C2		0.237	0.23	0.343		0.548	0.547	0.673
C3		0.215	0.214	0.248		0.561	0.567	0.674
C4		0.258	0.223	0.282		0.577	0.583	0.681
C5		0.215	0.224	0.255		0.583	0.596	0.706
C6		0.162	0.21	0.24		0.61	0.679	0.717
C7		N/A	0.211	0.236		0.654	0.684	0.726
C8		N/A	0.177	0.202		0.676	0.703	0.728
C9		N/A	0.151	0.179		0.712	0.741	0.746
C10		N/A	0.156	0.134		0.749	0.762	0.817
C11		N/A	N/A	N/A		0.75	0.777	0.834
C12		N/A	N/A	N/A		0.8	0.806	0.879

component of a higher crack level case does not necessarily have higher sparsity than a NNMF-decomposed component of a lower crack level case. For example, the first NNMF-decomposed component of Crack30 case has a lower sparsity (0.54) than the first component of Crack00 case (0.547). To better reflect the sparsity change with different sun gear tooth crack levels of NNMF-decomposed components, the average sparsity of components decomposed by the positive TFD-NNMF method is calculated for each sun gear tooth crack level. The plot of the average sparsity versus the sun gear tooth crack level is given in Fig. 4.19. Meanwhile, the average sparsity of decomposed components by the EEMD-ICA method for each sun gear tooth crack level is calculated and plotted as well in Fig. 4.19.

As shown in Fig. 4.19, the same observation can be noticed as from Table 4.4 that the decomposed components by the positive TFD-NNMF method have greater sparsity than the decomposed components by the EEMD-ICA method. Moreover, based on the results suggested by Fig. 4.11, Fig. 4.14, and Fig. 4.19, we can conclude that the driving force of the proposed positive TFD-NNMF method to a better performance on the fault feature extraction over the reported EEMD-ICA method in [125] is the sparse representation with

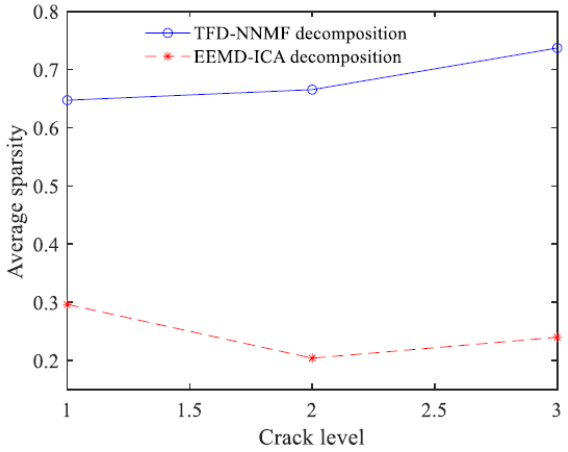

Fig. 4.19: Average sparsity plot with different crack levels

greater sparsity. As introduced in Subsection 4.2.2, the sparse representation by NNMF decomposition is related with the part-based representation, suppressing the disturbing information existing in ICA-decomposed components as introduced by the global-support characteristic, and the clustering property, enhancing the fault feature extraction by highlighting the localized fault-induced impulses.

Additionally, as NNMF decomposition is related with sparse representation intrinsically, the average sparsity of the decomposed components by the positive TFD-NNMF method is closely related to the sun gear tooth crack level, i.e., the monotonically increasing trend as shown in Fig. 4.19, for the simulated vibration signals. On the other hand, as ICA does not lead to sparse representation, the average sparsity of the decomposed components by the EEMD-ICA method has no monotonic trend with the growth of the sun gear tooth crack level as shown in Fig. 4.19. Consequently, besides the identification of the fault characteristic frequency, with the sparse representation of NNMF decomposition, the proposed positive TFD-NNMF method can also provide the average sparsity of the decomposed components to serve as a health condition indicator for planetary gearbox fault detection. Note that due to the uncertainty factors in experimental data, variability may exist in the changing trend of the average sparsity with growing crack levels. Further study with experimental vibration signals of different fault levels need to be conducted for

variability analysis.

4.6 Conclusions

In this chapter, a novel fault feature extraction method is developed based on part-based decomposition on Pseudo-Multi-Dimensional (PMD) signals of a one-dimensional vibration signal for planetary gearbox fault detection. Specifically, the developed fault feature extraction method is based on positive Time-Frequency energy Distribution (TFD) and Non-Negative Matrix Factorization (NNMF). The positive TFD is constructed with the copula theory. Waveforms at different frequency components are treated as PMD signals for input to NNMF. Fault feature extraction is achieved through dimension reduction of PMD signals by NNMF with part-based decomposition. To evaluate the performance of the developed positive TFD-NNMF method on fault feature extraction, its applications for simulated and experimental planetary gearbox vibration signals with sun gear tooth cracks are analyzed. The simulated vibration signals are obtained with different sun gear tooth crack levels to evaluate the performance in cases with different fault levels, and experimental vibration signal analysis is used to demonstrate the performance for a real faulty case. The accuracy of the developed method in identifying fault characteristic frequency is compared with the accuracy obtained by the reported EEMD-ICA method. The results show that the developed positive TFD-NNMF method have higher accuracy than the reported EEMD-ICA method for the analyzed cases, suggesting that the developed positive TFD-NNMF method can serve better for planetary gearbox fault detection with more accurate fault characteristic frequency identification.

It is revealed that the driving force behind the better fault feature extraction performance of the positive TFD-NNMF method over the EEMD-ICA method is its sparser representation. The sparse representation of the positive TFD-NNMF method is related to part-based representation subject to the non-negative constraint and the clustering property with probabilistic interpretation. The part-based representation can suppress the generation

of nonexistent information in the original signal, and the clustering property can enhance fault feature extraction by highlighting localized fault-induced impulses with cluster centers. Moreover, the average sparsity of the components decomposed by the positive TFD-NNMF method can serve as a condition indicator for planetary gearbox fault detection, as it has a monotonically increasing trend with the growth of the gear tooth fault levels.

The developed positive TFD-NNMF method in this chapter is achieved by dimension reduction of the copula-based TFD in Chapter 3, which is based on the dependence between the instantaneous energy and the energy spectral density. The studies in Chapter 3 and Chapter 4 indicate the potential of dependence analysis in planetary gearbox fault diagnosis. Inspired by this indication, in the following study in Chapter 5, dependence analysis is further extended to develop a dependence-based feature vector for planetary gearbox fault classification. Specifically, the dependence is between the raw vibration signal and its EEMD-decomposed Intrinsic Mode Functions (IMFs).

Chapter 5

A dependence-based feature vector and its application for planetary gearbox fault classification

The studies reported in Chapter 3 and Chapter 4 suggest the potential of dependence analysis in planetary gearbox fault diagnosis. In this chapter, we extend dependence analysis to develop a dependence-based feature vector for planetary gearbox fault classification, the fourth research topic, as indicated in Fig. 1.12. Specifically, we focus on the dependence between the raw vibration signal and its Intrinsic Mode Functions (IMFs) decomposed by Ensemble Empirical Mode Decomposition (EEMD). EEMD is a self-adaptive algorithm for decomposing a one-dimensional signal to IMFs. The self-adaptation indicates that there is a dependence between the raw signal and the IMFs. The gist of this study is that, with different faults, different fault-induced impulses will be excited, which will be distributed differently to IMFs by EEMD decomposition, leading to different dependences between the raw vibration signal and IMFs. The dependence between the raw signal and each IMF is investigated by parametric Archimedean copulas. Using a goodness-of-fit test, the copula with the best dependence estimation is selected to represent the dependence by its parameter. Then the parameter of the selected copula is used to develop the dependence-based feature vector for planetary gearbox fault classification.

The organization of this chapter is as follows. In Section 5.1, an introduction to features with statistical extraction approaches is presented. Section 5.2 gives fundamentals

and theories on EEMD, copula theory, and Support Vector Machine (SVM). In Section 5.3, the proposed dependence-based feature vector is developed with simulated vibration signal analysis. The simulated signals are generated with the vibration signal modeling method described in Chapter 2. In Section 5.4, application of the developed feature vector is studied on planetary gearbox fault classification with different faulty experimental planetary gearbox vibration signals by an SVM classifier. Its advantage over a reported feature is addressed in terms of SVM classification accuracy. Discussion and conclusions are presented in Section 5.5 and Section 5.6, respectively. Results of this chapter are documented in an accepted journal paper [146] submitted to *Journal of Sound and Vibration* for publication.

5.1 Introduction

With gear faults, corresponding fault signatures are introduced into vibration signals [193]. By effective signal processing methods, features to represent the fault signatures can be extracted to indicate possible faults [83, 194], serving as Condition Indicators (CIs) in the field of machinery fault detection and fault diagnosis.

To date, various features have been reported as CIs by different statistical extraction approaches in the literature. The conventional features can be calculated from the time waveform and the frequency spectrum, such as skewness, shape factor, kurtosis, crest factor, frequency center, standard deviation frequency, and so on [29]. As these conventional features are well established, their descriptions are omitted. One who are interested can refer to [29] for detailed information. However, due to the complexity of a planetary gearbox vibration signal [140], it is difficult to classify the location or the severity of a fault in a planetary gearbox through the conventional features as CIs [195]. Consequently, more sophisticated algorithms for advanced CIs have received intensive investigation in recent years, such as algorithm combining fast Dynamic Time Warping (fast DTW) and Correlated Kurtosis (CK) techniques and the windowing and mapping strategy for gear tooth fault detection reported in [83] and [66], respectively, and the Accumulative Amplitudes of

Carrier Orders (AACOs) reported in [91] which is designed specifically for planetary gearboxes. However, for the algorithm reported in [83], the gear fault location identification is based on the analysis on a residual signal which is obtained by the absolute difference between the warped signals of the measured signal and the estimated reference signal. The performance of the algorithm highly depends on the estimated reference signal. Only when the accuracy and appropriate usage of the estimated reference signal are guaranteed, can the superiority of the method be highlighted [196]. As for the windowing and mapping strategy reported in [66], besides the complicated algorithm for windowing and mapping, its accuracy depends on the window function selection with a trade-off at the computational cost [80]. The AACO in [91] is based on the fault mechanism investigation and the observation that the gear characteristic frequencies in a planetary gearbox are integer multiples of the carrier rotating frequency. For a planetary gearbox with the ring gear fixed, characteristic frequencies of the planetary gearbox are given as follows in terms of the carrier rotating frequency [1]: $f_p = (N_p - N_r)f_c/N_p$, $f_s = (N_r + N_s)f_c/N_s$, $f_r = 0$, $f_m = N_r f_c$, and $f_{p-p} = M_p f_c$, where N_p, N_r, and N_s are the numbers of teeth of the planet gear, the ring gear, and the sun gear, respectively; M_p is the number of planet gears; f_p, f_s, f_r, and f_c are the rotating frequencies of the planet gear, the sun gear, the ring gear, and the carrier, respectively; f_m is the meshing frequency of the planetary gearbox; f_{p-p} is the passing frequency of planet gears. By the above equations, it can be noticed that f_r, f_m, and f_{p-p} are integer multiples of f_c while f_p and f_s are not integer multiples of f_c if N_r/N_p and N_r/N_s are not integers. Thus, the AACO may not work as well as presented in [91] for fault detection and fault diagnosis of a planetary gearbox whose N_r/N_p and N_r/N_s are not integers. Therefore, it is desirable to develop new features that are able to better extract the health status information from a vibration signal. In this chapter, this concern will be addressed and investigated with a novel signal processing method, aiming at developing a feature vector with more health status information to better serve planetary gearbox fault detection and fault diagnosis. The developed feature vector is expected to detect the existence of a

fault and diagnose fault position and fault level.

Specifically, the targeted feature vector is on the strength of Ensemble Empirical Mode Decomposition (EEMD) and tail dependence between the raw vibration signal and the EEMD-decomposed Intrinsic Mode Functions (IMFs). Different from orthogonal decomposition methods like Fourier transform and Wavelet transform, EEMD is an iterative data driven method that does not imply orthogonality amongst the decomposed IMFs and the raw signal [182], which results in a possible dependence between the raw signal and the IMFs [197]. In probability theory, the tail dependence describes the co-movement of variables in distribution tails [138]. For example, if we have two variables U and V, the upper (lower) tail dependence means that with large (small) values of U, large (small) values of V are expected. By intuitive understanding, when a fault-induced transient impulse is introduced in a vibration signal, the transient impulse will distribute in the EEMD-decomposed IMFs, i.e., more extreme values in the raw signal means more chance to observe extreme values in IMFs. Thus, there is a possible tail dependence between the raw vibration signal and the IMFs. Besides, different faults introduce different transient impulses which distribute differently in the IMFs, meaning that different faults correspond to different tail dependences. Consequently, if we could capture and describe the different tail dependences properly, novel features can be developed with the potential to achieve machinery fault detection and fault diagnosis.

To describe the tail dependence, copulas are used. A copula is an alternative to correlation for dependence description [198]. More powerful, copulas contain information about the joint behavior of variables in distribution tails, i.e., tail dependence, which correlation cannot describe [165]. For a parametric copula, the copula parameter works as the coefficient to describe the tail dependence [138]. As different faults correspond to different tail dependences, copula parameters have different values accordingly. Following the above logic and hypothesis, the targeted novel feature vector is developed with the parameter of a parametric copula.

Once the dependence-based feature vector is developed, next concern is the objective measure to its performance in machinery fault detection and fault diagnosis. To address this concern, its application on planetary gearbox fault classification as a pattern recognition problem is conducted. For a pattern recognition problem, various classification methods have been reported, such as Artificial Neural Network (ANN) [199], decision tree [200], and Support Vector Machine (SVM) [201]. Given a specific classification method, the classification accuracy is affected by its input [202]. To compare classification accuracies with different inputs, a classification method should be specified. In this study, SVM method is employed. The more useful information about the health status the input has the higher classification accuracy the SVM can obtain. The proposed dependence-based feature vector serves as the input to SVM to check the classification accuracy. For comparison, the reported AACO designed specifically for planetary gearbox fault diagnosis in [91] and an AACO-based feature vector are input into the same SVM model. Classification accuracies by the SVM model, as the objective performance measure, with different inputs are then compared to demonstrate the advantage of the proposed dependence-based feature vector.

In Section 5.2, fundamentals and theories on EEMD, copula theory, and SVM are reviewed. The development of the targeted dependence-based feature vector is given in Section 5.3 with simulated planetary gear set vibration signal analysis. After the development of the proposed feature vector, its application on experimental planetary gearbox vibration signal classification is studied with a multi-class SVM in Section 5.4. The performance of alternatives which are the AACO reported in [91] and the AACO-based feature vector is studied as well. The accuracies are compared to highlight the advantage of the developed dependence-based feature vector. At last, discussions and conclusions are given in Section 5.5 and Section 5.6, respectively.

5.2 Fundamentals and theory

In this section, fundamentals of EEMD theory and copula theory are provided as they are needed for development of the proposed feature vector in Section 5.3. The EEMD is used to decompose the raw vibration signal into IMFs and the copula is used to describe the tail dependence between the raw signal and each IMF. The SVM method is presented since it is used to provide classification accuracies with different inputs in Section 5.4, serving as the objective measure to indicate the health status information included in the different inputs.

5.2.1 Ensemble empirical mode decomposition

Empirical Mode Decomposition (EMD), developed by Huang et al. [203], is first reviewed as it is the fundamental of EEMD. Essentially, EMD is an adaptive signal decomposition method to decompose a signal into Intrinsic Mode Functions (IMFs) [204]. IMFs are oscillatory functions with varying amplitude and frequency, satisfying two conditions [182]: 1) Throughout the whole length of an IMF, the number of extrema and the number of zero-crossings must either be equal or differ at most by one; 2) At any data location, the mean value of the envelope defined by the local maxima and the envelope defined by the local minima is zero. By EMD, a time series $x(t)$ can be decomposed into

$$x(t) = \sum_{i=0}^{n} c_i + r_n \tag{5.1}$$

where c_i is the ith IMF and r_n is the residue of $x(t)$ after n IMFs are extracted. EMD is implemented by the following sifting process using local extrema [204]:

1) Initialize: let $r_0(t) = x(t)$ and $i = 1$;
2) Extract the ith IMF;
   (a) Initialize: let $j = 0$ and $h_{ij}(t) = r_{i-1}(t)$;
   (b) Find the local minima and the local maxima of $h_{ij}(t)$;
   (c) Interpolate the local minima and the local maxima by cubic spline to construct the lower envelope and the upper envelope of $h_{ij}(t)$;

(d) Calculate the local mean $m_{ij}(t)$ of the lower envelope and the upper envelope;

(e) Update: $h_{ij}(t) = h_{ij} - m_{ij}(t)$;

(f) Repeat step (2.b) to step (2.e) until the envelopes are symmetric with zero mean. The final $h_{ij}(t)$ is designated as the ith IMF $c_i(t)$, i.e., $c_i(t) = h_{ij}(t)$;

3) Let $r_i(t) = r_{i-1}(t) - c_i(t)$;

4) Let $i = i + 1$ and return to step 2) until the residual $r_i(t)$ becomes a monotonic function from which no more IMFs can be extracted.

The EMD works as an effective self-adaptive dyadic filter bank for a white noise series [182]. However, when the data series is of intermittency as a mixture of intermittent high-frequency oscillations riding on a continuous lower-frequency signal, the dyadic property of EMD is compromised, leading to mode mixing [182]. To overcome the mode mixing, EEMD was developed in [182].

The EEMD is a noise-assisted data analysis method taking advantage of statistical properties of white noise [182]. Adding white noise with finite amplitude could provide a uniformly distributed reference scale. When a signal is added to this uniformly distributed white noise background, the component in different scales of the signal are projected onto proper scales of the white noise, which collates the component of the signal with comparable scale into one IMF [182]. In this way, the drawback of mode mixing of EMD is overcome. Different white noises with finite amplitude are added to the signal for different trials. By the ensemble mean of enough trials, the noise can be averaged out. Detailed procedures of EEMD are as follows [205]:

1) Set the number of trials and the amplitude of zero-mean white noise;

2) Generate white noise series and add it to the signal;

3) Decompose the composite signal with the white noise into IMFs by EMD;

4) Return to Step 2) and redo Step 3) for the predefined number of trials. Each trial is with different white noise of the same amplitude;

5) Calculate the ensemble mean of corresponding IMFs obtained above as the final result.

The final standard deviation of error ε_n introduced by the added white noise follows the statistical rule [182]

$$\varepsilon_n = \varepsilon/\sqrt{N} \tag{5.2}$$

where N is the number of trials and ε is the amplitude of the added noise. To make EEMD effective in the extrema change with negligible standard deviation of error, the amplitude of the added noise can be set as 0.2 times the standard deviation of the signal and the number of trials can be set as a few hundred, as suggested in [182].

Another concern about EEMD is that the EEMD-decomposed components are not necessarily IMFs as the EEMD involves summation of numerous IMFs [182]. To address this concern, a post-processing method with another round of EMD is reported in [182]. Specifically, EMD is applied to the combination of the first two components obtained from EEMD. The first IMF from EMD is treated as the desired IMF. Then the summation of the remainder and the next component from the EEMD is decomposed by EMD again where the remainder is calculated as the difference between the combination and the desired IMF. This process is carried out consecutively until all the EEMD-decomposed components are traversed through.

5.2.2 Copula theory

5.2.2.1 Copulas

Copula, first proposed by Sklar [115], is a mathematical theory to describe the dependence between random variables [138]. A copula $\boldsymbol{C}$ is a function from $[0,1]^2$ to $[0,1]$ with the following properties [112]:

1) $\boldsymbol{C}(u,0) = \boldsymbol{C}(0,v) = 0$ for all $(u,v) \in [0,1]^2$;
2) $\boldsymbol{C}(u,1) = u$ and $\boldsymbol{C}(1,v) = v$ for all $(u,v) \in [0,1]^2$;

3) For all $(u_1,u_2,v_1,v_2)\in[0,1]^4$ with $u_1\leqslant u_2$ and $v_1\leqslant v_2$, it has

$\boldsymbol{C}(u_2,v_2)$-$\boldsymbol{C}(u_1,v_2)$-$\boldsymbol{C}(u_2,v_1)$+$\boldsymbol{C}(u_1,v_1)\geqslant 0$;

4) For all $(u,v)\in[0,1]^2$, $\max(u+v-1,0)\leqslant\boldsymbol{C}(u,v)\leqslant\min(u,v)$

To describe the tail dependence between the raw vibration signal and the EEMD-decomposed IMFs, parametric Archimedean copulas are used in this study as they have distinct upper and lower tail dependence coefficients [206] with simple mathematical forms. The function of an Archimedean copula is in the form of [138]

$$\boldsymbol{C}(u,v)=\phi^{-1}(\phi(u)+\phi(v)) \tag{5.3}$$

where $\phi:(0,1]\rightarrow[0,+\infty)$ is a decreasing convex function with $\phi(1)=0$ and $\phi(0)=+\infty$. The function ϕ is called the generator. Archimedean copulas used in this study are Frank copula, Clayton copula, and Gumbel-Hougaard (GH) copula, which can qualitatively show different tail dependences [138]. Specifically, Frank copula has no tail dependence while Clayton copula and GH copula have lower tail dependence and upper tail dependence, respectively, as shown in Fig. 5.1. Table 5.1 gives the function $\boldsymbol{C}_\theta(u,v)$, generator $\phi_\theta(t)$, and the range of parameter θ for each of the three Archimedean copulas.

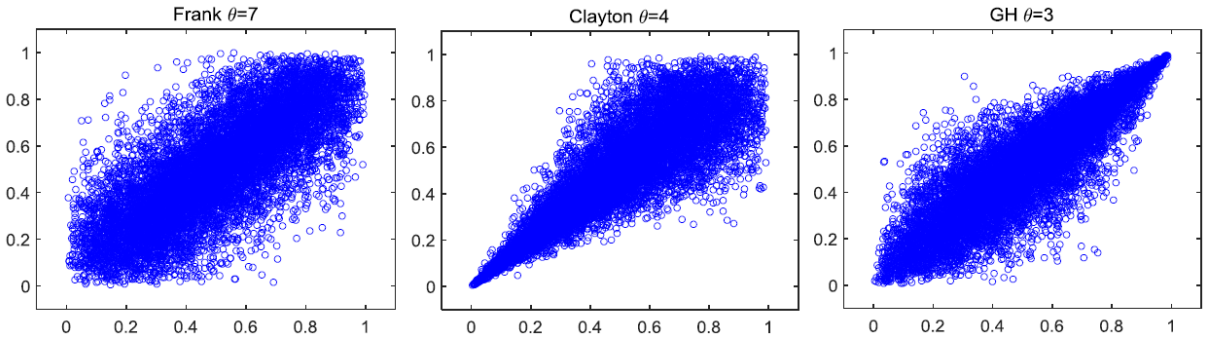

Fig. 5.1: Tail dependences represented by Archimedean copulas

5.2.2.2 Copula parameter estimation

Suppose we have data samples (X,Y), for dependence analysis by copulas, it is recommended to use rank pairs (R,S) associated with the data samples (X,Y) [138]. The rank

Table 5.1: Functions, generators, and parameter ranges of Archimedean copulas

Copula	$\boldsymbol{C}_\theta(u,v)$	$\phi_\theta(t)$	Range of θ
Frank	$-\frac{1}{\theta}\ln(1+\frac{(e^{-\theta u}-1)(e^{-\theta v}-1)}{e^{-\theta}-1})$	$-\ln\frac{e^{\theta t}-1}{e^{\theta}-1}$	$(-\infty,\infty)\backslash\{0\}$
Clayton	$(\max(u^{-\theta}+v^{-\theta}-1,0))^{-1/\theta}$	$(t^{-\theta}-1)/\theta$	$[-1,\infty)\backslash\{0\}$
GH	$\exp(-[(-\ln u)^{\theta}+(-\ln v)^{\theta}]^{1/\theta})$	$(-\ln t)^{\theta}$	$[1,\infty)$

pairs guarantee a unique copula which is invariant with the monotone transformation of data samples [165]. To obtain rank pairs (R,S), following equations are used [138]

$$R(i) = X(i)/(n+1) \tag{5.4}$$

$$S(i) = Y(i)/(n+1) \tag{5.5}$$

where n is the number of data samples in X or Y. Note that the number of data samples in X is the same as the number of data samples in Y.

With rank pairs (R,S) ready, the Matlab command "copulafit" is used to estimate coefficients of the three Archimedean copulas by Maximum Likelihood Estimation (MLE) method.

5.2.2.3 Goodness-of-fit test

Statistically, the goodness-of-fit describes how well an estimated model fits a set of data samples. In this study, QQ plot [165], short for quantile-quantile plot, is used to conduct the goodness-of-fit test for copula estimations. A quantile in the QQ plot means the percentage of points below the given value, for example the 0.3 quantile is the point where 30% of the data fall below and 70% fall above. Specifically, the QQ plot is made by plotting the pairs $(W_{i:n}, W_{(i)})$ [138] where $W_{(1)} \leqslant W_{(2)} \leqslant \cdots \leqslant W_{(n)}$ is the order statistics associated with $W_i = \frac{1}{n}\#\{j : X(j) \leqslant X(i), Y(j) \leqslant Y(i)\}$ and $W_{i:n}$ is given by

$$W_{i:n} = n\binom{n-1}{i-1}\int_0^1 w\{K_\theta(w)\}^{i-1}(1-K_\theta(w))^{n-i}dK_\theta(w) \tag{5.6}$$

In statistics, the ith order statistic is equal to the ith-smallest value in the sample. For Archimedean copulas, $K_\theta(w)$ is formulated as [138]

$$K_\theta(w) = w - \frac{\phi(w)}{\phi'(w)} \tag{5.7}$$

where $\phi(w)$ is the Archimedean copula generator and $w \in (0,1)$.

In the QQ plot, a reference diagonal line ($W_{i:n} = W_{(i)}$) is plotted to represent the perfect fit [138]. As a fitness measure of an estimated copula to the dependence between data samples, the average distance of the curve regarding the copula estimation to the reference diagonal line is calculated. The average distance is defined as the mean of the absolute difference of point coordinates on the curve. The shorter the average distance is the better fitness the estimated copula provides.

5.2.3 Support vector machine

SVM is a machine learning algorithm for pattern recognition to categorize data into different classes based on optimization theory [207]. The basic SVMs are originally developed to tackle binary classification problems. Consider a binary classification problem with training data as $\{(\boldsymbol{z}_1, y_1), (\boldsymbol{z}_2, y_2), \ldots, (\boldsymbol{z}_n, y_n)\}$ where $\boldsymbol{z}_i \in \mathbb{R}^m$ is the ith input data and $y_i \in \{1, -1\}$ is the class label associated with $\boldsymbol{z}_i$. If the training data are linearly separable, a separating plane can be found in the input space which is expressed by [29]

$$f(\boldsymbol{z}) = \boldsymbol{w}^T \boldsymbol{z} + b = \sum_{j=1}^{m} w_j z_j + b = 0 \tag{5.8}$$

where $\boldsymbol{w} \in \mathbb{R}^m$ is a weight vector; b is a scalar; and T means the transpose operator.

Fig. 5.2 demonstrates a linearly separable classification problem in a two-dimensional space. The solid squares and the solid circles on the boundaries $\boldsymbol{w}^T \boldsymbol{z} + b = \pm 1$ are called support vectors. All training data are constrained by the following inequality for the ideal without misclassification

$$y_i f(\boldsymbol{z}_i) = y_i(\boldsymbol{w}^T \boldsymbol{z} + b) \geq 1 \quad \text{for } i = 1, 2, \ldots, m \tag{5.9}$$

The distance between boundaries is called margin. Given the boundaries in Fig. 5.2, the margin can be calculated quantitatively by

$$d = \frac{|1-(-1)|}{\|\boldsymbol{w}\|} = \frac{2}{\|\boldsymbol{w}\|} \tag{5.10}$$

where $\|\boldsymbol{w}\|$ is the 2-norm of $\boldsymbol{w}$, defined as $\|\boldsymbol{w}\| = \sqrt{(w_1)^2 + (w_2)^2 + \cdots + (w_m)^2}$.

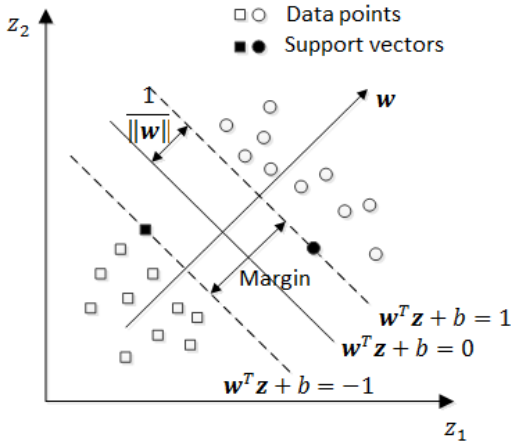

Fig. 5.2: Linear separation with SVM

To obtain the optimal separating plane, SVM employs an optimization process that maximizes margin and minimizes noise with slack variables [29]. Slack variables are used to relax constraints by considering points that fail the margin requirement as defined by Eq. (5.9). It allows a soft margin classification which ignores a few noise data to reduce the boundary complexity. Mathematically, the optimization problem is defined as [29]

$$\text{Minimize} \quad \frac{1}{2}\|\boldsymbol{w}\|^2 + q\sum_{i=1}^{m}\xi_i \tag{5.11}$$

$$\begin{aligned} \text{subject to} \quad & y_i(\boldsymbol{w}^T\boldsymbol{z}_i + b) \geq 1 - \xi_i,\ i = 1, 2, \ldots, m \\ & \xi_i \geq 0 \end{aligned} \tag{5.12}$$

where q is a positive constant serving as penalty parameter to define the trade-off between the misclassification and boundary complexity; ξ_i is the slack variable representing the distance of a data point of misclassification to the boundary of its true class. This optimization problem can be solved by Lagrangian method by introducing Lagrange multipliers α_i

and β_i. Its solution process can be found in [10]. After obtaining the solutions to α_i, $\boldsymbol{w}$, and b, the decision function is given by [29]

$$l_f = \text{sign}(\sum_{i=1}^{m} \alpha_i y_i (z_i^T z) + b) \tag{5.13}$$

where (z_i, y_i) is the ith training data pair; z is the a new input data; l_f is the label assigned by SVM to the new input data z; and sign(A) is the sign function of A which is defined as

$$\text{sign}(A) = \begin{cases} -1 & if\ A < 0 \\ \\ 1 & if\ A > 0 \end{cases} \tag{5.14}$$

When the given data are not linearly separable, Eq. (5.13) is no longer appropriate. To handle non-linearly separable data, a mapping strategy is introduced to project the original input data to a feature space where the features can be linearly separated. Fig. 5.3 shows an illustration of feature mapping from a two-dimensional input space to a two-dimensional feature space using a mapping function $\Phi(\cdot)$.

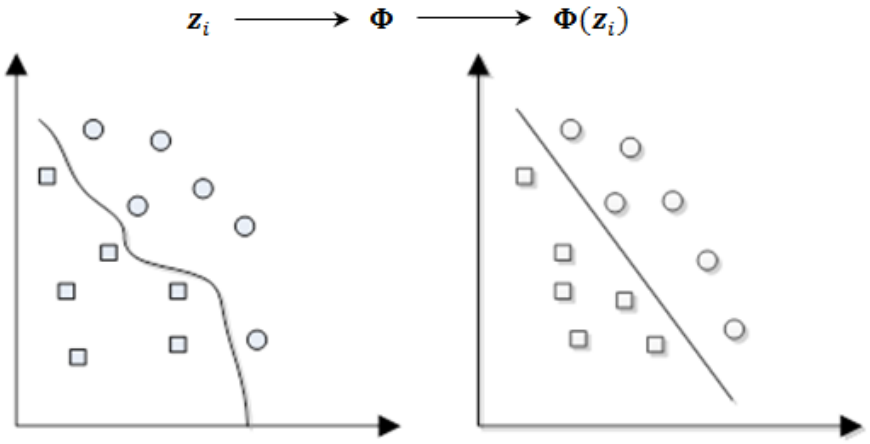

Fig. 5.3: Feature mapping enabling non-linear separation with SVM

With the feature mapping, the non-linear decision function is given with a similar form with Eq. (5.13) by [29]

$$l_f = \text{sign}(\sum_{i=1}^{m} \alpha_i y_i (\Phi^T(z_i)\Phi(z)) + b) \tag{5.15}$$

By applying a kernel function $K(z_i, z) = \Phi^T(z_i)\Phi(z)$ which satisfies Mercer's theorem [208], the explicit form of $\Phi(\cdot)$ can be avoided since only the inner product of $\Phi^T(z_i)\Phi(z)$

is needed in Eq. (5.15) [29]. Several kernel functions are available in the literature such as linear kernel, polynomial kernel, and Gaussian kernel [29]. With a kernel function, the non-linear decision function is given by

$$l_f = \text{sign}(\sum_{i=1}^{m} \alpha_i y_i K(z_i, z) + b) \tag{5.16}$$

To solve a multi-class pattern recognition problem, a multi-class SVM model disintegrates the multi-class problem into several binary problems [207]. Methods like one-versus-one, one-versus-all, and direct acyclic graph have been reported, among which the one-versus-one method is the most effective one with good generalization ability and less training period [209]. Consequently, one-versus-one method is adopted to solve the multi-class SVM classification problem in this study.

For a problem with N classes, $N(N-1)/2$ binary SVMs are constructed by one-versus-one method, where each SVM is trained with the data from two classes [207]. For a new input data z to be classified, a max wins voting strategy is applied [207], in which if $(\text{SVM})_{ij}$ decides z to be in the ith class, the vote for the ith class is added by one; otherwise, the vote for the jth class is added by one. This process is being conducted for all $N(N-1)/2$ binary SVMs. Eventually, the new input data z is predicted to be in the class with maximum votes.

5.3 Development of the proposed feature vector by simulated vibration signal analysis

In this section, to develop the proposed feature vector, simulated planetary gear set vibrations with different sun gear tooth crack levels are analyzed. With vibration sources generated by the dynamic model in [27], the simulated vibrations are constructed by the modeling method reported in Chapter 2 and then filtered by a Chebyshev low-pass filter with a cutoff frequency of 800Hz as in Chapter 3 and Chapter 4. The raw simulated vibration signals are decomposed into IMFs by EEMD. Then the tail dependence between the raw vibration signal and each IMF is analyzed by Archimedean copulas. Based on the de-

pendence analysis, the dependence-based feature vector is developed for planetary gearbox fault detection and fault diagnosis.

5.3.1 Simulated planetary gear set vibration signal

The simulated planetary gear set has the sun gear and the carrier as the power input and the power output, respectively, with the ring gear fixed [27]. Its physical parameters are shown in Table 3.1. The number 4 in the parentheses is the number of planet gears. The input rotational speed, i.e., the sun gear rotating speed, is constant at 46.667r/min and the load torque applied on the carrier is 2367Nm [27]. The sun gear tooth crack starts from the gear root circle with a crack angle of 45° along the whole tooth width. When the crack line reaches the tooth central line as demonstrated in Fig. 3.3, we call it 50% crack and denote it as Crack50. Three sun gear tooth crack levels are considered in this study, namely perfect, 10% crack and 50% crack with crack lengths of 0mm, 0.78mm and 3.90mm, respectively [23]. To mimic background noise, white Gaussian noise is added to simulated signals. For robustness analysis of the developed feature vector to noise interference, two noisy cases are considered with signal-to-noise ratios (SNRs) being 10dB and 5dB.

Fig. 5.4 shows the noisy vibration signals with SNR10 and SNR05 for the simulated Crack50 case where we omit the other simulated cases to save article length. As an example to show EEMD-decomposed IMFs, Fig. 5.5 shows the first 4 IMFs of the noisy vibration signal for the simulated Crack50 case with SNR05. With the raw vibration signal and IMFs ready, the tail dependence between the raw vibration signal and each IMF is analyzed to develop the targeted feature vector.

It is noteworthy that the targeted tail dependence regards the vibration strength but is regardless of the vibration direction. For the waveform of a vibration signal, the positive and negative signs indicate the vibration directions and the amplitudes suggest the vibration strength. Thus, in this study, the signal squared is applied to get the instantaneous vibration energy as the vibration strength for the tail dependence analysis. Alternatively, one also can

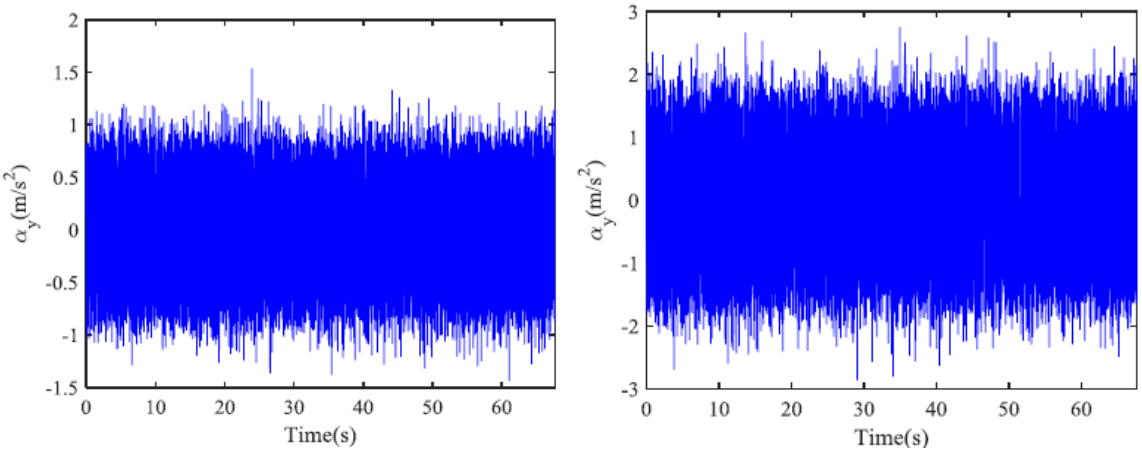

(a) SNR10 case (b) SNR05 case

Fig. 5.4: Noisy signals for simulated Crack50 case

apply the absolute values for the tail dependence analysis. The rational is that the signal squared and the absolute values are monotone transformation to each other while the tail dependence is invariant with the monotone transformation [145].

5.3.2 Tail dependence analysis

5.3.2.1 Copula model selection

With copula candidates as the three Archimedean copulas, namely Frank copula, Clayton copula, and GH copula, the coefficient of each copula candidate is estimated for the raw vibration signal and each IMF by the Matlab command "copulafit" with rank pairs associating with data samples. Then, to exam the fitness of estimated copulas to the tail dependence between data samples, goodness-of-fit test by QQ plot is conducted and the average distance of the curve regarding the estimated copula to the reference diagonal line is calculated. The copula with the shortest distance among the three copula candidates is selected to describe the tail dependence. Its coefficient is used to develop the targeted feature vector. As an example, Fig. 5.6 shows QQ plots regarding the first 4 IMFs of the raw vibration for simulated Crack50 case with SNR05. The average distance to the reference diagonal line is presented as well in Fig. 5.6 for each copula model. The result shows the GH copula provides the best fitness with the shortest average distance for the Crack50 case

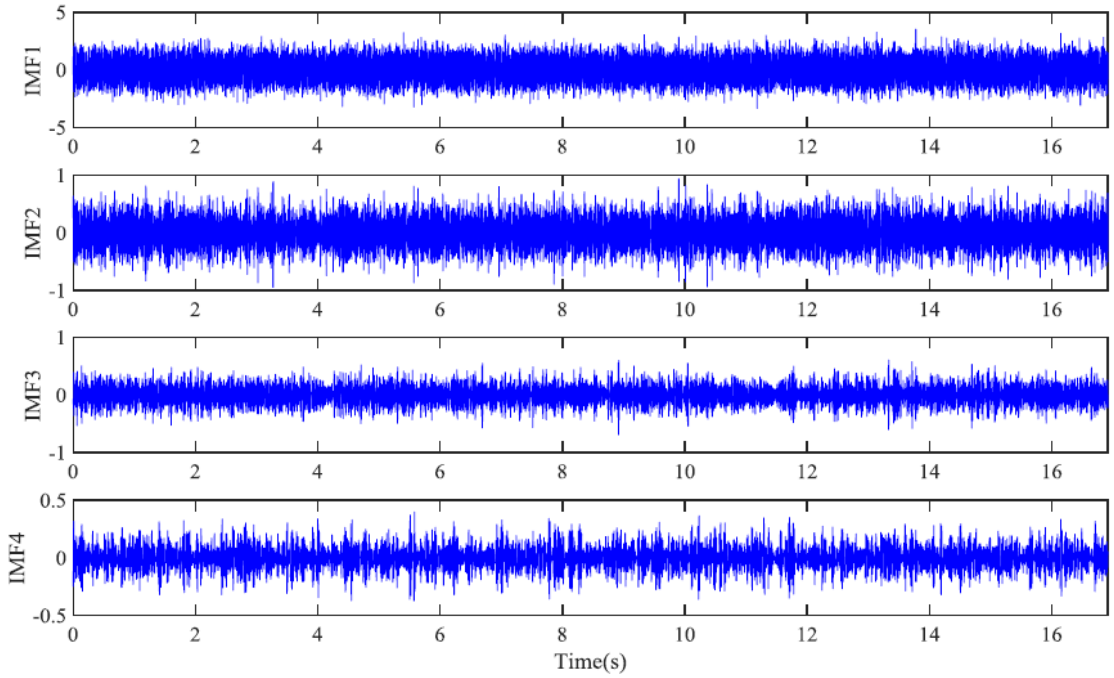

Fig. 5.5: IMF plots of simulated SNR05 Crack50 case

with SNR05. More comprehensively, Table 5.2 gives the average distances of the curves away from the reference diagonal line in the QQ plots for all simulated signals considered in this study.

From Table 5.2, it is noticed that for each case, GH copula always has the smallest average distance to the diagonal reference line, suggesting the GH copula provides the best fitness among the three Archimedean copulas for each case. Consequently, in the following, the GH copula coefficient is used to develop the targeted dependence-based feature vector.

5.3.2.2 Gumbel-Hougaard copula coefficient analaysis

Table 5.3 shows the GH copula coefficients for all cases considered in this study. From Table 5.3, following observations can be noted:

1) With more severe crack level, it is not necessary to have greater GH copula coefficient for each IMF, neither in SNR10 case nor in SNR05 case;
2) With the increase of the crack level, the GH copula coefficient does not have a monotone trend for each IMF, neither in SNR10 case nor in SNR05 case;

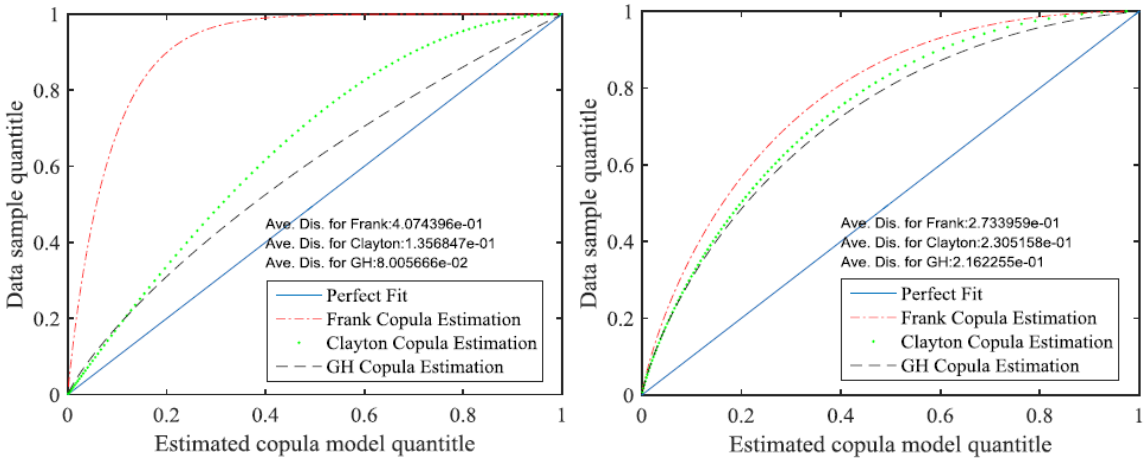

(a) QQ plot regarding IMF1

(b) QQ plot regarding IMF2

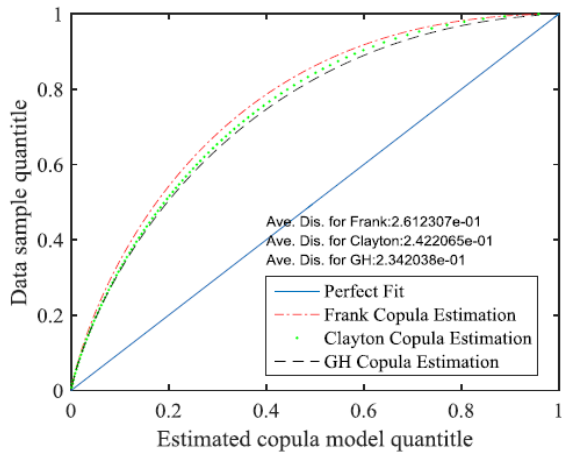

(c) QQ plot regarding IMF3

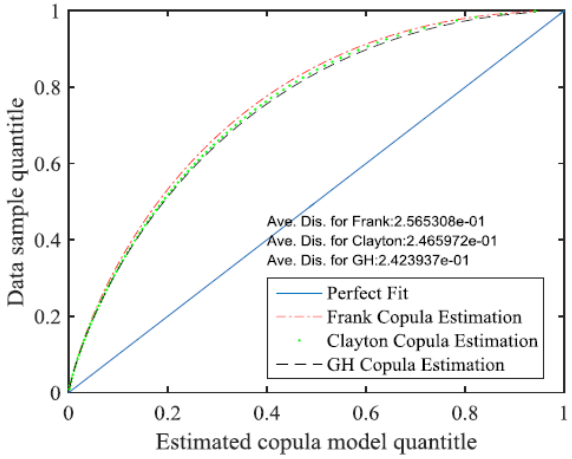

(d) QQ plot regarding IMF4

Fig. 5.6: QQ plots for Archimedean copulas of simulated SNR05 Crack50 case

Table 5.2: Average distance of estimated copula models to perfect fit

Simulated signal case	Copula model	IMF1	IMF2	IMF3	IMF4
Crack00 with SNR05	GH	0.0803	0.2159	0.2350	0.2417
	Frank	0.4074	0.2758	0.2634	0.2581
	Clayton	0.1357	0.2295	0.2416	0.2462
Crack00 with SNR10	GH	0.0798	0.2174	0.2348	0.2418
	Frank	0.4089	0.2746	0.2605	0.2565
	Clayton	0.1353	0.2303	0.2420	0.2464
Crack10 with SNR05	GH	0.0799	0.2172	0.2349	0.2425
	Frank	0.4084	0.2742	0.2610	0.2579
	Clayton	0.1354	0.2300	0.2422	0.2454
Crack10 with SNR10	GH	0.0791	0.2172	0.2358	0.2419
	Frank	0.4079	0.2742	0.2593	0.2553
	Clayton	0.1353	0.2305	0.2436	0.2465
Crack50 with SNR05	GH	0.0801	0.2162	0.2342	0.2424
	Frank	0.4074	0.2734	0.2612	0.2565
	Clayton	0.1357	0.2305	0.2422	0.2466
Crack50 with SNR10	GH	0.0792	0.2191	0.2349	0.2421
	Frank	0.4073	0.2733	0.2628	0.2566
	Clayton	0.1356	0.2313	0.2416	0.2465

Table 5.3: GH copula coefficient for each IMF

	Crack level	IMF1	IMF2	IMF3	IMF4
SNR10 case	Crack00	2.9332	1.1273	1.0540	1.0301
	Crack10	2.9492	1.1273	1.0515	1.0285
	Crack50	2.9464	1.1188	1.0581	1.0297
SNR05 case	Crack00	2.9134	1.1341	1.0589	1.0326
	Crack10	2.9371	1.1279	1.0572	1.0307
	Crack50	2.9202	1.1309	1.0586	1.0296

3) One earlier IMF always has a greater GH copula coefficient than the later ones for each crack level in both SNR10 case and SNR05 case.

Based on above observations, it can be concluded that by using single GH copula coefficient one cannot achieve fault detection or fault degradation level diagnosis. On the other hand, the combination of two features has been proved to be more effective in fault classification [91]. Inspired by this idea, in this study, the combination of the GH copula coefficients is used to achieve planetary gearbox fault classification. Moreover, as shown in Fig. 5.6 and Table 5.2, from IMF1 to IMF4, the fitness of an estimated GH copula to the data samples decreases. Following the principle of choosing copula estimations with fitness as good as possible, the estimated GH copulas regarding the first two IMFs are selected for the coefficient combination. Thus, in the following, the GH copula coefficients regarding the first two IMFs are paired and its performance on fault classification is checked, aiming at the development of the targeted dependence-based feature vector.

To check the performance of the GH copula coefficient pair regarding the first two IMFs on fault classification for different noisy cases, its scatter plots for SNR10 case and SNR05 case are presented in Fig 5.7 and Fig. 5.8, respectively. Moreover, to demonstrate the influence of different copula models with different goodness-of-fit as shown in Fig. 5.6 and Table 5.2, the scatter plots for Clayton copula coefficient pair and Frank copula coefficient pair regarding the first two IMFs are presented as well in Fig. 5.7 and Fig. 5.8.

From Fig. 5.7 and Fig. 5.8, the following observations regarding the categorization by

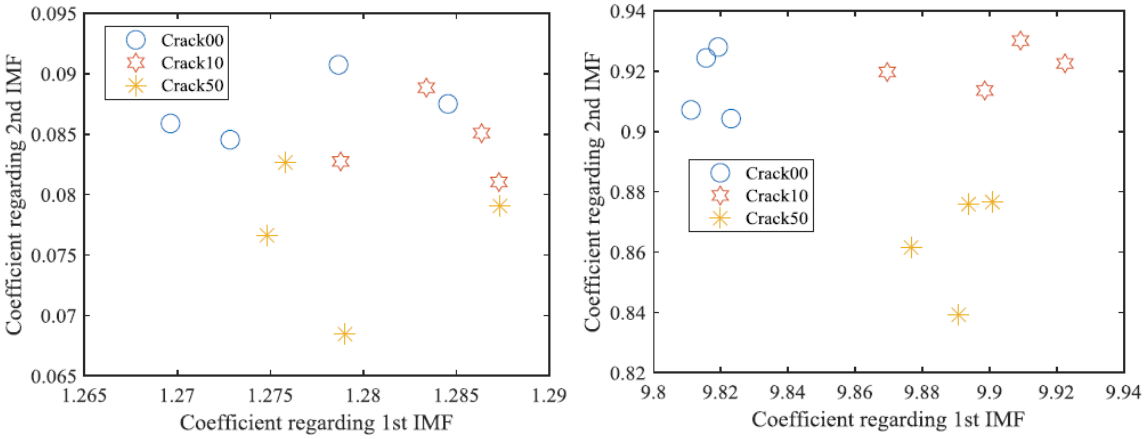

(a) Coefficient pair by Frank copula

(b) Coefficient pair by Clayton copula

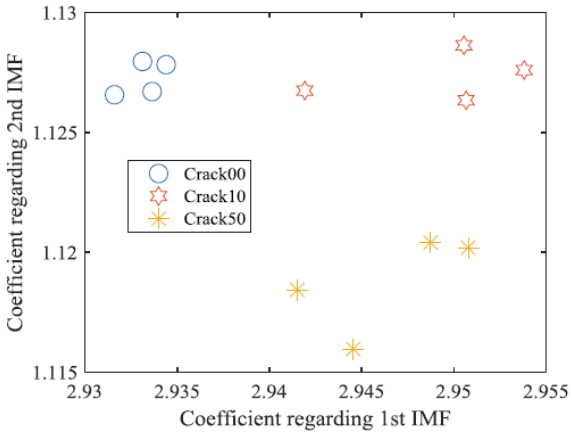

(c) Coefficient pair by GH copula

Fig. 5.7: Coefficient pairs by different Archimedean copulas for SNR10 cases

different Archimedean copulas can be noticed for different gear faults:

1) Frank copula coefficient pair cannot provide proper categorization for each crack level in neither SNR10 case nor SNR05 case as shown in Fig. 5.7(a) and Fig. 5.8(a);
2) Clayton copula coefficient pair can separate each crack level well in SNR10 case as shown in Fig. 5.7(b). However, when the noise level increases to SNR05, Clayton copula coefficient pair cannot separate crack10 and crack50 properly as shown in Fig. 5.8(b);
3) GH copula coefficient pair can separate each crack level with proper categorization for both SNR10 case and SNR05 case as shown in Fig. 5.7(c) and Fig. 5.8(c), respectively.

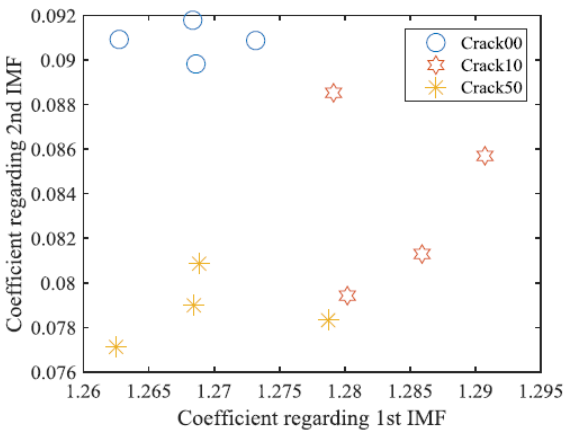

(a) Coefficient pair by Frank copula

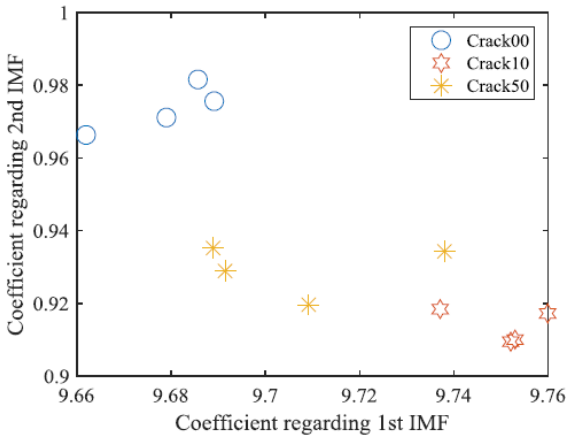

(b) Coefficient pair by Clayton copula

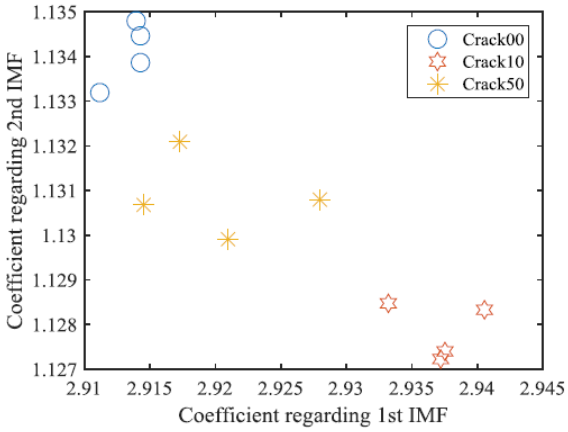

(c) Coefficient pair by GH copula

Fig. 5.8: Coefficient pairs by different Archimedean copulas for SNR05 cases

Based on above observations, the conclusion can be drawn that with the best fitness to the tail dependence among the three Archimedean copulas, GH copula can provide coefficient pair for fault detection and fault diagnosis in both SNR10 case and SNR05 case by proper classification with great robustness to the noise.

5.3.3 Definition of the proposed feature vector

Through the above analysis on the tail dependence between the raw vibration signal and the EEMD-decomposed IMFs, it is found that there is an upper tail dependence which can be described by GH copula. Then how the GH copula coefficient can be used in fault detection and fault diagnosis is analyzed and investigated. It is found that the GH copula

coefficient regarding a single IMF cannot achieve fault detection or fault diagnosis because there is no a monotone trend with the increase of the sun gear tooth crack level. On the other hand, when the pair of the GH copula coefficients regarding the first two IMFs are applied, they can be categorized properly with great robustness to noise interference for simulated vibration signals with different sun gear tooth crack levels, i.e., no crack, 10% crack, and 50% crack, indicating its great potential in fault classification for a real planetary gearbox by measured vibration signals. Consequently, the proposed dependence-based feature vector is defined as the pair of the GH copula coefficients regarding the first two IMFs. The dependence-based feature vector FV is obtained and expressed as

$$\begin{cases} FV &= (\theta_{GH1}(R_x, S_{IMF_1}), \theta_{GH2}(R_x, S_{IMF_2})) \\ R_x(i) &= \dfrac{x(i)}{n+1} \\ S_{IMF}(i) &= \dfrac{IMF(i)}{n+1} \end{cases} \tag{5.17}$$

where θ_{GH1} and θ_{GH2} are the GH copula coefficients regarding the first two IMFs; R_x and S_{IMF} are the ranks associated with the raw vibration signal x and the decomposed IMF, respectively.

5.4 Application to experimental planetary gearbox vibration signals

In this section, the developed dependence-based feature vector is applied to experimental data with gear tooth failures of different levels at different gears to check its ability in fault detection and fault diagnosis for a real planetary gearbox. Meanwhile, the AACO reported in [91] and the AACO-based feature vector are applied to the same experimental data for the purpose of comparison. The accuracies of classifying the gear faults by a multiclass SVM model are compared with the different inputs to outstand the advantage of the proposed dependence-based feature vector.

5.4.1 Experimental setup

The planetary gearbox test rig in the Reliability Research Lab at the University of Alberta has a configuration as shown in Fig. 2.11. For the planetary gearbox, all gears are spur gears without tooth profile modification. An accelerometer was installed on the casing of the second stage planetary gearbox vertically to acquire the vibration signal. The second stage planetary gearbox has the same structure configuration and the same gear parameters with the simulated planetary gear set. The input rotational speed to the second stage planetary gearbox and the torque on its carrier are the same with those values in the simulated case as 46.667r/min and 2367Nm, respectively [140].

In this study, vibration signals with perfect gears and different faulty gears in the second stage planetary gearbox are acquired and analyzed by the proposed feature vector for planetary gearbox fault detection and fault diagnosis. The fault diagnosis focuses on distinguishing the fault position and the fault level. The gear faults include the tooth damage on single tooth (i.e., Planet gear tooth crack on Ring gear meshing side (PR), Planet gear tooth crack on Sun gear meshing side (PS), Ring gear tooth Crack (RC), and Sun gear tooth Crack (SC)), the tooth damage on multiple teeth (i.e., Slight planet gear tooth Pitting (SP), Moderate planet gear tooth Pitting (MP), and Critical planet gear tooth Pitting (CP)), and the tooth breakage (i.e., Planet gear tooth Breakage (PB), Ring gear tooth Breakage (RB), and Sun gear tooth Breakage (SB)). The vibration signals were acquired in the year of 2011 by former group members. The detailed description to these gear damages can be found in [170] and [210]. The sampling frequency for cases with planet gear tooth pitting was 10000Hz and the sampling frequency for other cases was 5000Hz. The experimental vibration signals are with a time length of 300 seconds. In the following analysis, the experimental vibration signals are filtered by a Chebyshev low-pass filter with a cutoff frequency of 800Hz as in Chapter 3 and Chapter 4. As waveform examples of experimental vibrations, Fig. 5.9 shows the waveforms of the experimental data with perfect gears, RC, SC, PB, MP, and CP.

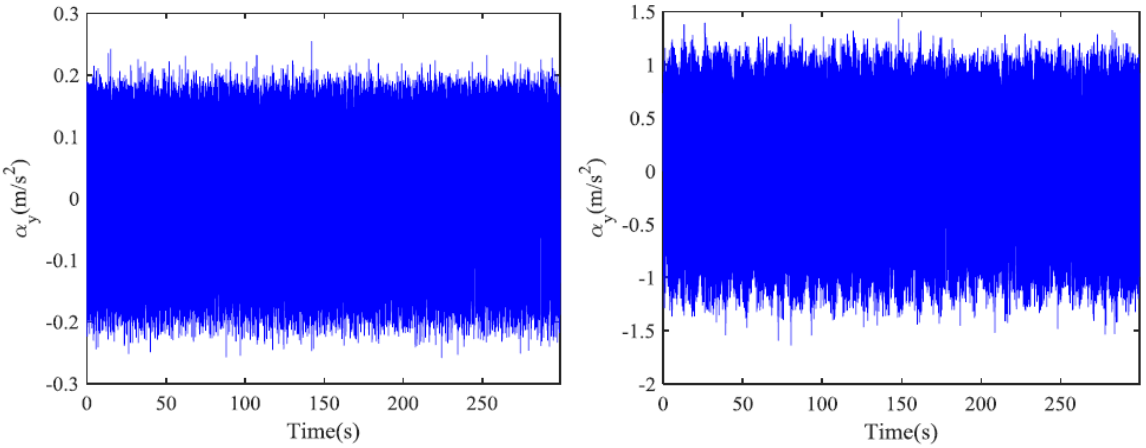

(a) Waveform with perfect gears

(b) Waveform with RC

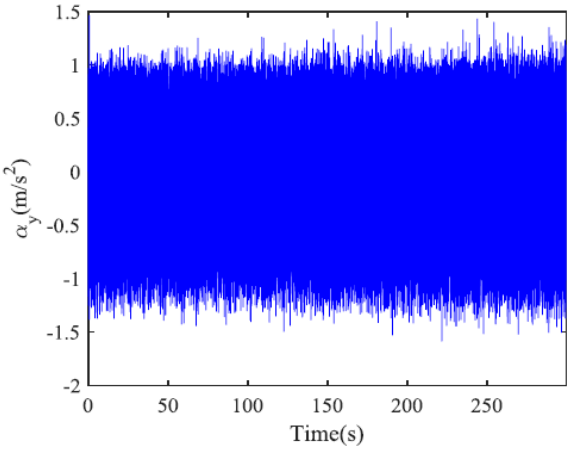

(c) Waveform with SC

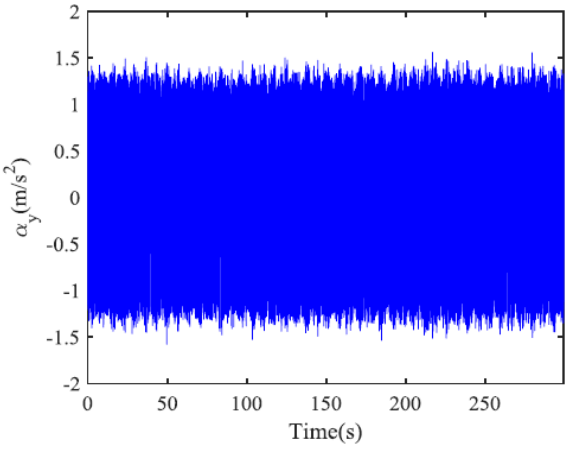

(d) Waveform with PB

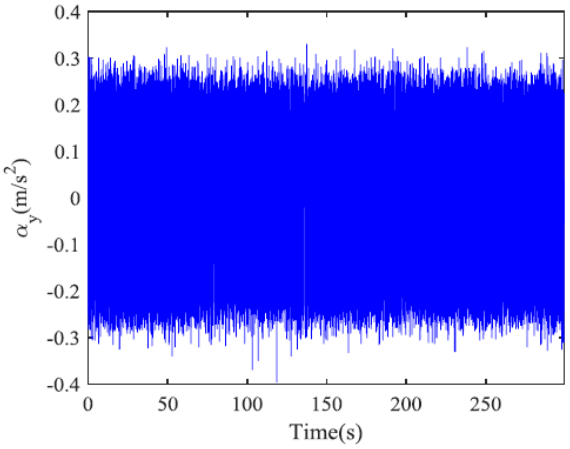

(e) Waveform with MP

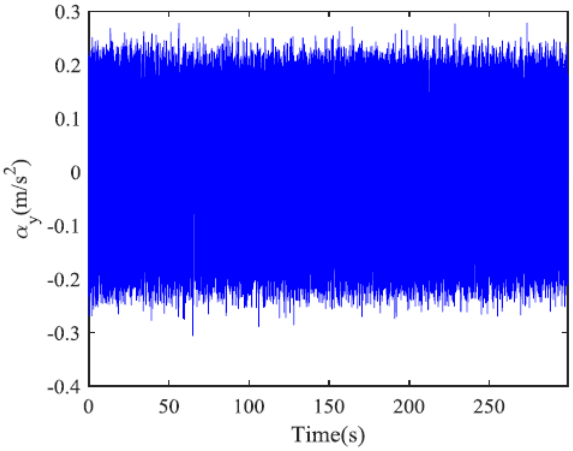

(f) Waveform with CP

Fig. 5.9: Experimental vibration waveforms with perfect gears and different gear tooth faults

5.4.2 Result of the dependence-based feature vector and a reported feature

As illustrated in the above discussion with the simulated vibration signal analysis, the performance of the proposed dependence-based feature vector in fault diagnosis is intuitively reflected by the categorization of the feature vectors. To achieve the categorization, multiple vibration signals are needed as one vibration signal can only get one feature vector. For this reason, each experimental vibration signal is divided into ten segments with equal time length of 30 seconds. Note that the lowest frequency component of interest in the 2nd stage planetary gearbox is 0.1478Hz, the carrier rotating frequency [140], corresponding to a time period of 6.76 seconds. With the segment time length as 30 seconds, it is guaranteed that the segment covers multiple (4.47) periods of the lowest frequency component. After the segmentation, the EEMD is then applied to decompose each segment into IMFs. As one example, Fig. 5.10 shows the IMF waveforms of the experimental vibration with the planet gear tooth breakage. GH copula coefficient is subsequently estimated to represent the upper tail dependence between the raw vibration signal and each IMF. The GH copula coefficient pair regarding the first two IMFs is obtained as the feature vector for classification of the experimental planetary gearbox vibration signals. The scatter plot of the GH coefficient pairs is given in Fig. 5.11.

For comparison purpose, the Accumulative Amplitude of Carrier Orders (AACO) reported in [91] is adopted as the alternative feature in this study for experimental planetary gearbox fault classification. The AACO is designed especially for planetary gearbox fault diagnosis based on the order spectrum [91]. For a planetary gearbox, the order spectrum is obtained through normalizing frequency scales of the frequency spectrum by the carrier rotating frequency [91]. The AACO is defined as the summation of the maximum amplitudes around different orders of the carrier rotating frequency in the order spectrum [91]. Different gear faults may result in different amplitude changes at the orders of the carrier rotating frequency. By the AACO, these amplitude changes can be captured to achieve

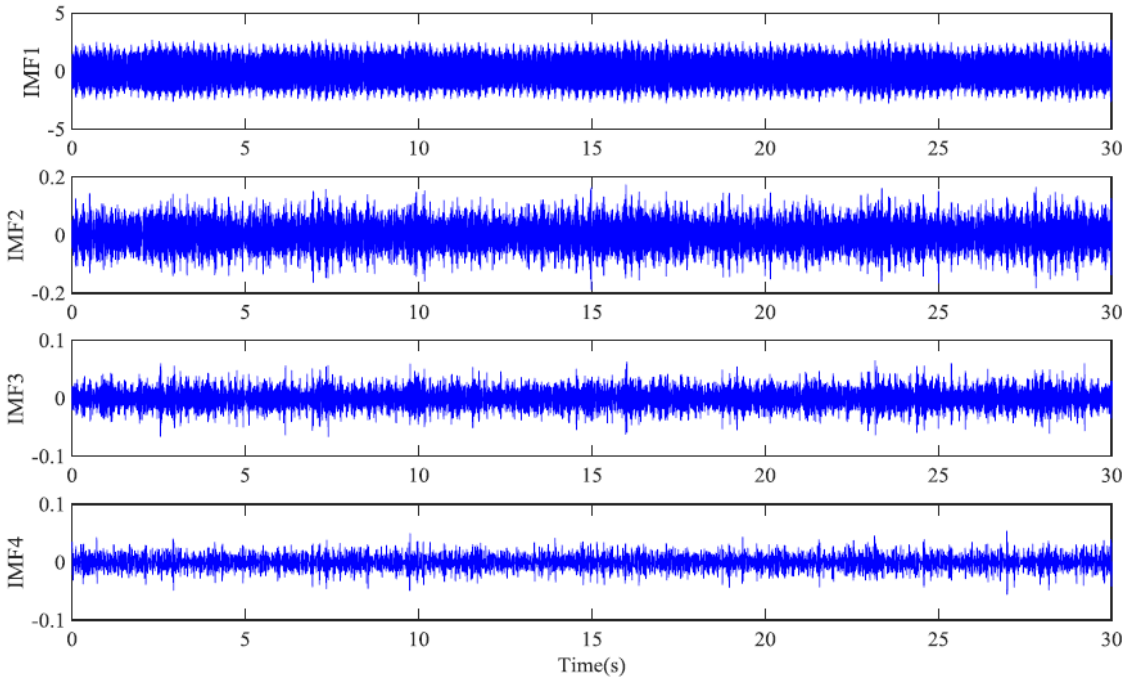

Fig. 5.10: IMF plots of experimental vibration with planet gear tooth breakage

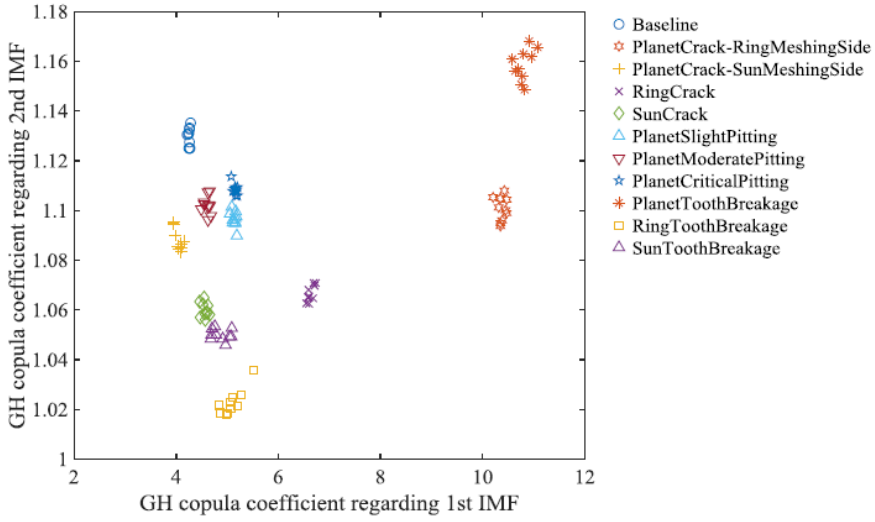

Fig. 5.11: Scatter plot of dependence-based feature vector for experimental vibration signals

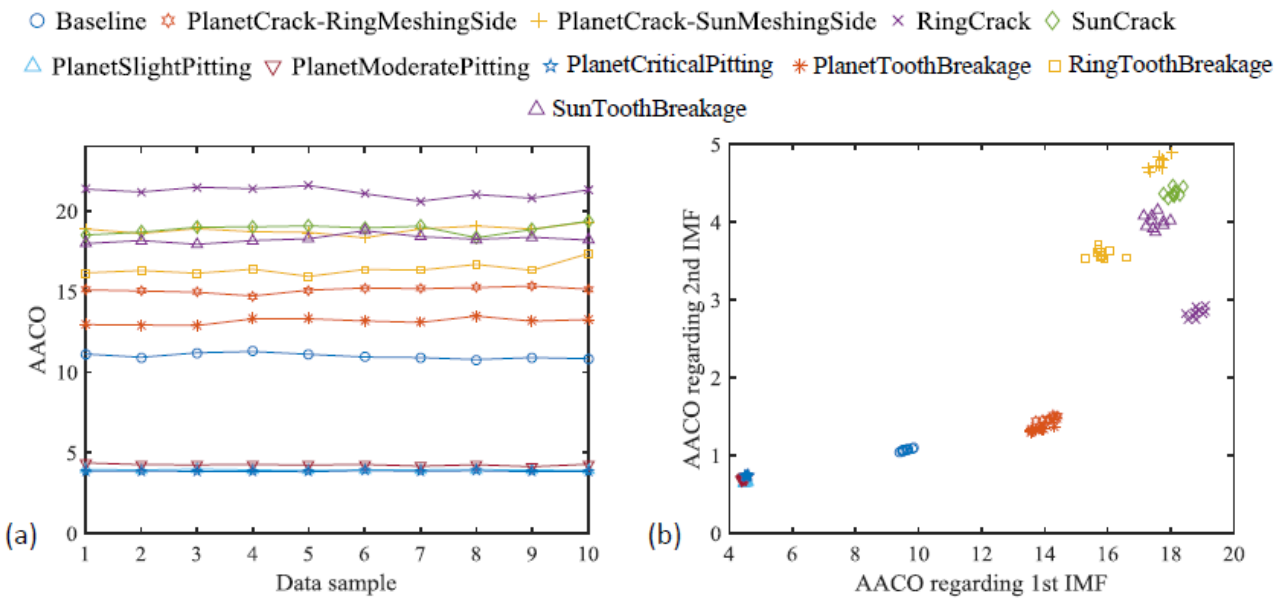

Fig. 5.12: AACO-based plot for experimental vibration signals

the fault diagnosis for a planetary gearbox. In addition, as we take the combination of GH copula coefficients regarding the first two IMFs as the proposed feature vector, even though Ref. [91] only gives out the individual AACO plot, the AACO pairs regarding the first two IMFs is also studied to be consistent in the data processing. The AACO pair regarding the first two IMFs is the AACO-based feature vector. Fig. 5.12 depicts the plots by AACO including the individual AACO plot of the raw data as given in Fig. 5.12(a) and the AACO pair plot regarding the first two IMFs as given in Fig. 5.12(b).

From Fig. 5.11, one can notice that the proposed dependence-based feature vector can distinguish well the perfect condition with the faulty conditions in the sense of fault detection. In the sense of fault diagnosis, it is observed that the proposed feature vector can categorize well for the cases of planet gear tooth crack on the ring meshing side, planet gear tooth crack on the sun meshing side, planet gear tooth breakage, ring gear tooth crack, ring gear tooth breakage, planet gear tooth pitting, and the faults (tooth crack and breakage) on the sun gear. Although the coefficient pairs regarding different planet gear tooth pitting levels are very close to each other, there is no overlap for the coefficient pairs with different pitting levels. The same observation can be obtained for the coefficient pairs with sun gear

tooth crack and sun gear tooth breakage. Overall, by Fig. 5.11, it can be conclude that the proposed dependence-based feature vector could properly reflect the health status of the system by proper categorization without overlap.

From Fig. 5.12, it can be noticed that both the AACO plot and the AACO pair plot can distinguish well the perfect condition with the faulty conditions to achieve the fault detection. In the sense of fault diagnosis, by the AACO plot in Fig. 5.12(a), ring gear tooth crack, ring gear tooth breakage, planet gear tooth crack on ring meshing side, planet gear tooth breakage can be distinguished clearly. However, the lines for sun gear tooth crack, sun gear tooth breakage and planet gear tooth crack on sun meshing side are mixed together; the lines subject to slight planet gear tooth pitting and critical planet gear tooth pitting are mixed together. On the other hand, as shown in Fig. 5.12(b), the AACO pairs can separate the baseline, planet crack on sun meshing side, ring crack, sun crack, ring tooth breakage and sun tooth breakage. However, the planet gear tooth breakage is mixed with planet gear tooth crack on the ring meshing side while the slight planet gear tooth pitting, the moderate planet gear tooth pitting, and the critical planet gear tooth pitting are mixed together. Thus, by Fig. 5.12, it can be found that neither AACO plot nor AACO pair plot is satisfactory for planetary gearbox fault categorization. One reason is that the design of the AACO in [91] is based on the observation that the gear rotating frequencies in a planetary gearbox are integer multiples of the carrier rotating frequency, which is not true for the 2nd stage planetary gearbox of the experimental test rig. Given the numbers of teeth for the sun gear, the ring gear and the planet gear being 19, 81, and 31, respectively, with 4 planet gears in the gearbox as shown in Table 3.1, the characteristic frequencies of the 2nd stage planetary gearbox are calculated by the formulas presented in Section 5.1 and the results are listed in Table 5.4 where f_s, f_p, f_c, f_{p-p}, and f_m are the sun gear rotating frequency, the planet gear rotating frequency, the carrier rotating frequency, the passing frequency of planet gears, and the meshing frequency, respectively. Table 5.4 shows that f_s and f_p are not the integer multiples of f_c, which results the AACO-based features cannot work well

Table 5.4: Characteristic frequencies of the 2nd stage planetary gearbox

	f_s	f_p	f_c	f_{p-p}	f_m
Rotating frequency /Hz	0.7778	0.23836	0.1478	0.5913	11.97
Ratio with f_c	5.26	1.61	1	4	81

in the fault categorization for the 2nd stage planetary gearbox.

5.4.3 Performance comparison

In Subsection 5.4.2, the features shown in Fig. 5.11 and Fig. 5.12 are analyzed subjectively with the observation on the categorization for different gear faults. In this subsection, the accuracy of classifying gear faults with features in Fig. 5.11 and Fig. 5.12 is compared objectively which is achieved by a multi-class SVM model. For an SVM-based classification problem, its accuracy is affected by the input which is the employed feature. The more useful information about the vibration signal the input has the higher classification accuracy the SVM can obtain. Therefore, to check the performance of the proposed dependence-based feature vector in fault classification, the developed feature vector and the reported AACO as well as the AACO-based feature vector are input into a multiclass SVM model with the same properties. Then the classification accuracies by the SVM with the different inputs are compared.

As an SVM classifier is a supervised machine learning method, conditions with different gear faults need to be labeled. In this study, labels for the cases of baseline, planet gear tooth crack on ring meshing side, planet gear tooth crack on sun gear meshing side, ring gear tooth crack, sun gear tooth crack, slight planet gear tooth pitting, moderate planet gear tooth pitting, critical planet gear tooth pitting, planet gear tooth breakage, ring gear tooth breakage, and sun gear tooth breakage are set as 0, 1, 2, 3, 4, 5, 6, 7, 8, 9, and 10, respectively.

With the features as the inputs and the corresponding labels as the output, Matlab function of "fitcecoc" is used to fit the multiclass SVM model by setting the learner of "fitcecoc"

as SVM method. The cross-validation method by Matlab function of "crossval" is then used to determine how well the estimated SVM model generalizes. Five-fold cross-validation is employed. By the five-fold cross-validation, five models are obtained by the training of in-fold observations which contain 4/5 of data, i.e., 8 segments for each case in this study. The rest 1/5 excluded data, i.e., 2 segments for each case in this study, works as the test fold for prediction. Specifically, the first model is trained with the first 1/5 of data excluded; the second model is trained with the second 1/5 of data excluded, and so on. For the prediction, responses to the excluded data are computed by the model trained with that data excluded, i.e., the first model computes predictions for the first 1/5 of data; the second model computes the prediction for the second 1/5 of data, and so on.

With the above setup, confusion matrices of the multiclass SVM with different inputs can be obtained and are given in Fig. 5.13. The confusion matrices show the predictions of the 1/5 excluded data by the corresponding trained model. In the confusion matrix, each column of the matrix represents the instances in a predicted class, while each row represents the instances in an actual class. The benefit of a confusion matrix is that it is easy to see if the system is confusing two classes, i.e., mislabeling one as another. In the last row and the last column, the rates of correct predictions and incorrect predictions regarding each column and row are given in percentage to show the prediction accuracy and classification accuracy for each labeled case. Note that the classification accuracy is defined as the rate of correct predictions in an actual class and the prediction accuracy is defined as the rate of correct predictions in a predicted class. The overall accuracy regarding all cases is given in the last cell at the bottom right corner of the matrix.

As confusion matrices shown in Fig. 5.13, the developed dependence-based feature vector provides high classification accuracy and prediction accuracy as 100% for each gear fault case; the AACO reported in [91] provides lower classification accuracies as 30% for labeled 2, 33% for labeled 4, 67% for labeled 5, 80% for labeled 7, and 75% for labeled 10 and lower prediction accuracy as 30% for labeled 2 and labeled 4, 80% for labeled 5,

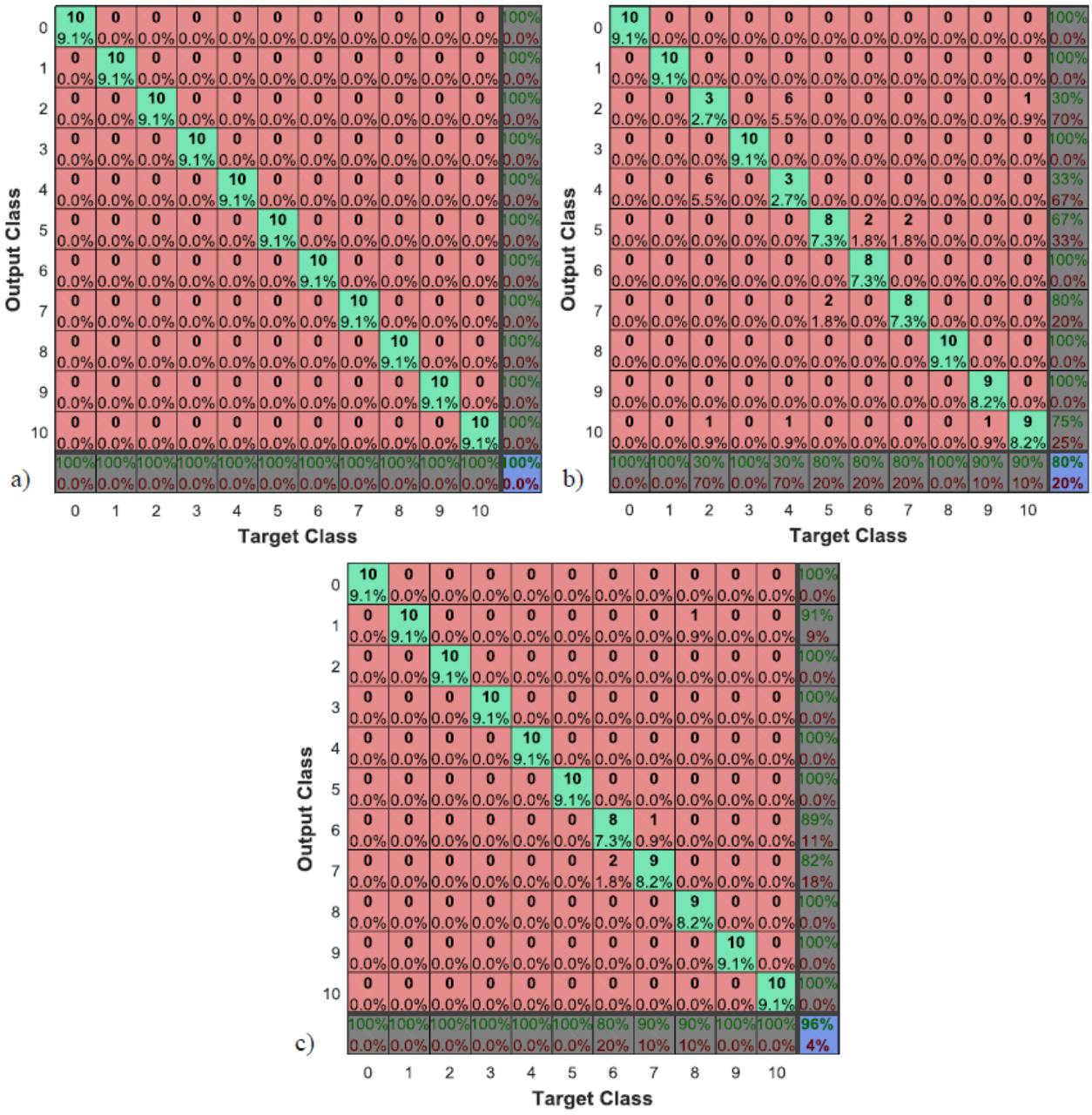

Fig. 5.13: Confusion matrix with: a) proposed feature vector; b) AACO; c) AACO pairs

labeled 6, and labeled 7, and 90% for labeled 9 and labeled 10; the AACO pairs as the AACO-based feature vector provides lower classification accuracy as 91%, 89%, and 82% for labeled 1, labeled 6, and labeled 7, respectively, and lower prediction accuracy as 80% for labeled 6, and 90% for labeled 8 and labeled 9. The overall accuracies of the SVM model with inputs as the developed dependence-based feature vector, AACO values and AACO pairs are 100%, 80%, and 96%, respectively, as given in Fig. 5.13.

Consequently, it can be drawn that the developed dependence-based feature vector can lead to better classification results than the AACO-based features. This conclusion suggests that the developed dependence-based feature vector, i.e., the GH copula coefficient pair regarding the first two IMFs, can better extract and reflect the health status information about a planetary gearbox, thus serving better as a condition indicator for planetary gearbox fault detection and fault diagnosis.

5.5 Discussion

To check the performance of the developed feature vector in fault classification by a multi-class SVM, besides the confusion matrix as shown in Fig. 5.13, another alternative way is the maximum posterior probability plot. By setting the "FitPosterior" in the Matlab command "fitcecoc" being true, the binary-leaner classification score can be transformed to posterior probability which can then be extracted by the Matlab command "resubPredict". Note that the SVM score for classifying the observation is the distance from the observation to the decision boundary. The posterior probability in a SVM model can be calculated based on Bayes' theorem where the prior probabilities are computed from the training data [211]. Defining a grid of values in the predictor space, the posterior probability regarding each class can be calculated for each coordinate on the grid. The maximum posterior probability is plotted in Fig. 5.14 for the experimental vibration signals with a grid size of 2500×2500. The numbers on Fig. 5.14 are the labels for the gear tooth faults in the experimental planetary gearbox as defined in Subsection 5.4.3. From Fig. 5.14, it can

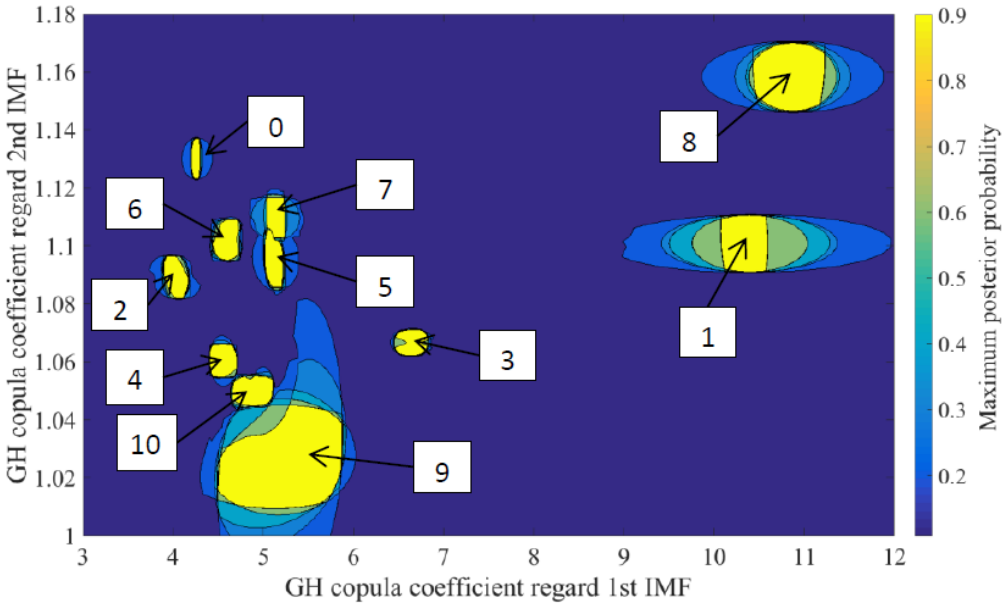

Fig. 5.14: Maximum posterior probability plot

be found that the decision boundaries for the gear tooth faults are separated clearly. The well-separated decision boundaries in Fig. 5.14 validate the conclusion drawn based on the subjective categorization observation in Subsection 5.4.2.

It should be noted that the foundation of the developed dependence-based feature vector is the correlation/dependence between the extreme values in the EEMD-decomposed IMFs and the extreme values in the raw vibration signal. It is noteworthy that the extreme values in the IMFs can be introduced by both the fault-induced impulses and the noise in the raw vibration signal. In this study, the raw vibration signal is constrained to be with the same noise level of the same SNR. In this way, the extreme values introduced by the noise in the EEMD-decomposed IMFs are set to be consistent. Thus, the change of the extreme values in an IMF is mainly caused by the occurrence of the fault-induced impulses. Accordingly, for possible real applications, the developed dependence-based feature vector aims at the situation with the operation condition under the same noise level. In the cases where the system noise level is changing subject to the structural dynamic noise and the environmental noise, the acquired vibration signals would be with different noise levels. For such cases, the pre-process of de-nosing is needed. The de-noising is to guarantee the noise

levels of the vibration signals are similar before the extraction of the dependence-based feature vector for its effectiveness.

5.6 Conclusions

In this chapter, rather than continuing to study the dependence between the instantaneous energy and the energy spectral density as in Chapter 3 and Chapter 4, we turn our attention to a study of the dependence between a one-dimensional vibration signal and its EEMD-decomposed IMFs. Specifically, a dependence-based feature vector is developed based on the tail dependence between the raw vibration signal and its EEMD-decomposed IMFs for planetary gearbox fault classification. Based on the goodness-of-fit test with the QQ plot, it is found that the tail dependence is best described by the Gumbel-Hougaard (GH) copula with an upper tail dependence among the three Archimedean copula candidates, namely Frank copula, Clayton copula, and GH copula. Accordingly, the GH copula coefficient, which measures the upper tail dependence level, is adopted to develop the proposed dependence-based feature vector. Eventually, through the simulated vibration signal analysis, the dependence-based feature vector is defined as the pair of GH copula coefficients regarding the first two IMFs.

To evaluate the performance of the developed dependence-based feature vector, it is applied to experimental planetary gearbox vibration signals with different gear tooth faults. The gear tooth faults are of different levels of different gears. The developed dependence-based feature vector, reported AACO, and AACO-based feature vector are input into a multi-class SVM model with the same properties. Then the classification accuracies of the SVM models with the different inputs are compared. The results show that the developed dependence-based feature vector leads to the highest classification accuracy, suggesting that the dependence-based feature vector serves better for planetary gearbox fault classification with more health status information about the planetary gearbox.

Chapter 6

Summary and future work

In this chapter, the main contributions of the thesis study are summarized in Section 6.1. Then, in Section 6.2, some research problems that could be further studied in future work are suggested.

6.1 Summary

Vibration signal analysis has been widely employed for planetary gearbox condition monitoring and fault diagnosis, as vibration signals are easily measured and contain rich information about health conditions. This thesis study aims to understand the characteristics of planetary gearbox vibration signals and to develop novel and effective vibration signal analysis methods for planetary gearbox fault diagnosis. The thesis study is conducted in stationary operation condition under constant speed and constant load. The main contributions of this thesis study are summarized in four categories as follows.

Planetary gear set vibration signal modeling with transmission path effect

Vibration signal modeling is helpful for understanding the vibration characteristics of planetary gearboxes. By generating simulated vibration signals, vibration signal modeling provides valuable aid in exploring and developing effective vibration signal analysis methods for planetary gearbox fault diagnosis. A comprehensive vibration signal model is essential for vibration characteristic understanding and realistic vibration signal generation. In this

thesis, a comprehensive vibration signal modeling method is developed for a planetary gear set. In the proposed modeling method, vibration sources from the sun gear, the ring gear, and the planet gears are all included; the transmission path effect covers the part along the casing to the transducer position and the part from the vibration source to the casing. Moreover, given the sizes of gears in a planetary gear set, attenuation coefficients for transmission path effect estimation are formulated by considering vibration transmission distance, radiation damping, and material damping. Incorporating multiple vibration sources and their transmission path effects, the simulated vibration signal as measured at the transducer position is constructed for a healthy planetary gear set in Chapter 2. Vibration properties are analyzed with different transmission path effects. The simulated vibration signal is validated by an experimental signal in both the time domain and the frequency domain.

The developed comprehensive vibration signal model is used to generate the simulated vibration signals for development of the novel vibration signal analysis methods for planetary gearbox fault diagnosis as described in Chapter 3, Chapter 4, and Chapter 5.

Copula-based time-frequency energy density representation for a vibration signal

Various Time-Frequency Distribution (TFD) construction methods for representing the time-frequency energy density of a vibration signal have been reported, such as short-time Fourier transform, Wavelet transform, Wigner-Ville distribution, Cohen's class distribution, and copula-based TFD. Among them, copula-based TFD has desirable properties of being positive, free from cross-term interference, with high time-frequency resolution and correct energy marginals. In this study, a spectrogram-free copula-based TFD construction method is proposed. The proposed copula-based TFD construction method starts with the instantaneous energy and the energy spectral density rather than spectrogram-based marginals as the reported copula-based TFD construction method does. In this way, the proposed method eliminates the negative influence of the spectrogram on copula-based TFD construction. The proposed spectrogram-free copula-based TFD is developed with

a non-parametric copula which has less model error than a parametric copula. A simulated case study and an experimental case study are conducted as described in Chapter 3. The simulated signals are generated by the developed vibration signal modeling method reported in Chapter 2. The experimental vibration signals come from the planetary gearbox test rig of the Reliability Research Lab (RRL) at the University of Alberta. Both simulated signals and experimental signals are with stationary operation conditions of constant speed and constant load. The results show that the developed spectrogram-free copula-based TFD can serve better for time-frequency energy density representation with smaller energy marginal deviations than the reported spectrogram-based copula-based TFD.

The developed spectrogram-free copula-based TFD represents the energy density in the time-frequency domain with increased time-frequency resolution than the spectrogram. As the constructed copula-based TFD can identify the fault-related frequencies in its frequency energy marignal with high frequency resolution and simultaneously locate the fault-induced impulses in the time-frequency domain with high time resolution, i.e., free from the Heisenberg uncertainty principle, the constructed copula-based TFD serves better than the spectrogram for planetary gearbox fault diagnosis.

Moreover, the constructed spectrogram-free copula-based TFD can provide pseudo-multi-dimensional signals to extract the gear tooth fault characteristic frequency through dimension reduction for planetary gearbox fault diagnosis, as described in Chapter 4.

Fault feature extraction by non-negative matrix factorization

Given a one-dimensional vibration signal, a fault feature extraction method is proposed for planetary gearbox fault detection through dimension reduction of its time-frequency energy density. Non-Negative Matrix Factorization (NNMF) is used for dimension reduction. The spectrogram-free copula-based TFD constructed by the proposed method in Chapter 3 serves as the time-frequency energy density. Time waveforms at different frequency positions in the TFD are treated as the input to NNMF. Unlike Principal Component Analysis

(PCA) and Independent Component Analysis (ICA), which are globally supported, NNMF is a part-based multivariate data analysis method with non-negative constraint. Part-based representation alleviates the shortcoming of global support representation which generates non-existing information while disturbing fault information extraction. A simulated case study and an experimental case study are investigated in Chapter 4. The simulated signals are generated by the developed vibration signal model in Chapter 2. The experimental vibration signals are from the planetary gearbox test rig in RRL at the University of Alberta. Both the simulated signals and the experimental signals are conducted in stationary operation conditions under constant speed and constant load. The results show that the proposed positive TFD-NNMF method can better extract fault features with more accurate fault characteristic frequency identification than the reported EEMD-ICA method, thus serving better for planetary gearbox fault diagnosis.

The driving force behind the better fault feature extraction performance is revealed to be the sparse representation with NNMF, which is intrinsically related to the part-based decomposition by NNMF. Furthermore, it is found that the average sparsity of decomposed components by the proposed positive TFD-NNMF method can serve as a condition indicator, as it has a monotonically increasing trend with the increase of the gear tooth fault.

Studies involving the dependence between the instantaneous energy and the energy spectral density, as discussed in Chapter 3 and Chapter 4, indicate the potential of dependence analysis in planetary gearbox fault diagnosis. Inspired by this indication, in the next research topic, as documented in Chapter 5, dependence analysis is extended to develop a dependence-based feature vector for planetary gearbox fault classification by turning the attention to the dependence between a one-dimensional vibration signal and its EEMD-decomposed IMFs.

Development of a dependence-based feature vector for fault classification

EEMD is a self-adaptive algorithm for decomposing a vibration signal into its IMFs. The

self-adaptation indicates there is a dependence between the raw signal and IMFs. In this thesis, a dependence-based feature vector is developed for planetary gearbox fault classification. The gist is that different fault-induced impulses will be excited with different faults and will be distributed differently in IMFs, thus leading to different dependences between the raw vibration signal and IMFs. Through the study in Chapter 5, the underlying dependence is captured and described by the Gumbel-Hougaard (GH) copula as an upper tail dependence. The proposed dependence-based feature vector is developed with simulated vibration signal analysis and is defined by GH copula coefficients regarding the first two IMFs. The simulated signals are generated by the developed vibration signal model in Chapter 2. After the development of the dependence-based feature vector, experimental vibration signals with different gear tooth faults from the planetary gearbox test rig in RRL are classified. The results show that the developed dependence-based feature vector provides higher classification accuracy than the reported methods, suggesting that the dependence-based feature vector contains more health status information about a planetary gearbox, thus serving better as the input to an intelligent diagnosis method for planetary gearbox fault diagnosis.

Overall

With the generated knowledge, this thesis study advances the state of the art of the research on planetary gearbox fault diagnosis by vibration signal analysis. The proposed comprehensive vibration signal model can generate more realistic simulated vibration signals to develop effective vibration signal analysis methods for planetary gearbox fault diagnosis. The developed vibration signal analysis methods could provide more effective fault diagnosis tools to prevent unexpected failures in a planetary gearbox, thus reducing operation and maintenance costs.

6.2 Future work

Although the methods proposed in this thesis study have addressed the shortcomings of relevant reported work on the diagnosis of planetary gearbox faults by vibration signal analysis, there are still some interesting topics and challenges worth further consideration, including development of novel features with further study on the constructed spectrogram-free copula-based TFD for planetary gearbox fault diagnosis, development of effective vibration signal analysis methods for fault diagnosis of planetary gearbox with non-stationary operation condition, development of intelligent diagnosis methods with adaptive feature learning, and condition-based maintenance optimization with diagnosed machinery health information. More details are provided as follows.

Instantaneous equivalent bandwidth estimation with time-frequency energy distribution for planetary gearbox fault diagnosis

In the time-frequency domain with energy distribution, fault-induced impulses are represented by vertical lines as shown in Fig 3.17 and Fig 3.18. The length of a vertical line indicates the duration of energy density in the frequency direction at a time instant. As suggested by Kikkawa and Yoshida [212], this duration can be described by Equivalent BandWidth (EBW). The longer the duration is, the larger the EBW [213]. Thus, we can take advantage of time instants with larger EBW values to locate fault-induced impulses, indicating that EBW is potentially applicable for planetary gearbox fault diagnosis. In [212], EBW is formulated by a unified representation with Renyi's α-order entropy. However, how to determine the order α is still an open question [212]. To date, no such research work is found in the literature on planetary gearbox fault diagnosis. It would be interesting and meaningful to use EBW to explore and develop methods for planetary gearbox fault diagnosis by properly determining the order α.

Vibration signal modeling and fault diagnosis with non-stationary operation

The planetary gearbox of interest in this thesis study is operated in stationary operation conditions of constant speed and constant load. However, in real industrial applications, such as a wind turbine planetary gearbox under wind turbulence, the speed and the load are usually time varying. The vibration properties of a planetary gearbox will be much more complicated under non-stationary operation conditions of time-varying speed and/or time-varying load [214]. Vibration signal analysis methods that work well for planetary gearbox fault diagnosis in stationary operation conditions may not work well for cases with non-stationary operation conditions. Consequently, it is important to develop vibration signal modeling for a planetary gearbox with non-stationary operation conditions to understand the generation mechanism of its dynamic response and its vibration characteristics. With the understanding on the vibration properties, effective vibration analysis methods can then be explored and developed for planetary gearbox fault diagnosis with non-stationary operation conditions.

Intelligent diagnosis methods with adaptive feature learning

The aim of this thesis study is to develop vibration signal analysis methods to manually extract fault features for planetary gearbox fault diagnosis. Although such methods are demonstrated successfully, their implementation requires a high degree of expertise with knowledge of signal processing techniques, which may impede their practical applications by industrial engineers. On the other hand, intelligent fault diagnosis methods with adaptive feature learning, such as the intelligent fault diagnosis method using unsupervised feature learning reported by Lei et al. [215], have the potential to overcome this shortcoming. The intelligent diagnosis method reported in [215] learns features adaptive from raw data for mechanical fault diagnosis, thus reducing human labor and human expertise. Such intelligent diagnosis methods are not covered in this thesis. Intelligent diagnosis methods based on adaptive feature learning could be studied in future work.

Condition-based maintenance optimization for applications with planetary gearbox

The ultimate goal of this thesis study is to reduce the chance of economic losses and human casualties due to the deterioration in machinery health conditions. For this goal, after determining system health information through condition monitoring and fault diagnosis, the next concern is the maintenance decision. A maintenance decision should optimize maintenance activities while meeting required criteria within the life cycle. Required criteria include maintenance cost and system reliability. Optimal decision options could be [216] 1) the equipment should be replaced immediately; 2) the equipment should continue operating and be inspected at the next inspection time; and 3) the equipment should continue operating but be replaced at a specified time before the next planned inspection time. Thus, for optimal maintenance cost and/or optimal system reliability after determining health condition information, there is a need to make a specific maintenance decision as a condition-based maintenance optimization problem. Research on condition-based maintenance optimization will be conducted in future work.

Overall

It is expected that, through this thesis research work and the previously mentioned future research work, industrial engineers can benefit from more effective, efficient, and powerful tools for planetary gearbox condition monitoring and fault diagnosis, and can make maintenance decisions by optimizing maintenance activities with health information from diagnosed machinery. Eventually, the reliability and safety of industrial power transmission systems with planetary gearboxes can be improved with reduced operation and maintenance cost.

References

[1] Y. Lei, J. Lin, M. J. Zuo, and Z. He. Condition monitoring and fault diagnosis of planetary gearboxes: A review. *Measurement*, 48:292–305, 2014.

[2] F. Chaari, T. Fakhfakh, and M. Haddar. Dynamic analysis of a planetary gear failure caused by tooth pitting and cracking. *Journal of Failure Analysis and Prevention*, 6(2):73–78, 2006.

[3] D. G. Astridge. Helicopter transmissions - design for safety and reliability. *Proceedings of the Institution of Mechanical Engineers, Part G: Journal of Aerospace Engineering*, 203(2):123–138, 1989.

[4] H. Link, W. LaCava, J. Dam, B. McNiff, S. Sheng, R. Wallen, M. McDade, S. Lambert, S. Butterfield, and F. Oyague. Gearbox reliability collaborative project report: findings from phase 1 and phase 2 testing. Technical report, National Renewable Energy Laboratory (NREL), Golden, CO., 2011.

[5] Technical University of Denmark. Final report on investigation of a catastrophic turbine failures, February 22 and 23, 2008. Technical report, Danish Ministry of Science, Technology and Innovation, Riso, Denmark, Accessed on http://www.windaction.org/posts/20929-final-report-on-investigation-of-a-catastrophic-turbine-failures-february-22-and-23-2008, 2008.

[6] Accident Investigation Board Norway. Investigation of helicopter accident at turoy near bergen in hordaland county, norway. Technical report, AIBN, Lillestrom, Norway, Accessed on https://www.aibn.no/Aviation/Investigations/16-286, 2017.

[7] A. R. Nejad, Z. Gao, and T. Moan. Fatigue reliability-based inspection and maintenance planning of gearbox components in wind turbine drivetrains. *Energy Procedia*, 53:248–257, 2014.

[8] American Gear Manufacturers Association. AGMA 1010-E95: Appearance of gear teeth - Terminology of wear and failure, 1995.

[9] P. M. Ku. Gear failure modes - importance of lubrication and mechanics. *ASLe Transactions*, 19(3):239–249, 1976.

[10] Y. Lei, M. J. Zuo, Z. He, and Y. Zi. A multidimensional hybrid intelligent method for gear fault diagnosis. *Expert Systems with Applications*, 37(2):1419–1430, 2010.

[11] M. Lebold, K. McClintic, R. Campbell, C. Byington, and K. Maynard. Review of vibration analysis methods for gearbox diagnostics and prognostics. In *Proceedings of the 54th meeting of the society for machinery failure prevention technology*, pages 623–634, 2000.

[12] R. Bajric, D. Sprecic, and N. Zuber. Review of vibration signal processing techniques towards gear pairs damage identification. *International Journal of Engineering & Technology*, 11(4):124–128, 2011.

[13] K. S. Jardine, D. Lin, and D. Banjevic. A review on machinery diagnostics and prognostics implementing condition-based maintenance. *Mechanical Systems and Signal Processing*, 20(7):1483–1510, 2006.

[14] X. Liang. *Dynamics Based Vibration Signal Modeling and Fault Detection of Planetary Gearboxes*. PhD thesis, University of Alberta, 2016.

[15] D. Lockner. The role of acoustic emission in the study of rock fracture. *International Journal of Rock Mechanics and Mining Sciences & Geomechanics Abstracts*, 30(7):883–899, 1993.

[16] C. K. Tan, P. Irving, and D. Mba. A comparative experimental study on the diagnostic and prognostic capabilities of acoustics emission, vibration and spectrometric oil analysis for spur gears. *Mechanical Systems and Signal Processing*, 21(1):208–233, 2007.

[17] J. Yoon, D. He, and B. V. Hecke. On the use of a single piezoelectric strain sensor for wind turbine planetary gearbox fault diagnosis. *IEEE Transactions on Industrial Electronics*, 62(10):6585–6593, 2015.

[18] N. B. Salem, M. K. Budzik, J. Jumel, M. E. R. Shanahan, and F. Lavelle. Investigation of the crack front process zone in the double cantilever beam test with backface strain monitoring technique. *Engineering Fracture Mechanics*, 98:272–283, 2013.

[19] P. J. Dempsey. A comparison of vibration and oil debris gear damage detection methods applied to pitting damage. Technical report, Glenn Research Center, NASA, 2000.

[20] P. D. McFadden and J. D. Smith. An explanation for the asymmetry of the modulation sidebands about the tooth meshing frequency in epicyclic gear vibration. *Proceedings of the Institution of Mechanical Engineers, Part C: Journal of Mechanical Engineering Science*, 199(1):65–70, 1985.

[21] Y. Guo and R. G. Parker. Analytical determination of mesh phase relations in general compound planetary gears. *Mechanism and Machine Theory*, 46(12):1869–1887, 2011.

[22] M. Inalpolat and A. Kahraman. A theoretical and experimental investigation of modulation sidebands of planetary gear sets. *Journal of Sound and Vibration*, 323(3):677–696, 2009.

[23] X. Liang, M. J. Zuo, and M. Pandey. Analytically evaluating the influence of crack on the mesh stiffness of a planetary gear set. *Mechanism and Machine Theory*, 76:20–38, 2014.

[24] P. D. McFadden. A technique for calculating the time domain averages of the vibration of the individual planet gears and the sun gear in an epicyclic gearbox. *Journal of Sound and Vibration*, 144(1):163–172, 1991.

[25] Z. Feng and M. J. Zuo. Vibration signal models for fault diagnosis of planetary gearboxes. *Journal of Sound and Vibration*, 331(22):4919–4939, 2012.

[26] M. Inalpolat and A. Kahraman. A dynamic model to predict modulation sidebands of a planetary gear set having manufacturing errors. *Journal of Sound and Vibration*, 329(4):371–393, 2010.

[27] X. Liang, M. J. Zuo, and M. R. Hoseini. Vibration signal modeling of a planetary gear set for tooth crack detection. *Engineering Failure Analysis*, 48:185–200, 2015.

[28] B. D. Forrester. *Advanced Vibration Analysis Techniques for Fault Detection and Diagnosis in Geared Transmission Systems*. PhD thesis, Swinburne University of Technology, 1996.

[29] J. Qu. *Support-Vector-Machine-Based Diagnostics and Prognostics for Rotating Systems*. PhD thesis, University of Alberta, 2011.

[30] S. Tian and Z. Qian. Planetary gearbox fault feature enhancement based on combined adaptive filter method. *Advances in Mechanical Engineering*, 7(12):1–12, 2015.

[31] J. Sanz-Corretge, O. Lúquin, and A. García-Barace. An efficient demodulation technique for wind turbine tower resonance monitoring. *Wind Energy*, 17(8):1179–1197, 2014.

[32] J. Wang and Q. He. Exchanged ridge demodulation of time-scale manifold for enhanced fault diagnosis of rotating machinery. *Journal of Sound and Vibration*, 333(11):2450–2464, 2014.

[33] D. G. Lewicki, K. E. LaBerge, R. T. Ehinger, and J. Fetty. Planetary gearbox fault detection using vibration separation techniques. Technical report, Glenn Research Center, NASA, 2011.

[34] S. Goldman. *Vibration Spectrum Analysis: A Practical Approach*. Industrial Press Inc., 1999.

[35] R. B. Randall. A new method of modeling gear faults. *Journal of Mechanical Design*, 104(2):259–267, 1982.

[36] P. P. Schon. *Unconditionally Convergent Time Domain Adaptive and Time-Frequency Techniques for Epicyclic Gearbox Vibration*. PhD thesis, University of Pretoria, 2007.

[37] E. Wigner. On the quantum correction for thermodynamic equilibrium. *Physical Review*, 40(5):749–759, 1932.

[38] J. G. Kirkwood. Quantum statistics of almost classical assemblies. *Physical Review*, 44(1):31–37, 1933.

[39] D. Gabor. Theory of communication. part 1: The analysis of information. *Journal of the Institution of Electrical Engineers-Part III: Radio and Communication Engineering*, 93(26):429–441, 1946.

[40] J. Ville. Théorie et applications de la notion de signal analytique. *Cables et Transmission*, 2(1):61–74, 1948.

[41] C. H. Page. Instantaneous power spectra. *Journal of Applied Physics*, 23(1):103–106, 1952.

[42] L. Cohen. Time-frequency distributions-a review. *Proceedings of the IEEE*, 77(7):941–981, 1989.

[43] Z. Feng, M. Liang, and F. Chu. Recent advances in time–frequency analysis methods for machinery fault diagnosis: A review with application examples. *Mechanical Systems and Signal Processing*, 38(1):165–205, 2013.

[44] H. K. Kwok and D. L. Jones. Improved instantaneous frequency estimation using an adaptive short-time fourier transform. *IEEE Transactions on Signal Processing*, 48(10):2964–2972, 2000.

[45] S. Mallat. *A Wavelet Tour of Signal Processing: The Sparse Way*. Academic press, 2008.

[46] L. Debnath and F. A. Shah. The wigner–ville distribution and time–frequency signal analysis. In *Wavelet Transforms and their Applications*, pages 287–336. Springer, 2015.

[47] L. Cohen and T. Posch. Positive time-frequency distribution functions. *IEEE Transactions on Acoustics, Speech, and Signal Processing*, 33(1):31–38, 1985.

[48] M. Davy and A. Doucet. Copulas: a new insight into positive time-frequency distributions. *IEEE Signal Processing Letters*, 10(7):215–218, 2003.

[49] A. Kahraman. Planetary gear train dynamics. *Transactions-American Society of Mechanical Engineers Journal of Mechanical Design*, 116:713–713, 1994.

[50] R. G. Parker and J. Lin. Mesh phasing relationships in planetary and epicyclic gears. *Transactions-American Society of Mechanical Engineers Journal of Mechanical Design*, 126(2):365–369, 2004.

[51] X. Liang, M. J. Zuo, and Z. Feng. Dynamic modeling of gearbox faults: A review. *Mechanical Systems and Signal Processing*, 98:852–876, 2018.

[52] G. Li, F. Li, Y. Wang, and D. Dong. Fault diagnosis for a multistage planetary gear set using model-based simulation and experimental investigation. *Shock and Vibration*, 2016, 2016.

[53] J. McNames. Fourier series analysis of epicyclic gearbox vibration. *Journal of Vibration and Acoustics*, 124(1):150–153, 2002.

[54] A. L. Gu and R. H. Badgley. Planet-pass-induced vibration in planetary reduction gears. *Mechanical Engineering*, 96(12):63–63, 1974.

[55] A. L. Gu and R. H. Badgley. Prediction of vibration sidebands in gear meshes. *Mechanical Engineering*, 96(12):63–63, 1974.

[56] D. G. Lewicki and J. J. Coy. Vibration characteristics of OH-58A helicopter main rotor transmission. Technical report, Lewis Research Center, NASA, 1987.

[57] M. Mosher. Results from a new separation algorithm for planetary gear system vibration measurements. In *Proceedings of ASME International Design Engineering Technical Conferences and Computers and Information in Engineering Conference*, pages 1–8, 2005.

[58] W. Yu. *Dynamic Modelling of Gear Transmission Systems with and without Localized Tooth Defects*. PhD thesis, Queen's University (Canada), 2017.

[59] J. Lin and R. G. Parker. Mesh stiffness variation instabilities in two-stage gear systems. *Journal of Vibration and Acoustics*, 124(1):68–76, 2002.

[60] W. Kim, J. Y. Lee, and J. Chung. Dynamic analysis for a planetary gear with time-varying pressure angles and contact ratios. *Journal of Sound and Vibration*, 331(4):883–901, 2012.

[61] X. Liang, M. J. Zuo, and T. H. Patel. Evaluating the time-varying mesh stiffness of a planetary gear set using the potential energy method. *Proceedings of the Institution of Mechanical Engineers, Part C: Journal of Mechanical Engineering Science*, 228(3):535–547, 2014.

[62] D. C. H. Yang and J. Y. Lin. Hertzian damping, tooth friction and bending elasticity in gear impact dynamics. *Journal of Mechanisms, Transmissions, and Automation in Design*, 109(2):189–196, 1987.

[63] X. Tian, M. J. Zuo, and K. R. Fyfe. Analysis of the vibration response of a gearbox with gear tooth faults. In *Proceedings of ASME International Mechanical Engineering Congress and Exposition*, pages 1–9, 2004.

[64] S. Wu, M. J. Zuo, and A. Parey. Simulation of spur gear dynamics and estimation of fault growth. *Journal of Sound and Vibration*, 317(3):608–624, 2008.

[65] X. Zhou, Y. Shao, Y. Lei, and M. J. Zuo. Time-varying meshing stiffness calculation and vibration analysis for a 16DOF dynamic model with linear crack growth in a pinion. *Journal of Vibration and Acoustics*, 134(1):1–11, 2012.

[66] X. Liang, M. J. Zuo, and L. Liu. A windowing and mapping strategy for gear tooth fault detection of a planetary gearbox. *Mechanical Systems and Signal Processing*, 80:445–459, 2016.

[67] S. A. Abouel-seoud, E. S. Dyab, and M. S. Elmorsy. Influence of tooth pitting and cracking on gear meshing stiffness and dynamic response of wind turbine gearbox. *International Journal of Science and Advanced Technology*, 2(3):151–165, 2012.

[68] Z. Chen and Y. Shao. Dynamic features of a planetary gear system with tooth crack under different sizes and inclination angles. *Journal of Vibration and Acoustics*, 135(3):1–12, 2013.

[69] C. G. Cooley and R. G. Parker. A review of planetary and epicyclic gear dynamics and vibrations research. *Applied Mechanics Reviews*, 66(4):1–15, 2014.

[70] S. De and W. Clarence. *Modeling and Control of Engineering Systems*. CRC Press, 2009.

[71] A. Kahraman. Load sharing characteristics of planetary transmissions. *Mechanism and Machine Theory*, 29(8):1151–1165, 1994.

[72] J. Lin and R. G. Parker. Analytical characterization of the unique properties of planetary gear free vibration. *Journal of Vibration and Acoustics*, 121(3):316–321, 1999.

[73] F. Chaari, T. Fakhfakh, R. Hbaieb, J. Louati, and M. Haddar. Influence of manufacturing errors on the dynamic behavior of planetary gears. *The International Journal of Advanced Manufacturing Technology*, 27(7-8):738–746, 2006.

[74] Z. Cheng, N. Hu, F. Gu, and G. Qin. Pitting damage levels estimation for planetary gear sets based on model simulation and grey relational analysis. *Transactions of the Canadian Society for Mechanical Engineering*, 35(3):403–417, 2011.

[75] Z. Chen and Y. Shao. Dynamic simulation of planetary gear with tooth root crack in ring gear. *Engineering Failure Analysis*, 31:8–18, 2013.

[76] D. J. Inman. *Engineering Vibration*. Prentice Hall New Jersey, 2008.

[77] J. A. Keller and P. Grabill. Vibration monitoring of UH-60A main transmission planetary carrier fault. In *Annual Forum Proceedings-American Helicopter Society*, pages 1–11. American Helicopter Society, 2003.

[78] B. Wu, A. Saxena, T. S. Khawaja, R. Patrick, G. Vachtsevanos, and P. Sparis. An approach to fault diagnosis of helicopter planetary gears. In *Proceedings of Autotestcon*, pages 475–481. IEEE, 2004.

[79] P. D. McFadden and I. M. Howard. The detection of seeded faults in an epicyclic gearbox by signal averaging of the vibration. Technical report, Aeronautical Research Labs Melbourne (Australia), 1990.

[80] P. D. McFadden. Window functions for the calculation of the time domain averages of the vibration of the individual planet gears and sun gear in an epicyclic gearbox. *Transactions-American Society of Mechanical Engineers Journal of Vibration and Acoustics*, 116:179–187, 1994.

[81] F. Combet and L. Gelman. An automated methodology for performing time synchronous averaging of a gearbox signal without speed sensor. *Mechanical Systems and Signal Processing*, 21(6):2590–2606, 2007.

[82] P. Sparis and G. Vachtsevanos. A helicopter planetary gear plate crack analysis and feature extraction based on ground and aircraft data. In *Proceedings of the 2005 IEEE International Symposium on, Mediterrean Conference on Control and Automation Intelligent Control, 2005*, pages 646–651. IEEE, 2005.

[83] L. Hong and J. S. Dhupia. A time domain approach to diagnose gearbox fault based on measured vibration signals. *Journal of Sound and Vibration*, 333(7):2164–2180, 2014.

[84] K. R. Fyfe and E. S. Munck. Analysis of computed order tracking. *Mechanical Systems and Signal Processing*, 11(2):187–205, 1997.

[85] J. A. Hines, D. S. Muench, J. A. Keller, and A. K. Garga. Effects of time-synchronous averaging implementations on HUMS features for UH-60A planetary carrier cracking. In *61st Annual Forum Proceedings-American Helicopter Society*, pages 1–10. American Helicopter Society, 2005.

[86] P. Sparis and G. Vachtsevanos. Automatic diagnostic feature generation via the fast fourier transform. Technical report, Democritus University of Thrace and Georgia Institute of Technology.

[87] W. D Mark and J. A. Hines. Stationary transducer response to planetary-gear vibration excitation with non-uniform planet loading. *Mechanical Systems and Signal Processing*, 23(4):1366–1381, 2009.

[88] W. D. Mark. Stationary transducer response to planetary-gear vibration excitation ii: effects of torque modulations. *Mechanical Systems and Signal Processing*, 23(7):2253–2259, 2009.

[89] W. D. Mark, H. Lee, R. Patrick, and J. D. Coker. A simple frequency-domain algorithm for early detection of damaged gear teeth. *Mechanical Systems and Signal Processing*, 24(8):2807–2823, 2010.

[90] Y. Lei, D. Kong, J. Lin, and M. J. Zuo. Fault detection of planetary gearboxes using new diagnostic parameters. *Measurement Science and Technology*, 23(5):1–10, 2012.

[91] Y. Lei, N. Li, J. Lin, and Z. He. Two new features for condition monitoring and fault diagnosis of planetary gearboxes. *Journal of Vibration and Control*, 21(4):755–764, 2015.

[92] P. D. Samuel and D. J. Pines. Health monitoring and damage detection of a rotorcraft planetary geartrain system using piezoelectric sensors. In *Proceedings of SPIE 3041*, pages 44–53, 1997.

[93] P. D. Samuel and D. J. Pines. Vibration separation methodology for planetary gear health monitoring. In *Proceedings-SPIE The International Society for Optical Engineering*, pages 250–260. International Society for Optical Engineering, 2000.

[94] G. Meltzer and Y. Y. Ivanov. Fault detection in gear drives with non-stationary rotational speed-part i: the time-frequency approach. *Mechanical Systems and Signal Processing*, 17(5):1033–1047, 2003.

[95] G. Meltzer and Y. Y. Ivanov. Fault detection in gear drives with non-stationary rotational speed-part ii: the time-quefrency approach. *Mechanical Systems and Signal Processing*, 17(2):273–283, 2003.

[96] A. Saxena, B. Wu, and G. Vachtsevanos. A methodology for analyzing vibration data from planetary gear systems using complex Morlet wavelets. In *Proceedings of the 2005 American Control Conference*, pages 4730–4735. IEEE, 2005.

[97] P. D. Samuel and D. J. Pines. Constrained adaptive lifting and the cal4 metric for helicopter transmission diagnostics. *Journal of Sound and Vibration*, 319(1):698–718, 2009.

[98] R. Zimroz, F. Millioz, and N. Martin. A procedure of vibration analysis from planetary gearbox under non-stationary cyclic operations by instantaneous frequency estimation in time-frequency domain. In *Conference on Condition Monitoring and Machinery Failure Prevention Technologies (CM and MFPT 2010)*, page nc, 2010.

[99] R. Zimroz, J. Urbanek, T. Barszcz, W. Bartelmus, F. Millioz, and N. Martin. Measurement of instantaneous shaft speed by advanced vibration signal processing-application to wind turbine gearbox. *Metrology and Measurement Systems*, 18(4):701–712, 2011.

[100] Y. Jiang, B. Tang, Y. Qin, and W. Liu. Feature extraction method of wind turbine based on adaptive morlet wavelet and svd. *Renewable Energy*, 36(8):2146–2153, 2011.

[101] Z. Feng and M. Liang. Fault diagnosis of wind turbine planetary gearbox under nonstationary conditions via adaptive optimal kernel time–frequency analysis. *Renewable Energy*, 66:468–477, 2014.

[102] F. Hlawatsch and G. F. Boudreaux-Bartels. Linear and quadratic time-frequency signal representations. *IEEE Signal Processing Magazine*, 9(2):21–67, 1992.

[103] N. Hess-Nielsen and M. V. Wickerhauser. Wavelets and time-frequency analysis. *Proceedings of the IEEE*, 84(4):523–540, 1996.

[104] O. Rioul and P. Flandrin. Time-scale energy distributions: A general class extending wavelet transforms. *IEEE Transactions on Signal Processing*, 40(7):1746–1757, 1992.

[105] F. Auger and P. Flandrin. Improving the readability of time-frequency and time-scale representations by the reassignment method. *IEEE Transactions on Signal Processing*, 43(5):1068–1089, 1995.

[106] X. Chen and Z. Feng. Iterative generalized time–frequency reassignment for planetary gearbox fault diagnosis under nonstationary conditions. *Mechanical Systems and Signal Processing*, 80:429–444, 2016.

[107] R. Yan, R. X. Gao, and X. Chen. Wavelets for fault diagnosis of rotary machines: A review with applications. *Signal Processing*, 96:1–15, 2014.

[108] L. Cohen. Representable local kinetic energy. *The Journal of Chemical Physics*, 80(9):4277–4279, 1984.

[109] J. R. Fonollosa. Positive time-frequency distributions based on joint marginal constraints. *IEEE Transactions on Signal Processing*, 44(8):2086–2091, 1996.

[110] D. Groutage. A fast algorithm for computing minimum cross-entropy positive time-frequency distributions. *IEEE Transactions on Signal Processing*, 45(8):1954–1970, 1997.

[111] M. K. Emresoy and P. J. Loughlin. Weighted least squares implementation of cohen-posch time-frequency distributions. *IEEE Transactions on Signal Processing*, 46(3):753–757, 1998.

[112] H. Yoshida, S. Kikkawa, H. Nakajima, and N. Kira. Positive time-frequency distributions: A least square approach and a copula-based approach. *Memoirs of the School of Biology-Oriented Science and Technology of Kinki University*, (13):57–71, 2004.

[113] A. Francos and M. Porat. Analysis and synthesis of multicomponent signals using positive time-frequency distributions. *IEEE Transactions on Signal Processing*, 47(2):493–504, 1999.

[114] J. W. Pitton, L. E. Atlas, and P. J. Loughlin. Applications of positive time-frequency distributions to speech processing. *IEEE Transactions on Speech and Audio Processing*, 2(4):554–566, 1994.

[115] M. Sklar. Fonctions de répartitionan dimensions et leurs marges. *Université Paris*, 8:229–231, 1959.

[116] B. Zhang, T. Khawaja, R. Patrick, and G. Vachtsevanos. Blind deconvolution denoising for helicopter vibration signals. *IEEE/ASME Transactions on Mechatronics*, 13(5):558–565, 2008.

[117] B. Zhang, T. Khawaja, R. Patrick, G. Vachtsevanos, M. E. Orchard, and A. Saxena. Application of blind deconvolution denoising in failure prognosis. *IEEE Transactions on Instrumentation and Measurement*, 58(2):303–310, 2009.

[118] B. Zhang, T. Khawaja, R. Patrick, G. Vachtsevanos, M. E. Orchard, and A. Saxena. A novel blind deconvolution de-noising scheme in failure prognosis. *Transactions of the Institute of Measurement and Control*, 32(1):3–30, 2010.

[119] T. Barszcz and R. B. Randall. Application of spectral kurtosis for detection of a tooth crack in the planetary gear of a wind turbine. *Mechanical Systems and Signal Processing*, 23(4):1352–1365, 2009.

[120] W. Bartelmus. *Vibration Diagnostic Method for Planetary Gearboxes Under Varying External Load With Regard To Cyclostationary Analysis*. Oficyna Wydawnicza Politechniki Wrocĺawskiej, 2009.

[121] R. Zimroz and W. Bartelmus. Gearbox condition estimation using cyclo-stationary properties of vibration signal. *Key Engineering Materials*, 413:471–478, 2009.

[122] R. Zimroz and A. Bartkowiak. Two simple multivariate procedures for monitoring planetary gearboxes in non-stationary operating conditions. *Mechanical Systems and Signal Processing*, 38(1):237–247, 2013.

[123] Y. Lei, D. Han, J. Lin, and Z. He. Planetary gearbox fault diagnosis using an adaptive stochastic resonance method. *Mechanical Systems and Signal Processing*, 38(1):113–124, 2013.

[124] M. J. Zuo, J. Lin, and X. Fan. Feature separation using ICA for a one-dimensional time series and its application in fault detection. *Journal of Sound and Vibration*, 287(3):614–624, 2005.

[125] J. Wang, R. X. Gao, and R. Yan. Integration of EEMD and ICA for wind turbine gearbox diagnosis. *Wind Energy*, 17(5):757–773, 2014.

[126] A. Sotiras, S. M. Resnick, and C. Davatzikos. Finding imaging patterns of structural covariance via non-negative matrix factorization. *NeuroImage*, 108:1–16, 2015.

[127] T. Han, D. Jiang, X. Zhang, and Y. Sun. Intelligent diagnosis method for rotating machinery using dictionary learning and singular value decomposition. *Sensors*, 17(4):689, 2017.

[128] H. Chin, K. Danai, and D. G. Lewicki. Fault detection of helicopter gearboxes using the multi-valued influence matrix method. *Journal of Mechanical Design*, 117(2A):248–253, 1995.

[129] P. D. Samuel and D. J. Pines. Classifying helicopter gearbox faults using a normalized energy metric. *Smart Materials and Structures*, 10(1):145, 2001.

[130] M. Dong, D. He, P. Banerjee, and J. Keller. Equipment health diagnosis and prognosis using hidden semi-markov models. *The International Journal of Advanced Manufacturing Technology*, 30(7-8):738–749, 2006.

[131] R. Li, D. He, and E. Bechhoefe. Investigation on fault detection for split torque gearbox using acoustic emission and vibration signals. In *Annual Conference of the Prognostics and Health Management Society*, pages 1–11, 2009.

[132] Z. Liu, M. J. Zuo, J. Qu, and H. Xu. Classification of gear damage levels in planetary gearboxes. In *2011 IEEE International Conference on Computational Intelligence for Measurement Systems and Applications*, pages 1–5. IEEE, 2011.

[133] J. Qu, Z. Liu, M. J. Zuo, and H. Z. Huang. Feature selection for damage degree classification of planetary gearboxes using support vector machine. *Proceedings of the Institution of Mechanical Engineers, Part C: Journal of Mechanical Engineering Science*, 225(9):2250–2264, 2011.

[134] Z. Liu, M. J. Zuo, and H. Xu. Feature ranking for support vector machine classification and its application to machinery fault diagnosis. *Proceedings of the Institution of Mechanical Engineers, Part C: Journal of Mechanical Engineering Science*, 227(9):2077–2089, 2013.

[135] M. Khazaee, H. Ahmadi, M. Omid, and A. Moosavian. An appropriate approach for condition monitoring of planetary gearbox based on fast fourier transform and least-square support vector machine. *International Journal of Multidisciplinary Sciences and Engineering*, 3(5):22–26, 2012.

[136] Y. Lei, J. Lin, Z. He, and D. Kong. A method based on multi-sensor data fusion for fault detection of planetary gearboxes. *Sensors*, 12(2):2005–2017, 2012.

[137] J. Dybała. Vibrodiagnostics of gearboxes using nbv-based classifier: A pattern recognition approach. *Mechanical Systems and Signal Processing*, 38(1):5–22, 2013.

[138] M. Zagórski and M. Orkisz. Dependence structure analysis of the inverter operational data by means of copula theory. *Mechanical Systems and Signal Processing*, 40(2):439–451, 2013.

[139] L. Qu, H. Chen, and Y. Tu. Nonparametric copula density estimation in sensor networks. In *2011 Seventh International Conference on Mobile Ad-hoc and Sensor Networks*, pages 1–8. IEEE, 2011.

[140] L. Liu, X. Liang, and M. J. Zuo. Vibration signal modeling of a planetary gear set with transmission path effect analysis. *Measurement*, 85:20–31, 2016.

[141] L. Liu, X. Liang, and M. J. Zuo. Vibration signal modeling for a planetary gear set. In *19th World Conference on Non-Destructive Testing*, pages 1–8, 2016.

[142] L. Liu and M. J. Zuo. Copula-based time-frequency distribution analysis for planetary gearbox fault detection. In *ASME 2017 International Design Engineering Technical Conferences and Computers and Information in Engineering Conference*, pages 1–8. ASME, 2017.

[143] L. Liu, X. Liang, and M. J. Zuo. Energy density construction by spectrogram-free non-parametric copula for planetary gearbox fault diagnosis. *Mechanical Systems and Signal Processing*, Revised, May 11, 2018.

[144] L. Liu and M. J. Zuo. Feature extraction by non-negative matrix factorization for planetary gearbox fault detection. *Journal of Sound and Vibration*, Submitted, May 09, 2018.

[145] L. Liu, M. J. Zuo, and X. Liang. Dependence analysis of planetary gearbox vibration marginals. In *2016 Prognostics and System Health Management Conference*, pages 1–6. IEEE, 2016.

[146] L. Liu, X. Liang, and M. J. Zuo. A dependence-based feature vector and its application on planetary gearbox fault classification. *Journal of Sound and Vibration*, Accepted, Jun. 06, 2018.

[147] J. Meagher, X. Wu, D. Kong, and C. H. Lee. A comparison of gear mesh stiffness modeling strategies. *Structural Dynamics*, 3:255–263, 2011.

[148] S. Jia and I. Howard. Comparison of localised spalling and crack damage from dynamic modelling of spur gear vibrations. *Mechanical Systems and Signal Processing*, 20(2):332–349, 2006.

[149] F. Chaari, W. Baccar, M. S. Abbes, and M. Haddar. Effect of spalling or tooth breakage on gearmesh stiffness and dynamic response of a one-stage spur gear transmission. *European Journal of Mechanics-A/Solids*, 27(4):691–705, 2008.

[150] F. Chaari, T. Fakhfakh, and M. Haddar. Analytical modelling of spur gear tooth crack and influence on gearmesh stiffness. *European Journal of Mechanics-A/Solids*, 28(3):461–468, 2009.

[151] A. Printz, R. Kasuba, J. L. Frater, and R. August. Dynamic effects of internal spur-gear drives. Technical report, Lewis Research Center, NASA, 1986.

[152] A. Al-Shyyab and A. Kahraman. A non-linear dynamic model for planetary gear sets. *Proceedings of the Institution of Mechanical Engineers, Part K: Journal of Multi-body Dynamics*, 221(4):567–576, 2007.

[153] M. Mosher. Understanding vibration spectra of planetary gear systems for fault detection. In *Proceedings of ASME Design Engineering Technical Conferences*, pages 1–8, 2003.

[154] X. Liang, M. J. Zuo, and M. R. Hoseini. Understanding vibration properties of a planetary gear set for fault detection. In *2014 IEEE Conference on Prognostics and Health Management*, pages 1–6. IEEE, 2014.

[155] D. S. Kim and J. S. Lee. Propagation and attenuation characteristics of various ground vibrations. *Soil Dynamics and Earthquake Engineering*, 19(2):115–126, 2000.

[156] F. Orban. Damping of materials and members in structures. *Journal of Physics: Conference Series*, 268(1):1–15, 2011.

[157] D. S. Carlstone. Radiation damping in the mechanical oscillator. *Proceedings of the Oklahoma Academy of Science*, 72:45–49, 1992.

[158] M. Hoseini, Y. Lei, J. Qu, X. Zhou, M. Pandey, and M. J. Zuo. Planetary gearbox test rig repeatability tests: data collection and analysis. Technical report, University of Alberta, 2010.

[159] S. Sheng and P. Veers. Wind turbine drivetrain condition monitoring-an overview. Technical report, National Renewable Energy Laboratory (NREL), Golden, CO., 2011.

[160] B. Boashash. *Time-frequency signal analysis and processing: a comprehensive reference*. Academic Press, 2015.

[161] G. Bai, B. Fleck, and M. J. Zuo. A stochastic power curve for wind turbines with reduced variability using conditional copula. *Wind Energy*, 19(8):1519–1534, 2016.

[162] F. Durante and C. Sempi. Copula theory: an introduction. In *Copula Theory and its Applications*, pages 3–31. Springer, 2010.

[163] W. C. Kallenberg. Estimating copula densities, using model selection techniques. *Insurance: Mathematics and Economics*, 45(2):209–223, 2009.

[164] S. X. Chen and T. M. Huang. Nonparametric estimation of copula functions for dependence modelling. *Canadian Journal of Statistics*, 35(2):265–282, 2007.

[165] C. Genest and A. C. Favre. Everything you always wanted to know about copula modeling but were afraid to ask. *Journal of Hydrologic Engineering*, 12(4):347–368, 2007.

[166] O. Scaillet, A. Charpentier, and J. D. Fermanian. The estimation of copulas: Theory and practice. In *Copulas: from Theory to Applications in Finance*, pages 36–62. London:Risk Books, 2007.

[167] T. Nagler, C. Schellhase, and C. Czado. Nonparametric estimation of simplified vine copula models: comparison of methods. *ArXiv Preprint ArXiv:1701.00845*, 2017.

[168] S. X. Chen. Beta kernel estimators for density functions. *Computational Statistics & Data Analysis*, 31(2):131–145, 1999.

[169] F. J. Harris. On the use of windows for harmonic analysis with the discrete fourier transform. *Proceedings of the IEEE*, 66(1):51–83, 1978.

[170] M. Pandey, T. Patel, X. Liang, T. Tian, and M. J. Zuo. Descriptions of pitting experiments, run-to-failure experiments, various load and speed experiments, and crack experiments carried out on the planetary gearbox test rig. Technical report, University of Alberta, 2011.

[171] Q. He, Z. Feng, and F. Kong. Detection of signal transients using independent component analysis and its application in gearbox condition monitoring. *Mechanical Systems and Signal Processing*, 21(5):2056–2071, 2007.

[172] R. B. Randall, N. Sawalhi, and M. Coats. A comparison of methods for separation of deterministic and random signals. *International Journal of Condition Monitoring*, 1(1):11–19, 2011.

[173] J. Y. Lee and A. K. Nandi. Extraction of impacting signals using blind deconvolution. *Journal of Sound and Vibration*, 232(5):945–962, 2000.

[174] W. X. Yang and W. T. Peter. Development of an advanced noise reduction method for vibration analysis based on singular value decomposition. *Ndt & E International*, 36(6):419–432, 2003.

[175] J. Antoni and R. B. Randall. Unsupervised noise cancellation for vibration signals: part I – evaluation of adaptive algorithms. *Mechanical Systems and Signal Processing*, 18(1):89–101, 2004.

[176] J. Antoni and R. B. Randall. Unsupervised noise cancellation for vibration signals: part II – a novel frequency-domain algorithm. *Mechanical Systems and Signal Processing*, 18(1):103–117, 2004.

[177] G. A. Skrimpas, T. Ursin, C. Sweeney, K. Marhadi, N. Mijatovic, and J. Holboell. Residual signal feature extraction for gearbox planetary stage fault detection. *Wind Energy*, 20(8):1389–1404, 2017.

[178] Z. Feng, F. Chu, and M. J. Zuo. Time–frequency analysis of time-varying modulated signals based on improved energy separation by iterative generalized demodulation. *Journal of Sound and Vibration*, 330(6):1225–1243, 2011.

[179] E. Sejdić, I. Djurović, and J. Jiang. Time–frequency feature representation using energy concentration: An overview of recent advances. *Digital Signal Processing*, 19(1):153–183, 2009.

[180] H. Shao, X. Shi, and L. Li. Power signal separation in milling process based on wavelet transform and independent component analysis. *International Journal of Machine Tools and Manufacture*, 51(9):701–710, 2011.

[181] Y. Yang and S. Nagarajaiah. Blind identification of damage in time-varying systems using independent component analysis with wavelet transform. *Mechanical Systems and Signal Processing*, 47(1-2):3–20, 2014.

[182] Z. Wu and N. E. Huang. Ensemble empirical mode decomposition: a noise-assisted data analysis method. *Advances in Adaptive Data Analysis*, 1(01):1–41, 2009.

[183] D. D. Lee and H. S. Seung. Learning the parts of objects by non-negative matrix factorization. *Nature*, 401(6755):788, 1999.

[184] J. Kim and H. Park. Sparse nonnegative matrix factorization for clustering. Technical report, Georgia Institute of Technology, 2008.

[185] J. Yoo and S. Choi. Orthogonal nonnegative matrix tri-factorization for co-clustering: Multiplicative updates on stiefel manifolds. *Information Processing & Management*, 46(5):559–570, 2010.

[186] C. Ding, X. He, and H. D. Simon. On the equivalence of nonnegative matrix factorization and spectral clustering. In *Proceedings of the 2005 SIAM International Conference on Data Mining*, pages 606–610. SIAM, 2005.

[187] H. Gao, L. Liang, X. Chen, and G. Xu. Feature extraction and recognition for rolling element bearing fault utilizing short-time fourier transform and non-negative matrix factorization. *Chinese Journal of Mechanical Engineering*, 28(1):96–105, 2015.

[188] A. C. Turkmen. A review of nonnegative matrix factorization methods for clustering. *arXiv preprint arXiv: 1507.03194*, 2015.

[189] E. Gaussier and C. Goutte. Relation between PLSA and NMF and implications. In *Proceedings of the 28th annual international ACM SIGIR conference on Research and development in information retrieval*, pages 601–602. ACM, 2005.

[190] C. Ding, T. Li, and W. Peng. On the equivalence between non-negative matrix factorization and probabilistic latent semantic indexing. *Computational Statistics & Data Analysis*, 52(8):3913–3927, 2008.

[191] N. Sawalhi, R. B. Randall, and H. Endo. The enhancement of fault detection and diagnosis in rolling element bearings using minimum entropy deconvolution combined with spectral kurtosis. *Mechanical Systems and Signal Processing*, 21(6):2616–2633, 2007.

[192] P. O. Hoyer. Non-negative matrix factorization with sparseness constraints. *Journal of Machine Learning Research*, 5(Nov):1457–1469, 2004.

[193] C. Hu, W. A. Smith, R. B. Randall, and Z. Peng. Development of a gear vibration indicator and its application in gear wear monitoring. *Mechanical Systems and Signal Processing*, 76:319–336, 2016.

[194] Y. Zhang, B. Tang, Y. Han, and L. Deng. Bearing performance degradation assessment based on time-frequency code features and som network. *Measurement Science and Technology*, 28(4):045601, 2017.

[195] Y. Zhang, H. Zuo, and F. Bai. Classification of fault location and performance degradation of a roller bearing. *Measurement*, 46(3):1178–1189, 2013.

[196] Y. Miao, M. Zhao, J. Lin, and Y. Lei. Application of an improved maximum correlated kurtosis deconvolution method for fault diagnosis of rolling element bearings. *Mechanical Systems and Signal Processing*, 92:173–195, 2017.

[197] L. G. Martins, S. D. Miller, and O. C. Acevedo. Using empirical mode decomposition to filter out non-turbulent contributions to air–sea fluxes. *Boundary-Layer Meteorology*, 163(1):123–141, 2017.

[198] J. C. Rodriguez. Measuring financial contagion: A copula approach. *Journal of Empirical Finance*, 14(3):401–423, 2007.

[199] J. B. Ali, N. Fnaiech, L. Saidi, B. Chebel-Morello, and F. Fnaiech. Application of empirical mode decomposition and artificial neural network for automatic bearing fault diagnosis based on vibration signals. *Applied Acoustics*, 89:16–27, 2015.

[200] M. Boumahdi, J. P. Dron, S. Rechak, and O. Cousinard. On the extraction of rules in the identification of bearing defects in rotating machinery using decision tree. *Expert Systems with Applications*, 37(8):5887–5894, 2010.

[201] M. Cerrada, R. V. Sánchez, C. Li, F. Pacheco, D. Cabrera, J. V. de Oliveira, and R. E. Vásquez. A review on data-driven fault severity assessment in rolling bearings. *Mechanical Systems and Signal Processing*, 99:169–196, 2018.

[202] Y. Lei, Z. He, and Y. Zi. Application of an intelligent classification method to mechanical fault diagnosis. *Expert Systems with Applications*, 36(6):9941–9948, 2009.

[203] N. E. Huang, Z. Shen, S. R. Long, M. C. Wu, H. H. Shih, Q. Zheng, N. C. Yen, C. C. Tung, and H. H. Liu. The empirical mode decomposition and the hilbert spectrum for nonlinear and non-stationary time series analysis. *Proceedings of the Royal Society of London A: Mathematical, Physical and Engineering Sciences*, 454(1971):903–995, 1998.

[204] Z. Feng, M. Liang, Y. Zhang, and S. Hou. Fault diagnosis for wind turbine planetary gearboxes via demodulation analysis based on ensemble empirical mode decomposition and energy separation. *Renewable Energy*, 47:112–126, 2012.

[205] Y. Lei, J. Lin, Z. He, and M. J. Zuo. A review on empirical mode decomposition in fault diagnosis of rotating machinery. *Mechanical Systems and Signal Processing*, 35(1):108–126, 2013.

[206] J. de Kort. Modeling tail dependence using copulas-literature review, 2007.

[207] P. Gangsar and R. Tiwari. Comparative investigation of vibration and current monitoring for prediction of mechanical and electrical faults in induction motor based on multiclass-support vector machine algorithms. *Mechanical Systems and Signal Processing*, 94:464–481, 2017.

[208] N. Cristianini and J. Shawe-Taylor. *An Introduction to Support Vector Machines and Other Kernel-Based Learning Methods*. Cambridge university press, 2000.

[209] C. W. Hsu and C. J. Lin. A comparison of methods for multiclass support vector machines. *IEEE Transactions on Neural Networks*, 13(2):415–425, 2002.

[210] M. Hoseini, Y. Lei, D. V. Tuan, T. Patel, and M. J. Zuo. Experiment design of four types of experiments: pitting experiments, run-to-failure experiments, various load and speed experiments, and crack experiments. Technical report, University of Alberta, 2011.

[211] J. Platt. Probabilistic outputs for support vector machines and comparisons to regularized likelihood methods. *Advances in Large Margin Classifiers*, 10(3):61–74, 1999.

[212] S. Kikkawa and H. Yoshida. On unification of equivalent bandwidths of a random process. *IEEE Signal Processing Letters*, 11(8):670–673, 2004.

[213] W. J. Williams, M. L. Brown, and A. O. Hero. Uncertainty, information, and time-frequency distributions. In *Advanced Signal Processing Algorithms, Architectures, and Implementations II*, volume 1566, pages 144–157. International Society for Optics and Photonics, 1991.

[214] F. Chaari, M. S. Abbes, F. V. Rueda, A. F. del Rincon, and M. Haddar. Analysis of planetary gear transmission in non-stationary operations. *Frontiers of Mechanical Engineering*, 8(1):88–94, 2013.

[215] Y. Lei, F. Jia, J. Lin, S. Xing, and S. X. Ding. An intelligent fault diagnosis method using unsupervised feature learning towards mechanical big data. *IEEE Transactions on Industrial Electronics*, 63(5):3137–3147, 2016.

[216] A. H. Tsang, W. K. Yeung, A. K. Jardine, and B. P. Leung. Data management for cbm optimization. *Journal of Quality in Maintenance Engineering*, 12(1):37–51, 2006.